



1

**2 Search for the Electroweak Production of  
3 Supersymmetric Particles in  
4 Three-Lepton Events at the ATLAS  
5 Detector with Focus on Compressed  
6 Mass Spectra**

7

**Yusufu Shehu**

8

QUALIFICATION Submitted for the degree of Doctor of Philosophy  
9 University of Sussex

10

DATE OF SUBMISSION: 30<sup>th</sup> June 2016

# **Declaration**

<sup>11</sup> I hereby declare that this thesis has not been and will not be submitted in whole or in  
<sup>12</sup> part to another University for the award of any other degree.

<sup>13</sup> Signature:

<sup>14</sup> Yusufu Shehu

16

UNIVERSITY OF SUSSEX

17

YUSUFU SHEHU, DOCTOR OF PHILOSOPHY

18

SEARCH FOR THE ELECTROWEAK PRODUCTION OF

19

SUPERSYMMETRIC PARTICLES IN THREE-LEPTON EVENTS

20

AT THE ATLAS DETECTOR WITH FOCUS ON COMPRESSED MASS SPECTRA

21

SUMMARY

22 This thesis presents a search for the electroweak production of supersymmetry using the  
 23 dataset taken by the ATLAS detector at the Large Hadron Collider with  $\sqrt{s} = 8$  TeV  
 24 during 2012. Events with three leptons are selected and required to satisfy additional  
 25 kinematic criteria that define optimised signal regions. In these signal regions, Stand-  
 26 ard Model processes are discriminated against, whilst retaining a large fraction of events  
 27 produced by specified compressed supersymmetry scenarios. Compressed refers to near  
 28 mass-degeneracy between the decaying gauginos and the final state gauginos. The expec-  
 29 ted number of Standard Model events are estimated using a combination of Monte Carlo  
 30 and data-driven methods, where the predictions are tested against data in specifically de-  
 31 signed validation regions. Exclusion limits are then set at 95% confidence level (CL) on  
 32 via  $\tilde{\ell}_L$ - and via WZ-decay scenarios for the decaying charginos and neutralinos. With the  
 33  $\tilde{\ell}_L$  halfway between the decaying charginos and neutralinos and the final state neutrali-  
 34 nos, there is a new sensitivity up to 250 GeV. In scenarios with large mass splitting, the  
 35 decaying chargino and neutralino masses are excluded up to 740 GeV. Looking forward  
 36 to the 13 TeV data-taking, a search for the electroweak production of supersymmetry  
 37 with three-lepton final states is presented, with a first look at an optimisation strategy to  
 38 improve sensitivity to charginos and neutralinos.

# <sup>39</sup> Acknowledgements

<sup>40</sup> There are many people I would like to acknowledge for helping me bring my PhD endeav-  
<sup>41</sup> ours to completion and I will do my best to list them. Firstly, I would like to thank my  
<sup>42</sup> supervisor Antonella De Santo for providing guidance, encouragement and support every  
<sup>43</sup> step of the way. Thanks to my second supervisor Fabrizio Salvatore for being a warm and  
<sup>44</sup> welcoming presence and a pleasure to work with.

<sup>45</sup> My student and post-doctoral colleagues within the Experimental Particle Physics  
<sup>46</sup> group at the University of Sussex have all been there to lend to the friendly and fun en-  
<sup>47</sup> vironment I have been privileged to work in. I would like to mention and thank Stewart  
<sup>48</sup> Martin-Haugh and Anthony Rose who have since moved on from the group and were there  
<sup>49</sup> during the first year of my PhD, when I asked the most questions and was in need of the  
<sup>50</sup> most guidance. Special thanks to Nicky Santoyo for all the help within the electroweak  
<sup>51</sup> SUSY multilepton group. I would like to give special thanks to Zara Grout, James Water-  
<sup>52</sup> field, Ed Leming, James Sinclair, Fabrizio Miano and Nicola Abraham for moral support  
<sup>53</sup> and countering stresses of analysis and deadlines with drink-breaks and great banter.  
<sup>54</sup> Thanks to Daniel Gibbon, who has since moved on from the group, Giuseppe, Fabio,  
<sup>55</sup> Olly, Tristan, Mark, Sam, Luke, Emma and Diana who have also made Sussex a great  
<sup>56</sup> place to be. Thanks to Mark Pickering for the fun times at CERN and various conferences.

<sup>57</sup> Thank you to all the friends I have made at University of Sussex and at CERN who  
<sup>58</sup> have also helped make my PhD experience enjoyable and full of memories.

<sup>59</sup> Finally I would like to thank my parents and my little sister for always encouraging  
<sup>60</sup> me to achieve whatever I set my mind to.

# <sup>61</sup> Contents

<sup>62</sup> <b>1</b>	<b>Introduction</b>	<b>1</b>
<sup>63</sup> <b>2</b>	<b>The Standard Model and Supersymmetry</b>	<b>2</b>
64	2.1 Introduction . . . . .	2
65	2.2 The Importance of Symmetries . . . . .	3
66	2.3 The Particle Zoo . . . . .	4
67	2.4 Forces of Nature . . . . .	5
68	2.4.1 Quantum Electrodynamics . . . . .	6
69	2.4.2 Electroweak Symmetry Breaking and the Higgs Mechanism . . . . .	7
70	2.4.3 Quantum Chromodynamics . . . . .	8
71	2.5 Limitations of the SM . . . . .	9
72	2.5.1 Hierarchy Problem . . . . .	9
73	2.5.2 Neutrino Masses . . . . .	10
74	2.5.3 Dark Matter . . . . .	10
75	2.6 Supersymmetry . . . . .	11
76	2.6.1 Motivations for SUSY . . . . .	13
77	2.6.2 The Minimal Supersymmetric Standard Model . . . . .	14
78	2.6.3 Soft SUSY Breaking . . . . .	15
79	2.6.4 MSSM Mass Spectra . . . . .	16
80	2.6.5 Naturalness in SUSY . . . . .	18
81	2.6.6 R-Parity . . . . .	19
82	2.6.7 Models of SUSY . . . . .	20
83	2.6.8 Simplified Models . . . . .	21
84	2.7 Motivation for Compressed Spectra SUSY . . . . .	23
<sup>85</sup> <b>3</b>	<b>The ATLAS Detector at the LHC</b>	<b>25</b>
86	3.1 The Large Hadron Collider . . . . .	25

87	<b>3.2 The ATLAS Detector</b>	27
88	<b>3.3 ATLAS Detector Geometry and Nomenclature</b>	28
89	<b>3.4 Magnet System</b>	29
90	<b>3.5 Inner Detector</b>	30
91	<b>3.5.1 Pixel Detector</b>	31
92	<b>3.5.2 Semiconductor Tracker</b>	31
93	<b>3.5.3 Transition Radiation Tracker</b>	32
94	<b>3.6 Calorimeters</b>	32
95	<b>3.6.1 The Electromagnetic Calorimeter</b>	33
96	<b>3.6.2 The Hadronic Calorimeter</b>	35
97	<b>3.7 Muon Spectrometer</b>	36
98	<b>3.8 Trigger and Data Acquisition System in Run-1</b>	38
99	<b>3.8.1 The ATLAS Trigger System</b>	38
100	<b>3.8.2 Trigger Chains and Menus</b>	41
101	<b>3.9 ATLAS Run-2 Upgrades</b>	43
102	<b>3.9.1 Insertable B-layer</b>	43
103	<b>3.9.2 ATLAS TDAQ Upgrades for Run-2</b>	43
104	<b>4 The Generation, Simulation and Reconstruction of ATLAS Data</b>	46
105	<b>4.1 Event Generation</b>	46
106	<b>4.1.1 Parton Distribution Functions</b>	48
107	<b>4.1.2 Matrix Element Calculation</b>	49
108	<b>4.1.3 Parton Showers</b>	49
109	<b>4.1.4 Hadronisation</b>	49
110	<b>4.1.5 Underlying Event</b>	50
111	<b>4.2 Detector Simulation</b>	50
112	<b>4.3 Digitisation</b>	51
113	<b>4.4 Reconstruction</b>	51
114	<b>4.4.1 Pile-up in the Inner Detector</b>	52
115	<b>4.4.2 Inner Detector Track Reconstruction</b>	52
116	<b>4.4.3 Vertex Reconstruction</b>	54
117	<b>4.4.4 Electron Reconstruction</b>	54
118	<b>4.4.5 Electron Identification</b>	55
119	<b>4.4.6 Muon Reconstruction and Identification</b>	58
120	<b>4.4.7 Jet Reconstruction</b>	60

121	4.4.8	Tau Reconstruction and Identification . . . . .	62
122	4.4.9	Missing Transverse Energy . . . . .	64
123	4.5	Object Selection for the Analysis . . . . .	66
124	4.5.1	Baseline Light Lepton Selection . . . . .	66
125	4.5.2	Baseline Jet Selection . . . . .	66
126	4.5.3	Baseline Tau Selection . . . . .	66
127	4.5.4	Overlap Removal . . . . .	66
128	4.5.5	Signal Electrons . . . . .	67
129	4.5.6	Signal Muons . . . . .	68
130	4.5.7	Signal Jet Selection . . . . .	69
131	4.5.8	Signal Tau Selection . . . . .	69
132	4.6	MC Samples . . . . .	69
133	4.6.1	MC Generators . . . . .	69
134	4.6.2	SM Background MC Samples For Run-1 . . . . .	70
135	4.6.3	MC Signal Samples For Run-1 . . . . .	73
136	4.6.4	SM Background MC Samples For Run-2 . . . . .	73
137	4.6.5	MC Signal Samples For Run-2 . . . . .	73
138	<b>5</b>	<b>The E/Gamma Signature Trigger on ATLAS</b>	<b>76</b>
139	5.1	Trigger Efficiency . . . . .	76
140	5.1.1	Determining Efficiencies with $Z \rightarrow ee$ events . . . . .	78
141	5.2	Data-Driven Efficiency Measurement . . . . .	78
142	5.2.1	Efficiency Measurement Results with Run-1 8 TeV Data . . . . .	79
143	5.3	The E/Gamma Signature Trigger Efficiency with Early Run-2 Data . . . . .	81
144	5.3.1	Likelihood-based (LH) Electron Identification for Run-2 . . . . .	81
145	5.3.2	Results and Trigger Performance . . . . .	82
146	<b>6</b>	<b>A Search for Electroweak SUSY in Three-Lepton Final States with Compressed Spectra in 8 TeV Data at ATLAS</b>	<b>87</b>
147	6.1	Introduction . . . . .	87
148	6.2	Analysis Overview . . . . .	88
149	6.3	Dataset and Event Selection . . . . .	89
150	6.3.1	Trigger Selection . . . . .	89
151	6.3.2	Event Cleaning . . . . .	90
152	6.4	Signal Region Optimisation . . . . .	91

154	6.4.1	Optimisation Strategy . . . . .	92
155	6.4.2	ISR Signal Region Procedure . . . . .	97
156	6.4.3	Soft Lepton Signal Region Procedure . . . . .	103
157	6.4.4	Signal Region Summary . . . . .	103
158	6.4.5	Significance in Soft Lepton and ISR Signal Regions . . . . .	106
159	6.5	Standard Model Background Estimation . . . . .	111
160	6.5.1	Standard Model Background Model Overview . . . . .	111
161	6.5.2	MC Background Estimation . . . . .	112
162	6.5.3	Data Driven Background Estimation: The Matrix Method . . . . .	113
163	6.6	Background Model Validation . . . . .	119
164	6.6.1	Validation Regions . . . . .	119
165	6.7	Systematic Uncertainties . . . . .	125
166	6.7.1	MC Statistics . . . . .	125
167	6.7.2	MC Cross Section . . . . .	125
168	6.7.3	PDF . . . . .	125
169	6.7.4	MC Background Uncertainties . . . . .	126
170	6.7.5	Electrons . . . . .	126
171	6.7.6	Muons . . . . .	126
172	6.7.7	Jets . . . . .	126
173	6.7.8	Missing Transverse Energy . . . . .	127
174	6.7.9	B-tagging Efficiency . . . . .	127
175	6.7.10	Trigger . . . . .	127
176	6.7.11	Luminosity . . . . .	127
177	6.7.12	Pile-up . . . . .	127
178	6.7.13	Signal . . . . .	128
179	6.7.14	Theoretical Systematic Uncertainties . . . . .	128
180	6.7.15	Systematic uncertainties on the reducible background . . . . .	133
181	6.7.16	Systematic Uncertainties Summary . . . . .	133
182	<b>7</b>	<b>Results and Interpretations for Run-1 Compressed Spectra SUSY Analysis</b>	<b>135</b>
183	7.1	Statistical Procedure . . . . .	135
184	7.1.1	The $CL_s$ Method . . . . .	135
185	7.1.2	Combination of Signal Regions . . . . .	138
186	7.2	Observations in 8 TeV Data . . . . .	138

188	7.2.1 Kinematic Distributions . . . . .	139
189	7.3 Statistical Interpretation of Results . . . . .	143
190	7.3.1 Model Independent Limits . . . . .	143
191	7.3.2 Model Dependent Limits: Simplified Models . . . . .	144
192	7.3.3 Summary of Electroweak SUSY Searches at 8 TeV . . . . .	145
193	<b>8 Looking Into the Future: A First Optimisation for an Electroweak SUSY</b>	
194	<b>Search with Three-Lepton Final States at 13 TeV</b>	148
195	8.1 Introduction . . . . .	148
196	8.2 Analysis Overview . . . . .	149
197	8.3 SUSY Simplified Models Considered . . . . .	149
198	8.4 Trigger Selection . . . . .	150
199	8.5 Object Selection . . . . .	150
200	8.5.1 Electrons . . . . .	150
201	8.5.2 Muons . . . . .	150
202	8.5.3 Jets . . . . .	151
203	8.5.4 Missing Transverse Momentum . . . . .	151
204	8.6 Signal Region Optimisation . . . . .	152
205	8.6.1 High Mass Signal Region - SR $3\ell$ -H . . . . .	153
206	8.6.2 Intermediate Mass Signal Region - SR $3\ell$ -I . . . . .	157
207	8.6.3 Signal Region Summary . . . . .	159
208	8.7 Significance in Signal Regions . . . . .	160
209	8.7.1 Significance in Intermediate Mass Signal Region . . . . .	160
210	8.7.2 Significance in High Mass Signal Region . . . . .	162
211	8.7.3 Combined Significance in Signal Regions . . . . .	162
212	<b>9 Conclusions</b>	167
213	<b>A Multilepton Trigger Results</b>	169
214	A.1 Introduction . . . . .	169
215	A.2 Three-Lepton Trigger Efficiencies . . . . .	170
216	<b>B Appendix B Systematic Uncertainties</b>	182
217	B.1 Introduction . . . . .	182
218	B.2 Glossary . . . . .	182
219	B.3 Systematic Uncertainty Figures . . . . .	184



# <sup>221</sup> Chapter 1

## <sup>222</sup> Introduction

<sup>223</sup> The content of this thesis is taken from work carried out during the author's PhD over  
<sup>224</sup> the course of just under 4 years on the ATLAS experiment [1] at the Large Hadron  
<sup>225</sup> Collider [2]. Two analyses are presented in this thesis, each searching for electroweak  
<sup>226</sup> production of supersymmetric particles. The  $\sqrt{s} = 8$  TeV analysis uses events containing  
<sup>227</sup> three electrons or muons and an initial state radiation (ISR) from the ATLAS dataset  
<sup>228</sup> taken in 2012. The  $\sqrt{s} = 13$  TeV analysis uses events containing three electrons or muons  
<sup>229</sup> with ATLAS Run-2 conditions. The results from the 8 TeV analysis were made public  
<sup>230</sup> in the Physical Review D journal in March 2016 [3]. Chapter 2 provides an overview  
<sup>231</sup> of the current status of particle physics theory, the unanswered questions of the current  
<sup>232</sup> model and an introduction to supersymmetry as an extension to this model. The Large  
<sup>233</sup> Hadron Collider and the ATLAS detector, which are used for producing and detecting the  
<sup>234</sup> high energy data used by this analysis are described in Chapter 3. Chapter 4 discusses  
<sup>235</sup> the electron/photon signature trigger in ATLAS, which is an essential signature for the  
<sup>236</sup> analyses described in this thesis. Chapter 5 discusses the software required to process data  
<sup>237</sup> collected at ATLAS and to produce simulated events. The 8 TeV three lepton analysis is  
<sup>238</sup> presented in Chapter 6 including the signal region optimisation, background estimation  
<sup>239</sup> and systematic uncertainties. The results of this analysis are then presented in Chapter  
<sup>240</sup> 7. The 13 TeV three lepton analysis is presented in Chapter 8 including the signal region  
<sup>241</sup> optimisation and expected sensitivity to considered supersymmetry scenarios.

## <sup>242</sup> Chapter 2

# <sup>243</sup> The Standard Model and <sup>244</sup> Supersymmetry

<sup>245</sup> The Standard Model (SM) is an effective theory motivated to provide a general description  
<sup>246</sup> of fundamental physical phenomena at the microscopic level. There are, however, some  
<sup>247</sup> limitations to the theory and unknown entities that are not addressed by the SM. Su-  
<sup>248</sup> persymmetry (SUSY) provides explanatory power and solutions to the limitations which  
<sup>249</sup> arise in the SM.

<sup>250</sup> This chapter gives an overview of the most successful model in particle physics, the  
<sup>251</sup> SM, starting with an introduction in Section 2.1 then the theoretical motivation, starting  
<sup>252</sup> from its basis in gauge invariance in Section 2.2. A description of the fundamental particles  
<sup>253</sup> and the forces that govern their behaviour in nature is presented in Sections 2.3 and 2.4  
<sup>254</sup> respectively, which includes the phenomenon of electroweak symmetry breaking and the  
<sup>255</sup> proposal of the existence of a new fundamental scalar (the Higgs boson). The limitations of  
<sup>256</sup> the SM are discussed in 2.5. SUSY as a theory beyond the SM is described and motivated  
<sup>257</sup> in Section 2.6. Finally, compressed SUSY scenarios, which are targeted specifically in this  
<sup>258</sup> thesis, is described and motivated theoretically in Section 2.7.

### <sup>259</sup> 2.1 Introduction

<sup>260</sup> During the 1960's and 1970's, through the combination of theory and experiment, a pre-  
<sup>261</sup> dictive model that describes many fundamental physical phenomena at the microscopic  
<sup>262</sup> level was developed, known as the SM [4]. It serves to explain the most fundamental  
<sup>263</sup> particles which make up all matter in existence and the interactions between them. It  
<sup>264</sup> is the most general renormalizable quantum field theory locally invariant under the trans-

265 formations of the gauge symmetry  $SU(3) \otimes SU(2) \otimes U(1)$ , which describes interactions of  
266 three of the four fundamental forces in nature (weak, electromagnetic (EM) and strong).

267 The SM predicts many measurable quantities that have been experimentally well  
268 verified, and has predicted the existence of particles prior to their discovery, for example  
269 the W boson, the Z boson and the  $\tau$  lepton [5]. The most recent discovery was that  
270 of the Higgs Boson at the Large Hadron Collider (LHC) in 2012 [6, 7], with a mass of  
271  $125.09 \pm 0.21(\text{stat.}) \pm 0.11(\text{syst.}) \text{ GeV}/c^2$  (combined CMS and ATLAS result [8]) falling well  
272 within the SM predicted mass of a missing large spin 0 scalar.

273 However, there are some problems with the SM: there is no inclusion of gravity as a  
274 quantum field theory; dark matter and dark energy has been observed or inferred experi-  
275 mentally which is not consistent with the current model; neutrino oscillations are observed  
276 yet there is no mechanism to explain the mass generation of neutrinos; the mass hierarchy  
277 of the SM particles is not explained.

278 Several theories serving as extensions to the SM have been developed since the 1970's [9].  
279 In these theories, the SM works as an effective theory in the low energy regime, whilst the  
280 extension has explanatory power in the higher energy regimes. A compelling theory for  
281 these regimes is SUSY, which is a proposed space-time symmetry that relates fermions  
282 (half integer spin) to bosons (integer spin). A new set of particles are postulated with  
283 masses much heavier (GeV-TeV scale) than those present in the SM, which could in prin-  
284 ciple be observed with high energy collider experiments. The search for SUSY will be the  
285 focus of most of the original work presented in later chapters.

## 286 2.2 The Importance of Symmetries

287 A symmetry is a property of a physical system, whether observed or intrinsic, which is pre-  
288 served or remains unchanged under some transformation. The transformations describing  
289 physical symmetries typically form a mathematical group, thus group theory is used to  
290 describe the symmetries conserved in the SM. Within quantum field theory, if the Lag-  
291 rangian is invariant under a continuous group of local transformations. This description of  
292 the Lagrangian is referred to as a gauge theory. Here gauge refers to the redundant degrees  
293 of freedom in the Lagrangian. Symmetries inherent in a gauge theory are known as gauge  
294 symmetries and these are the symmetries which exist in the SM. Gauge transformations  
295 refer to the transformations between possible gauges and collectively form a *Lie Group*,  
296 with an associated *Lie Algebra* of group generators. For each group generator therein  
297 arises a corresponding gauge field, which exists to ensure Lagrangian invariance under the

298 local group transformations (gauge invariance). The quanta of the gauge fields are called  
299 *gauge bosons*. Three of the four fundamental forces of nature can be described as gauge  
300 theories. Quantum electrodynamics is an Abelian gauge theory with the symmetry group  
301  $U(1)$  [10], and has one gauge field, the electromagnetic four-potential, and a single gauge  
302 boson, the photon. The strong and weak forces are associated with *non-Abelian* gauge  
303 groups. These groups have non-vanishing commutators between the generators for their  
304 gauge fields, which consequently means the gauge bosons can self interact. Non-Abelian  
305 Lie groups are used to describe elementary particle behaviour in the Yang-Mills theory.  
306 Quantum chromodynamics (QCD) is mediated by gauge bosons invariant under the non-  
307 Abelian group  $SU(3)$  and the weak theory is mediated by gauge bosons invariant under  
308 the non-Abelian group  $SU(2)$ .

### 309 2.3 The Particle Zoo

310 All particles that exist within the SM can be categorised into two groups based on the  
311 values of their spin. Fermions have half-integer spin values and are the matter particles,  
312 whilst bosons have integer-spin values. So-called gauge bosons form a subset of bosons  
313 with spin=1 and are the fundamental force mediators of the SM.

314 The six quarks of the SM are arranged into  $SU(2)$  doublets of three families:

$$\begin{pmatrix} u \\ d \end{pmatrix}, \begin{pmatrix} c \\ s \end{pmatrix}, \begin{pmatrix} t \\ b \end{pmatrix},$$

315 The up-type quarks (top half of the doublets shown above) have a fractional charge  
316 of  $+\frac{2}{3}e$  and the down-type quarks (bottom half of the doublets shown above) have a  
317 fractional charge of  $-\frac{1}{3}e$ , where  $e$  is the magnitude of the electron charge. All quarks  
318 possess a quantum number as an analogue to electric charge, known as colour charge. It  
319 can have three different values, labelled as “red”, “green” and “blue”. Due to *confinement*,  
320 a property which will be discussed in more detail in Section 2.4.3 quarks do not exist in  
321 isolation. Instead they group together to form *hadrons*. Hadrons containing three quarks  
322 are referred to as baryons, with the most common examples being the proton and the  
323 neutron. Each quark has a baryon number of  $\frac{1}{3}$ . Quark and anti-quark pairs can be  
324 bound together to form mesons.

Particle	Charge ( $e$ )	Mass [MeV]
Up (u)	$+\frac{2}{3}$	2.3
Down (d)	$-\frac{1}{3}$	4.8
Charm (c)	$+\frac{2}{3}$	1275
Strange (s)	$-\frac{1}{3}$	95
Top (t)	$+\frac{2}{3}$	173070
Bottom (b)	$-\frac{1}{3}$	4180

Table 2.1: Some properties of the three generations of quarks present within the SM [11].

325 There are three lepton generations: electron  $e$ , muon  $\mu$  and tau  $\tau$ , forming doublets  
 326 with an electrically neutral neutrino  $\nu_\alpha$  and charged lepton of the same flavour.

$$\begin{pmatrix} \nu_e \\ e^- \end{pmatrix}, \begin{pmatrix} \nu_\mu \\ \mu^- \end{pmatrix}, \begin{pmatrix} \nu_\tau \\ \tau^- \end{pmatrix},$$

327 Each lepton generation possesses a characteristic quantum number, called the lepton  
 328 number: the electron lepton number ( $L_e$ ), muon ( $L_\mu$ ) and tau lepton number ( $L_\tau$ ). Some  
 329 of the properties of the three lepton generations are summarised in Table 2.2.

Particle	Charge ( $e$ )	Mass [MeV]	$L_e$	$L_\mu$	$L_\tau$
$\nu_e$	0	$< 2.25 \times 10^{-7}$	1	0	0
$e^-$	-1	0.51	1	0	0
$\nu_\mu$	0	$< 0.19 \times 10^{-7}$	0	1	0
$\mu^-$	-1	105.66	0	1	0
$\nu_\tau$	0	$< 18.2 \times 10^{-7}$	0	0	1
$\tau^-$	-1	1776.82	0	0	1

Table 2.2: Some properties of the three generations of leptons present within the SM [11].

## 330 2.4 Forces of Nature

331 The fermionic particles in the SM interact via the electromagnetic (EM), weak and strong  
 332 forces. These interactions are mediated by vector gauge bosons. The EM force is as-  
 333 sociated with electric charge and therefore affects only charged leptons and quarks but  
 334 not the electrically neutral neutrinos. The weak force is related to particle *chirality* or  
 335 handedness, and only the left-handed components of particles experience the weak interac-  
 336 tion. The lepton and quark doublets discussed in Section 2.3 are comprised of left-handed

<sup>337</sup> components of the particles, which are accompanied by right-handed singlets:  $e_R^-, \mu_R^-, \tau_R^-$ ;  
<sup>338</sup> and  $u_R, d_R, s_R, c_R, b_R$  and  $t_R$ ; in the lepton and quark sectors respectively. Only the  
<sup>339</sup> left-handed component for neutrinos has been observed and only the right-handed com-  
<sup>340</sup> ponent for anti-neutrinos. This exclusivity in action of the weak force on only left-handed  
<sup>341</sup> particles violates parity conservation. Quark states which interact via the weak force are  
<sup>342</sup> mixtures of the mass eigenstates of the SM, as defined by the CKM mixing matrix [11].  
<sup>343</sup> The strong force is associated with colour charge and only interacts with particles with  
<sup>344</sup> colour charge, i.e. quarks and the strong force mediators, gluons  $g$ .

<sup>345</sup> The mathematical formulation of the fundamental forces will be covered in the fol-  
<sup>346</sup> lowing sections. Section 2.4.1 describes Quantum Electrodynamics (QED), the effective  
<sup>347</sup> description of the EM force. The weak interaction is discussed in unification with the  
<sup>348</sup> EM force, referred to as the electroweak interaction in Section 2.4.2. Finally, the strong  
<sup>349</sup> interaction is described almost independently of the electroweak interaction is discussed  
<sup>350</sup> with the formalism of Quantum Chromodynamics (QCD) in Section 2.4.3.

### <sup>351</sup> 2.4.1 Quantum Electrodynamics

<sup>352</sup> QED was the first theory to be developed which merges quantum mechanics and special  
<sup>353</sup> relativity. It is invariant under the unitary gauge group  $U(1)_Q$ , where  $Q$  refers to the  
<sup>354</sup> electric charge, which is the conserved charge in this interaction [5]. The gauge field,  
<sup>355</sup> which mediates the interaction between the charged spin- $\frac{1}{2}$  fields is the electromagnetic  
<sup>356</sup> field. The QED Lagrangian [12] for a spin- $\frac{1}{2}$  field  $\Psi$  with mass  $m$  interacting with the EM  
<sup>357</sup> field is given as:

$$\mathcal{L} = -\frac{1}{4}F_{\mu\nu}F^{\mu\nu} + \bar{\Psi}(i\gamma^\mu D_\mu - m)\Psi, \quad (2.1)$$

<sup>358</sup> where  $\gamma^\mu$  are the Dirac matrices. The electromagnetic field tensor  $F_{\mu\nu}$  is defined in  
<sup>359</sup> terms of the covariant four-potential of the EM field  $A_\nu$  as:

$$F_{\mu\nu} = \partial_\mu A_\nu - \partial_\nu A_\mu, \quad (2.2)$$

<sup>360</sup> where  $\partial_\mu$  is the derivative in four dimensional space-time derivative  $\frac{\partial}{\partial x_\mu}$ . The gauge  
<sup>361</sup> covariant derivative  $D_\mu$  is defined as:

$$D_\mu = \partial_\mu + iqA_\mu, \quad (2.3)$$

<sup>362</sup> where  $q$  is the electric charge of the spin- $\frac{1}{2}$  field. QED is an Abelian gauge theory,  
<sup>363</sup> meaning that the generators of the group all commute with one another. The physical  
<sup>364</sup> interpretation of this is the electrical neutrality of the photon and the fact that it does  
<sup>365</sup> not self-interact.

#### <sup>366</sup> 2.4.2 Electroweak Symmetry Breaking and the Higgs Mechanism

<sup>367</sup> The electroweak theory is an  $SU(2)_L \otimes U(1)_Y$  gauge symmetric field theory. It has four  
<sup>368</sup> gauge fields, three associated with weak isospin, these being the  $W_\mu^{i=1,2,3}$  fields. The  
<sup>369</sup> subscript on the  $SU(2)_L$  indicates that these fields only couple to left handed fermions.  
<sup>370</sup> The remaining  $B_\mu$  field couples to the weak hypercharge ( $Y$ ) of particles. In order to  
<sup>371</sup> obtain photon fields without coupling to neutrinos, the gauge bosons  $B_\mu$  and  $W_\mu^a$  are  
<sup>372</sup> required to mix as follows:

$$\begin{pmatrix} A_\mu \\ Z_\mu \end{pmatrix} = \begin{pmatrix} \cos \theta_W & \sin \theta_W \\ -\sin \theta_W & \cos \theta_W \end{pmatrix} \begin{pmatrix} B_\mu \\ W_\mu^3 \end{pmatrix}, \quad (2.4)$$

<sup>373</sup> where  $\theta_W$  is the weak mixing angle and can be expressed in terms of the coupling  
<sup>374</sup> strengths of the  $B_\mu$  ( $g_1$ ) and the  $W_\mu^a$  ( $g_2$ ) to the fermions:

$$\tan \theta_W = \frac{g_1}{g_2}, \quad (2.5)$$

<sup>375</sup> and

$$W_\mu^\pm = \frac{1}{\sqrt{2}}(W_\mu^1 \mp iW_\mu^2). \quad (2.6)$$

<sup>376</sup> The photon is identified with the field  $A_\mu$  and the Z and W bosons are manifestations  
<sup>377</sup> of the fields  $Z_\mu$  and  $W_\mu^\pm$ .

<sup>378</sup> The electroweak gauge symmetry forbids mass terms for the gauge bosons as well  
<sup>379</sup> as fermionic masses as they are not invariant under gauge transformations. This how-  
<sup>380</sup> ever is clearly contradicted by the measurements of the massive W and Z bosons. This  
<sup>381</sup> can be solved by introducing a Higgs field as a complex scalar Higgs doublet as shown  
<sup>382</sup> in Equation 2.7 to the model for mass generation through spontaneous symmetry break-  
<sup>383</sup> ing [13, 14, 15].

$$\phi = \begin{pmatrix} \phi^+ \\ \phi^0 \end{pmatrix} = \begin{pmatrix} G^+ \\ \frac{1}{\sqrt{2}}(v + H + iG^0) \end{pmatrix} \quad (2.7)$$

<sup>384</sup> This introduces a complex scalar field  $G^+$  and two real scalar fields  $H$  and  $G^0$ .  $G^+$  and  $G^0$   
<sup>385</sup> correspond to three spinless Goldstone bosons [16]. These massless scalars exist for each  
<sup>386</sup> spontaneously broken, continuous symmetry and are absorbed due to the gauge trans-  
<sup>387</sup> formations by the electroweak gauge bosons of the SM. The real scalar field  $H$  is referred  
<sup>388</sup> to as the SM Higgs boson field, whose ground state has a non-zero vacuum expectation  
<sup>389</sup> value (VEV)  $v$ . This can be represented as:

$$\Phi_0 = \begin{pmatrix} 0 \\ \frac{1}{\sqrt{2}}v \end{pmatrix}, \quad (2.8)$$

<sup>390</sup> which is still invariant under  $U(1)_{EM}$  guaranteeing electric charge conservation. As  
<sup>391</sup> a result, the SM gauge symmetry  $SU(3)_C \otimes SU(2)_L \otimes U(1)_Y$  is broken into  $SU(2)_L \otimes U(1)_Y$ .  
<sup>392</sup> The interaction of the Higgs field at this VEV with the  $SU(2)_L \otimes U(1)_Y$  gauge fields creates  
<sup>393</sup> screening currents, which result in the three  $W_\mu^{i=1,2,3}$  fields acquiring mass. The fourth  
<sup>394</sup> gauge field  $B^0$  remains massless. The Higgs field is reduced to a spinless scalar, corre-  
<sup>395</sup> sponding to a massive Higgs boson particle. The fermions do not gain non-zero mass values  
<sup>396</sup> as a result of electroweak symmetry breaking but afterwards due to interactions with the  
<sup>397</sup> Higgs boson.

### <sup>398</sup> 2.4.3 Quantum Chromodynamics

<sup>399</sup> QCD is the gauge field theory that describes the strong interactions of coloured quarks and  
<sup>400</sup> gluons and is the  $SU(3)_C$  component of the  $SU(3)_C \otimes SU(2)_L \otimes U(1)_Y$  SM. Here  $C$  refers  
<sup>401</sup> to colour charge. Each quark in the SM has three associated fields corresponding to the  
<sup>402</sup> different flavour states of red, green and blue. Quarks can be described as colour triplets  
<sup>403</sup> i.e.:

$$\mathbf{q} = \begin{pmatrix} q_r \\ q_g \\ q_b \end{pmatrix}.$$

<sup>404</sup> These triplets are invariant under  $SU(3)_C$  transformations, which describe strong in-  
<sup>405</sup> teractions. There are eight generators associated with this group, which correspond to the  
<sup>406</sup> eight gluon gauge fields, each of which is defined by a linear combination of colour and  
<sup>407</sup> anti-colour states. The group is non-Abelian. The physical interpretation of this is the

<sup>408</sup> self-interaction between gluons. The Lagrangian density of the strong force is:

$$\mathcal{L} = -\frac{1}{4} \sum_{a=1}^8 G_{\mu\nu}^a G^{a\mu\nu} + \sum_{f=1}^6 [\bar{\mathbf{q}}_f i\gamma^\mu (\partial_\mu + ig\mathbf{G}_\mu) \mathbf{q}_f - m_f \bar{\mathbf{q}}_f \mathbf{q}_f], \quad (2.9)$$

<sup>409</sup> where

$$\mathbf{G}_\mu = \frac{1}{2} \sum_{a=1}^8 G_\mu^a \lambda_a, \quad (2.10)$$

<sup>410</sup> is a sum over all the gluon states and  $\lambda_a$  are the *Gell-Mann matrices*. The index  $f$   
<sup>411</sup> refers to the quark flavours and  $\mathbf{q}$  are quark colour triplet states.

<sup>412</sup> The coupling of strong interactions increases with increasing distance, corresponding  
<sup>413</sup> to decreasing energy, and is smaller at short range, which corresponds to high energy.  
<sup>414</sup> This is due to gluon self interactions and has two main consequences. Firstly, in nature,  
<sup>415</sup> neither quarks nor gluons are observed as free particles. Only colourless “singlet” states  
<sup>416</sup> are observed. Tetra- and pentaquark states could in principle be realised in nature and  
<sup>417</sup> there are ongoing experiments verifying their existence [17]. This is referred to as confine-  
<sup>418</sup> ment and results in coloured particles at collider experiments being observed as “jets” -  
<sup>419</sup> collimated showers of hadronic particles which have formed in the detector. The second  
<sup>420</sup> consequence is that at higher energy the strong interaction is weaker, which is referred  
<sup>421</sup> to as *asymptotic freedom*, which allows the interaction to be calculated perturbatively,  
<sup>422</sup> whereas at lower energies, non-perturbative methods must be used, which is discussed in  
<sup>423</sup> detail in Section 4.1.1.

## <sup>424</sup> 2.5 Limitations of the SM

### <sup>425</sup> 2.5.1 Hierarchy Problem

<sup>426</sup> The fermion masses are introduced via coupling terms with the Higgs boson. However the  
<sup>427</sup> Higgs mass squared term receives corrections for each of these fermionic couplings due to  
<sup>428</sup> additional higher-order loops. The term due to fermionic loop coupling is given by:

$$\Delta m_H^2 = -\frac{|\lambda_f|^2}{8\pi^2} \Lambda_{UV}^2 + \dots, \quad (2.11)$$

<sup>429</sup> where only quadratic terms have been considered in this case. Here  $|\lambda_f|$  is the coupling  
<sup>430</sup> between the fermion and the Higgs field and  $\Lambda_{UV}$  is the ultraviolet momentum cut-off  
<sup>431</sup> which has been selected as the cut-off value for the loop integral. This cut-off choice is

432 required to correspond to the energy scale at which higher energy physics processes occur.  
 433 If this is set equal to the Planck mass  $M_{Pl} \simeq 2.4 \times 10^{18}$  GeV, which is the scale at which a  
 434 quantum field theory description of gravity becomes possible, then the one loop correction  
 435 to  $m_H^2$  would be more than 30 orders of magnitude larger than  $m_H^2$  itself. Furthermore,  
 436 this correction is independent of  $m_H^2$ . This implies that, in the context of the SM,  $m_H^2$  is  
 437 an unnatural parameter. Even if the quadratic divergences are renormalised, a residual  
 438 finite correction is left of the order of  $\frac{m_f^2 \lambda_f^2}{8\pi}$  (where  $m_f$  is the mass of the fermion). This  
 439 correction is manageably small for a SM fermion like the electron but an unnatural amount  
 440 of fine tuning would be required to cancel any contributions for any heavy fermions that  
 441 couple to the SM Higgs.

442 It is observed that the EM and weak interaction unify at  $\approx 100$  GeV however there  
 443 are no further unifications observed. This difference between the scale of electroweak  
 444 physics  $O(100$  GeV) and the Planck scale, with the absence of any new phenomena at any  
 445 intermediate energy scale, which is manifested in the quantum corrections to the Higgs  
 446 mass is known as the hierarchy problem [18].

### 447 **2.5.2 Neutrino Masses**

448 Within the SM, neutrinos do not couple to the Higgs boson as they are purely left-handed  
 449 in nature, therefore there is no mechanism for mass generation for the neutrinos. However,  
 450 measurements of the neutrino flux from solar and atmospheric sources as well as reactor  
 451 and accelerator based experiments support the idea that neutrinos can oscillate between  
 452 mass eigenstates, which is a feature that explicitly requires neutrinos to have mass [19].  
 453 Neutrino mass can be added to the SM in various ways. One approach involves adding  
 454 Majorana mass terms for the neutrinos and/or adding additional right-handed neutrinos  
 455 with a very heavy mass, known as the see-saw mechanism [20]. The addition of right-  
 456 handed neutrinos and other more exotic solutions involving new physics scales could reveal  
 457 physics beyond the SM.

### 458 **2.5.3 Dark Matter**

459 In the 1930's measurements of the orbital velocities of visible galactic matter in galaxies  
 460 against radial distance was performed [21]. It was observed that galaxies rotate at speeds  
 461 higher than expected given the amount of visible matter. To date there are only two  
 462 possible explanations: either general relativity must be modified at galactic distance scales,  
 463 or there is unseen matter that is responsible for the additional galactic mass. This would

imply that there exists another form of “dark” matter that does not interact via the electromagnetic force, and therefore neither emits nor reflects light. Further indications for dark matter are measurements of the cosmic microwave background and the gravitational lensing of galaxy clusters [22], such as the bullet cluster. One well-motivated postulate for the existence of dark matter is as yet undiscovered weakly interacting massive particles (WIMPs). Neutrinos have been proposed as dark matter candidates, but from the analysis of CMB anisotropies [23], combined with large-scale structure data, suggests that neutrinos are a sub-dominant component of non-baryonic dark matter. Even less is known about Dark Energy, which is a cosmological feature that arose from observations of the red-shift of supernovae in the universe as a function of distance [24]. It was seen that galaxies further away were expanding at a more rapid rate than what can be explained with particle physics and cosmology. It is accounted for in cosmological models with a cosmological constant but the explanation for the true nature of the phenomenon is still sought after.

There are other limitations to the SM. The generations of fermions are not explained, specifically, why there are three generations with apparently arbitrary mass differences; the matter dominance in the universe is not explained, as matter and anti-matter would be expected to be produced equally after the Big Bang, which would result in complete annihilation, with no matter in the universe. This can be explained by charge-parity (CP) violation, which allowed matter generating processes to occur at a higher frequency than anti-matter processes. Within the SM, CP is expected to be conserved and has yet to be experimentally shown to be violated to the degree required for the level of matter anti-matter asymmetry observed.

## 2.6 Supersymmetry

SUSY is a proposed space-time symmetry that relates fermions to bosons. A SUSY transformation transforms a bosonic state into a fermionic state and vice versa. The operator  $Q$  that generates transformations must be an anti-commuting spinor, with

$$Q|\text{Boson}\rangle = |\text{Fermion}\rangle, \quad Q|\text{Fermion}\rangle = |\text{Boson}\rangle. \quad (2.12)$$

Each SM particle has a supersymmetric partner, referred to as *sparticles*, with a difference in spin of  $\Delta s = \frac{1}{2}$ , and their symbols are identical to the SM convention but with an additional tilde. Spinors are intrinsically complex objects, so  $Q^\dagger$  is also a symmetry generator. The Coleman-Mandula theorem [25], implies that the generators  $Q$  and  $Q^\dagger$  must

<sup>494</sup> satisfy an algebra of anti-commutation and commutation relations as follows:

$$\{Q, Q^\dagger\} = P^\mu, \quad (2.13)$$

$$\{Q, Q\} = \{Q^\dagger, Q^\dagger\} = 0, \quad (2.14)$$

$$[P^\mu, Q] = [P^\mu, Q^\dagger] = 0, \quad (2.15)$$

<sup>495</sup> where  $P_\mu$  is the four-momentum generator of space-time translations. The first anti-  
<sup>496</sup> commutator relation returns the generator of space-time translations,  $P_\mu$ , which suggests  
<sup>497</sup> SUSY is in fact a *space-time* symmetry. The Coleman-Mandula theorem states that no  
<sup>498</sup> new space-time symmetries can exist with non-trivial Lorentz transformation properties,  
<sup>499</sup> but this is ignoring the instance where conserved quantities can transform as spinors.  
<sup>500</sup> Consequently, it is postulated that SUSY is the only possible extension of the known  
<sup>501</sup> space-time symmetries of particle physics.

<sup>502</sup> Each pair of partners is arranged in a *supermultiplet*, which is an irreducible repres-  
<sup>503</sup> entations of the SUSY algebra. Each supermultiplet contains both fermionic and bosonic  
<sup>504</sup> states. Particles in the same supermultiplet must also be in the same representation of the  
<sup>505</sup> gauge group, and so must have the same electric charge, weak isospin and colour degrees  
<sup>506</sup> of freedom. The number of bosonic degrees of freedom  $n_B$  must equal the number of  
<sup>507</sup> fermionic degrees of freedom  $n_F$  in each supermultiplet.

<sup>508</sup> The first possible supermultiplet has a single Weyl fermion (with two spin helicity  
<sup>509</sup> states, so  $n_F = 2$ ) and two scalars (each with  $n_B = 1$ ), where the two scalars are grouped  
<sup>510</sup> into one complex scalar field. This type of supermultiplet is called a *chiral supermul-*  
<sup>511</sup> *tiplet*. The individual chirality states of the SM fermions are each in their own chiral  
<sup>512</sup> supermultiplet with a corresponding complex scalar.

<sup>513</sup> The second possible supermultiplet contains a spin-1 vector boson. In order for the  
<sup>514</sup> theory to be renormalisable, this must be a massless gauge boson, in the instance that the  
<sup>515</sup> gauge symmetry is not spontaneously broken. A massless spin-1 boson has two helicity  
<sup>516</sup> states and so  $n_B = 2$ . Its superpartner is a massless spin-1/2 Weyl fermion, with two  
<sup>517</sup> helicity states, so  $n_F = 2$ . Such a supermultiplet is called a *gauge* or *vector* supermultiplet.

518 **2.6.1 Motivations for SUSY**

519 **2.6.1.1 Cancellation of Quadratic Divergences**

520 The introduction of sparticles with  $\Delta s = \frac{1}{2}$  compared to their SM partners elegantly  
521 provides a solution to the hierarchy problem. The Higgs mass squared potential receives  
522 corrections from a new scalar of mass  $m_s$  of the form:

$$\Delta M_H^2 = \frac{|\lambda_S|^2}{16\pi^2} \Lambda_{UV}^2 + \dots \quad (2.16)$$

523 Two scalar particles with Yukawa couplings equal to that of the top quark will exactly  
524 cancel the corrections to the Higgs mass provided the SM particle and the supersymmetric  
525 partner are mass degenerate. This applies for all SM fermions and has been shown to  
526 continue to all orders.

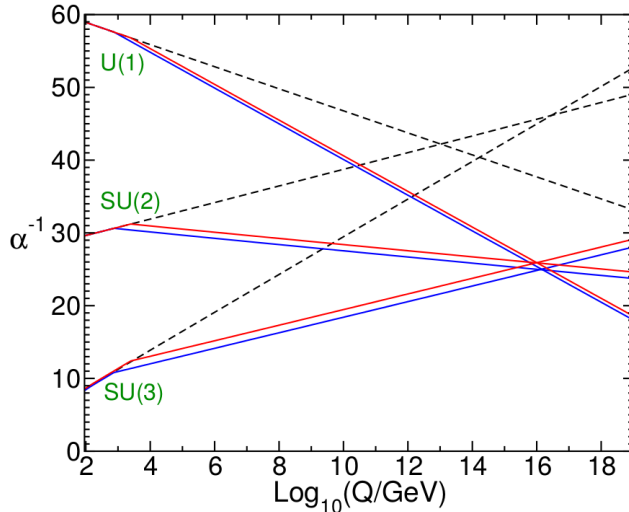


Figure 2.1: The running of the inverse gauge couplings of electromagnetic, weak and strong interactions with the SM (dashed lines) and for the MSSM with two possible sparticle mass scales at 500 GeV and 1.5 TeV (red and blue solid lines)

527 **2.6.1.2 Running of Gauge Couplings**

528 The SM predicts the running of gauge couplings, i.e. strength of the couplings as a function  
529 of energy is calculable given a value at some fixed scale. It was aforementioned that  
530 although the coupling strengths of EM and weak interaction unify at  $\simeq 100$  GeV, that is not  
531 true for the strong force. Within the Minimal Supersymmetric Standard Model (MSSM),  
532 which is a supersymmetric extension to the SM which has minimal additional particle  
533 content and will be discussed in more detail in Section 2.6.2, different coefficients arise

<sup>534</sup> due to additional particles involved in the gauge interactions. This leads to an approximate  
<sup>535</sup> unification of all three gauge couplings at the Planck scale as shown in Figure 2.1. This is  
<sup>536</sup> indicative of a Grand Unified Theory (GUT) that is attainable within a supersymmetric  
<sup>537</sup> model.

### <sup>538</sup> 2.6.2 The Minimal Supersymmetric Standard Model

<sup>539</sup> The Minimal Supersymmetric Standard Model (MSSM) is the model with supersymmetric  
<sup>540</sup> theory that assumes the minimal particle content to solve the hierarchy problem, with no  
<sup>541</sup> additional supermultiplets. The equations used to describe the behaviour of quantum fields  
<sup>542</sup> within the SM can be modified to describe the supermultiplets using *chiral superfields*. The  
<sup>543</sup> *superpotential* - supersymmetric equivalent of the potential - which describes the general  
<sup>544</sup> non-gauge interactions of the chiral supermultiplets within the MSSM is as follows:

$$W_{MSSM} = \bar{u} \mathbf{y}_u Q H_u - \bar{d} \mathbf{y}_d Q H_d - \bar{e} \mathbf{y}_e L H_d + \mu H_u H_d, \quad (2.17)$$

<sup>545</sup> where  $\mathbf{y}_u$ ,  $\mathbf{y}_d$  and  $\mathbf{y}_e$  are Yukawa couplings and  $\bar{u}$ ,  $Q$ ,  $H_u$ ,  $\bar{d}$ ,  $H_d$ ,  $\bar{e}$  and  $L$  are the chiral  
<sup>546</sup> superfields corresponding to the supermultiplets described in Table 2.3 and Table 2.4.

Names		spin 0	spin $\frac{1}{2}$
squarks, quarks ( $\times 3$ families)	$Q$ $\bar{u}$ $\bar{d}$	$(\tilde{u}_L \tilde{d}_L)$ $\tilde{u}_R^*$ $\tilde{d}_R^*$	$(u_L d_L)$ $u_R^\dagger$ $\tilde{d}_R^\dagger$
sleptons, leptons ( $\times 3$ families)	$L$ $\bar{e}$	$(\tilde{\nu} \tilde{e}_L)$ $\tilde{e}_R^*$	$(\nu e_L)$ $e_R^\dagger$
Higgs, higgsinos	$H_u$ $H_d$	$(H_u^+ H_u^0)$ $(H_d^0 H_d^-)$	$(\tilde{H}_u^+ \tilde{H}_u^0)$ $(\tilde{H}_d^0 \tilde{H}_d^-)$

Table 2.3: Particle content of the MSSM chiral supermultiplets. The left-hand column gives the type of particle and the symbols used for the supermultiplets containing them. The second and third columns contain the spin-0 and spin- $\frac{1}{2}$  components of each of these supermultiplets. The first generation of the quarks and leptons are included as an example and the other two generations follow the same convention. The Higgs fields are given a subscript label depending on whether they give mass to  $u$ -type or  $d$ -type quarks.

<sup>547</sup> All SM particles have supersymmetric versions with the inclusion of two Higgs doublets  
<sup>548</sup> to generate mass terms for the up and down type quarks via the Yukawa interactions.  
<sup>549</sup> Massive quarks and leptons are constructed from pairs of Weyl spinors with opposite  
<sup>550</sup> chirality. This means that in a supersymmetric theory, every massive quark and lepton  
<sup>551</sup> must be accompanied by a pair of scalar partners, which are known as squarks and sleptons  
<sup>552</sup> respectively.

Names	spin $\frac{1}{2}$	spin 1
gluino, gluon	$\tilde{g}$	$g$
winos, W bosons bino, B bosons	$\tilde{W}^\pm, \tilde{W}^0$ $\tilde{B}^0$	$W^\pm, W^0$ $B^0$

Table 2.4: The gauge supermultiplet particle content of the MSSM. The left-hand column gives the names of the particles and the second and third columns contain the spin- $\frac{1}{2}$  and spin-1 components of the associated supermultiplets.

Though the scalar partners of the SM fermions are given the labels “right” and “left” they have no “handedness” themselves. Instead the labels refers to the helicity of their respective fermion partners, so for example the “right up squark” ( $\tilde{u}_R$ ) is the scalar partner of the  $u_R$  Weyl fermion.

The gauge supermultiplets are the SUSY equivalent of the SM gauge bosons - the minimal additional fields necessary to create a theory at once supersymmetric and gauge invariant. In addition to a vector boson, each gauge multiplet contains a spin  $\frac{1}{2}$ , known as a gaugino. Those corresponding to unbroken  $SU(3) \otimes SU(2) \otimes U(1)$  are called the gluinos, winos and bino respectively.

### 2.6.3 Soft SUSY Breaking

It has been previously shown in Section 2.6.1 that with the addition of sparticles in the MSSM, the quadratic divergent corrections can be cancelled provided the particle-sparticle pairs are mass degenerate. However there have been no discoveries of sparticles at the mass scale of their SM partners. This suggests there must be a spontaneous SUSY breaking mechanism to generate sparticle masses akin to the electroweak spontaneous symmetry breaking. The mechanism must be spontaneous and the symmetry breaking must be done by a non-zero VEV in order to preserve Lagrangian invariance under SUSY and providing a solution to the hierarchy problem. If the relationship between the fermionic and bosonic couplings is altered, then the corrections to the Higgs mass squared parameter from SM fermions will not be cancelled by their SUSY partners correction terms. This equates to adding terms to the SUSY Lagrangian which are gauge invariant and violate SUSY, but contain only masses and couplings with positive mass dimension. The total Lagrangian is defined as:

$$\mathcal{L} = \mathcal{L}_{SUSY} + \mathcal{L}_{soft}, \quad (2.18)$$

where all additional terms are contained within  $\mathcal{L}_{soft}$  and the original SUSY invari-

ant interaction terms are contained within  $\mathcal{L}_{SUSY}$ . New free parameters are introduced by the soft SUSY breaking, with the key parameters summarised in Table 2.5. These parameters determine the mixing between the flavour eigenstates and consequently the SUSY phenomenology. The phenomenology of supersymmetric theories will be discussed in Section 2.6.4. The actual mechanism for SUSY breaking is unknown, but there are several proposed ideas that have been studied in depth. The general approach involves a coupling to a separate *hidden sector* of fields, in which, spontaneous SUSY breaking occurs [25]. The hidden sector then communicates the SUSY breaking to the MSSM sector via *messenger fields* such that the soft SUSY-breaking terms are generated. There are several ways in which this communication occurs, including gauge mediation [26], gravity mediation [27], extra-dimensional [28] or anomaly-mediation [29]. This thesis considered scenarios in SUSY which specify gauge mediated SUSY breaking, where the soft terms are generated via electroweak and strong interaction loop diagrams with new messenger particles. The messengers are new chiral supermultiplets that are charged under  $SU(3)_C \times SU(2)_L \times U(1)_Y$ .

Parameters	Definition
$M_1, M_2, M_3$	Masses of the bino, wino and gluino
$m_{\tilde{Q}_L}, m_{\tilde{u}_R}, m_{\tilde{d}_R}, m_{\tilde{L}_L}, m_{\tilde{e}_R}$	Masses of the left-handed squarks, up-type and down-type right-handed squarks, left-handed sleptons and right-handed sleptons.
$m_{H_u^2}, m_{H_d^2},  \mu , B$	Up and down-type higgsino mass squared parameters, the higgs-higgsino mass and the bilinear higgs term.
$A_u, A_d, A_e$	Up and down-type squark and sfermion Higgs interaction trilinear couplings.
$\tan \beta$	Ratio of the VEVs of the two higgs doublet fields.

Table 2.5: Key free parameters introduced by soft SUSY breaking in the MSSM.

## 2.6.4 MSSM Mass Spectra

The general properties of the supersymmetric mass terms, mixing and the resulting phenomenology are discussed here.

### 2.6.4.1 Higgs Sector

The Higgs scalar fields in the MSSM consist of two complex  $SU(2)_L$ -doublet, or eight real, scalar degrees of freedom. As a consequence of electroweak symmetry breaking ( $SU(2)_L \times U(1)_Y \rightarrow U(1)_{EM}$ ), three of them are the Nambu-Goldstone bosons  $G^0, G^\pm$ ,

which become longitudinal modes of the  $Z^0$  and  $W^\pm$  massive vector bosons. The remaining five Higgs scalar mass eigenstates consist of two CP-even neutral scalars  $h^0$  and  $H^0$ , one CP-odd neutral scalar  $A^0$  and a charge +1 scalar  $H^+$  and its conjugate charge -1 scalar  $H^-$ . The masses of  $A^0$ ,  $H^0$  and  $H^\pm$  are not bound by theory and can be arbitrarily large as their mass terms are proportional to  $1/\sin \beta$ . However the mass of  $h^0$  is bounded from above, at tree level as follows:

$$m_{h^0} < m_Z |\cos(2\beta)|, \quad (2.19)$$

where,  $\tan\beta$  is the ratio of the electroweak vacuum expectation values. The lightest Higgs mass is bounded below the Z mass without radiative corrections. However the tree level formula for the squared mass of  $h^0$  is subject to large quantum corrections, the largest of which come from top and stop loops. The corrections can however be tuned in order to match the observed SM Higgs mass of  $\approx 126$  GeV [30].

#### 2.6.4.2 Gauginos

The neutral higgsinos ( $\tilde{H}_u^0$ ,  $\tilde{H}_d^0$ ) and the neutral gauginos ( $\tilde{B}^0$ ,  $\tilde{W}^0$ ) combine to form four mass eigenstates called *neutralinos*. These are denoted as  $\tilde{\chi}_1^0$ ,  $\tilde{\chi}_2^0$ ,  $\tilde{\chi}_3^0$ ,  $\tilde{\chi}_4^0$  and increase in mass from  $1 \rightarrow 4$ . The mixing can be represented by a matrix:

$$\begin{pmatrix} \tilde{\chi}_1^0 \\ \tilde{\chi}_2^0 \\ \tilde{\chi}_3^0 \\ \tilde{\chi}_4^0 \end{pmatrix} = \begin{pmatrix} M_1 & 0 & -c_\beta m_Z s_W & s_\beta m_Z s_W \\ 0 & M_2 & c_\beta m_Z c_W & -s_\beta m_Z c_W \\ -c_\beta m_Z s_W & c_\beta m_Z c_W & 0 & -\mu \\ s_\beta m_Z s_W & -s_\beta m_Z c_W & -\mu & 0 \end{pmatrix} \begin{pmatrix} \tilde{B}^0 \\ \tilde{W}^0 \\ \tilde{H}_u^0 \\ \tilde{H}_d^0 \end{pmatrix},$$

where  $c_\beta = \cos \beta$ ,  $s_\beta = \sin \beta$ ,  $c_W = \cos \theta_W$  and  $s_W = \sin \theta_W$ .

The charged higgsinos ( $\tilde{H}_u^+$ ,  $\tilde{H}_d^-$ ) and winos ( $\tilde{W}^+$ ,  $\tilde{W}^-$ ) mix to form two mass eigenstates with charge  $\pm$  called *charginos*. These are denoted by  $\tilde{\chi}_1^\pm$  and  $\tilde{\chi}_2^\pm$  and increase in mass from  $1 \rightarrow 2$ . This mixing can also be represented by a matrix:

$$\begin{pmatrix} \tilde{\chi}_1^\pm \\ \tilde{\chi}_2^\pm \end{pmatrix} = \begin{pmatrix} M_2 & \sqrt{2}M_W s_\beta \\ \sqrt{2}M_w c_\beta & \mu \end{pmatrix} \begin{pmatrix} \tilde{W}^\pm \\ \tilde{H}^\pm \end{pmatrix}.$$

The gluino is colour charged, therefore it does not mix with the other gauginos. The

<sup>619</sup> gaugino mass is given by a third gaugino mass parameter,  $M_3$ .

#### <sup>620</sup> 2.6.4.3 Squarks and Sleptons

<sup>621</sup> There is mixing of the slepton and squark states due to electroweak symmetry breaking,  
<sup>622</sup> although this is considered negligible with the exception of the third generation particles  
<sup>623</sup> which have large masses and Yukawa couplings. The  $\tilde{\tau}_L$  and  $\tilde{\tau}_R$  states mix to give the mass  
<sup>624</sup> eigenstates  $\tilde{\tau}_1$  and  $\tilde{\tau}_2$ , the  $\tilde{b}_L$  and  $\tilde{b}_R$  states mix to give the mass eigenstates  $\tilde{b}_1$  and  $\tilde{b}_2$  and  
<sup>625</sup> the  $\tilde{t}_L$  and  $\tilde{t}_R$  states mix to give the mass eigenstates  $\tilde{t}_1$  and  $\tilde{t}_2$ . It is conventional for the  
<sup>626</sup> eigenstate with lower mass to have the lower index as with the neutralinos and charginos.  
<sup>627</sup> Mixing is also observed in the Higgs sector, with five mass eigenstates arising. The resulting  
<sup>628</sup> mass eigenstates which differ from the gauge eigenstates are given in Table 2.6.

Names	Gauge Eigenstates	Mass Eigenstates
Higgs	$H_u^0 \ H_d^0 \ H_u^+ \ H_d^-$	$h^0 \ H^0 \ A^0 \ H^\pm$
Squarks	$\tilde{t}_L \ \tilde{t}_R \ \tilde{b}_L \ \tilde{b}_R$	$\tilde{t}_1 \ \tilde{t}_2 \ \tilde{b}_1 \ \tilde{b}_2$
Slepton	$\tilde{\tau}_L \ \tilde{\tau}_R \ \tilde{\nu}_\tau$	$\tilde{\tau}_1 \ \tilde{\tau}_2 \ \tilde{\nu}_\tau$
Neutralinos	$\tilde{B}^0 \ \tilde{W}^0 \ \tilde{H}_u^0 \ \tilde{H}_d^0$	$\tilde{\chi}_1^0 \ \tilde{\chi}_2^0 \ \tilde{\chi}_3^0 \ \tilde{\chi}_4^0$
Charginos	$\tilde{W}^\pm \ \tilde{H}_u^\pm \ \tilde{H}_d^\pm$	$\tilde{\chi}_1^\pm \ \tilde{\chi}_2^\pm$

Table 2.6: Mass eigenstates of the MSSM - only those which differ from the gauge eigenstates are listed.

#### <sup>629</sup> 2.6.5 Naturalness in SUSY

<sup>630</sup> The concept of “natural SUSY” is understood as a supersymmetric scenario where the ad-hoc adjusting of relevant parameters (fine-tuning) is as minimal as possible and is taken as a useful guide for exploring supersymmetric phenomenology. The motivation is to discover SUSY in a region of the MSSM parameter space where the electroweak breaking is not fine-tuned. This is because the main phenomenological virtue of SUSY is precisely to avoid the large fine-tuning which arises to deal with the hierarchy problem. If it is considered that the SM-like Higgs doublet,  $H$ , is a linear combination of two supersymmetric Higgs doublets,  $H = \sin \beta H_u + \cos \beta H_d$  then the absence of fine tuning can be expressed as minimal contributions to the Higgs mass parameter squared,  $m^2$  [31]. Given that the physical Higgs mass is  $m_h^2 = 2|m|^2$  it follows that:

$$\tilde{\Delta} = \left| \frac{\delta m^2}{m^2} \right| = \frac{2\delta m^2}{m_h^2}. \quad (2.20)$$

<sup>640</sup> For large values of  $\tan \beta$  the value of  $m^2$  is given by  $m^2 = |\mu|^2 + m_{H_u}^2$ . The higgsino mass

is constrained as the  $\mu$  parameter should not be too large to avoid large fine-tuning [32].  
 Constraints are also set on the particles which contribute radiative corrections to  $m_{H_u}^2$ .  
 The most important contributions come from the stop and the gluino. Once a criteria for ranking models of naturalness is defined, the features of natural models can be used to draw conclusions about sparticle mass spectra. Assuming that the new Higgs-like boson discovered recently at the LHC is the lightest Higgs boson of the MSSM, and taking into account current experimental constraints, a summary of the minimal requirements for a natural SUSY spectrum is given as [32]:

- two stops and one (left-handed) sbottom, both below 500-700 GeV
- two higgsinos, i.e., one chargino and two neutralinos below 200 - 350 GeV. In the absence of other chargino/neutralinos, their spectrum is quasi-degenerate
- a not too heavy gluino, below 900 GeV - 1.5 TeV

These constraints, particularly for light higgsinos provide motivation for compressed spectra SUSY, which will be described and discussed in Section 2.7.

### 2.6.6 R-Parity

Within the MSSM there are terms that are gauge-invariant but violate either baryon number (B) or total lepton number (L). Taking the most general gauge-invariant and renormalisable superpotential includes terms not only from Equation 2.17 but also the terms

$$W_{\Delta L=1} = \frac{1}{2} \lambda^{ijk} L_i L_j \bar{e}_k + \lambda'^{ijk} L_i Q_j \bar{d}_k + \mu'^i L_i H_u \quad (2.21)$$

$$W_{\Delta B=1} = \frac{1}{2} \lambda''^{ijk} \bar{u}_i \bar{d}_j \bar{d}_k \quad (2.22)$$

where  $i, j, k$  refer to flavour and  $\lambda^{ijk}, \lambda'^{ijk}, \lambda''^{ijk}$  and  $\mu'^i$  are coupling constants for the interactions between the chiral superfields.  $Q_i$  have a baryon number of  $+1/3$ ,  $\bar{u}_i, \bar{d}_i$  have a baryon number of  $-1/3$ , with  $B=0$  for all other terms.  $L_i$  have a lepton number of  $+1$  and  $\bar{e}_i$  have a lepton number of  $-1$  with  $L=0$  for all other terms. This means that the terms in Equation 2.21 violate total lepton number by 1 unit (as well as the individual lepton flavours) and the terms in Equation 2.22 violate baryon number by 1 unit. The presence of the  $\lambda'$  and  $\lambda''$  couplings would result in an extremely short proton lifetime, i.e. much shorter than the current measurement of the proton lifetime at  $> 5.8 \times 10^{29}$  years [11]. This is due to the fact that the proton is only able to decay into lighter leptons which

would violate baryon number by 1 unit and lepton number by 1 unit and can occur if the aforementioned couplings are non-zero. In order to remove the B and L violating terms in the renormalisable superpotential, a new quantum number is assumed within the MSSM, called “R-parity”. R-parity is a multiplicatively conserved quantum number defined as

$$R_P = (-1)^{3(B-L)+2S} \quad (2.23)$$

for each particle in the theory [25]. This will have a value of +1 for SM particles and -1 for SUSY particles. The imposed symmetry is that any additional candidate term in the Lagrangian (or in the superpotential) is allowed only if the product of  $R_P$  for all of the fields in it is +1. If R-parity is conserved, SUSY particles are forbidden from decaying to SM particles as this would give  $\Delta R_P = 2$ . An important consequence of R-parity conservation is the lightest supersymmetric particle (LSP) will be stable, as there are no lighter particles with the same  $R_P$  number for it to decay into. As a weakly interacting, stable and massive particle this makes it a key potential candidate for dark matter. Another experimental consequence is that sparticles can only be produced in even numbers if the initial  $R_p = +1$ .

The MSSM will not be rendered inconsistent if R-parity conservation is not imposed. Furthermore the laws of baryon and lepton number conservation is accepted not as a consequence of any symmetry but because all observed interactions are seen to obey them. R-parity violating terms are permitted to exist but their coupling are limited by measurements like the proton lifetime. The MSSM can be extended to models that do not conserve R-parity, however within the scope of this thesis only R-parity conserving models are considered.

### 2.6.7 Models of SUSY

Recent LHC limits place powerful constraints on the production of strongly interacting sparticles (squarks and gluinos) [33]. Depending on the SUSY breaking mechanism, strongly interacting squarks and gluinos may be too massive to be produced at the LHC. This motivates electroweak SUSY particle production, which may be the dominant SUSY production at the LHC, despite the comparatively low production cross sections to strongly interacting SUSY. The pair production cross section as a function of mass for the electroweak and strong processes are shown in Figure 2.2 to illustrate the difference production cross section between the electroweak processes  $\tilde{\chi}_2^0 \tilde{\chi}_1^\pm$  and  $\tilde{\chi}_2^0 \tilde{g}$  and the strong processes  $\tilde{g}\tilde{g}, \tilde{q}\tilde{q}$  and  $\tilde{q}\tilde{g}$ .

700 Electroweak SUSY production can be searched for at the LHC through the detection  
 701 of events with multiple charged leptons in the final state. This is because charginos and  
 702 neutralinos can decay via intermediate sleptons, gauge bosons or Higgs bosons to charged  
 703 leptons. Charged sleptons can be produced directly if they are sufficiently light. Chargino  
 704 or slepton decays can produce one charged lepton in the final state. Neutralino decays  
 705 can produce two charged leptons in the final state. Thus the combination of chargino  
 706 and neutralino decays can yield three leptons in the final state. Leptonic decays of direct  
 707 chargino and neutralino production is the electroweak SUSY production mode explored  
 708 in this thesis.

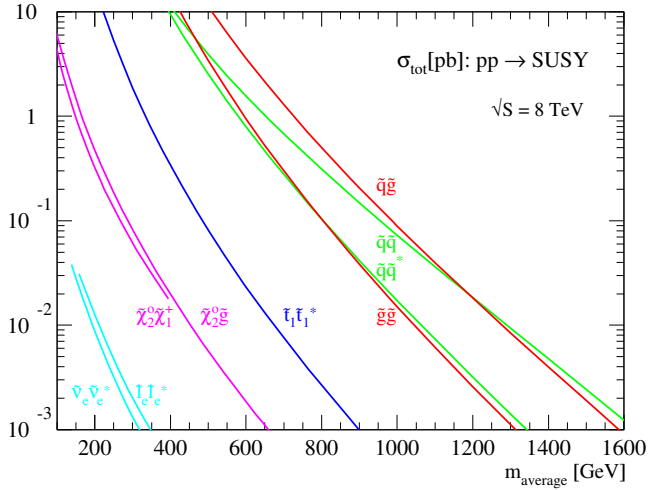


Figure 2.2: Production cross section for supersymmetric particles at the LHC energy of  $\sqrt{s} = 8 \text{ TeV}$  as a function of mass

### 709 2.6.8 Simplified Models

710 Experimentally, SUSY can be explored by focusing on one or more SUSY production  
 711 processes with a fixed decay chain and considering minimal particle content necessary  
 712 to reproduce such events. This approach is referred to as *simplified models* [34]. Only  
 713 simplified models for the direct production of the lightest chargino ( $\tilde{\chi}_1^\pm$ ) and the second-  
 714 lightest neutralino ( $\tilde{\chi}_2^0$ ) are considered in this analysis. It is a pair-production process -  
 715 due to the conservation of R-parity - that can lead to three leptons and missing transverse  
 716 energy ( $E_T^{\text{miss}}$ ) in the final state. The masses of the relevant particles in the decay chain  
 717 are the only free parameters in these models. The following assumptions are made for  
 718 the considered simplified models: the  $\tilde{\chi}_1^\pm$  and  $\tilde{\chi}_2^0$  consist purely of the wino component  
 719 and are degenerate in mass; the  $\tilde{\chi}_1^0$  consists purely of the bino component; the squark and  
 720 gluino masses are set as high as a few hundred TeV.

721 The different scenarios for the decay of  $\tilde{\chi}_1^\pm$  and  $\tilde{\chi}_2^0$  are classified according to the

<sup>722</sup> particles (or sparticles) in the intermediate step of the decay chain. Two simplified models  
<sup>723</sup> are explored in the analysis discussed in this thesis and are described in the following  
<sup>724</sup> sections.

#### <sup>725</sup> 2.6.8.1 Simplified Models with Three Lepton Final States via Sleptons

<sup>726</sup> In this simplified model scenario, the left-handed charged sleptons and sneutrinos are  
<sup>727</sup> assumed to be light, whereas the right-handed charged sleptons are assumed to have  
<sup>728</sup> masses at the TeV scale. Therefore, the wino-like chargino and neutralino will dominantly  
<sup>729</sup> decay through left-handed charged sleptons or sneutrinos as shown in Figure 2.3. For these  
<sup>730</sup> models, the masses of  $\tilde{\chi}_1^\pm$ ,  $\tilde{\chi}_2^0$ ,  $\tilde{\ell}_L$ ,  $\tilde{\nu}$  and  $\tilde{\chi}_1^0$  are the free parameters. Lepton universality  
<sup>731</sup> requires that the branching ratios to e,  $\mu$  and  $\tau$  are equal. Mass degeneracy of  $m_{\tilde{\ell}_L, \tilde{\nu}}$  for  
<sup>732</sup> various flavours is assumed for simplicity, these are set such that  $m_{\tilde{\ell}_L} = (m_{\tilde{\chi}_1^\pm} + m_{\tilde{\chi}_2^0})/2$ .  
<sup>733</sup> Both the branching ratio branching ratio of the  $\tilde{\chi}_1^\pm$  into  $\ell\tilde{\nu}$  and the branching ratio into  $\tilde{\ell}_L\nu$   
<sup>734</sup> are set to equal 50%. Also, both the branching ratio of the  $\tilde{\chi}_2^0$  into  $\ell\tilde{\ell}_L$  and the branching  
<sup>735</sup> ratio into  $\tilde{\nu}\nu$  are set equal to 50%.

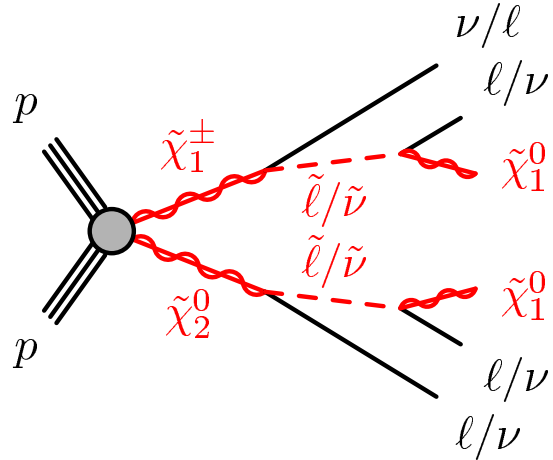


Figure 2.3: Schematic diagram for  $\tilde{\chi}_2^0 \tilde{\chi}_1^\pm$  via sleptons, yielding three leptons in the final state [35].

#### <sup>736</sup> 2.6.8.2 Simplified Models with Three Lepton Final States via WZ

<sup>737</sup> In the second simplified model scenario, all sleptons and sneutrinos are assumed to be at  
<sup>738</sup> the TeV scale and the  $\tilde{\chi}_1^\pm$  and  $\tilde{\chi}_2^0$  dominantly decay via  $W^{(*)}$  and  $Z^{(*)}$  bosons, respectively,  
<sup>739</sup> with a branching fraction of 100%, leading to three leptons and missing transverse energy  
<sup>740</sup> in the final state. The decay chain for this process is shown in Figure 2.4.

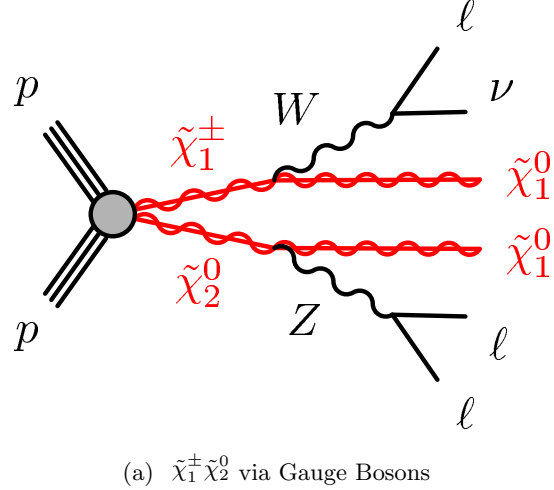


Figure 2.4: Schematic diagram for  $\tilde{\chi}_2^0 \tilde{\chi}_1^\pm$  simplified models with intermediate  $WZ$  boson decays yielding three leptons in the final state [36].

## 741 2.7 Motivation for Compressed Spectra SUSY

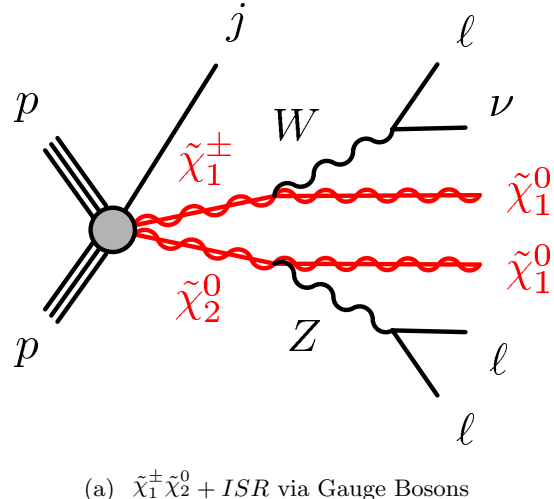


Figure 2.5: Schematic diagram for  $\tilde{\chi}_2^0 \tilde{\chi}_1^\pm$  simplified models with intermediate  $WZ$  boson decays and an ISR jet yielding three leptons in the final state [37].

742 Compressed spectra SUSY refers to the scenario where the final state sparticles are  
743 near mass degenerate with the heavier decaying sparticles. The specific scenario discussed  
744 in this thesis is  $\tilde{\chi}_1^\pm \tilde{\chi}_2^0$  production. This scenario is well-motivated theoretically due to the  
745 requirement of a low  $\mu$  parameter and therefore low Higgsino mass for minimal fine-tuning  
746 in the MSSM. In the case of  $\mu \ll M_1, M_2$ , the three lightest neutralino and chargino mass  
747 eigenstates,  $\tilde{\chi}_1^0$ ,  $\tilde{\chi}_2^0$  and  $\tilde{\chi}_1^\pm$  are quasi-degenerate these states are nearly pure higgsinos [38].  
748 In this scenario the dark matter relic density is typically below the WMAP [39] and

749 PLANCK [40] measurements due to the high rate of higgsino annihilation to SM gauge and  
 750 Higgs bosons and the higgsino Co-annihilation processes. Although the relic abundance  
 751 would be below experimental constraints, this parameter space is not excluded, since  
 752 the remaining relic abundance can be accounted for by other additional sources, e.g.  
 753 axions [38]. If the mass gap between the  $\tilde{\chi}_1^\pm \tilde{\chi}_2^0$  and  $\tilde{\chi}_1^0$  is large enough to provide final  
 754 states with leptons, this parameter space can be explored with the LHC. However the  
 755 leptons produced will have diminishing  $p_T$  compared to non-compressed scenarios. One  
 756 way to circumvent the challenges of compressed SUSY scenarios is to search for events  
 757 with an energetic jet from initial state radiation (ISR) [41] [42] [43]. In such events the  
 758 invisible particles can recoil against the jet such that  $E_T^{\text{miss}} \sim p_T(j)$ , and the signal event  
 759 can at least be triggered. In addition, the lepton momenta receive a part of the boost,  
 760 which increases the likelihood of passing the leptonic triggers. The topology of the event  
 761 with an ISR present can be exploited to enhance signal sensitivity, where there will be  
 762 large angular separation between the jet and the invisible decay products. This method  
 763 is discussed in further detail in Section 6.4.1. The monojet decay chain considered in  
 764 this analysis is illustrated in Figure 2.5, for this simplified model, the constraints on the  
 765 relevant particles are the same as in Section 2.6.8.2.

## <sup>766</sup> Chapter 3

# <sup>767</sup> The ATLAS Detector at the LHC

<sup>768</sup> This chapter discusses the experimental apparatus that was used to complete the analysis  
<sup>769</sup> detailed in this thesis. The Large Hadron Collider (LHC), which supplies proton-proton  
<sup>770</sup> ( $pp$ ) collisions for the experiment and the ATLAS detector which is used to contain and  
<sup>771</sup> measure the particles produced from these collisions. The scope of this thesis covers two  
<sup>772</sup> distinct periods of data taking for the ATLAS detector, Run-1 and Run-2. During the  
<sup>773</sup> transition from Run-1 to Run-2 referred to as the Long Shutdown 1 (LS1), upgrades were  
<sup>774</sup> made to the ATLAS detector for continued optimal physics analysis. This chapter will  
<sup>775</sup> discuss the LHC and the ATLAS detector to include Run-1 and Run-2 aspects as follows:  
<sup>776</sup> The Large Hadron Collider (LHC), is introduced in Section 3.1. The ATLAS detector is  
<sup>777</sup> described in 3.2. The ATLAS trigger system during Run-1 is described in Section 3.8.  
<sup>778</sup> The upgrades made to the ATLAS detector and trigger system for Run-2 is discussed in  
<sup>779</sup> Section 3.9.

### <sup>780</sup> 3.1 The Large Hadron Collider

<sup>781</sup> The Large Hadron Collider (LHC) is a large scale circular particle accelerator and collider  
<sup>782</sup> based in the former LEP [44] tunnel at the European Organisation for Nuclear Research  
<sup>783</sup> (CERN). Located on the Franco-Swiss border, near Geneva, the LHC has been running  
<sup>784</sup> since September 2008, although CERN has been conducting particle collision and nuclear  
<sup>785</sup> physics experiments since the 1950s. The tunnel is 27 km in circumference and varies in  
<sup>786</sup> depth between 40 - 170m below ground level.

<sup>787</sup> The collider was designed to extend the frontiers of particle physics by utilising unpre-  
<sup>788</sup> cedented beam energies and luminosity. Bunches of up to  $10^{11}$  protons collide 40 million  
<sup>789</sup> times per second to provide 8-13 TeV  $pp$  collisions at a design luminosity of  $10^{34}\text{cm}^{-2}\text{s}^{-1}$ .

The LHC also collides heavy ions, in particular lead nuclei at 5.5 TeV per nucleon pair [45], at a design luminosity of  $10^{27} \text{ cm}^{-2}\text{s}^{-1}$ . The luminosity is related to properties of the proton beam and bunches:

$$L = \frac{f N_1 N_2}{4\pi\sigma_x\sigma_y}, \quad (3.1)$$

where  $N_1$  and  $N_2$  are the number of protons per bunch in each of the colliding beams,  $f$  is the frequency of the bunch collisions, and  $\sigma_x$  and  $\sigma_y$  are the horizontal and vertical dimensions of the beam.

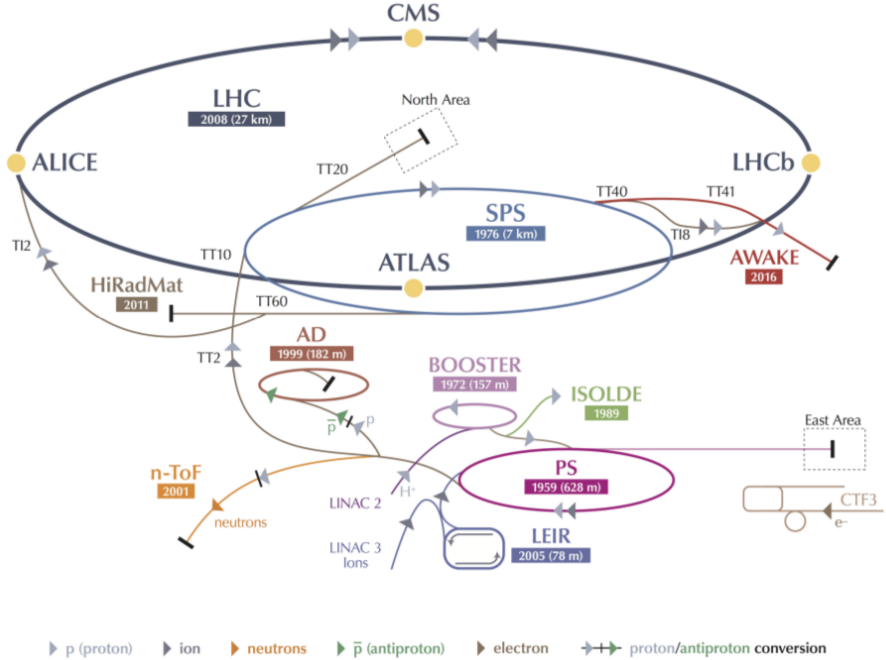


Figure 3.1: Diagram of the layout of the accelerators connected to and including the LHC at CERN, as well as the locations of the four major detector sites [46].

The LHC receives high energy protons that are supplied after passing through a chain of smaller accelerators. The energies of the protons are gradually increased through each step in the chain. The acceleration of the beams of protons begin at the linear accelerator LINAC 2, where they are accelerated to energies of 50 MeV. They are then passed to the Proton Synchrotron Booster (PSB) where they reach energies of 1.4 GeV. Next in the sequence is the Proton Synchrotron (PS), which pushes energies up to 25 GeV, and then the Super Proton Synchrotron (SPS), at energies up to 450 GeV. Finally the proton beams are injected in bunches into the LHC, which circulates them in opposite directions, accelerating them to energies of 8 TeV for Run-1 and 13 TeV for Run-2. Upon attaining these energies the bunches are made to collide at four key positions around the ring where

806 the particle detector experiments are based.

807 For the heavy ion collisions, the bunches are processed by LINAC 3 and the Low  
 808 Energy Ion Ring (LEIR) before they are passed to the PS whereby they then follow the  
 809 same path as the protons.

810 The four large detectors on the collision points are; the multi-purpose detectors A Tor-  
 811 oidal LHC ApparatuS (ATLAS), and Compact Muon Solenoid (CMS) [47], Large Hadron  
 812 Collider beauty (LHCb) [48], which focuses on flavour physics, and A Large Ion Collider  
 813 Experiment (ALICE) [49], which specialises in heavy ion physics. In addition there are a  
 814 number of smaller experiments located in the the four caverns about the collision points,  
 815 but this is beyond the scope of this thesis and will not be discussed any further.

### 816 3.2 The ATLAS Detector

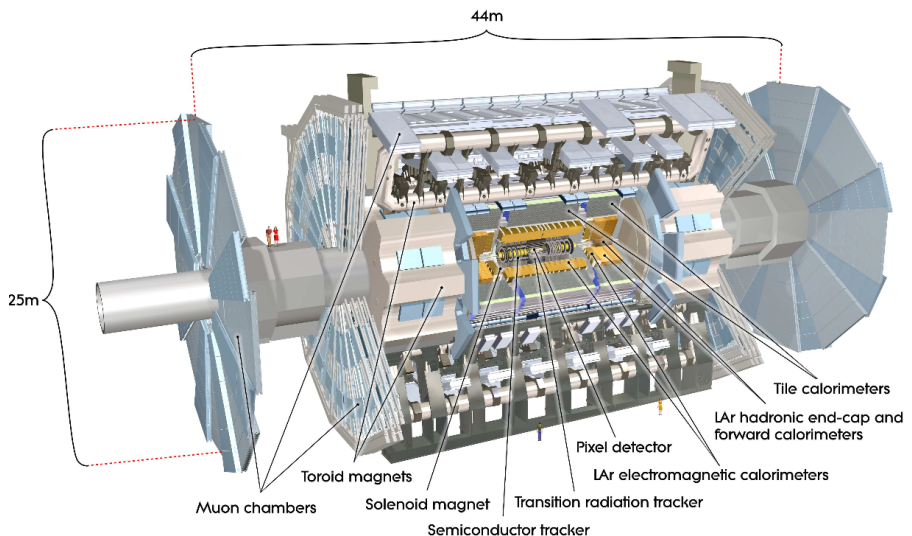


Figure 3.2: Cut-away view of the ATLAS detector. [1].

817 The ATLAS detector is a general purpose detector that sits on the LHC ring in the  
 818 Point 1 cavern. It has cylindrical symmetry, measuring 45 m in length and 25 m in  
 819 diameter. It is designed to reconstruct and measure physics objects, including electrons,  
 820 muons, photons and hadronic jets that are created from the  $pp$  collisions supplied by the  
 821 LHC. The detector was optimised for the discovery potential for the Higgs boson and  
 822 beyond-the-Standard-Model (BSM) physics. The detector is composed of several sub-  
 823 detector systems, which are designed to measure different particle properties, and will be  
 824 discussed in more detail below.

### <sup>825</sup> 3.3 ATLAS Detector Geometry and Nomenclature

<sup>826</sup> The nominal interaction point is defined as the origin of the coordinate system, while the  
<sup>827</sup> beam direction defines the  $z$ -axis and the  $x$ - $y$  plane is transverse to the beam direction.  
<sup>828</sup> The positive  $x$ -axis is defined as pointing from the interaction point to the centre of the  
<sup>829</sup> LHC ring and the positive  $y$ -axis is defined as pointing upwards. The side-A of the detector  
<sup>830</sup> is defined as that with positive  $z$  and side C is that with negative  $z$ . The azimuthal angle  
<sup>831</sup>  $\phi$  is measured around the beam axis, and the polar angle  $\theta$  is the angle from the beam  
<sup>832</sup> axis.

<sup>833</sup> A special coordinate is defined to describe the angle of a particle with respect to the  
<sup>834</sup> beam axis, known as the pseudorapidity. It is defined as

$$\eta = -\ln \left[ \tan \left( \frac{\theta}{2} \right) \right]. \quad (3.2)$$

<sup>835</sup> In the case of massive objects such as jets, the rapidity is defined as

$$y = \frac{1}{2} \left[ \frac{E + p_z}{E - p_z} \right], \quad (3.3)$$

<sup>836</sup> where  $E$  is the particle's energy and  $p_z$  is the  $z$ -component of its momentum. The distance  
<sup>837</sup>  $\Delta R$  in the pseudorapidity-azimuthal angle space is defined as

$$\Delta R = \sqrt{\Delta\eta^2 + \Delta\phi^2}, \quad (3.4)$$

<sup>838</sup> where  $\Delta\eta$  and  $\Delta\phi$  are the distance in  $\eta$  and  $\phi$  between the two considered objects. Re-  
<sup>839</sup> quirements on spatial proximity between objects can be made by imposing conditions  
<sup>840</sup> on  $\Delta R$ . The boundary of a  $\Delta R$  condition describes a cone around the considered object.  
<sup>841</sup> The transverse momentum  $p_T$  and transverse energy  $E_T$  and the missing transverse energy  
<sup>842</sup>  $E_T^{miss}$  are defined in the  $x$ - $y$  plane. The transverse momentum is defined as:

$$p_T = \sqrt{p_x^2 + p_y^2}, \quad (3.5)$$

<sup>843</sup> where  $p_x$  and  $p_y$  are the  $x$  and  $y$  components of the momentum. The initial momentum  
<sup>844</sup> in the  $x$ - $y$  plane of a proton-proton interaction is taken to be zero and therefore the final  
<sup>845</sup> total transverse momentum is also zero as a consequence of momentum conservation.  
<sup>846</sup> The total visible transverse momentum,  $p_T^{vis}$  can be used to infer the amount of missing  
<sup>847</sup> transverse energy in the event if it is measured as non-zero. This indicates there were

848 additional undetected particles present in the event, resulting in an invisible  $p_T$  component,  
 849 responsible for the perceived momentum imbalance. The missing transverse energy or  
 850  $E_T^{miss}$  is the magnitude of the momentum of all undetected particles in the event, defined  
 851 as:

$$\vec{p}_T^{miss} = -\vec{p}_T^{vis} = -\Sigma \vec{p}_T, \quad (3.6)$$

852 where the  $p_T$  of all visible particles are summed.

### 853 3.4 Magnet System

854 A fundamental method of identification and measurements of charged particles is the  
 855 direction and curvature of the particles' path in a magnetic field. These two parameters  
 856 are related to the particles charge and momentum. The ATLAS detector features a hybrid  
 857 system of four large superconducting magnets which deflect charged particles within the  
 858 detector. The magnetic system is 22 m in diameter and 26 m in length, with a stored  
 859 energy of 1.6 GJ. More specifically, the ATLAS magnet system consists of:

- 860 • A solenoid which is aligned on the beam axis and provides a 2 T axial magnetic field  
 861 for the Inner Detector (ID), while minimising the radiative thickness in front of the  
 862 barrel Electromagnetic Calorimeter (ECAL). It is located in between the ID and the  
 863 ECAL. It has an axial length of 5.8 m, an inner radius of 2.46 m and an outer radius  
 864 of 2.56 m.
- 865 • A barrel toroid and two end-cap toroids, which produce a toroidal magnetic field  
 866 of approximately 0.5 and 1 T for the muon detectors in the central and end-cap  
 867 regions, respectively. The magnetic field supplied is orthogonal to the trajectory  
 868 of the particles in the muon spectrometer, allowing for measurements of the muon  
 869 momenta. The barrel toroid has an axial length of 25.3 m, an inner diameter of  
 870 9.4 m and an outer diameter of 20.1 m. The endcaps are 5 m in length and have  
 871 inner and outer diameters of 1.65 and 10.7 m respectively.

872 All components are made from NbTi, which is a superconducting material with a critical  
 873 temperature of 10 K. The magnets are cooled to 4.5 K by liquid helium.

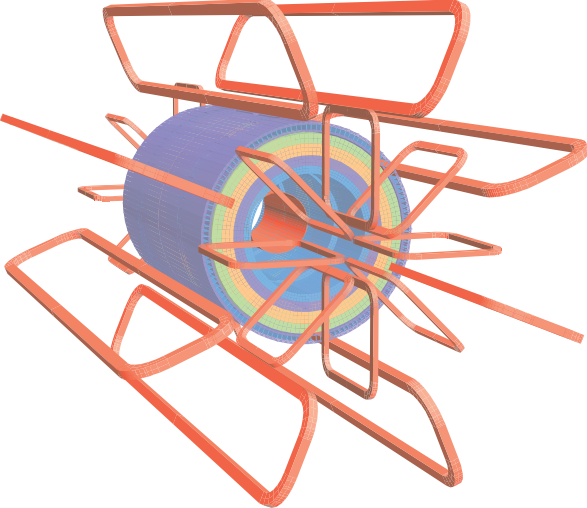


Figure 3.3: Geometry of magnet windings and tile calorimeter steel. The eight barrel toroid coils, with the end-cap coils interleaved are visible. The solenoid winding lies inside the calorimeter volume [1].

### <sup>874</sup> 3.5 Inner Detector

The ATLAS Inner Detector [50] is designed to provide robust pattern recognition, momentum resolution and both primary and secondary vertex measurements, for charged tracks above a given threshold (nominally 0.5 GeV) and within  $|\eta| < 2.5$ . It also provides electron identification over  $|\eta| < 2.0$  and a wide range of energies (between 0.5 GeV and 150 GeV).

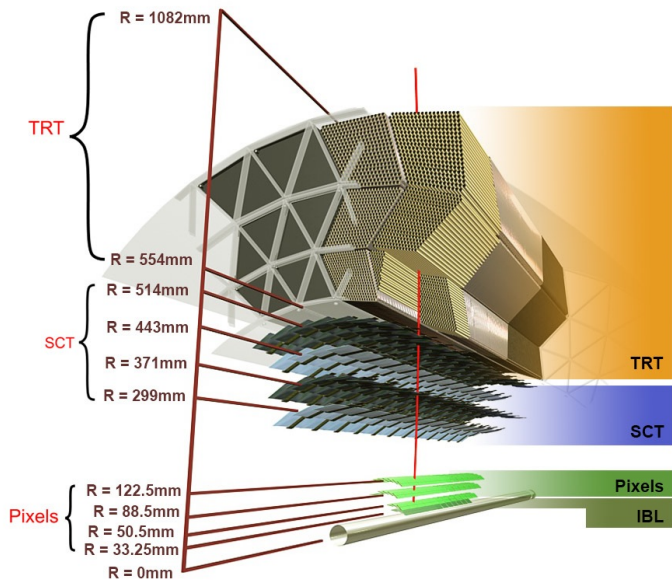


Figure 3.4: Diagram of the ATLAS inner detector and its components, including the new insertable B-layer (IBL) [51].

880 The ID is contained within a cylindrical envelope of length  $\pm 3512$  mm and a radius  
 881 of 1150 mm, within a solenoidal magnetic field of 2T.

882 The ID is composed of three independent but complementary sub-detectors:

- 883 • The inner most component is the Pixel Detector, comprised of silicon pixel layers.  
 884 It is utilised primarily in the reconstruction of both the primary interaction vertex  
 885 and also secondary vertices in an event.
- 886 • The intermediate layer is the Semiconductor Tracker (SCT), comprised of silicon mi-  
 887 crostrip layers, focuses primarily on the accurate measurement of particle momenta.
- 888 • The final layer is the Transition Radiation Tracker (TRT), comprised of many layers  
 889 of gaseous straw tube elements interleaved with transition radiation material. This  
 890 layer contains average 36 hits per track, it provides continuous tracking to enhance  
 891 the pattern recognition, and improve the momentum resolution over  $|\eta| < 2.0$  and  
 892 electron identification complementary to that of the ECAL over a wide range of  
 893 energies.

894 All three sub-detectors have barrel and end cap components.

### 895 3.5.1 Pixel Detector

896 The pixel detector is composed of 1750 identical sensorchip-hybrid modules, each covering  
 897 an active area of  $16.4 \times 60.8$  mm. The total number of modules correspond to approx-  
 898 imately 80 million semiconductor silicon pixels ( $50 \times 400 \mu\text{m}^2$  rectangular segments of  
 899 silicon sensors). This large number of pixels is necessary to cope with the high luminosity  
 900 of the ATLAS detector. Each pixel is read out with an independent electronics channel.

901 The silicon pixel detector forms a cylindrical envelope 48.4 cm in diameter and 6.2 m  
 902 in length providing a pseudorapidity coverage of  $|\eta| < 2.5$ . The three concentric barrel  
 903 layers of radii are at 50.5 mm, 88.5 mm and 122.5 mm and are shown in Figure 3.4. It  
 904 also consists of a total of six disk layers, three at each forward region. Charged tracks  
 905 produced by particles will cross these three layers, yielding at least three space points.  
 906 The main feature of the pixel detector is the fine granularity or size of each pixel, which  
 907 is essential for high resolution measurement and precise vertex information as it provides  
 908 more detection area and therefore a more accurate position.

### 909 3.5.2 Semiconductor Tracker

910 The SCT is designed to measure four precision space points (corresponding to eight silicon  
 911 layers) on the track of a charged particle over a range  $|\eta| < 2.5$ , which is mainly used for

912 precise momentum reconstruction. Each module has an intrinsic resolution of 17  $\mu\text{m}$  in  
913 the  $R - \phi$  direction and 580  $\mu\text{m}$  in the  $z$  direction.

914 The SCT consists of 4088 modules of semi-conducting silicon micro-strip detectors  
915 arranged in four concentric barrel layers, with radii ranging from 299 mm to 514 mm  
916 and two end-cap layers, as shown in Figure 3.4. The silicon-strip sensors are read out by  
917 radiation hard front-end chips, with each chip reading out 128 channels. Due to the SCT  
918 being further away from the beam-pipe, there is reduced particle density expected within  
919 the SCT, which allows for reduced granularity compared to the pixel detector to maintain  
920 the same level of performance while using  $\approx 6.3$  million read-out channels ( $\approx 2$  million  
921 fewer than the pixel detector).

### 922 3.5.3 Transition Radiation Tracker

923 The TRT [52] is the outermost of the three subsystems of the ID. It utilises layers polyimide  
924 straw tube elements, 4 mm in diameter. Transition radiation material surrounds, which is  
925 made of polypropylene fibres in the barrel or polypropylene foils in the end-caps. The tubes  
926 are filled with 70% Xe, 27% CO<sub>2</sub> and 3% O<sub>2</sub>. As a charged particle goes through the TRT  
927 it will ionise the gase inside the straw tubes. It has an average of 36 hits per track in the  
928 central region, providing continuous tracking to enhance pattern recognition and improve  
929 the momentum resolution over the pseudorapidity range  $|\eta| < 2.0$ , which is important for  
930 electron identification. The TRT aims to improve the  $p_T$  resolution for particles with longer  
931 track length, to compliment the pixel detector. It also provides particle identification  
932 capability through the detection of transition radiation X-ray photons generated by high  
933 velocity particles traversing through various materials with different dielectric constants.

934 The TRT barrel section is arranged in three concentric layers with radii ranging from  
935 544 mm to 1082 mm (as shown in Figure 3.4), each with 32 modules jointly containing  
936 approximately 50,000 straws, 1.44 m in length, which are aligned parallel to the beam  
937 direction with independent read-out at both ends. The two end-cap sections are each  
938 divided into 14 wheels, with approximately 320,000 straws that run in the  $R$ -direction.

## 939 3.6 Calorimeters

940 The ATLAS Calorimeter system is composed a number of sampling detectors, which form  
941 the electromagnetic calorimeter (ECAL) and hadronic calorimeter (HCAL), which is de-  
942 signed to stop and measure the energy of electromagnetic and hadronic particles respect-

943 ively. They provide full  $\phi$  coverage and  $|\eta| < 4.95$  around the beam axis. Sampling involves  
 944 utilising layers which cause the particles to lose energy and slow down (absorber), which  
 945 are alternated with layers which measure the energy of the resulting showers (sampler).  
 946 All energy must be contained within the calorimeters, both to improve energy measure-  
 947 ments and to avoid particles showers penetrating into the muon spectrometer, which is  
 known as punch-through.

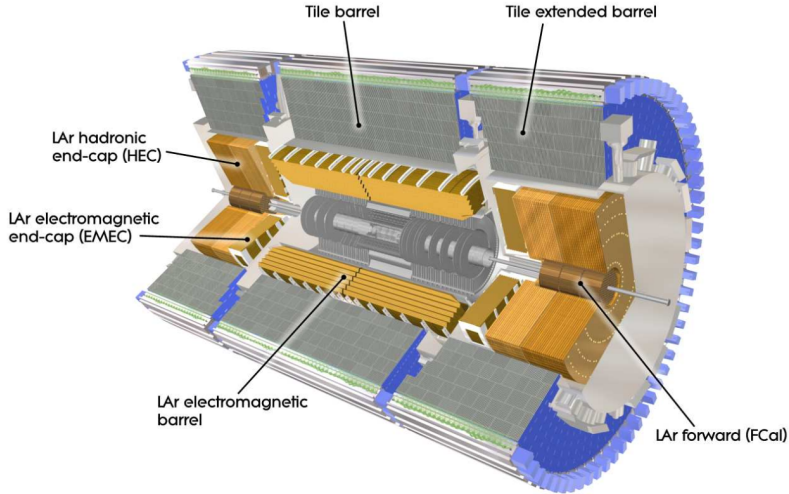


Figure 3.5: Cut-away view of ATLAS electromagnetic and hadronic calorimeter systems [1].

948  
 949 The lengths of barrel and endcap sections of the calorimeter systems can be defined in  
 950 terms of radiation length ( $X_0$ ) for the ECAL, which is defined as the distance over which  
 951 an electron loses  $1/e$  of its energy within a given material, and for strongly interacting  
 952 particles in the HCAL, the nuclear interaction length ( $\lambda_I$ ) for. The ECAL is at least 22  
 953  $X_0$  thick in the barrel, and 24  $X_0$  in the end caps. Although this can vary in some regions  
 954 of  $|\eta|$ . The HCAL is 10  $\lambda_I$  thick on average, this also varies with  $\eta$ . On average the  
 955 nuclear interaction length is of the order of a factor ten larger than the average radiation  
 956 length, hence hadronic particles are much more penetrating within the ATLAS detector  
 957 than electromagnetic particles. Figure 3.7 shows the simulated thickness of material from  
 958 the interaction point up to and including the calorimeters for both radiation lengths and  
 959 nuclear interaction lengths.

### 960 3.6.1 The Electromagnetic Calorimeter

961 The ECAL consists of modules alternating layers of lead absorber and liquid Argon (LAr)  
 962 sampler, which are folded into an accordion geometry. This design was used to provide full  
 963  $\phi$  coverage without any regions of non-interactive material (cracks) and for fast extraction

of the signal from the front or rear end of the electrodes. The calorimeter is divided in two half-barrel wheels covering in pseudorapidity up to  $|\eta| < 1.475$ , housed in the barrel cryostat and two end-cap detectors ( $1.375 \leq |\eta| \leq 3.20$ ) in two end-cap cryostats. There is a region defined as the crack region at the junction of the barrel and end cap components. Signal from this region is discarded in analysis due to the large volume of material in this region, which makes it particularly obscure. In the barrel, the accordion layers are axial and run in  $\phi$ , the folding angles of the layers vary with radius to keep the liquid-argon gap constant. In the end-caps the layers are parallel to the radial direction and run axially. The LAr is ionised by electromagnetic showers. The read-out circuits are made of three copper layers insulated by two layers of polyimide. The two outer layers, split in sectors, are connected to high-voltage sources and polarize the LAr gap to the absorber. The inner layer is where the signal is collected through capacitive coupling and is then segmented into read-out pads.

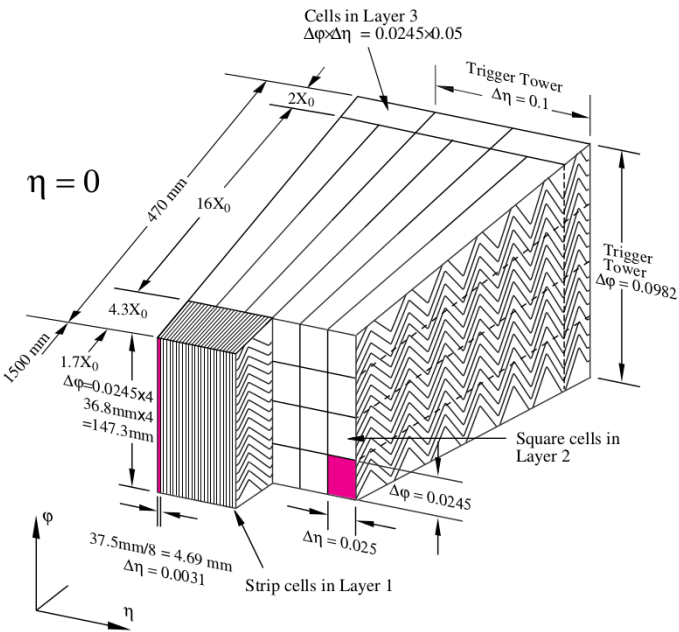


Figure 3.6: Sketch of a barrel module where the different layers are clearly visible with the ganging of electrodes in  $\phi$ . The granularity in  $\eta$  and  $\phi$  of the cells of each of the three layers and of the trigger towers is also shown [1].

In the region of  $|\eta| < 1.8$  there is an additional presampler layer. This consists of a thin (0.5 cm in the end-cap and 1.1 cm in the barrel) LAr layer with no absorber. This is placed at the front of the calorimeter [53]. This to correct for the energy lost at the front of the calorimeter, by taking a measurement just before the ECAL is reached and the majority of the showering occurs. The granularity of the barrel presampler is very fine in  $\eta$  (0.003) to allow precise pointing of photons. The first layer of the calorimeter is

designed for precision measurements, in particular distinguishing between prompt photons and those from neutral pion decays or single, double showers respectively. By necessity it has the smallest measurable segment size of the three layers with  $\Delta\eta \times \Delta\phi = 0.025 \times 0.025$ . The second layer will contain the largest fraction of energy deposited by an EM shower and is designed mainly for energy measurements. Because of this it is used to distinguish between EM showers and hadronic showers which are much more penetrating. As a discriminatory layer, it can have a coarser granularity at  $\Delta\eta \times \Delta\phi = 0.05 \times 0.025$ .

The depth of the three sampling layers has been subject to thorough optimisation, mostly based on the criterion of  $\pi^0$  rejection. The depth of the first layer is  $6 X_0$  (including dead material and presampler). The end of the second (main) layer was chosen to be  $24 X_0$ . The depth of the last layer varies between 2 to  $12 X_0$  (for  $\eta$  less than 0.6). The depth of the second sampling is limited to  $22 X_0$ , in order to have at least  $2 X_0$  in the third sampling.

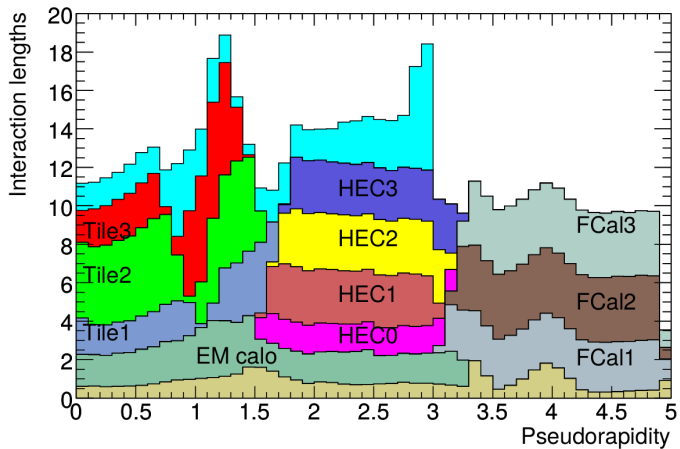


Figure 3.7: Cumulative amount of material, in units of interaction length, as a function of  $|\eta|$ , in front of the electromagnetic calorimeters, in the electromagnetic calorimeters themselves, in each hadronic layer, and the total amount at the end of the active calorimetry. Also shown for completeness is the total amount of material in front of the first active layer of the muon spectrometer (up to  $|\eta| < 3.0$ ) [1].

### 3.6.2 The Hadronic Calorimeter

The HCAL uses slightly different materials and techniques to the ECAL, which also vary between the tile calorimeter, end-cap (HEC) and forward calorimeter (FCal) components.

The barrel section at  $|\eta| < 1.0$  and extended barrel sections at  $0.8 < |\eta| < 1.7$  make up the tile calorimeter, which uses steel absorber layers and plastic scintillating tiles as the active medium [1]. These are read out from both sides by wavelength-shifting fibres to photo-multiplier tubes (PMTs). There are three layers of modules in each barrel section,

1003 which are  $1.5$ -,  $4.1$ - and  $1.8\lambda_I$  thick in the barrel, and  $1.5$ -,  $2.6$ - and  $3.3\lambda_I$  thick in the  
 1004 extended barrels. Module layers are offset with respect to the layers of their neighbours for  
 1005 increased granularity, which is  $\Delta\eta \times \Delta\phi = 0.1 \times 0.1$  in the first two layers and  $\Delta\eta \times \Delta\phi =$   
 1006  $0.1 \times 0.2$  in the final layer. The electronics are contained with girder plastic rings, which  
 1007 also provide flux return for the central solenoidal magnetic field.

1008 The HEC consists of two wheels, each consisting of two layers of wedge-shaped modules  
 1009 which use copper absorber layers alternated with LAr with a flat plate design. The end-  
 1010 caps provide  $1.5 < |\eta| < 3.2$  coverage, overlapping slightly with both the tile calorimeter  
 1011 and the FCAL in  $\eta$ .

1012 The FCAL is located in the same cryostats as the end-cap calorimeters and provide  
 1013 coverage over  $3.1 < |\eta| < 4.9$  and uses an absorber metal matrix combined with rod and  
 1014 tube electrodes, where LAr fills all of the small gaps in between. It is comprised of three  
 1015 modules, the first using copper as the shower-initiating metal, which is focused on EM  
 1016 measurements and the last two, which both use tungsten as the absorber and are primarily  
 1017 for the measurement of hadronic energy and to provide containment and minimise lateral  
 1018 spread of hadronic showers.

### 1019 3.7 Muon Spectrometer

1020 The Muon Spectrometer (MS) [54] is the outermost part of the ATLAS detector, which  
 1021 surrounds the calorimeters and measures the muon tracks in conjunction with the charged  
 1022 tracks in the ID and small energy deposits in the calorimeters for muon reconstruction. It  
 1023 is divided into the barrel, containing three layers at radius 5, 7.5 and 10 m in the region  
 1024  $|\eta| < 10$ , and two end-caps, comprised of wheels at 7.4, 10.8, 14 and 21.5 from the origin  
 1025 and covering the range  $1.0 < |\eta| < 2.7$ . A cut-away showing the structure and individual  
 1026 components can be seen in Figure 3.9 and examples of muon trajectories in the barrel and  
 1027 end-cap are shown in Figure 3.8.

1028 The magnetic field used to bend particle trajectories is provided by the barrel toroids  
 1029 for  $|\eta| < 1.4$ , by the end-cap toroids for  $1.6 < |\eta| < 2.7$ , and a combination of the two in  
 1030 the “transition” region  $1.4 < |\eta| < 1.6$ . In the barrel region, the toroidal field is produced  
 1031 by eight very large superconducting coils arranged in an open geometry, with a  $B$ -field  
 1032 varying from 0.5 to 2T.

1033 The components of the muon system are: resistive plate chambers (RPCs), thin gap  
 1034 chambers (TGCs), cathode strip chambers (CSCs), and monitored drift tube chambers

(MDTs). The layout of the individual components can be seen in 3.9. The MDTs and CSCs are used to precisely measure the muon tracks. The MDTs provide a precise momentum measurement. They cover the pseudorapidity range  $|\eta| < 2.7$  in each layer except the innermost end-cap layer where their coverage is limited to  $|\eta| < 2.0$ . Each chamber consists of three to eight layers of 29.970 mm drift tubes, each filled with Ar/CO<sub>2</sub> gas and with a tungsten-rhenium wire through the centre. The wire is kept at a potential to collect gas ionised by charged particles passing through. They achieve an average resolution of 80  $\mu\text{m}$  per tube, or about 35  $\mu\text{m}$  per chamber.

The CSCs are placed at high pseudorapidity ( $2.0 < |\eta| < 2.7$ ) in the inner-most tracking layer. They possess a high rate capability and time resolution. They are comprised of multiwire proportional chambers filled with AR/CO<sub>2</sub>/CF<sub>4</sub> gas. There are cathode planes segmented into strips in orthogonal directions, which allows both coordinates to be measured from the induced charge distribution. The solution of a chamber is 40 mm in the bending plane ( $\eta$ ) and approximately 5 mm in the transverse plane.

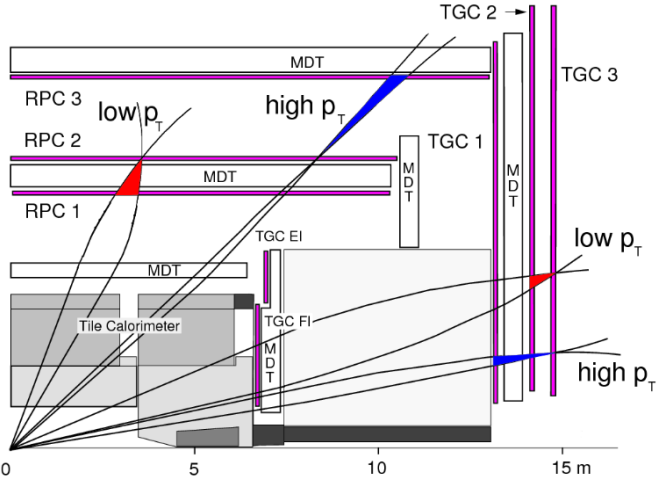


Figure 3.8: Muon trajectories exemplified for the barrel (RPCs) and the end-cap (TGCs) [1].

The trigger chambers are operational in the region  $|\eta| < 2.4$ , with two different types of chamber employed to handle the increased rates in the forward region. The RPCs are located in the barrel and cover the region  $|\eta| < 1.05$  and the TGCs are in the end-caps covering  $1.05 < |\eta| < 2.4$ . As well as providing a fast enough read-out (less than 50 ns) for triggering, these also determine a second reading of the muon coordinate which is orthogonal and complementary to that taken by the precision chambers. The RPCs consist of gaseous (C<sub>2</sub>H<sub>2</sub>F<sub>4</sub>/Iso-C<sub>4</sub>H<sub>10</sub>/SF<sub>6</sub>) parallel electrode-plate detector. The resistive plastic plates used are at a spacing of 2 mm and with a voltage of 4.9 kV/mm across them. The

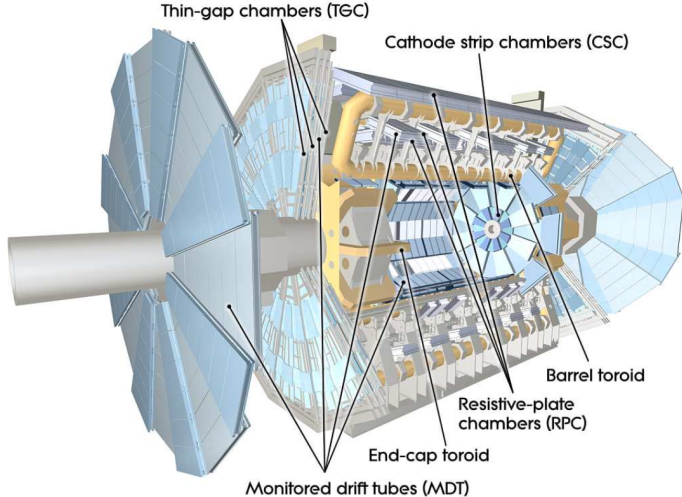


Figure 3.9: Cut-away view of ATLAS muon system [1].

1057 gas mixture forms ionising avalanches when a charged particle passes through. These  
 1058 are read off by metallic couplings on the outside of the resistive plates. The TGCs are  
 1059 multi-wire proportional chambers similar to the CSCs, with a higher granularity than the  
 1060 RPCs.

### 1061 3.8 Trigger and Data Acquisition System in Run-1

1062 The Trigger and Data Acquisition (TDAQ) system is designed with the purpose of reducing  
 1063 the event rate taken from the LHC at 40 MHz (during Run-1) to a recordable size of  
 1064 approximately 200 Hz, which corresponds to an average data rate of  $\approx 300$  MB/s. It  
 1065 consists of two subsystems: the trigger; and data acquisition; which handle the event  
 1066 selection and data flow respectively.

#### 1067 3.8.1 The ATLAS Trigger System

1068 The trigger consists of three levels of event selection: Level 1 (L1), Level 2 (L2) and the  
 1069 Event Filter (EF). The L2 and event filter form the High-Level Trigger (HLT). The L1  
 1070 trigger searches for signatures from high- $p_T$  muons, electrons, photons, jets, hadronically  
 1071 decaying  $\tau$ -leptons and large missing transverse energy. It selects a region of interest  
 1072 (RoI) in  $\eta$  and  $\phi$  based on these signatures using reduced granularity information from the  
 1073 calorimeters and the muon spectrometer. During the decision making process, the event  
 1074 information from the detectors is stored in front-end pipelines and is then passed to the  
 1075 Read Out Buffers (ROBs) if the decision is positive along with RoI information from the  
 1076 L1. The maximum L1 accept rate which the detector read-out systems can handle is 75

1077 kHz (For Run-2 100 kHz). The L1 decision must reach the front end electronics with 2.5  
 1078  $\mu$ s after the bunch crossing with which it is associated. The L2 trigger is “seeded” by RoIs,  
 1079 which contain possible trigger objects within the event. The L2 takes RoI information from  
 1080 the RoBs for co-ordinates, energy and signature type combined with tracking information  
 1081 from the ID to limit the amount of data transferred from the detector read-out. In doing  
 1082 so, the L2 trigger reduces the rate to below 3.5 kHz, with an average event processing time  
 1083 of  $\approx$  40ms. If the event is accepted, the data is passed to the Event Builder and stored in  
 1084 the Full Event Buffer. The EF then accesses the fully built event using offline algorithms,  
 1085 with access to full detector granularity, maximum calorimeter and muon chamber preci-  
 1086 sion to refine trigger selection. Improved information on energy deposition improves the  
 1087 threshold cuts, while the track reconstruction in the ID vastly improves particle identi-  
 1088 fication, particularly for electrons and photons. A higher latency is utilised to achieve a  
 1089 more accurate reconstruction. It reduces the event rate to approximately 200 Hz with an  
 1090 average event processing time of the order of four seconds. Figure 3.10 shows a flowchart  
 representing this process.

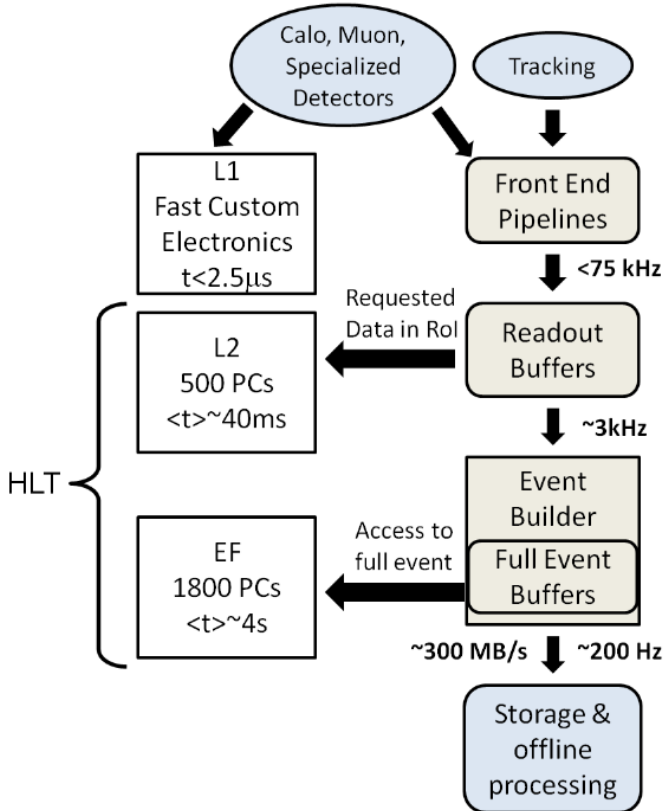


Figure 3.10: Schematic of the ATLAS Trigger System [55]

### 1092 3.8.1.1 Level 1 Trigger

1093 The L1 trigger uses custom fast electronics to perform the initial event selection based on  
1094 detector information. It then passes its decision to the Central Trigger Processor (CTP).  
1095 The L1 Calorimeter (L1Calo) seeks to identify high- $E_T$  objects, in addition to the objects  
1096 highlighted in the introduction, a trigger on the scalar sum of the jet transverse energies is  
1097 also available and for the electron/photon triggers, isolation can be required. The isolation  
1098 requirement implies that the energetic particle must have a minimum angular separation  
1099 from all other significant energy deposits within the same trigger.

1100 To identify RoIs for electrons, photons, taus and jets, coarse granularity segments of  
1101 the HCAL and ECAL, referred to as trigger towers are used. They cover blocks of size  
1102  $\Delta\eta \times \Delta\phi = 0.1 \times 0.1$  in the central calorimeters and up to  $\Delta\eta \times \Delta\phi = 0.4 \times 0.4$  in the  
1103 forward calorimeters.

1104 The L1 Muon trigger is based on signals in the muon trigger chambers; using the  
1105 three layers of RPCs and TGCs in the barrel and end-cap of the muon spectrometer. The  
1106 trigger searches for patterns of hits consistent with high  $p_T$  muons originating from the  
1107 point of interaction.

1108 If an event passes the L1 trigger requirements, an accept signal (L1A) is sent to the  
1109 CTP. The CTP then sends information about the trigger decision for all trigger items to  
1110 the L2 trigger (RoI builder) and the data acquisition (ROS). To prevent an overwhelming  
1111 rate of data flow through the front-end buffers, the CTP enforces two types of dead-time;  
1112 simple and complex. The simple dead time requires a given period has to pass after an  
1113 L1A decision from the L1 before another is allowed. For Run-1 during 2011 and 2012  
1114 this was five bunch crossings. The CTP vetoes any L1A signals within this time period.  
1115 The complex dead time sets a limit on the number of L1A allowed within a given period,  
1116 which, for Run-1 during 2011 and 2012 was set to 8 accepts per 416 bunch crossings.  
1117 Part of the read-out data of the CTP is the number of the corresponding luminosity  
1118 block. A luminosity block is defined as the shortest time interval for which the integrated  
1119 luminosity, corrected for dead time and pre-scale effects, can be determined. A luminosity  
1120 block should be small enough such that, in the event of detector failures, the data can be  
1121 rejected with unnecessary data loss. However, a luminosity block, should contain enough  
1122 data such that the uncertainty on the luminosity is only determined by systematics and  
1123 by the available statistics. For ATLAS this is of the order of minutes.

### 1124 3.8.1.2 High Level Trigger

1125 The High Level Trigger (HLT) consists of the L2 and EF triggers. Both are implemen-  
1126 ted in software and run mostly on commodity hardware (farms) [56]. The L2 trigger  
1127 uses signature-based algorithms, which have a limited precision in order to operate on a  
1128 short timescale. It uses the RoI information (type, position and  $p_T$  of the highest trigger  
1129 threshold passed) from the L1 trigger seed. This keeps the amount of raw data passed to  
1130 the L2 trigger at a few percent of the total event information. In addition to the muon  
1131 detector and calorimeter data, the L2 also has access to the tracking information from the  
1132 ID.

1133 Two separate algorithm strategies were used during Run-1. Both strategies start by  
1134 identifying a primary vertex, using the hit occupancy for the event in the pixel and SCT  
1135 sub-detectors as a function of the z co-ordinate. The point with the highest hit occupancy  
1136 is taken as the primary vertex for the event. The algorithms generate final tracks from the  
1137 space points using a Kalman filter [57], which is a general type of linear filtering algorithm  
1138 that iteratively compensates for the effect of noise on a signal. In the case of tracking  
1139 algorithms, the signal is the true trajectory of the particle and the noise is the effect of  
1140 associating incorrect space points to the true trajectory. If an event passes the L2 Trigger,  
1141 the information from the RoI is sent to the the final trigger layer, the Event Filter. This  
1142 has access to the full granularity data from the whole event and is not restricted to the  
1143 RoIs. It uses standard ATLAS offline reconstruction algorithms. It has been configured  
1144 to reject or accept an event in around 1 s. The average rate after the EF decision was  
1145 approximately 400 Hz in 2011 and approximately 1 kHz in 2012.

### 1146 3.8.2 Trigger Chains and Menus

1147 Physics events of interest can contain a multitude of important physics signatures, to  
1148 achieve full information on these events, a sequence of algorithms for the L1, L2 and EF  
1149 triggers must be satisfied. The combination of these algorithms forms a specific trigger  
1150 selection, which is referred to as a chain. For each signature used for triggers there are a  
1151 set of chains defined. Each chain is composed of a Feature Extraction (FEX) algorithms,  
1152 which create the objects (like calorimeter clusters) and Hypothesis (HYPO) algorithms  
1153 that apply selection criteria to the objects (for example  $p_T > 20$  GeV). Caching in the  
1154 trigger system allows features extracted from one chain to be recycled in another chain.  
1155 This reduces both the data access and processing time of the trigger system.

1156 To illustrate, take the example of the single electron trigger, *e24\_medium*. This chain

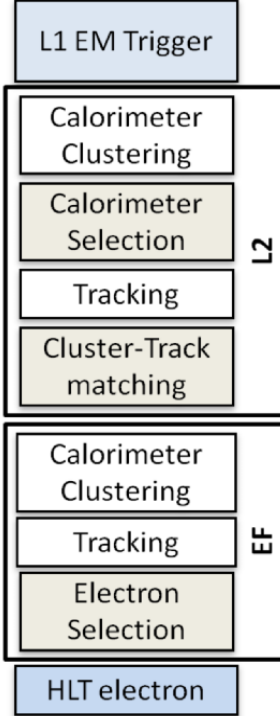


Figure 3.11: Schematic example of an electron trigger chain [55] .

is built on the L1EM18 trigger, which has a threshold of 18 GeV and uses the EM trigger tower to determine this threshold is passed. The detector information in the ROI provided by the L1EM18 trigger is seeded to the *L2\_e24\_medium* trigger, which has a 25 GeV threshold, lastly the full detector information is sent to the *EF\_e24\_medium* trigger, which also has a 25 GeV threshold. Primary chains are physics-based and used for analyses. Backup chains have a higher threshold than the primary chains and can be used if the detector malfunctions or the luminosity increases unexpectedly, supporting chains provide support for physics analyses, for example background estimation methods and the monitoring chains are used to monitor data performance.

Events which have passed the EF are classified into streams. An event can be contained in more than one stream, and the type of stream is dependent on the category of chain that accepted the event. The four physics streams are muon, electron/photon, jet/tau/ $E_T^{miss}$  and minimum bias. Data from these streams are recorded separately, to allow analyses to focus only on events containing objects of interest. In addition to the physics streams 10% of events are written to the express stream for fast reprocessing to validate the recorded data and data collections for calibration.

The full collection of all trigger chains for all signatures is referred to as the trigger menu. These menus may change depending on the running conditions. Changes in collision

1175 energy or pile-up has an effect on the I/O rates of the various triggers, which would in  
1176 turn require a change to the trigger menu. The trigger menu was updated for Run-2 to  
1177 account for the higher centre-of-mass energy and increase in pile-up.

### 1178 3.9 ATLAS Run-2 Upgrades

1179 The LHC during Run-2 of its planned schedule will attain its design energy and nominal  
1180 luminosity with a centre of mass energy of  $\sqrt{s} = 13\text{-}14 \text{ TeV}$ ,  $\mathcal{L} = 1 \times 10^{34} \text{ cm}^{-2}\text{s}^{-1}$ , a bunch  
1181 spacing of 25 ns and a pile up  $\langle \mu \rangle$  of  $\approx 40$ . It is essential for the ATLAS detector and the  
1182 TDAQ system to be upgraded in order to cope with the increased event rate at higher  
1183 energies to continue with physics analysis. This section will discuss the main changes to  
1184 the ATLAS detector in preparation for Run-2, which took place during Long Shutdown 1  
1185 (LS1).

#### 1186 3.9.1 Insertable B-layer

1187 The Insertable B-Layer [58] is the fourth layer added to the Pixel Detector between a new  
1188 beam pipe and the current innermost pixel layer (*B*-layer), as shown in Figure 3.4. The  
1189 IBL improves the overall performance of the Pixel Detector and the ATLAS experiment  
1190 by enhancing the quality of impact parameter reconstruction of tracks. This is done by  
1191 improving vertexing and tagging of *b*-quark containing jets (*b*-tagging, see Section 4.4.7).  
1192 Furthermore, in case of a complete *B*-layer failure, the IBL can restore the full *b*-tagging  
1193 efficiency. The addition of a fourth layer also helps to mitigate luminosity effects such  
1194 as the increase in event pile-up, which leads to high occupancy and read-out inefficiency.  
1195 Detailed simulations of the ID performance with and without the IBL have been performed.  
1196 The IBL detector has been fully integrated into the ATLAS ID software and its response  
1197 is based on the existing pixel digitisation algorithm [59].

#### 1198 3.9.2 ATLAS TDAQ Upgrades for Run-2

1199 With beam energies of 13-14 TeV and up to 80 *pp* interactions per bunch crossing, to  
1200 access physics events of interest under these conditions required improvements to the  
1201 Run-1 trigger system. In particular:

- 1202 • Make the HLT code more robust and faster to compensate for increased processing  
1203 time due to high pile up and allow for use of slower offline reconstruction algorithms.
- 1204 • Harmonise trigger and offline analysis selections to increase trigger selection effi-

1205 ciency.

- 1206 • Introduce specialised, selective triggers to help reduce trigger rates.

### 1207 3.9.2.1 L1 Topological Trigger

1208 Previously, the L1 trigger system was only able to look for single objects or apply simple  
 1209 combinations of such single objects to be present in the event. The L1 topological trigger  
 1210 (L1-Topo) [60] has been added to extend the functionality of the L1 trigger. It receives  
 1211 energy and direction information about the objects found by the L1 calorimeter and the  
 1212 muon trigger. This information is then processed by dedicated algorithms implemented in  
 1213 its FPGAs. Signatures that will be looked for include, a muon close to a jet, an object with  
 1214 a certain transverse mass or an event with an effective mass above a certain threshold.  
 1215 However the L1-Topo will only be able to send limited information to the HLT due to the  
 1216 100 kHz read-out rate. The HLT has the challenge of using the specific L1 object combin-  
 1217 ation with the correct topological criteria to seed the RoI-guided HLT reconstruction. In  
 1218 answer to this challenge, the L1 topological trigger hardware is simulated, i.e. the FPGA  
 1219 code will also be implemented in C++ and validated against the hardware response and  
 1220 run online in the HLT.

### 1221 3.9.2.2 Fast TracKing Trigger System (FTK)

1222 As the LHC luminosity approaches its design luminosity, the combinatorial problem arising  
 1223 from charged particle tracking becomes increasingly difficult, resulting in lower signal effi-  
 1224 ciencies for larger pile up and constant rates of fake physics objects. The Fast TracKer [61]  
 1225 or FTK is a proposed system of electronics which will perform global track reconstruction  
 1226 after each L1 trigger decision to enable the L2 trigger to have early access to tracking  
 1227 information. The FTK will use data from the pixel and semiconductor tracker detectors  
 1228 as well as the new IBL pixel detector. The necessity for improved track reconstruction per-  
 1229 formance at higher luminosities is essential for identifying heavy particles such as  $b$ -quarks  
 1230 and  $\tau$  leptons.

1231 The FTK will receive all the semi-conductor data from the inner detector charged  
 1232 particle tracker at each L1A signal, with up to 100 kHz rate. The hardware then finds and  
 1233 reconstructs charged track candidates using pattern matching on specially pre-processed  
 1234 data in an associative memory. In this sense the hardware provides tracking information  
 1235 for the whole detector very quickly, with no need for HLT processing time or read-out band-  
 1236 width. This information can be used in several ways: Calculating the isolation of identified

1237 leptons from other charged particles; finding the primary vertices of the event using all  
 1238 reconstructed tracks; Seeding the HLT track reconstruction to reconstruct charged tracks  
 1239 with high precision in a large area of the detector; The reconstructed tracks may be used  
 1240 directly in the b-tagging and tau reconstruction algorithms to improve their performance  
 1241 with the additional tracking information.

1242 Data taking with the FTK is to start in the middle of Run-2 with limited detector  
 1243 coverage and full coverage by the end of 2016.

### 1244 **3.9.2.3 The Merged High Level Trigger**

1245 In Run-1 the ATLAS trigger system had distinct L2 and EF farms. For Run-2, these  
 1246 farms were merged into a single farm running a unified HLT process, that retains the on-  
 1247 demand data read-out of the old L2 and uses offline based algorithmic code from the EF.  
 1248 This new system reduces code and algorithm duplication and results in a more flexible  
 1249 HLT. The majority of the trigger selections were reoptimised during LS1 to minimize  
 1250 differences between the HLT and the offline analysis selections, which in some cases reduced  
 1251 trigger inefficiencies by more than a factor of two. The HLT tracking algorithms also were  
 1252 prepared for the inclusion of the FTK system. The average output rate of the HLT has  
 1253 been increased from 400 Hz to 1 kHz. The HLT processing performed within RoIs has  
 1254 been augmented for some triggers to also allow for merging of RoIs into a single object,  
 1255 referred to as a super-RoI. This reduces the trigger processing for events with a large  
 1256 multiplicity of partially overlapping RoIs.

1257 The upgraded ATLAS trigger system has been commissioned using cosmic ray data  
 1258 and early 13 TeV collisions. It works efficiently allowing ATLAS to efficiently select events  
 1259 for physics analysis in Run-2.

## <sup>1260</sup> Chapter 4

# <sup>1261</sup> The Generation, Simulation and <sup>1262</sup> Reconstruction of ATLAS Data

<sup>1263</sup> Monte Carlo (MC) simulation is used in ATLAS to mimic particle interactions or decays,  
<sup>1264</sup> with each referred to as an “event”. These events are used to understand SM and beyond  
<sup>1265</sup> the SM processes and are validated with events from real data taken by the detector. The  
<sup>1266</sup> process of generating an event using MC simulation can be categorised into two parts:  
<sup>1267</sup> event generation and detector simulation. Data which has been recorded by the ATLAS  
<sup>1268</sup> detector requires processing to reconstruct physics objects to be used in analysis. The  
<sup>1269</sup> Athena software framework [62], which is based on the GAUDI [63] framework developed  
<sup>1270</sup> by LHCb [48] is used to do this. This framework is implemented for all aspects of the  
<sup>1271</sup> experiment software including the triggering of events, event reconstruction and event  
<sup>1272</sup> processing for simulated data. This chapter discusses event generation in Section 4.1,  
<sup>1273</sup> event simulation in Section 4.2 and digitisation in Section 4.3. Reconstruction algorithms  
<sup>1274</sup> are the same for both real data and MC simulated events, these are described in Section 4.4.  
<sup>1275</sup> The objects used for the analysis in this thesis are selected from the reconstructed objects  
<sup>1276</sup> based on a set of criteria, which are described in Section 4.5. Finally the MC simulated  
<sup>1277</sup> samples used for the SM and SUSY processes are described in Section 4.6.

### <sup>1278</sup> 4.1 Event Generation

<sup>1279</sup> All SM and beyond the SM physics processes are simulated by MC event generators [64].  
<sup>1280</sup> These generators use a combination of perturbative and phenomenological calculations to  
<sup>1281</sup> produce randomly distributed “events” of a given type with stable final state particles.  
<sup>1282</sup> The ATLAS detector collects information from proton-proton collisions, which essentially

1283 involves the collisions of the constituent *partons*. These partons include the three valence  
 1284 quarks (uud); the gluons mediating the strong interactions between the valence quarks;  
 1285 and the sea quarks which are produced in virtual  $q\bar{q}$  pairs by interactions of the gluons.  
 1286 These interactions are collectively known as Deep Inelastic Scattering (DIS) processes.  
 1287 They are called as such because the substructure of the proton is probed by an incoming  
 1288 particle (deep), for example another proton, and the proton's momentum is not conserved  
 1289 in the scattering (inelastic) as shown in Figure 4.1.

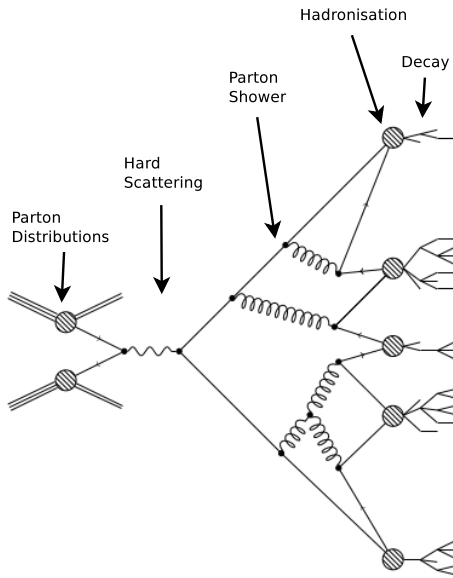


Figure 4.1: Diagram of a simulated high energy proton-proton collision process.

1290 If  $Q^2$  represents the squared 4-momentum-transfer vector  $q$  of the exchanged virtual  
 1291 photon. The interacting parton carries a fraction of the proton's momentum  $x$ , known as  
 1292 the Bjorken scaling variable.

1293 The measure of momentum transfer in the event  $Q^2$  is related to the momentum  
 1294 transferred by the exchanged boson  $q$  by:

$$Q^2 = -q^2. \quad (4.1)$$

1295 To effectively describe partons within the protons colliding at the LHC, parton distri-  
 1296 bution functions (PDFs) are used, this will be discussed in Section 4.1.1.

1297 Scattering interactions involving protons at the LHC can be grouped into two categor-  
 1298 ies: Hard processes, which can be described with perturbation theory, or soft processes,  
 1299 which involve non-perturbative QCD effects. Hard processes involve large momentum  
 1300 transfer and soft processes involve low momentum transfer, with inelastic interactions at

the LHC being dominated by soft processes [65]. Each  $pp$  collision will typically contain a hard scattering process between two colliding partons, and a number of soft processes, which can include Initial State Radiation (ISR), Final State Radiation (FSR) and the Underlying Event (UE). ISR refers to the particles radiated by the partons which will interact in the hard process prior to scattering. Additional parton interactions in hard processes due to beam remnants and the rest of the proton constituents form the UE. The particles radiated from the final state products of the hard scatter form the FSR. Coloured particles in the event are capable of radiating gluons and/or producing  $q\bar{q}$  pairs, resulting in a cascade of radiation in the detector, known as parton showering.

The following sections will briefly describe the techniques used to model the hard process, PS and hadronisation within the event, in addition to the modelling of the UE.

MC generated samples are categorised on the basis of the hard-process specified before generation, which allows analysers to choose samples with relevant processes.

#### 4.1.1 Parton Distribution Functions

PDFs [66] describe the probability density of constituent partons of the interacting protons to have proportion  $x$  of the overall momentum. PDFs, denoted  $f_a(x, Q^2)$  are functions of the momentum fraction, parton species  $a$  and momentum transfer  $Q^2$ . The factorisation theorem [67] states that the differential cross section  $d\sigma$  of any hard process can be written in the form

$$d\sigma = \sum_{i,j} \int_0^1 dx_i \int_0^1 dx_j \quad d\sigma_{i,j}^{part} f_i(x_i, Q^2) f_j(x_j, Q^2). \quad (4.2)$$

Here  $i$  and  $j$  are the indices of the interacting partons with momentum fractions  $x_i$ ,  $x_j$  and the  $d\sigma_{i,j}^{part}$  is the differential cross section of the hard process between partons  $i$  and  $j$  with momentum fractions  $x_i$ ,  $x_j$ . The PDFs are functions of the momentum fraction and are thus independent of the hard process. They are also dependent on the parton type (valence quark, gluon or sea quark). It is not possible to calculate the PDFs perturbatively, but their evolution as a function of  $Q^2$  for a given parton can be obtained using the DGLAP evolution equations [68], using a range of hard scattering data from both fixed target and collider experiments. These equations describe the evolution of the structure functions of the proton's constituent quarks and gluons as a function of the “running” strong coupling  $\alpha_s$ , where running refers to  $Q^2$  dependence. A range of PDF sets are used by the MC samples considered by this analysis.

### 1331 4.1.2 Matrix Element Calculation

1332 The hard process involves a large momentum transfer ( $Q^2 > \mathcal{O}(1 \text{ GeV})$ ), the simulation  
1333 of this process can be calculated using quantum field theory techniques - this is known  
1334 as the matrix element calculation. PDFs simulate partons coming into the hard scatter  
1335 process using matrix elements to leading order (LO) or next-to-leading order (NLO) in an  
1336 expansion in  $\alpha_s$  to calculate a probabilistic distribution of the outgoing partons. Additions  
1337 can be made to the matrix element to include *hard emission*, which refers to the production  
1338 of high momentum quarks and gluons in the event. This includes several processes; a gluon  
1339 splitting into two gluons ( $g \rightarrow gg$ ), a gluon decaying to a quark-antiquark pair ( $g \rightarrow q\bar{q}$ ),  
1340 and a quark radiating a gluon ( $q \rightarrow gq$ ). These processes are included and can be repeated,  
1341 provided they are at high  $Q^2$ .

### 1342 4.1.3 Parton Showers

1343 The processes mentioned in the Matrix Element section can also occur at lower energies,  
1344 but cannot be modelled by the matrix element calculation due to their non-perturbative  
1345 nature. They are handled with the parton shower (PS) phenomenological modelling, which  
1346 is valid for  $Q^2$  values above  $\mathcal{O}(\text{GeV})$ , the QCD scale. PS models have been developed by  
1347 the HERWIG [69], PYTHIA [70] and SHERPA [71] collaborations. The algorithms used to  
1348 simulated PS are based on a Markov chain [72], using probabilities that a gluon is radiated  
1349 or a  $q\bar{q}$  pair is produced. The decision of whether or not these processes will occur is made  
1350 at each point in the chain. At intermediate  $Q^2$ , gluon/quark radiation may be treated as  
1351 a hard emission or part of the PS, which can lead to double-counting of the total radiation  
1352 in a given event. The CKKW [73] and MLM [74] schemes are used to determine whether  
1353 emissions form part of the matrix element or PS. Eventually the energy of the partons  
1354 will decrease below 1 GeV and undergo hadronisation, which is modelled separately.

### 1355 4.1.4 Hadronisation

1356 Free partons are not observed directly in nature due to confinement, only hadrons. Res-  
1357 ulting partons produced in showering from  $pp$  collisions hadronise at low energy scale. At  
1358 this scale perturbation theory is not valid, so modelling is used to simulate what occurs.  
1359 The two common approaches are the Lund string model [75] used by the PYTHIA MC and  
1360 the Cluster model used by the HERWIG MC program [76].

### 1361 4.1.5 Underlying Event

1362 The “spectator” partons, which are the partons not involved in the hard process of an  
1363 event are referred to as the underlying event (UE) [77]. These partons hadronise to  
1364 form colour-singlet state. This hadronisation is described by phenomenological models  
1365 developed by the JIMMY [78], PYTHIA and SHERPA collaborations. The modelling involves  
1366 many additional free parameters, which are tuned to data and are described in further  
1367 detail in Section 4.6.1.

## 1368 4.2 Detector Simulation

1369 The MC generated events need to be passed through an accurate simulation of the ATLAS  
1370 detector, which mimics the response of the real detector to the physics processes. This  
1371 is done by the GEANT4 framework [79]. It is the only officially supported software for  
1372 the ATLAS detector simulation and is integrated into the ATLAS offline software. The  
1373 detector simulation involves the interaction of particles within the detector volume, this  
1374 includes particle ionisation, energy deposition in the calorimeters and intermediate particle  
1375 decays, radiation and scattering. These interactions are recorded as GEANT4 “hits”.  
1376 Output files containing data of the detector simulation, known as “hit files”, are generated.  
1377 These are then “digitised” to produce voltages and currents in the detector. The simulation  
1378 of electronic noise, pile-up and other effects from the detector electronics are factored in  
1379 at the digitisation stage. It is vital to mention the detector geometry and simulation  
1380 infrastructure remains the same for simulation, digitisation and reconstruction to ensure  
1381 agreement between simulation and reconstruction. With the completion of the detector  
1382 simulation, the simulated data (in the form of digits) are in an equivalent format to the  
1383 data recorded with the ATLAS detector.

1384 Fully simulating each event traversing the detector can be very time consuming, with  
1385 some events taking up to ten minutes. A faster simulation process can also be performed  
1386 using the ATLFASTII package [80], which does not run all of the aforementioned stages for  
1387 full simulation. Instead, the energy of single particle showers is deposited directly using  
1388 parameterisations of their longitudinal and lateral energy profile and a simplified geometry  
1389 is applied. The calorimeter is simulated using FastCaloSim [81]. Scattering of particles  
1390 within the inner detector is simulated using a simplified model. The GEANT4 simulation  
1391 time can be reduced by more than one order of magnitude by using the ATLFASTII. A fast  
1392 simulation is important in cases when the total number of events simulated is a limiting

1393 factor for analysis, for example SUSY “signal” processes. In this case, samples can be  
1394 generated with a large number of events given that this fast simulation is well validated  
1395 against the full simulation samples.

### 1396 4.3 Digitisation

1397 The hits produced during simulation are passed through a simulation of the detector in  
1398 order to produce digitised values for voltages, associated times etc. Any noise within the  
1399 detector is included. Soft collisions, beam halo, cosmic rays and the cavern background  
1400 are independent of the event itself, therefore are not simulated each time. These hits can  
1401 be overlaid at this stage. The MC is then output in a raw data object (RDO) format,  
1402 which contains the equivalent information to the real data recorded by the detector. A  
1403 *truth* record for the simulated events is stored in a simulated data object (SDO) format,  
1404 which contains the information on the true identity of particles at each vertex and the  
1405 corresponding tracks left behind and consequent decays. The truth objects do not neces-  
1406 sarily correspond exactly to the objects reconstructed from the RDO, for example a lepton  
1407 can be mistakenly identified as a photon. The truth record is stored to study detector be-  
1408 haviour, for example potential misreconstruction rates of various particles. Truth objects  
1409 can be “matched” to reconstructed objects by requiring a minimum spatial requirement  
1410 between the objects. In addition, matching can be used to trace back the decay chain and  
1411 identify the “parent” of a particle, using the particle identifier and vertex information.

### 1412 4.4 Reconstruction

1413 Both the data and the simulated MC events are passed through the same reconstruction  
1414 algorithms. At this stage, the electronic pulses from the digitisation stage are reconstructed  
1415 into tracks and calorimeter deposits, which are in turn reconstructed into physics objects,  
1416 such as jets, electrons, muons, taus, photons and missing transverse energy or  $E_T^{miss}$ .  
1417 Loose definitions for physics objects are made initially for most analyses to use. More  
1418 stringent requirements can be applied on top to focus on the needs of particular analyses.  
1419 The benefit of this approach is the increased purity of selected objects. The definitions for  
1420 the physics objects relevant to the analysis presented in this thesis are described in the  
1421 following sections.

#### 1422 4.4.1 Pile-up in the Inner Detector

1423 Characterisation of pile-up is an important step in event reconstruction. The number of  
1424 proton-proton interactions per bunch crossing follows a Poisson distribution with mean  
1425 value  $\mu$ . During a bunch fill,  $\mu$  decreased with decreasing intensity and increasing emit-  
1426 tance, such that the peak value, or  $\mu^{peak}$ , is the highest value in a single bunch crossing  
1427 at the start of the stable beam period of the fill. The number of interactions per bunch  
1428 crossing also varies between bunches. The number of interactions per bunch crossing av-  
1429 eraged over a specific luminosity block and over all colliding branch crossing IDs (BCIDs)  
1430 is referred to as  $\langle \mu \rangle$ .

1431 In data,  $\mu$  is calculated using the following formula [82]:

$$\mu = \frac{L \times \sigma_{inel}}{n_{bunch} f_r}, \quad (4.3)$$

1432 where  $L$  is the luminosity,  $\sigma_{inel}$  is the total inelastic cross-section,  $n_{bunch}$  is the number  
1433 of colliding bunches and  $f_r$  is the LHC revolution frequency. The uncertainty on  $\mu$  depends  
1434 on the uncertainties on the luminosity and the total inelastic cross-section. Figure 4.2  
1435 shows the luminosity-weighted mean number of interactions per bunch crossing  $\mu$  for the  
1436 7 TeV and 8 TeV centre-of-mass luminosities. The inelastic cross section was taken to be  
1437 71.5 mb for 7 TeV collisions and 73.0 mb for 8 TeV collisions.

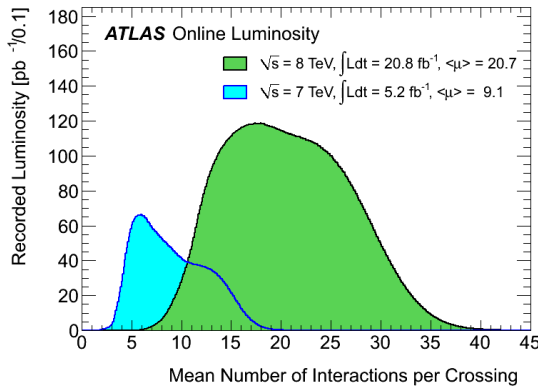


Figure 4.2: Luminosity-weighted distribution of the mean number of interactions per crossing for the 7 and 8 TeV data [83].

#### 1438 4.4.2 Inner Detector Track Reconstruction

1439 Charged particles leave tracks in the ID, they are reconstructed using three different al-  
1440 gorithms. The main track reconstruction strategy is the “inside-out” strategy, which starts  
1441 by finding a track candidate in the pixel and SCT detectors and then extends the trajec-

1442 ories of successfully fitted tracks to the TRT to reconstruct a full inner detector track.  
 1443 It starts from 3-point seeds in the silicon detectors and adds hits moving away from the  
 1444 interaction point using a combinatorial Kalman filter [57]. Primary particles are defined  
 1445 as particles with a mean lifetime of greater than  $3 \times 10^{-11}$ s directly produced in a  $pp$  in-  
 1446 teraction or from the subsequent decays or interactions of particles with a lifetime shorter  
 1447 than  $3 \times 10^{-11}$ s. The tracks reconstructed by the inside-out algorithm are required to  
 1448 have transverse momentum  $p_T > 400$  MeV. This track reconstruction strategy is com-  
 1449 plemented by an “outside-in” strategy, which starts from unassigned TRT segments and  
 1450 looks for matching hits in the pixel and SCT detectors. This type of track reconstruction  
 1451 targets the late decays of neutral particles and photon conversions to  $e^+e^-$  pairs and is  
 1452 also able to recover the remaining trajectory after a catastrophic energy loss. Finally there  
 1453 are tracks with a TRT segment but no extension to the silicon detectors are referred to as  
 1454 TRT-standalone tracks. A track in ATLAS can be parameterised at the point of closest  
 1455 approach with the global  $z$ -axis using five parameters:

- 1456     • the charge of the particle divided by its momentum
- 1457     • The space co-ordinates  $\eta$  and  $\phi$  are defined by the track direction when extrapolated  
1458       to the origin.
- 1459     •  $d_0$  is the distance of closest approach of the track to the origin
- 1460     •  $z_0$  is the component of  $d_0$  in the  $z$  plane, and  $z_0 \sin\theta$  is the projection of  $d_0$  onto the  
1461        $z$  axis.
- 1462     • The transverse momentum  $p_T$ , is defined by the bending radius  $R$  of the track in the  
1463       solenoidal magnetic field  $B$ , according to the formula  $p_T$  [GeV] =  $0.3 \times B[T] \times R[m]$ .

1464 In general, track parameters are defined relative to the position of the primary vertex.  
 1465 The following generic cuts are applied to all tracks referred to from this point, unless  
 1466 specified otherwise:

- 1467     •  $p_T > 1$  GeV,
- 1468     •  $|\eta| < 2.5$ ,
- 1469     •  $d_0 < 1.5$  mm,
- 1470     •  $z_0 \sin\theta < 1.0$  mm,
- 1471     • Number of hits in the pixel detector  $\geq 2$ ,
- 1472     • Number of hits in the SCT detector  $\geq 7$ .

### **1473 4.4.3 Vertex Reconstruction**

1474 A *vertex* is defined as the point in space at which two particles interact or a single particle  
 1475 decays. They are extrapolated with sufficient accuracy using at least two ID tracks back  
 1476 to a common interaction point. The primary vertex, which is supposed to be the source  
 1477 of the hardest interaction, is defined by finding the vertex with the largest summed track  
 1478  $p_T$ . Primary vertices are reconstructed using an iterative vertex finding algorithm. Vertex  
 1479 seeds are obtained from the  $z$ -position at the beam-line of the reconstructed tracks. An  
 1480 iterative  $\chi^2$  fit is made using the seed and nearby tracks. Each track is assigned a weight  
 1481 which is a measure of its compatibility with the fitted vertex depending on the  $\chi^2$  of the  
 1482 fit. Tracks that are displaced by more than  $7\sigma$  from the vertex are used to seed a new  
 1483 vertex and the procedure is repeated until no additional vertices can be found. The decays  
 1484 of particles with extended decay lengths measurable at ATLAS, which include  $b$ -quarks  
 1485 and hadrons are known as secondary particles. These particles generate tracks from a  
 1486 displaced vertex relative to the primary vertex, known as a secondary vertex.

### **1487 4.4.4 Electron Reconstruction**

1488 The electron-reconstruction algorithm used in the central region of the detector where the  
 1489 ID is operational ( $|\eta| < 2.5$ ) identifies energy deposits in the EM calorimeter and associates  
 1490 these clusters of energy with reconstructed tracks in the inner detector. This process is a  
 1491 three-step reconstruction:

#### **1492 4.4.4.1 Cluster reconstruction**

1493 The EM clusters are seeded by energy deposits with total transverse energy  $E_T > 2.5$  GeV  
 1494 by using a sliding-window algorithm [84]. The window size is  $3 \times 5$  in units of  $0.025 \times 0.025$   
 1495 in  $(\eta, \phi)$  space.

#### **1496 4.4.4.2 Track association with the cluster**

1497 Within the tracking volume, tracks with  $p_T > 0.5$  GeV are extrapolated from the last  
 1498 point of measurement to the middle layer of the EM calorimeter. The extrapolated  $\eta$  and  
 1499  $\phi$  co-ordinates of the impact point are compared to a corresponding seed cluster position  
 1500 in that layer. The match between the track and a cluster is successful if the distance  
 1501 between the track impact point and the EM cluster barycentre is  $|\Delta\eta| < 0.05$ . To account  
 1502 for the bremsstrahlung losses on the azimuthal distance, the size of the  $\Delta\phi$  track-cluster

1503 matching window is 0.1 on the side where the extrapolated track bends as it traverses the  
 1504 solenoidal magnetic field. An electron candidate is considered to be reconstructed if at  
 1505 least one track is matched to the seed cluster.

#### 1506 4.4.4.3 Reconstructed electron candidate

1507 After successful track-to-cluster matching, the cluster sizes are optimised to take into ac-  
 1508 count the overall energy distributions in the different regions of the calorimeter. In the  
 1509 EM barrel region, the energy of the electron cluster is collected by enlarging its size to  
 1510  $3 \times 7$  in units of  $0.025 \times 0.025$  in the  $(\eta, \phi)$  space. In the EM endcaps the size is changed  
 1511 to  $5 \times 5$ . The total reconstructed electron-candidate energy is determined from the sum of  
 1512 four contributions: the estimated energy deposit in the material in front of the EM calor-  
 1513 imeter; the measured energy deposit in the cluster, corrected for the estimated fraction of  
 1514 energy measured by the sampling calorimeter; the estimated energy deposit outside the  
 1515 cluster (lateral leakage); and the estimated energy deposit beyond the EM calorimeter  
 1516 (longitudinal leakage).

### 1517 4.4.5 Electron Identification

1518 Electrons in the central region of the detector are identified based on sequential cuts on  
 1519 the calorimeter, tracking and combined track-cluster variables. Three sets of reference  
 1520 selection criteria are used [85], labelled LOOSE++, MEDIUM++ and TIGHT++ are designed  
 1521 for use in analyses. These criteria are hierarchical as to provide increasing background-  
 1522 rejection power at the cost of losing some identification efficiency moving from LOOSE++  
 1523 to TIGHT++. The efficiency for each of the three electron identifications can be seen in  
 1524 Figure 4.3 as a function of the number of primary vertices, which is a measure of pile-up  
 1525 for 2011 and 2012 data.

#### 1526 4.4.5.1 Loose++

1527 This selection uses shower-shape variables in both the first and second layers of the EM  
 1528 calorimeter. Hadronic leakage information is used as well as requirements on the qual-  
 1529 ity of the electron track and track-cluster matching improve the rejection of hadronic  
 1530 backgrounds by a factor of five in the  $E_T$  range 30-40 GeV while maintaining a high  
 1531 identification efficiency. The loose ID variables are summarised in Table 4.1.

Category	Description	Variable
<b>Loose++</b>		
Acceptance	$ \eta  < 2.47$	
Hadronic leakage	In $ \eta  < 0.8$ and $ \eta  > 1.37$ , ratio of $E_T$ in the first layer of the hadronic calorimeter to $E_T$ of the EM cluster	$R_{had,1}$
	In $0.8 <  \eta  < 1.37$ : ratio of $E_T$ in whole hadronic calorimeter to $E_T$ of the EM cluster	$R_{had}$
Middle layer of the EM	Ratio of energies in $3 \times 7$ cells over $7 \times 7$ cells	$R_\eta$
	Lateral width of the shower	$w_{\eta 2}$
Front layer of the EM	Total shower width Energy difference of the largest and second largest energy deposits in the cluster divided by their sum	$w_{stot}$ $E_{ratio}$
Track quality and track-cluster matching	Number of hits in the pixel detector ( $> 0$ ) Number of hits in the silicon detectors ( $\geq 7$ ) $ \Delta\eta $ between the cluster position in the first layer and the extrapolated track ( $< 0.015$ )	
		$\Delta\eta_1$

Table 4.1: LOOSE++ ID variables [86].

#### 1533 4.4.5.2 Medium++

1534 This selection builds on the LOOSE++ selection by requiring the presence of a measured hit  
 1535 in the innermost layer of the pixel detector (to reject electrons from photon conversions),  
 1536 applying a LOOSE++ selection requirement on the transverse impact parameter  $|d_0|$  and  
 1537 identifying the transition radiation in the TRT (to reject charged-hadron background),  
 1538 when available. All common discriminating variables with the loose selection are tightened,  
 1539 improving the background rejection by an order of magnitude with respect to LOOSE++.

1540 The medium variables are summarised in Table 4.2.

Category	Description	Variable
<b>Medium++ (includes Loose++ with tighter requirements on shower shapes)</b>		
Track quality and track-cluster matching	Number of hits in the b-layer $> 0$ for $ \eta  < 2.01$ Number of hits in the pixel detector $> 1$ for $ \eta  > 2.01$ Transverse impact parameter $ d_0  < 5$ mm Tighter $ \Delta\eta_1 $ cut ( $< 0.005$ )	$d_0$
TRT	Loose cut on TRT high-threshold fraction	

Table 4.2: MEDIUM++ ID variables [86].

#### 1542 4.4.5.3 Tight++

1543 This selection uses all particle-identification tools available for electron ID. Tighter re-  
 1544 quirements are placed on the existing MEDIUM++ selection discriminating variables, as  
 1545 well as stricter requirements on the track quality in the presence of a track extension in  
 1546 the TRT detector, on the ratio of the EM cluster energy to the track momentum and a veto  
 1547 on reconstructed photon conversion vertices associated with the cluster are applied. The  
 1548 background rejection power is increased by a factor of two with respect to the MEDIUM++  
 1549 selection. The efficiency for each of the three identifications can be seen in Figure 4.3 as a  
 1550 function of the number of reconstructed primary vertices (a measure of the aforementioned  
 1551 pile-up), for 2011 and 2012 data. The tight variables are summarised in Table 4.3.

Category	Description	Variable
<b>Tight++ (includes Medium++)</b>		
Track quality and track-cluster matching	Tighter transverse impact parameter cut ( $ d_0  < 1$ mm) Asymmetric cut on $\Delta\phi$ between the cluster position in the middle layer and the extrapolated track	$\Delta\phi$
	Ratio of the cluster energy to the track momentum	$E/p$
TRT	Total number of hits in the TRT Tighter cut on the TRT high-threshold fraction	
Conversions	Reject electron candidates matched to reconstructed photon conversions	

Table 4.3: TIGHT++ ID variables [86].

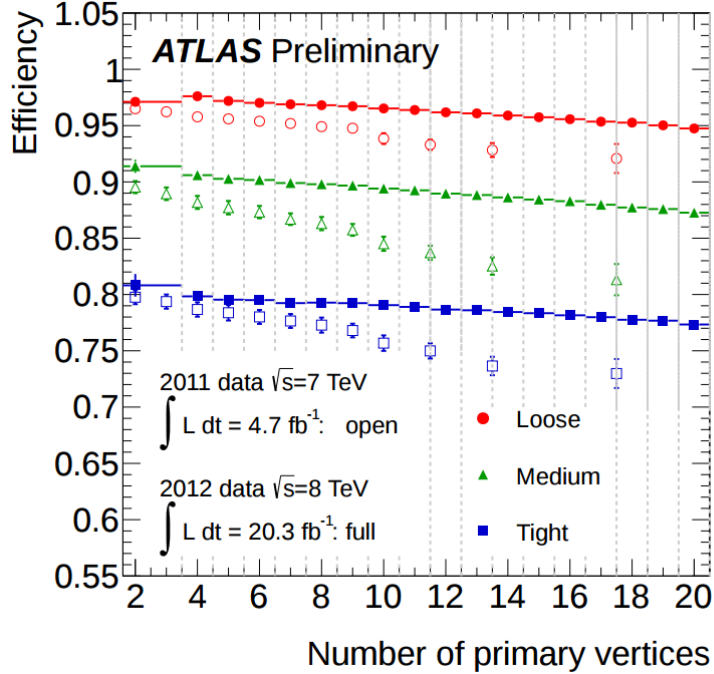


Figure 4.3: Electron identification efficiency in data for the various cut-based selections measured with 2011 and 2012 datasets as a function of the number of reconstructed primary vertices. Taken from [87].

#### 1553 4.4.6 Muon Reconstruction and Identification

1554 Muon identification is performed according to several reconstruction criteria, which lead  
1555 to different “types” of muon, taking into account the available information from the ID,  
1556 the MS and the calorimeter sub-systems. The three types are:

- 1557 • Stand-alone (SA) muons: The muon trajectory is reconstructed only in the MS. The  
1558 direction of flight and the impact parameter of the muon at the interaction point  
1559 are determined by extrapolating the track left in the MS back to the point of closest  
1560 approach to the beam line, taking into account the energy loss of the muon in the  
1561 calorimeters.
- 1562 • Combined (CB) muons: the track reconstruction is performed independently in the  
1563 ID and the MS, a combined track is formed from the successful combination of a SA  
1564 track with an ID track.
- 1565 • Segment-tagged (ST) muons: A track in the ID is identified as a muon if the track  
1566 extrapolated to the MS is associated with at least one track segment in the MDT or  
1567 CSC.
- 1568 • Calorimeter-tagged (CaloTag) muons: a track in the ID is identified as a muon if  
1569 the track can be associated to an energy deposit in the calorimeter corresponding

1570 to a minimum ionising particle. Although this type has the lowest purity of all  
 1571 muon types it recovers acceptance in the uninstrumented region of the MS. The  
 1572 identification criteria of this muon type are optimised for a region of  $|\eta| < 0.1$  and a  
 1573 momentum range of  $25 \lesssim p_T \lesssim 100$  GeV.

1574 The following quality requirements are applied to the ID tracks used for CB, ST or  
 1575 CaloTag muons:

- 1576 • At least 1 Pixel hit;
- 1577 • At least 5 SCT hits;
- 1578 • At most 2 active Pixel or SCT sensors traversed by the track but without hits;
- 1579 • In the region of full TRT acceptance,  $0.1 < |\eta| < 1.9$  at least 9 TRT hits.

1580 The number of hits required in the first two points is reduced by one if the track  
 1581 traverses a sensor known to be inefficient according to a time-dependent database. The  
 1582 above requirements are dropped in the region  $|\eta| > 2.5$ , where the short ID track segments  
 1583 can be matched to SA muons to form a CB muon.

1584 The muons used in this analysis are reconstructed using the statistical combination  
 1585 (STACO) algorithm [88], complemented by the tagging algorithm MuTAG [88], which  
 1586 uses a  $\chi^2$  procedure for tagging. STACO reconstructs straight track segments in the MS  
 1587 chambers using pattern recognition algorithms on the hits, beginning in the outer layer  
 1588 and working inwards. All tubes crossed by a segment must contain a hit for the track to be  
 1589 considered. The hits are then extrapolated back to the ID, where they are geometrically  
 1590 matched to independently reconstructed ID tracks, provided that their kinematic proper-  
 1591 ties, e.g.  $p_T$ , are compatible. Statistically combining the parameters of both tracks takes  
 1592 advantage of the momentum sensitivity of both the ID and MS systems. The MuTAG  
 1593 algorithm works from the ID tracks which are extrapolated to the MS and then matched  
 1594 to straight track segments. This algorithm heavily relies on the hits in the MS. The energy  
 1595 lost between ID and MS is applied as a correction to the reconstructed muons in data,  
 1596 the simulated muons have their energy distributions smeared using random numbers to  
 1597 reflect how well the ID and MS can measure the momentum of any given muon.

1598 Figure 4.4 shows the reconstruction efficiency for muons using the methods described  
 1599 in this section over most of the covered phase space ( $|\eta| < 2.7$  and  $5 \lesssim p_T \lesssim 100$  GeV).  
 1600 The combination of all the muon reconstruction types (for CB, ST and CaloTag muons)  
 1601 gives a uniform muon reconstruction efficiency of about 99% over most of the detector  
 1602 regions.

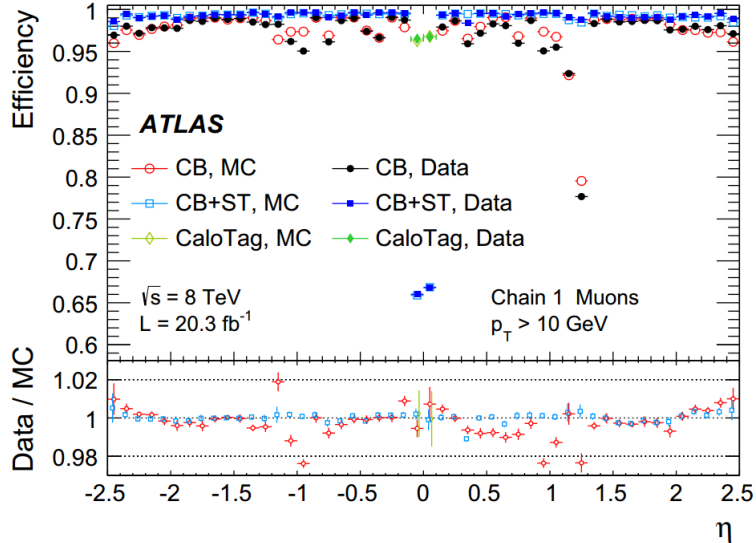


Figure 4.4: Muon reconstruction efficiency as a function  $\eta$  measured in  $Z \rightarrow \mu\mu$  events for muons with  $p_T > 10 \text{ GeV}$  and different muon reconstruction types. The uncertainties considered here are statistical only. The error bars on the ratios are combined statistical and systematic uncertainties. CB muons refer to STACO muons, CB+ST refer to MuTAG muons and CaloTag muons are not considered in this analysis. Taken from [89].

Muons only have one set of identification criteria available. The backgrounds considered comes mostly from charged pions, which usually leave larger energy deposits in the electromagnetic and hadronic calorimeters and tend not to reach the MS. Muons must pass the STACO requirements, although those in the region  $|\eta| < 1.05$  can also pass the MuTAG requirements.

#### 4.4.7 Jet Reconstruction

Jets are reconstructed beginning with the formation of *topological* clusters in the hadronic calorimeter using the topological algorithm [90]. The topo-cluster formation algorithm [84] is an iterative procedure which starts from a seed cell with a signal to noise ratio  $S/N \geq 4$ , where  $S$  is the energy measured in the seed cell and  $N$  is defined as the root mean squared (RMS) of the cell energy measured in random bunch crossings. Any neighbouring cells with  $S/N \geq 2$  are then added to form a cluster. Neighbouring cells are then added to the seed to form a topo-cluster. This cluster is then used in an additional splitting step: every calorimeter cell with energy  $> 500 \text{ MeV}$  is tested for a local maximum, and any cell passing this criterion is used as a trial seed for a new topo-cluster. Topo-clusters are defined to have zero mass, with energy equal to the sum of the energy of the constituent calorimeter cells.

The topological clusters need to be calibrated before being used as input for the anti- $k_T$

1621 recombination algorithm. For this analysis, local cluster weighting (LCW) calibration was  
 1622 used, which uses an algorithm to determine whether topological clusters originate from a  
 1623 hadronic or EM shower. The energy measured in the hadronic topological clusters is then  
 1624 corrected according to the simulated response of single hadrons in the cells. Corrections  
 1625 for energy deposition in dead material and noise effects are applied.

1626 In the next step, the LCW calibrated topological clusters are provided as input to the  
 1627 anti- $k_T$  jet algorithm [91] with a distance parameter  $R = 0.4$  and a four momentum re-  
 1628 combination scheme. The anti- $k_T$  algorithm works iteratively, in the first step the distance  
 1629 parameter  $d_{ij}$  is calculated, which is defined as

$$d_{ij} = \left( \frac{1}{k_{T_i^2}}, \frac{1}{k_{T_j^2}} \right) \frac{\Delta R_{ij}}{R^2}, \quad (4.4)$$

1630 where  $i$  and  $j$  are topo-cluster indices  $k_T$  is the transverse momentum of each topo-  
 1631 cluster,  $\Delta R_{ij} = \sqrt{\Delta\phi_{ij}^2 + \Delta\eta_{ij}^2}$  is the distance between the two topological clusters, and  $R$   
 1632 is a free parameter determining the size of the reconstructed jets. The topological clusters  
 1633  $i$  and  $j$  which minimise  $d_{ij}$  are then combined to form larger individual clusters. The next  
 1634 iteration takes into account the larger individual clusters as well as the remaining initial  
 1635 topological clusters and combines them according to the same procedure. This process is  
 1636 repeated until all remaining topo-cluster pairs satisfy the criterion  $\Delta R_{ij} > R$ .

1637 After cluster calibration and jet reconstruction, additional corrections are needed to  
 1638 calculate the jet energy properly. The jet energy scale corrections are determined using  
 1639 MC, where the truth jet energy is compared to the reconstructed value. The results from  
 1640 this comparison are then validated by comparing with in-situ methods such as di-jet and  
 1641  $\gamma$ -jet balancing method, uncertainties are also determined [92].

1642 Jet reconstruction can be affected by the presence of pileup events. Pileup interactions  
 1643 can increase the total energy deposited in the calorimeters, which then affects the energy  
 1644 calibration of the jets. To correct for this problem, an offset pileup contribution to the  
 1645 energy density is subtracted, which is parameterised by the number of vertices in the  
 1646 event [93]. Pileup interactions can also introduce additional jets. These jets do not  
 1647 originate from the interaction of interest, therefore it is useful to suppress them. Pileup  
 1648 jets can be effectively suppressed using the jet-vertex-fraction (JVF) variable. It is a  
 1649 quantification of how much of a jet's energy is associated with the primary vertex of

1650 interest in the event. The JVF for a jet is defined as

$$\text{JVF} = \frac{\sum_{\text{tracks}_{\text{jet}, \text{PV}}} p_T}{\sum_{\text{tracks}_{\text{jet}}} p_T}, \quad (4.5)$$

1651 where the sums are taken over the tracks matched to the jet and PV denotes the tracks  
1652 associated to the primary vertex. Jets that have no associated tracks are assigned  
1653  $\text{JVF} = -1$ . Pileup jets will have a higher fraction of jet energy associated with pileup  
1654 vertices, making this variable a good discriminator.

1655  $B$ -hadron jets have a displaced secondary vertex due to the long lifetime of the  $b$ -  
1656 quark. There are different jet origins: those from  $b$ -quarks,  $c$ -quarks and light flavour  
1657 quarks or  $\tau$  leptons. Several algorithms are used to “tag” jets as  $b$ -jets. The algorithm  
1658 which is most commonly used with 2012 data is the MV1 algorithm, which is based on a  
1659 neural network. The input algorithms used are described in [94]. For a  $b$ -tagging efficiency  
1660 of 80%, the algorithm gives rejection factors for  $c$ -jets of about 3, for taus of about 5.6,  
1661 and for light flavour quarks about 27.

#### 1662 4.4.8 Tau Reconstruction and Identification

1663 The reconstruction and identification of  $\tau$  leptons is a challenging task, as purely leptonic  $\tau$   
1664 decays are virtually impossible to distinguish from prompt electrons or muons in ATLAS,  
1665 the  $\tau$  identification algorithms are developed to reconstruct and identify the visible part of  
1666 the hadronic decay modes, referred to by the term  $\tau_{\text{had-vis}}$  [95]. However the hadronic  $\tau$   
1667 decay signatures in the detector are very similar to quark- or gluon-initiated jets from QCD  
1668 processes. Leptonic decays are treated as indistinguishable from the prompt production of  
1669 light leptons in this analysis. The hadronic decays can be divided into modes, “1-prong”  
1670 and “3-prong” decays, where the number corresponds to the charged particles produced  
1671 in the decay.

1672 These signatures produce relative narrow clustering of tracks and energy deposits  
1673 in the calorimeters, which is useful for discriminating against the multi-jet background.  
1674 Decays producing more than three charged particles are not considered by ATLAS due to  
1675 their very small branching ratios and the increased difficulty of reconstructing them into  
1676 taus.

1677 The  $\tau_{\text{had-vis}}$  reconstruction algorithm is seeded from jets reconstructed using the anti-  
1678  $k_T$  algorithm, with a distance parameter  $R = 0.4$ . LCW calibrated topological clusters are  
1679 used as an input for the jet algorithm. All jets with  $p_T > 10$  GeV and  $|\eta| < 2.5$  seed the

reconstruction algorithm. The reconstructed four-momentum of the  $\tau_{had-vis}$  candidate is defined in terms of three degrees of freedom:  $p_T, \eta$  and  $\phi$ . The  $\eta$  and  $\phi$  are taken from the seed jet, which are determined by calculating the sum of the four vectors of the constituent topological clusters, assuming zero mass for each of the constituents. The mass of the  $\tau_{had-vis}$  candidate is defined to be zero, consequently the  $p_T$  and the  $E_T$  are identical. Due to the specific mixture of charged and neutral pions in hadronic  $\tau$  decays, the energy scale of hadronic  $\tau$  candidates is calibrated independent of the jet energy scale. The reconstructed energy of  $\tau_{had-vis}$  candidates is corrected to the final energy scale by a Monte Carlo based calibration procedure using clusters, within  $\Delta R = \sqrt{(\Delta\eta)^2 + (\Delta\phi)^2} < 0.2$  of the seed jet barycentre axis.

For a track to be associated with a  $\tau_{had-vis}$  candidate they must lie within the *core cone*, defined as the region with  $\Delta R < 0.2$  of the axis of the seed jet and satisfy the track quality criteria outlined in Section 4.4.2.

The identification of taus is based on a boosted decision tree (BDT) which takes many different track and calorimeter based variables as input to discriminate against the hadronic jet background. Tracks within the *isolation annulus* of  $0.2 < \Delta R < 0.4$  are useful for the discrimination. Additional quantities used in the BDT include shower shape variables, the proportion of energy deposited in the ECAL and HCAL, the ratio of normal to high threshold TRT deposits and coordinates of the  $\tau$  decay vertex. Full details of all variables used in these selections can be found in [96].

Three working points, *loose*, *medium* and *tight* corresponding to the different  $\tau$  identification efficiency values are provided. The corresponding signal efficiency values, defined with respect to 1-prong or 3-prong reconstructed  $\tau_{had-vis}$  candidates matched to true  $\tau_{had-vis}$  are shown in Figure 4.5.

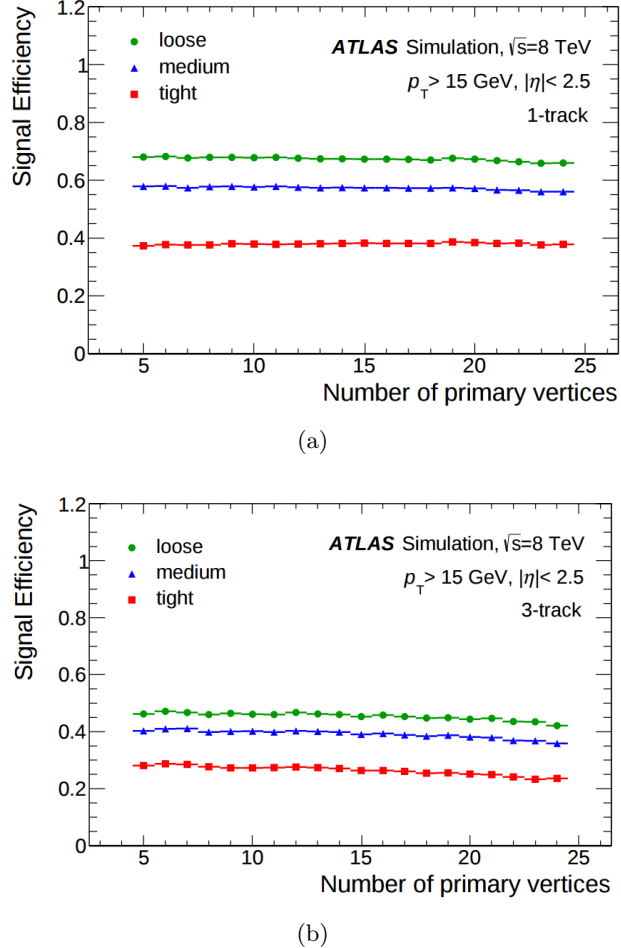


Figure 4.5: Offline  $\tau$  reconstruction efficiency dependence on the number of reconstructed primary vertices for (a) 1-track and (b) 3-track  $\tau_{had-vis}$  decays matched to true  $\tau_{had-vis}$  from  $Z \rightarrow \tau\tau$ ,  $Z' \rightarrow \tau\tau$  and  $W \rightarrow \tau\nu$  simulated samples. Taken from [95].

1704 It is observed that the signal efficiencies for taus are significantly lower than for elec-  
 1705 trons, muons and jets, due to the difficulty in distinguishing real taus from the QCD  
 1706 background.

#### 1707 4.4.9 Missing Transverse Energy

1708 Stable neutral particles produced in ATLAS that are relevant to this analysis such as  
 1709 neutrinos or the SUSY LSP in R-parity conserving models will escape the detection and  
 1710 lead to an imbalance of momentum. The missing transverse energy refers to the magnitude  
 1711 of the momentum imbalance in the plane transverse to the beam axis. It is reconstructed  
 1712 by taking the vector sum of all energy deposits in the detector calorimeters and muon  
 1713 spectrometer [97]. This is a measure of the total momentum of all the visible particles  
 1714 in order to infer the remaining invisible momentum. These are summed in the following

1715 order for the  $x$  and  $y$  axes:

$$E_{x(y)}^{miss} = -(E_{x(y)}^e + E_{x(y)}^\gamma + E_{x(y)}^\tau + E_{x(y)}^{jets} + E_{x(y)}^{soft jets} + E_{x(y)}^{calo\mu} + E_{x(y)}^{cellout} + E_{x(y)}^{MS\mu}). \quad (4.6)$$

1716 The first three terms give the energies from topological clusters associated to electrons,  
1717 photons and hadronically decaying taus respectively. The energy term for jets includes all  
1718 deposits for jets with  $p_T > 20$  GeV, whilst *soft jets* with  $10 < p_T < 20$  GeV are added  
1719 separately. Energy lost by muons within the calorimeters is included in the “calo  $\mu$ ” term.  
1720 All clusters not associated to reconstructed objects are also summed and included in the  
1721 “cell out” term. These terms together give the total energy deposited in the calorimeter  
1722 subsystems. Finally, the sum of transverse momenta of all muons in the muon spectrometer  
1723 is added. The terms included for electrons, muons, taus and jets are calibrated and no  
1724 calibration is required for the soft jet or cell out terms. The missing transverse energy is  
1725 calculated using the energy in the  $x$  and  $y$  axes:

$$E_T^{miss} = \sqrt{(E_x^{miss})^2 + (E_y^{miss})^2}. \quad (4.7)$$

1726 An optimised reconstruction and calibration of  $E_T^{miss}$  was developed by the ATLAS Collab-  
1727 oration [97]. The  $E_T^{miss}$  measurement is significantly affected by pile-up, so methods were  
1728 devised to suppress pile-up. Event samples used to assess the quality of the  $E_T^{miss}$  recon-  
1729 struction are minimum bias events, events with leptonically decaying W and Z bosons and  
1730 simulated events with large jet multiplicity and/or large missing transverse momentum,  
1731 such as  $H \rightarrow \tau\tau, t\bar{t}$  and simulated SUSY events. These test the detector capability in the  
1732 reconstruction and calibration of different physics objects, the optimisation of the  $E_T^{miss}$   
1733 calculation and the methods of pile-up suppression. An important requirement on the  
1734 measurement of  $E_T^{miss}$  is maximising detector coverage and reducing the effect of finite  
1735 detector resolution, the presence of dead regions and different sources of noise as well as  
1736 cosmic-ray and beam-halo muons crossing the detector can produce fake  $E_T^{miss}$ .

1737 The ATLAS calorimeter coverage extends to large pseudorapidities to reduce the im-  
1738 pact of high energy particles escaping in the very forward direction. However, there are  
1739 transition regions between different calorimeters containing inactive material which lead  
1740 to increased fake  $E_T^{miss}$ . Selection criteria are applied to reduce the impact of these sources  
1741 of fake  $E_T^{miss}$ . Full details on the reconstruction of  $E_T^{miss}$  is discussed in [98].

## <sup>1742</sup> 4.5 Object Selection for the Analysis

<sup>1743</sup> The reconstructed objects read from data storage files are not used directly by analysers,  
<sup>1744</sup> instead they are subjected to further selection criteria. “Baseline objects”, which provide  
<sup>1745</sup> a general description of the particle are defined first. These then undergo the “overlap  
<sup>1746</sup> removal” procedure is applied before more stringent cuts are applied to define “signal  
<sup>1747</sup> objects”. Taus are an exception to this ordering, signal taus are used as the input to  
<sup>1748</sup> overlap removal, rather than baseline taus.

### <sup>1749</sup> 4.5.1 Baseline Light Lepton Selection

<sup>1750</sup> Electrons are required to have  $p_T > 7$  GeV and muons  $p_T > 5$  GeV. The ECAL cluster of  
<sup>1751</sup> an electron must have  $|\eta| < 2.47$  and muons must have  $|\eta| < 2.5$ . Electrons are required to  
<sup>1752</sup> pass the MEDIUM++ identification criteria described in Section 4.4.5. Muons are required to  
<sup>1753</sup> pass a loose identification criteria with the STACO algorithm as described in Section 4.4.6  
<sup>1754</sup> and have specific hits present in the ID, as well as requests based on the number of normal  
<sup>1755</sup> hits in the TRT compared to outliers. The total number of hits  $n$  is defined as the sum  
<sup>1756</sup> of the normal and outlier hits and the condition  $n > 5$  must be satisfied. In addition the  
<sup>1757</sup> proportion of outliers must be less than 90%.

### <sup>1758</sup> 4.5.2 Baseline Jet Selection

<sup>1759</sup> Baseline jets must have  $p_T > 20$  GeV and  $|\eta| < 4.5$  and are reconstructed as described in  
<sup>1760</sup> Section 4.4.7.

### <sup>1761</sup> 4.5.3 Baseline Tau Selection

<sup>1762</sup> Baseline taus are seeded from jets which must have  $p_T > 10$  GeV and  $|\eta| < 2.5$  as described  
<sup>1763</sup> in Section 4.4.8. The taus themselves are then required to satisfy  $p_T > 20$  GeV and  $|\eta| <$   
<sup>1764</sup> 2.5. They must also have either one or three tracks associated with them, corresponding  
<sup>1765</sup> to a one or three prong tau decay. No identification criteria are required at this stage.

### <sup>1766</sup> 4.5.4 Overlap Removal

<sup>1767</sup> Objects that are geometrically close (i.e. within a  $\Delta R$  cone of a given size), can pose  
<sup>1768</sup> issues for reconstruction due to spatial resolution. Selections are placed on the spatial  
<sup>1769</sup>  $(\eta, \phi)$  proximity of objects, corresponding to the type of object to improve the accuracy of

Object	$\eta$	$p_T$ [GeV]	Identification	Other
Electron	$ \eta ^{cl} < 2.47$	$p_T > 7$	MEDIUM++	
Muon	$ \eta  < 2.5$	$p_T > 5$	STACOloose	$n_{b-layer} \geq 1, n_{pixel} \geq 1,$ $n_{SCT} \geq 6, n_{holes(pix+SCT)} < 3$ $n_{TRT}^{total} > 5, \frac{n_{outliers}}{n_{TRT}^{total}} < 0.9$
Jet	$ \eta  < 4.5$	$p_T > 20$	-	-
Tau	$ \eta  < 2.5$	$p_T > 20$	-	$n_{tracks} = 1$ or $3,$ $charge = \pm 1$

Table 4.4: Summary of cuts used to define baseline objects in this analysis.

1770 identification. The overlap removal procedure is performed between baseline objects and  
1771 is applied in the order shown in Table 4.5.

Overlap Removal Cuts	Overlap Removal Criterion
$\Delta R_{e1,e2} < 0.05$	Discard the lowest $E_T$ electron to remove duplicated electrons with different clusters and shared tracks.
$\Delta R_{e,j} < 0.2$	Discard jet to remove electrons duplicated in jet container.
$\Delta R_{e,\tau} < 0.2$	Discard $\tau$ to remove electrons duplicated in $\tau$ container.
$\Delta R_{\mu,\tau} < 0.2$	Discard $\tau$ to remove muons duplicated in $\tau$ container.
$\Delta R_{e,j} < 0.4$	Discard electron to remove electrons within jets.
$\Delta R_{\mu,j} < 0.4$	Discard muon to remove muons within jets.
$\Delta R_{e,\mu} < 0.01$	Discard both electron and muon due to muons undergoing bremsstrahlung.
$\Delta R_{\mu,\mu} < 0.05$	Discard both muons due to shared tracks.
$\Delta R_{signal\tau,j} < 0.2$	Discard jets to remove taus duplicated among the jets.

Table 4.5: Overlap removal criteria for objects used in the analysis presented in this thesis. The indices refer to the object pair being evaluated.

#### 1772 4.5.5 Signal Electrons

1773 Signal electrons are required to pass the TIGHT++ identification criteria, in addition to  
1774 isolation and  $d_0$  and  $z_0 \sin\theta$  conditions:

$$\frac{|d_0|}{\sigma(d_0)} < 5, \\ z_0 \sin\theta < 0.4\text{mm.} \quad (4.8)$$

1775 The isolation conditions for the leading electron require one for the track and one for the  
1776 cluster in the calorimeter. The track isolation requires that:

$$\frac{p_T^{cone30}}{p_T} < 0.16, \quad (4.9)$$

1777 where  $E_T$  is the transverse energy of the electron, and  $p_T^{cone30}$  is the combined transverse  
1778  $p_T$  of all tracks with  $\Delta R \geq 0.3$  of the electron track, where tracks satisfy the requirements

<sup>1779</sup> given in Section 4.4.2. The cluster isolation requires:

$$\frac{E_T^{cone30corr}}{E_T} < 0.18, \quad (4.10)$$

<sup>1780</sup> where the energy-density corrected isolation,  $E_T^{cone30corr}$ , is defined as:

$$E_T^{cone30corr} = E_T^{cone30} - A \times N_{vtx}. \quad (4.11)$$

<sup>1781</sup>  $N_{vtx}$  is the number of vertices with at least 5 associated tracks and  $A$  is a scale factor to  
<sup>1782</sup> account for energy leakage in the calorimeter and additional deposits from pile-up condi-  
<sup>1783</sup> tions. Values of 20.15 MeV for data and 17.97 MeV for MC simulation are used, due to  
<sup>1784</sup> differences between the modelling and data measurement.  $E_T^{cone30}$  is defined equivalently  
<sup>1785</sup> to  $p_T^{cone30}$ , as the combined  $E_T$  of all tracks within  $\Delta R \geq 0.3$  of the electron track.

<sup>1786</sup> If the electron is not the leading lepton in  $p_T$ , it must satisfy tighter isolation require-  
<sup>1787</sup> ments than those prescribed above in order to remove fake contributions introduced with  
<sup>1788</sup> lower lepton  $p_T$  thresholds. The track and cluster isolation requirements in this case are  
<sup>1789</sup> as follows:

$$\begin{aligned} \frac{p_T^{cone30}}{p_T} &< 0.07, \\ \frac{E_T^{cone30corr}}{E_T} &< 0.13. \end{aligned} \quad (4.12)$$

#### <sup>1790</sup> 4.5.6 Signal Muons

<sup>1791</sup> Signal muons do not require any additional identification criteria. Cuts on  $|d_0|$  and  $|z_0 \sin \theta|$   
<sup>1792</sup> are as follows:

$$\begin{aligned} \frac{|d_0|}{\sigma(d_0)} &< 3, \\ z_0 \sin \theta &< 1\text{mm}. \end{aligned} \quad (4.13)$$

<sup>1793</sup> The track isolation condition for the leading muon is:

$$\frac{p_T^{cone30corr}}{p_T} < 0.12, \quad (4.14)$$

<sup>1794</sup> where

$$p_T^{cone30corr} = p_T^{cone30} - A \times N_{vtx}, \quad (4.15)$$

<sup>1795</sup> and for muons the values used for  $A$  are 10.98 MeV for data and 6.27 MeV for MC

<sup>1796</sup> simulation.

<sup>1797</sup> If the muon is not the leading lepton in  $p_T$ , it must satisfy tighter isolation requirements than those prescribed above similarly to electrons. The track isolation requirements <sup>1798</sup> in this case is:

$$\frac{p_T^{cone30cor}}{p_T} < 0.06,$$

$$\frac{E_T^{cone30corr}}{E_T} < 0.14.$$
(4.16)

#### <sup>1800</sup> 4.5.7 Signal Jet Selection

<sup>1801</sup> Baseline jets are identified using criteria which aim to efficiently reject background jets <sup>1802</sup> while keeping the highest efficiency selection for jets produced in  $pp$  collisions. All selected <sup>1803</sup> jets must  $p_T > 20$  GeV; be within pseudorapidity coverage of the calorimeters,  $|\eta| < 4.5$ .

<sup>1804</sup> Signal jets are selected from baseline jets and are required to cover a pseudorapidity <sup>1805</sup> range, of  $|\eta| < 2.5$  and the fraction of jet transverse energy associated to tracks coming <sup>1806</sup> from the primary vertex, referred to as the Jet Vertex Fraction (JVF) is greater than 0.5. <sup>1807</sup> Large JVF values suppress jets from a different (not primary) interaction in the same <sup>1808</sup> beam crossing.

#### <sup>1809</sup> 4.5.8 Signal Tau Selection

<sup>1810</sup> Signal taus are required to pass additional medium identification criteria. This requires the <sup>1811</sup> muon veto to be passed, in addition to the loose definition of the electron BDT selection, <sup>1812</sup> and the medium jet BDT selection, all of which are described in Section 4.4.8. All baseline <sup>1813</sup> taus passing these criteria are defined as signal taus, and these are then used as input for <sup>1814</sup> the overlap removal described in Section 4.5.4.

### <sup>1815</sup> 4.6 MC Samples

#### <sup>1816</sup> 4.6.1 MC Generators

<sup>1817</sup> The main choices regarding the different types of MC generators employed in this thesis <sup>1818</sup> are described below.

#### **4.6.1.1 General Purpose MC Generators**

PYTHIA [70], HERWIG [69], and HERWIG++ [99] are general purpose MC event generators that use Matrix Element (ME) calculations to Leading Order (LO), which include the simulation of both hard and soft interactions. For the simulation of the UE, HERWIG is interfaced with JIMMY [78]. Both PYTHIA and JIMMY simulate the UE as a scattering between proton remnants using matrix elements at LO. SHERPA [100] is another multi-purpose event generator, which is interfaced with PYTHIA for simulation of the PS. A multiple parton scattering model is used for the UE simulation.

#### **4.6.1.2 Matrix Element MC Generators**

The ALPGEN [101], MADGRAPH [102] and ACERMC [103] generators simulate the hard process of a proton-proton collision using calculations at fixed order in perturbation theory. Events are generated with different multiplicities of outgoing partons. The cross sections are calculated at LO. For the PS and hadronisation. These generators are interfaced with PYTHIA or HERWIG because they can only provide generation of events to parton-level. The addition of PS introduces a double-counting of events. This is due to the additional jets which can be produced in a sample with n-partons from PS that are already taken into account in the n+1-partons sample. When more than two generators are interfaced, matching techniques such CKKW and MLM are used to remove double counting the matrix element and PS emissions.

#### **4.6.1.3 Next-to-Leading Order MC Generators**

MC@NLO [104] and POWHEG [105] provide alternative simulation methods by combining lowest-multiplicity Next-to-Leading Order (NLO) matrix elements with PS without double counting. MC@NLO and POWHEG produce hard scattering processes at NLO, where the former includes negative weighted events in the method to prevent double counting. The MC@NLO generated events are typically used as input to HERWIG for the PS and hadronisation, and to JIMMY for the UE. POWHEG events are interfaced with PYTHIA to include PS and UE effects.

#### **4.6.2 SM Background MC Samples For Run-1**

Several background samples have been considered in the Run-1 analysis and can be grouped into different categories, as detailed in the following.

<sup>1849</sup> **4.6.2.1 Diboson**

<sup>1850</sup> WW, WZ and ZZ processes are generated with the NLO generator POWHEG. These  
<sup>1851</sup> samples correspond to all SM diboson processes leading to  $\ell\nu\ell'\nu'$ ,  $\ell\ell\ell'\nu'$  and  $\ell\ell\ell'\ell'$ , re-  
<sup>1852</sup> spectively, with  $\ell, \ell' = e/\mu/\tau$  and  $\nu, \nu' = \nu_e/\nu_\mu/\nu_\tau$ . The SHERPA generator is used for the  
<sup>1853</sup> Z/W +  $\gamma$  processes.

<sup>1854</sup> **4.6.2.2 Triboson**

<sup>1855</sup>  $pp \rightarrow WWW \rightarrow \ell\nu\ell\nu\ell\nu$ ,  $pp \rightarrow ZWW \rightarrow \ell\ell\ell\nu\ell\nu$  and  $pp \rightarrow ZZZ \rightarrow \ell\ell\ell\nu\nu\nu$  processes  
<sup>1856</sup> (collectively referred to as VVV) were generated with MADGRAPH to LO in QCD.

<sup>1857</sup> **4.6.2.3  $t\bar{t}$ +boson**

<sup>1858</sup>  $t\bar{t}+Z(+\text{jets})$  and  $t\bar{t}+W(+\text{jets})$  samples were generated using the LO generator ALPGEN,  
<sup>1859</sup> while the  $t\bar{t}+WW$  and  $tZ$  samples were generated using MADGRAPH. All  $t\bar{t}$ +boson  
<sup>1860</sup> samples are collectively referred to as  $t\bar{t}V$  where at least one of the top quarks is de-  
<sup>1861</sup> caying semi-leptonically ( $t \rightarrow Wb \rightarrow b\ell\nu$ ).

<sup>1862</sup> **4.6.2.4 Top**

<sup>1863</sup> The top pair-production sample,  $t\bar{t}$ , was generated with POWHEG (+PYTHIA for simu-  
<sup>1864</sup> lating the PS, hadronisation and the UE); single top production in the  $t$ -channel ( $bq \rightarrow tq'$   
<sup>1865</sup> and  $b\bar{q}' \rightarrow t\bar{q}$ ) was generated with MC@NLO (+HERWIG for simulation of PS and hadron-  
<sup>1866</sup> isation); and single top processes in the  $s$ -channel ( $q\bar{q} \rightarrow W^* \rightarrow t\bar{b}$ ) and the associated pro-  
<sup>1867</sup> duction of a top quark and a W boson,  $Wt$ , was generated with ACERMC (+PYTHIA).  
<sup>1868</sup> All samples are produced using a top quark mass of 172.5 GeV and have been renormalised  
<sup>1869</sup> to Next-to-Next-to Leading Order (NNLO).

<sup>1870</sup> **4.6.2.5 Boson+jets**

<sup>1871</sup>  $Z/\gamma^*$  production and  $W$  production in association with jets (light and heavy flavour jets  
<sup>1872</sup> are taken into account) are produced with ALPGEN (+PYTHIA). For simplicity, these  
<sup>1873</sup> samples are referred to as “V+jets”. The  $W$  and  $Z/\gamma^*$  ALPGEN LO cross sections are  
<sup>1874</sup> re-normalised to NNLO.

#### **4.6.2.6 Standard Model Higgs**

Samples where the Higgs decays are via taus or via  $W/Z$  bosons are generated with PYTHIA.  $H \rightarrow \tau\tau$ ,  $H \rightarrow WW^*$  and  $H \rightarrow ZZ^*$  decaying into leptonic final states are considered, as these are expected to be the most important sources of Higgs background in this analysis. Five production mechanisms are included: gluon Fusion ( $ggF$ ), Vector Boson Fusion ( $VBF$ ), associated production with a  $W$  ( $WH$ ) or  $Z$  boson ( $ZH$ ), and associated production with  $t\bar{t}$  pair ( $t\bar{t}H$ ). All cross sections are calculated at NNLO, except  $pp \rightarrow t\bar{t}H$ , which is calculated at NLO QCD precision.

#### **4.6.2.7 Low-Mass Drell-Yan**

$DY \rightarrow ee$ ,  $DY \rightarrow \mu\mu$  processes are generated with SHERPA to NLO.

#### **4.6.2.8 $J/\Psi$**

$pp \rightarrow J/\Psi \rightarrow ee$ ,  $pp \rightarrow J/\Psi \rightarrow \mu\mu$   $pp \rightarrow J/\Psi \rightarrow \mu\mu Z\mu\mu$ ,  $pp \rightarrow J/\Psi \rightarrow \mu\mu Zee$   $bb \rightarrow J/\Psi \rightarrow ee$ ,  $bb \rightarrow J/\Psi \rightarrow \mu\mu$  processes are generated with PYTHIA to LO.

#### **4.6.2.9 $\Upsilon$**

$\Upsilon \rightarrow \mu\mu Z\mu\mu$   $\Upsilon \rightarrow \mu\mu Zee$   $pp \rightarrow \Upsilon \rightarrow \mu\mu$  processes are generated with PYTHIA to LO.

For all simulated processes, the propagation of particles through the ATLAS detector is modelled with GEANT4 using the full ATLAS detector simulation, except for the  $t\bar{t}$  POWHEG sample, for which ATLFAST-II is simulation is used.

Simulated events are weighted to match the distribution of the number of interactions per bunch crossing observed in data.

There are free parameters for the different PS, UE and hadronisation models are tuned to data. The three different parameter tunes used for the UE generation in all MC samples are the ATLAS UE Tune 2B (AUET2B), AU2 and PERUGIA2011C, which are discussed in detail in [106].

Dedicated calculations are used to provide a re-normalisation of the total cross sections for each SM process at NLO or NNLO, which have been specified in Table 4.7. The choice of PDF depends on the generator and for this analysis the CTEQ6L1 PDFs are used with MADGRAPH, ALPGEN, ACERMC, PYTHIA and the CT10 [107] PDFs with MC@NLO, POWHEG and SHERPA.

The choice of the generator type and the order of cross section calculations used for

<sup>1905</sup> yield normalisation for the SM processes are summarised in Table 4.7.

### <sup>1906</sup> 4.6.3 MC Signal Samples For Run-1

<sup>1907</sup> Signal samples referring to the models considered in this analysis (Section 2.6.8) are gener-  
<sup>1908</sup> ated with HERWIG++, using the CTEQ6L1 PDFs. Signal cross sections are calculated to  
<sup>1909</sup> NLO+NLL using PROSPINO2 [108]. Lepton filters are applied during event generation to  
<sup>1910</sup> enhance decays into a particular final state. A “light lepton filter” (electrons/muons) with  
<sup>1911</sup> the additional requirement of an electron/muon with  $p_T > 5$  GeV,  $|\eta| < 2.7$  is applied.  
<sup>1912</sup> The list of signal samples used in the analysis presented in this thesis can be found in  
<sup>1913</sup> Table 4.6.

Signal Grid	Generator	Cross section
Simplified Model via sleptons	HERWIG++ [69]	NLO+NLL
Simplified Model via WZ	HERWIG++ [69]	NLO+NLL

Table 4.6: MC signal samples used in this analysis.

<sup>1914</sup>

### <sup>1915</sup> 4.6.4 SM Background MC Samples For Run-2

<sup>1916</sup> The MC samples used for the Run-2 analysis are described briefly in the following. The use  
<sup>1917</sup> of generators for several of the processes are different to those used in Run-1. Comparisons  
<sup>1918</sup> can be made between Table 4.7 and Table 4.8 for Run-1 and Run-2 respectively.

### <sup>1919</sup> 4.6.5 MC Signal Samples For Run-2

<sup>1920</sup> The samples are generated from LO matrix elements with up to two extra partons, using  
<sup>1921</sup> the MG5\_AMC@NLO v2.2.3 generator [102] interfaced with PYTHIA with the A14 tune  
<sup>1922</sup> for the modelling of the SUSY decay chain, PS, hadronisation and the description of the  
<sup>1923</sup> UE. Parton luminosities are provided by the NNPDF23LO PDF set. Jet-parton matching  
<sup>1924</sup> has been done following the CKKW-L prescription [109], with a matching scale set to one  
<sup>1925</sup> quarter of the pair-produced superpartner mass. Signal cross sections are calculated to  
<sup>1926</sup> NLO in the strong coupling constant, adding the resummation of soft gluon emission at  
<sup>1927</sup> NLO+NLL accuracy [110]. The nominal cross section and the uncertainty are taken from  
<sup>1928</sup> an envelope of cross section predictions using different PDF sets and factorisation and  
<sup>1929</sup> renormalisation scales, as described in [111]. All the signal MC samples were generated  
<sup>1930</sup> using a 25 ns bunch spacing configuration and simulated with a fast simulation using

<sup>1931</sup> a parameterisation of the calorimeter response and GEANT4 for the other parts of the  
<sup>1932</sup> detector. To reduce the amount of statistics per point and to target specific final states to  
<sup>1933</sup> the analysis, a generator filter was applied to these samples. For the  $\tilde{\chi}_1^\pm \tilde{\chi}_2^0$  production a  
<sup>1934</sup> requirement of at least two leptons with  $p_T > 5$  GeV and  $|\eta| < 2.8$  in the event is required.

<sup>1935</sup>

Process	Generator	Cross section
<b>Dibosons</b>		
$WW, WZ, ZZ, W/Z\gamma$	POWHEG + PYTHIA 8	NLO QCD with MCFM [112] [113]
<b>Tribosons</b>		
$WWW, ZZZ, WWZ$	MADGRAPH + PYTHIA	NLO [114]
<b>Top+Boson</b>		
$t\bar{t}W/Z$	ALPGEN + HERWIG	NLO [114] [115]
$t\bar{t}WW$	MADGRAPH + PYTHIA	NLO [115]
$tZ$	MADGRAPH + PYTHIA	NLO [116]
<b>Top-quark pair-production</b>		
$t\bar{t}$	POWHEG + PYTHIA	NNLO+NNLL [117]
<b>Single top</b>		
$t$ -channel	ACERMC + PYTHIA	NNLO+NNLL [118]
$s$ -channel, $Wt$	MC@NLO + HERWIG	NNLO+NNLL [119] [120]
<b>W/Z+jets</b>		
<b>Higgs</b>	ALPGEN + PYTHIA	DYNNLO [121]
via gluon fusion	POWHEG + PYTHIA 8	NNLL QCD, NLO EW [122]
via vector-boson fusion	POWHEG + PYTHIA 8	NNLL QCD, NLO EW [122]
associated $W/Z$ production	PYTHIA 8	NNLL QCD, NLO EW [122]
associated $t\bar{t}$ production	PYTHIA 8	NNLO QCD [122]
Low-Mass Drell-Yan	SHERPA	NLO [123]
$J/\Psi$	PYTHIA 8	LO [124]
$\Upsilon$	PYTHIA 8	LO [124]

Table 4.7: MC samples used in the Run-1 analysis for signal optimisation and background estimation, the generator type and the order of cross section calculations used for yield normalisation are also reported.

<sup>1936</sup><sup>1937</sup>

Process	Generator	Cross section
<b>Dibosons</b> $WW, WZ, ZZ, W/Z\gamma$	SHERPA [125]	0 jets @ NLO + 1,2,3 jets @LO [125] 0 jets @ NLO + 1,2,3 jets @ LO 0 jets @ NLO + 2,3 jets @ LO 0 jets @ NLO + 1,2 jets @ LO [125] 0,1,2 jets @ LO 0 jets @ NLO + 1,2 jets @ LO 0 jets @ NLO + 1,2 jets @ LO
<b>Tribosons</b> $WWW, WWZ, ZZW, ZZZ$	SHERPA [125]	0 jets @ NLO + 1,2,3 jets @LO [125] 0 jets @ NLO + 1,2 jets @ LO [125] 0 jets @ NLO + 1,2 jets @ LO 0 jets @ NLO + 1,2 jets @ LO
<b>Top+Boson</b> $t\bar{t}W/Z$ $t\bar{t}WW$ $tZ$	MADGRAPH + PYTHIA [126]	LO [126]
<b>Top-quark pair-production</b> $t\bar{t}$	POWHEG + PYTHIA [127]	NNLO + NNLL [127]
<b>Single top</b> $t$ -channel $s$ -channel, $Wt$	POWHEG + PYTHIA [127]	NLO+NNLL [127]
<b>W/Z+jets</b> <b>Higgs</b> via gluon fusion via vector-boson fusion associated $W/Z$ production associated $t\bar{t}$ production	SHERPA [128] POWHEG + PYTHIA [129] POWHEG + PYTHIA POWHEG + PYTHIA aMC@NLO + HERWIG++	0,1,2 jets @ NLO + 3,4 @ LO [128] NNLO+NNLL QCD and NLO EW [129] NNLO QCD and NLO EW NNLO QCD and NLO EW NLO QCD

Table 4.8: MC samples used in the Run-2 analysis (Section 8 for signal optimisation, the generator type and the order of cross section calculations used for yield normalisation are also reported.

## <sup>1938</sup> Chapter 5

# <sup>1939</sup> The E/Gamma Signature Trigger <sup>1940</sup> on ATLAS

<sup>1941</sup> This chapter will address the electron-photon signature trigger (E/gamma), served as  
<sup>1942</sup> the author’s “technical task” whilst working on ATLAS. This particular signature also  
<sup>1943</sup> is important for the analysis discussed in this thesis as electrons, like other leptons are  
<sup>1944</sup> vital physics objects for electroweak SUSY searches. The concept of trigger efficiency and  
<sup>1945</sup> its uncertainty will be introduced in Section 5.1. The method of efficiency measurement  
<sup>1946</sup> of electron triggers using data, referred to as the Tag and Probe method is described in  
<sup>1947</sup> Section 5.2. The efficiencies of the Run-2 E/gamma trigger menu was assessed with early  
<sup>1948</sup> Run-2 data with 50 ns bunch crossings, the results are discussed in Section 5.3.

### <sup>1949</sup> 5.1 Trigger Efficiency

<sup>1950</sup> In order for a measurement on the number of electrons observed with the ATLAS detector  
<sup>1951</sup> to be related to physics analysis, the efficiency of ATLAS to select and reconstruct these  
<sup>1952</sup> electrons needs to be known. This efficiency is a convolution of the geometric acceptance  
<sup>1953</sup> of the detector, the efficiency of the trigger system and the efficiency of the offline re-  
<sup>1954</sup> construction. The studies in this thesis focus specifically on the efficiency of the trigger  
<sup>1955</sup> system. A combination of electron and muon triggers are used in the analysis discussed in  
<sup>1956</sup> this thesis, but for the discussion in this chapter, single electron triggers will be used. The  
<sup>1957</sup> principles of trigger efficiencies discussed here can be generalised to all leptonic triggers.

<sup>1958</sup> The efficiency of the single electron trigger,  $\epsilon$ , is interpreted as the probability,  $P$ , that  
<sup>1959</sup> an electron  $e$ , will pass the trigger given certain conditions,  $I$ , that describe the electron

<sup>1960</sup> and the event it is present within:

$$\epsilon = P(\text{ pass the electron trigger } | I, e). \quad (5.1)$$

<sup>1961</sup> As this is a probability, the actual value of this efficiency is unable to be directly  
<sup>1962</sup> determined. Instead it must be estimated with data. This estimation is done assuming  
<sup>1963</sup> the true efficiency,  $\epsilon$ , is a real number between zero and one, to which the measured  
<sup>1964</sup> probability of selection tends in the limit of an infinite number of measurements. In a  
<sup>1965</sup> binomial model of efficiency, the measured probability, or efficiency estimator,  $\hat{\epsilon}$ , is given  
<sup>1966</sup> by:

$$\hat{\epsilon} = \frac{k}{n}, \quad (5.2)$$

<sup>1967</sup> where  $n$  is the total number of electrons, and  $k$  is the number of electrons which pass  
<sup>1968</sup> the trigger. The estimator of the variance on this efficiency estimator,  $\hat{V}[\hat{\epsilon}]$ , is then defined  
<sup>1969</sup> by:

$$\hat{V}[\hat{\epsilon}] = \frac{\hat{\epsilon}(1 - \hat{\epsilon})}{n}. \quad (5.3)$$

<sup>1970</sup> The standard deviation is defined as:

$$\sigma = \sqrt{\hat{V}}, \quad (5.4)$$

<sup>1971</sup> and is used to define the uncertainties on efficiencies. These uncertainties are statistical  
<sup>1972</sup> only, systematical sources of error on the trigger efficiency are not discussed in this thesis.

<sup>1973</sup> Differential trigger efficiency, as a function of a given variable, can be measured by  
<sup>1974</sup> binning  $k$  and  $n$  in the appropriate variable and then computing the  $\hat{\epsilon}$  and  $\hat{V}[\hat{\epsilon}]$  for each  
<sup>1975</sup> bin. For example, the one-dimensional efficiency estimator as a function of transverse  
<sup>1976</sup> energy defined in each bin  $i$  of transverse energy as:

$$\hat{\epsilon}_i = \frac{k(E_T^i)}{n(E_T^i)}, \quad (5.5)$$

<sup>1977</sup> where  $k(E_T^i)$  is the number of electrons with transverse energy in the  $i$ -th  $E_T$  bin that  
<sup>1978</sup> pass the trigger, and  $n(E_T^i)$  is the total number of electrons with transverse energy in the  
<sup>1979</sup> same bin. This concept of differential efficiency can be extended to high dimensions. For  
<sup>1980</sup> example, two-dimensional efficiencies can be defined as a function of  $E_T$  and  $\eta$ .

### 1981 5.1.1 Determining Efficiencies with $Z \rightarrow ee$ events

1982 The process  $Z \rightarrow e^+e^-$ , as shown in Figure 5.1, is an example of a well understood SM  
1983 process, which produces energetic isolated leptons. The NLO cross section for this process  
1984 at an LHC centre of mass energy of 14 TeV is expected to be around 2,069 pb [130]. This  
1985 would result in the production of around 206,900 events with an integrated luminosity of  
1986 only  $\mathcal{L} = 100 \text{ pb}^{-1}$  of data. The relative abundance and simple topology of this process  
1987 means that is an excellent benchmark process for the evaluation of trigger efficiencies in a  
realistic detector environment.

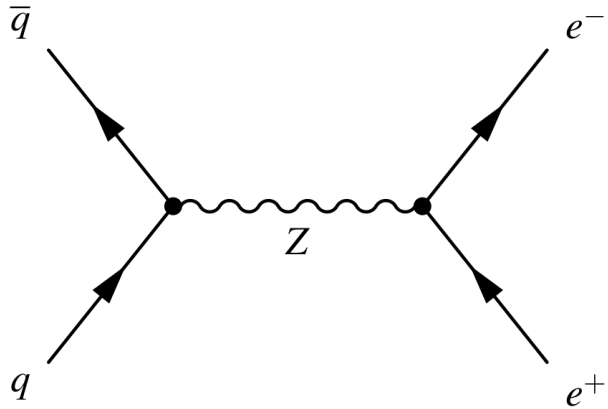


Figure 5.1: An example Feynman diagram of the  $Z \rightarrow e^+e^-$  process.

1988

1989 To determine the efficiency of lepton triggers in MC, the samples produced for  $Z/\gamma^*$   
1990 production as described in Section 4.6.2, specifically the  $Z \rightarrow e^+e^-$  samples for electron  
1991 triggers and  $Z \rightarrow \mu^+\mu^-$  for muon triggers.

## 1992 5.2 Data-Driven Efficiency Measurement

1993 The trigger efficiencies are measured relative to a well-defined offline electron passing one  
1994 of the identification criteria described in Section 4.4.5. When computing the efficiency  
1995 of the trigger on real data recorded by ATLAS, the sample of events needs to be defined  
1996 carefully to avoid a bias, since all events in data were already triggered by one or more  
1997 triggers. To obtain an unbiased measurement of the trigger efficiencies on real data, the  
1998 Tag and Probe method (TP) is used.

1999 This method utilises  $Z \rightarrow ee$  events. The strategy is to use a single trigger signature  
2000 which selects one of the electrons from the final state as a reference (the tag) and to  
2001 compute the efficiency using the other electron (the probe).

2002 The events are selected using a single electron trigger with an  $E_T$  threshold of 24

2003 GeV and MEDIUM++ identification requirements. These events are then required to have  
 2004 at least two reconstructed electron candidates in the central region of the detector  $|\eta| <$   
 2005 2.47, with opposite charges. One of the two electrons, the tag, must have  $E_T >$  GeV in  
 2006 order to be above the trigger threshold, be matched to a trigger electron object within  
 2007  $\Delta R < 0.07$  and be outside the transition region between the barrel and the end-cap of the  
 2008 EM calorimeter,  $1.37 < |\eta| < 1.52$ . The tag must satisfy an identification requirement,  
 2009 nominally TIGHT++. The probes, meanwhile, are required to pass the track quality criteria  
 2010 (as described in Section 4.4.2) and pass the trigger requirements for the trigger being  
 2011 studied.

2012 The overall trigger efficiency estimator, as computed by the TP method, is defined as  
 2013 the number of probes that pass the trigger selection,  $k^p$ , divided by the total number of  
 2014 probes,  $n^p$ :

$$\hat{\epsilon} = \frac{k^p}{n^p}. \quad (5.6)$$

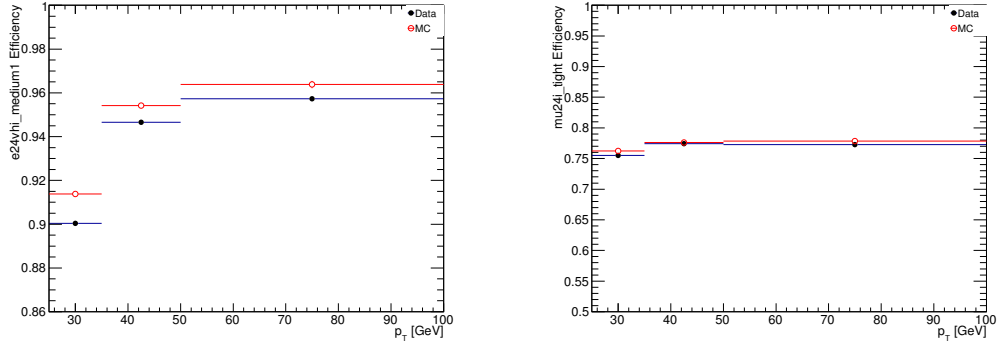
2015 This efficiency can also be measured as a function of one or more kinematic variables  
 2016 by binning in the appropriate variable of the probe.

### 2017 5.2.1 Efficiency Measurement Results with Run-1 8 TeV Data

2018 The efficiency of the leptonic triggers used in the Run-1 analysis was assessed. The results  
 2019 were calculated from the data produced by the LHC at a centre of mass energy of  
 2020  $\sqrt{s} = 8$  TeV. This amounts to  $20.3 \text{ fb}^{-1}$  after good data quality requirements. The tag and  
 2021 probe lepton are required to pass signal lepton requirements as outlined in Section 4.5. The  
 2022 tag is matched to one of the single lepton triggers EF\_mu24i\_tight or EF\_e24vhi\_medium1.  
 2023 The tag and probe lepton must form a SFOS lepton pair with an invariant mass with  $\pm 10$   
 2024 GeV of the Z mass. For the testing of multi-lepton triggers, the probe is tested against  
 2025 the given leg of the trigger. For example EF\_e24vh\_medium1\_e7\_medium1, has two legs:  
 2026 e24vh\_medium1 and e7\_medium1, which are tested individually. To avoid event overlap  
 2027 and to target events specific to the electron-photon signature, the e/ $\gamma$  data stream is used  
 2028 for the electron trigger efficiencies and the Muon stream for the muon trigger efficiencies  
 2029 (refer to Section 3.8.2). In this chapter, a selection of efficiency distributions are discussed  
 2030 for two triggers, the efficiency distributions of all the triggers used in the Run-1 analysis  
 2031 are contained in Appendix A.

2032 Figures 5.2, 5.3 and 5.4 show the efficiencies of two single lepton triggers, e24vhi\_medium1  
 2033 and mu24i\_tight, which were the primary triggers in the analysis discussed in this thesis.

2034 Figure 5.2 shows the efficiency as a function of  $E_T$ . As the electron or muon  $E_T$  reaches  
 2035 the energy threshold of the trigger, the efficiency increases sharply from zero to nearly one  
 2036 over the space of a few GeV. This is the *turn-on* region. Above the turn-on the efficiency  
 is observed to be very high and almost flat. This is known as the *plateau* region.

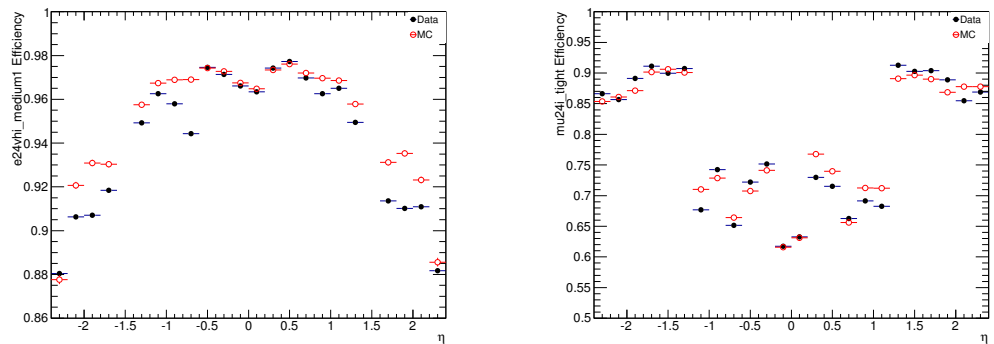


(a) e24vhi\_medium1 efficiency as a function of  $E_T$     (b) mu24i\_tight efficiency as a function of  $E_T$

Figure 5.2: Efficiencies of single lepton triggers as a function of  $E_T$ .

2037

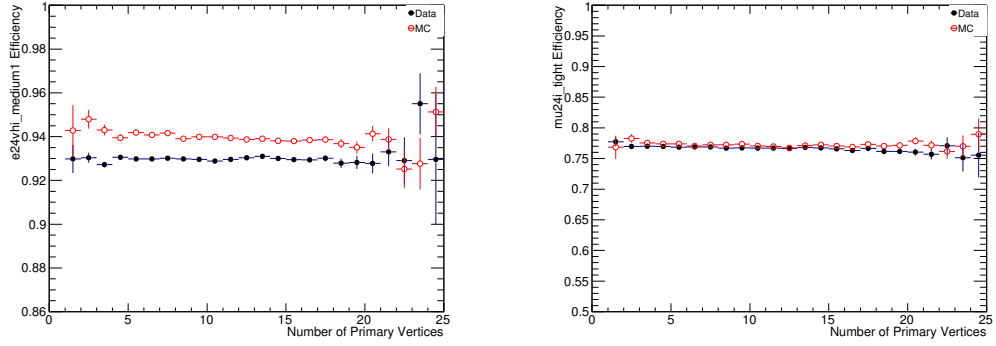
2038 Figures 5.3 shows the efficiency as a function of  $\eta$ . Figure 5.3(a) shows the efficiency  
 2039 for e24vhi\_medium, the barrel region  $|\eta| < 1.5$  shows the highest efficiency, with slight  
 2040 degradation in efficiency in the endcaps due to the inhomogeneities in the online and  
 2041 offline cuts in the endcap regions. This distribution includes electrons from the turn-on  
 2042 region, which contributes to the decrease in efficiency.



(a) e24vhi\_medium1 efficiency as a function of  $\eta$     (b) mu24i\_tight efficiency as a function of  $\eta$

Figure 5.3: Efficiencies of single lepton triggers as a function of  $\eta$ .

2043 Figure 5.3(b) shows the efficiency for mu24i\_tight, the barrel region shows a degra-  
 2044 dation in efficiency in the barrel region, which is due to the limited geometric coverage of the  
 2045 Level-1 muon trigger, which is about 99% in the end-cap regions and about 80% in the  
 2046 barrel region. The limited geometric coverage in the barrel region is due to gaps around  
 2047  $\eta = 0$  to provide space for services to the ID and calorimeters [131].



(a)  $e24vhi\_medium1$  efficiency as a function of  $Nvtx$   
(b)  $\mu24i\_tight$  efficiency as a function of  $Nvtx$

Figure 5.4: Efficiencies of single lepton triggers as a function of  $Nvtx$ .

2048     Figure 5.4 shows the efficiency as a function of the number of primary vertices  $Nvtx$ .  
2049     Both Figures 5.4(a) and (b) show no dependency on  $Nvtx$  and therefore, increasing pile-up  
2050     does not reduce the performance of these triggers.

### 2051     5.3 The E/Gamma Signature Trigger Efficiency with Early 2052     Run-2 Data

2053     Selection of events in real time based on electron and photon signatures is more challenging  
2054     in Run-2 of the LHC due to the higher centre-of-mass energy and higher luminosity,  
2055     which include a larger pile-up. These changes to the LHC beam conditions correspond to  
2056     more difficult signal-to-background discrimination and higher trigger rates. The upgrades  
2057     made to maintain performance is discussed in Section 3.9.2. This section will discuss the  
2058     transition to likelihood based electron identification, the electron trigger efficiencies with  
2059     early Run-2 data and the agreement in efficiency between data and MC simulated events.

#### 2060     5.3.1 Likelihood-based (LH) Electron Identification for Run-2

2061     During Run-1, the electron triggers utilised a cut-based ID, as described in Section 4.4.5,  
2062     while LH and cut-based electron ID both existed offline. In a cut-based ID, fixed re-  
2063     quirements are imposed on quantities that discriminate between signal and background.  
2064     The LH ID, by contrast, is based on PDFs of these various quantities for electrons and  
2065     background processes. These PDFs are then used to determine the probability for a given  
2066     electron candidate to be signal or background, and these probabilities are combined to  
2067     form a likelihood discriminant. Finally, a requirement is imposed on the likelihood dis-

2068 criminant to select signal-like objects and reject background-like objects [87]. These were  
 2069 both designed to have the same signal efficiency for a given operating point, which result in  
 2070 a background rejection that was approximately a factor of two better for the LH than the  
 2071 cut-based ID as shown in Figure 5.5(a), where the ratio of background efficiencies in Run-1  
 2072 for LH operating points with respect to corresponding cut-based operating points, where  
 2073 each ratio compares operating points which have approximately the same signal efficiency.  
 2074 Therefore, for a given signal efficiency, the LH operating points reduce backgrounds by  
 2075 about a factor of two with respect to the cut-based operating points on average.

### 2076 5.3.2 Results and Trigger Performance

2077 The LH signal efficiency is about 6% higher than that of the cut-based triggers as shown  
 2078 in Figure 5.5(b), where the efficiency is measured with respect to reconstructed electrons  
 2079 originating from the  $Z \rightarrow ee$  decay in simulation. This is because the Run 2 operating  
 2080 points were not designed to have the same absolute signal efficiency between the LH and  
 2081 cut-based operating points, due to rate requirements. The triggers in this figure require  
 2082 an electron candidate to have  $E_T > 24$  GeV, to satisfy the appropriate cut-based or LH  
 2083 identification criteria for the MEDIUM operating point and to pass a loose isolation re-  
 2084 quirement. The trigger efficiencies measured with respect to the corresponding offline ID  
 2085 for the LH and cut-based triggers are similar, with slight improvements seen in both MC  
 2086 and data as shown in Figure 5.6. Here the offline reconstructed electron is required to  
 2087 pass cut-based *medium* or likelihood-based *lhmedium* identification.

2088 The HLT\_e24\_(lh)medium\_iloose\_L1EM18VH triggers are two of the primary electron trig-  
 2089 gers used for the early Run-2 data taking and were used to provide data to MC scale  
 2090 factor recommendations for physics analysis groups. They require an electron candidate  
 2091 with  $E_T > 24$  GeV satisfying the cut-based *medium* or likelihood-based *lhmedium* identi-  
 2092 fication and a requirement  $p_T^{iso}/E_T < 0.1$  on the relative track isolation calculated within  
 2093 a cone of  $R = 0.2$ . Both triggers are seeded by a level-1 trigger L1\_EM18VH that applies  
 2094 an  $E_T$  dependent veto against energy deposited in the hadronic calorimeter behind the  
 2095 electron candidate's electromagnetic cluster. The efficiencies were measured with no back-  
 2096 ground subtraction applied and are compared to the expectation from  $Z \rightarrow ee$  simulation.  
 2097 The error bars show the statistical uncertainties only.

2098 The components of Figure 5.6 are split up for comparison in Figures 5.7 and 5.8, which  
 2099 show cut-based and likelihood compared for MC simulation, data, then MC simulation and  
 2100 data are compared for likelihood then cut-based identification respectively. Figure 5.7(a)

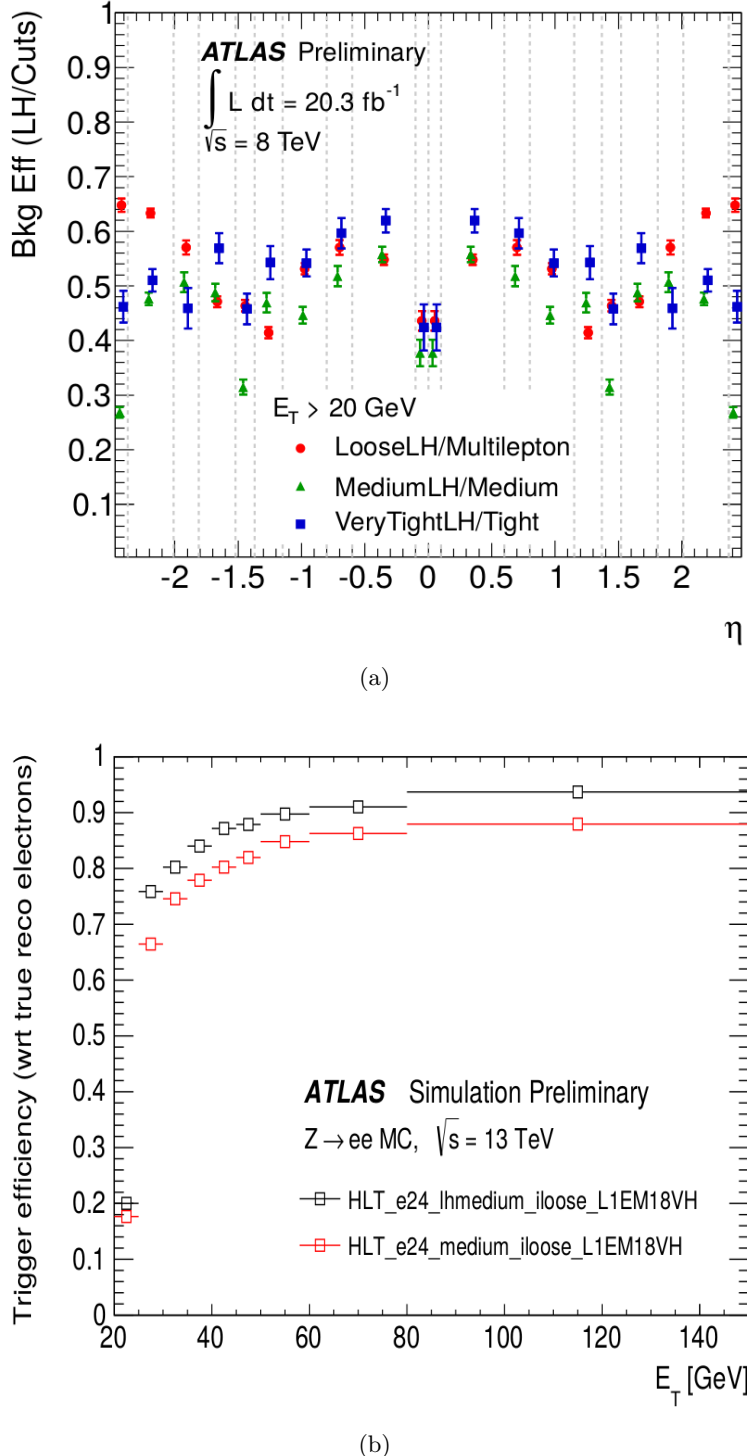


Figure 5.5: (a) Ratio of background efficiencies in Run-1 for LH operating points with respect to corresponding cut-based operating points. Taken from [132]. (b) Run-2 absolute trigger efficiencies expected for `HLT_e24_(lh)medium_iloose_L1EM18VH` triggers as a function of  $E_T$  of the offline electron candidate.

2101 shows the LH based trigger has a higher overall performance with less fluctuation than the  
 2102 cut-based trigger in data. Figure 5.7(b) shows that the LH- and cut-based triggers perform  
 2103 almost identically with MC simulation. Figures 5.8(c) and (d) show that the LH-based

trigger has better agreement between MC simulation and data than the cut-based trigger,  
as there is greater fluctuation in the central region of the efficiency plot with respect to  $\eta$   
for the cut-based trigger. The inefficiency in data that can be observed in the plateaus of  
the distributions primarily arises at the last step of the High Level Trigger selection that  
requires tracking related track-cluster matching criteria. These results show that the TP  
method is a reliable method for measuring trigger efficiencies and there is overall good  
agreement seen between early 2015 data and MC across the  $E_T$  and  $|\eta|$  spectra using the  
TP method. Many improvements have been made for the leptonic triggers since Run-1 in  
order to ensure rates remain manageable without degrading signal efficiencies. With the  
early Run-2 data, the ATLAS TDAQ system is shown to be performing well, allowing for  
analyses to be conducted using the leptons collected during this period.

2115

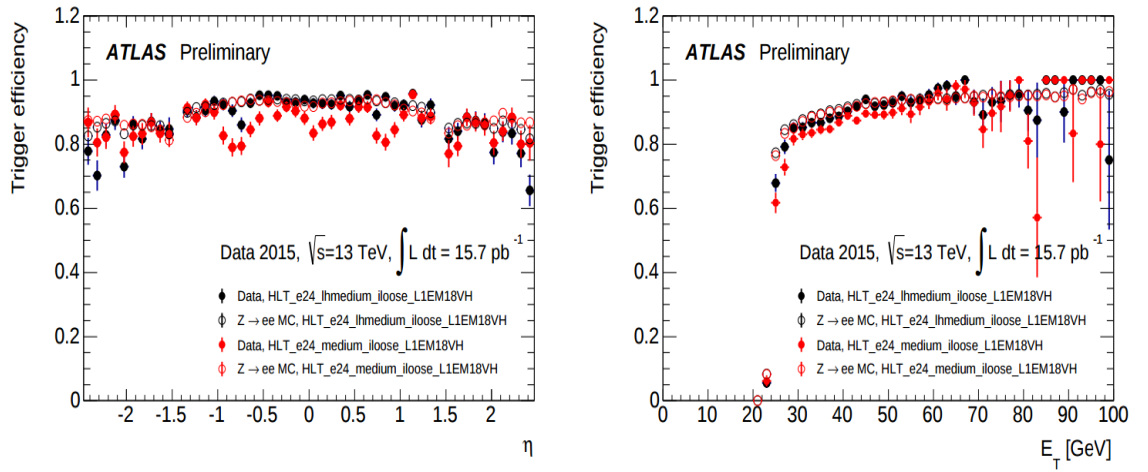


Figure 5.6: Single-electron trigger efficiencies for HLT\_e24\_(lh)medium\_iloose\_L1EM18VH triggers as a function of the offline electron candidate's  $E_T$  and  $\eta$ , measured with respect to the corresponding offline electron ID using data collected in June and July 2015.

2116

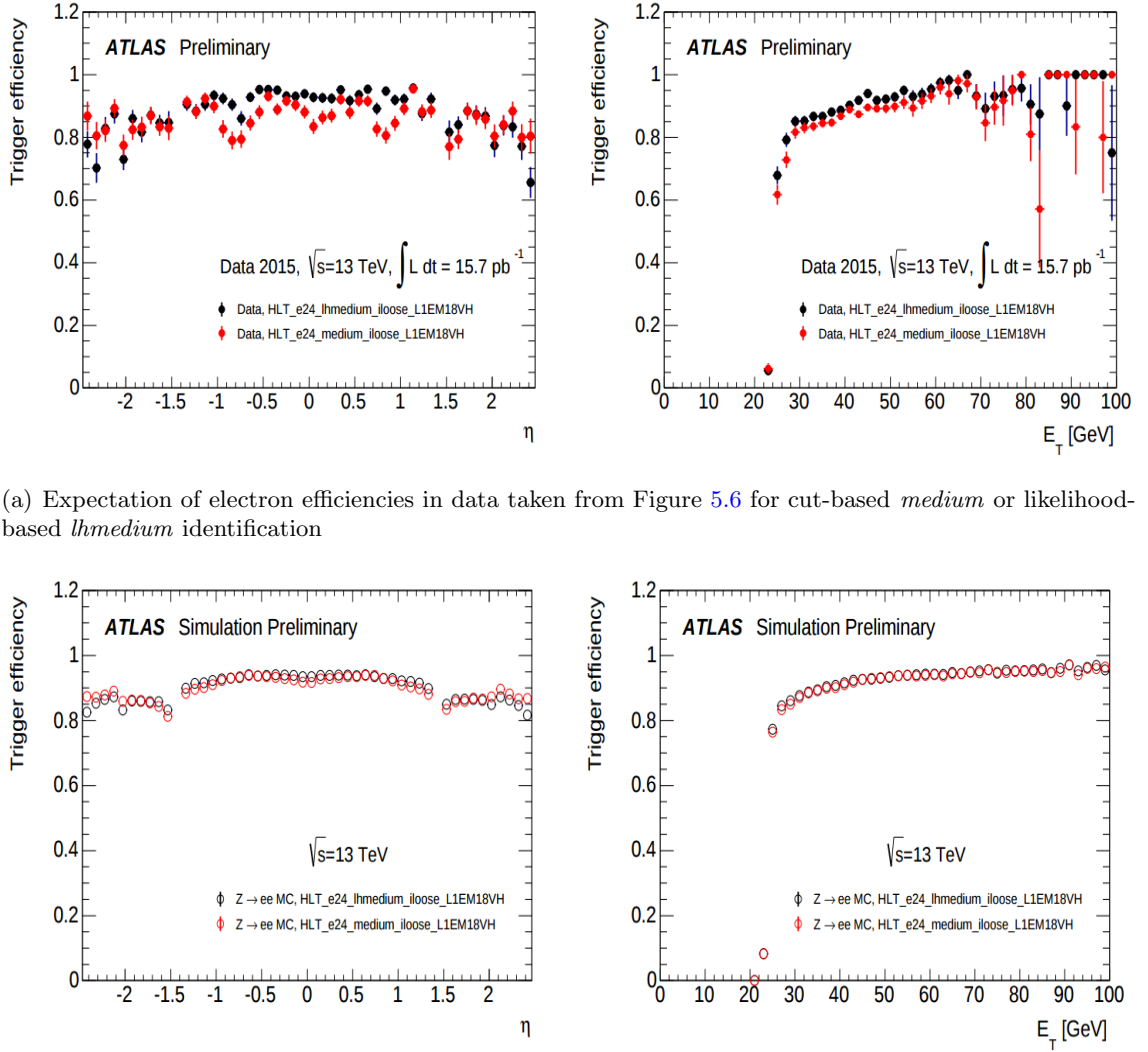


Figure 5.7: Single-electron trigger efficiencies for HLT\_e24\_(lh)medium\_iloose\_L1EM18VH triggers as a function of the offline electron candidate's  $E_T$  and  $\eta$ , measured with respect to the corresponding offline electron ID using data collected in June and July 2015. Data (a) and simulation (b) are split for comparison with cut-based and likelihood identification.

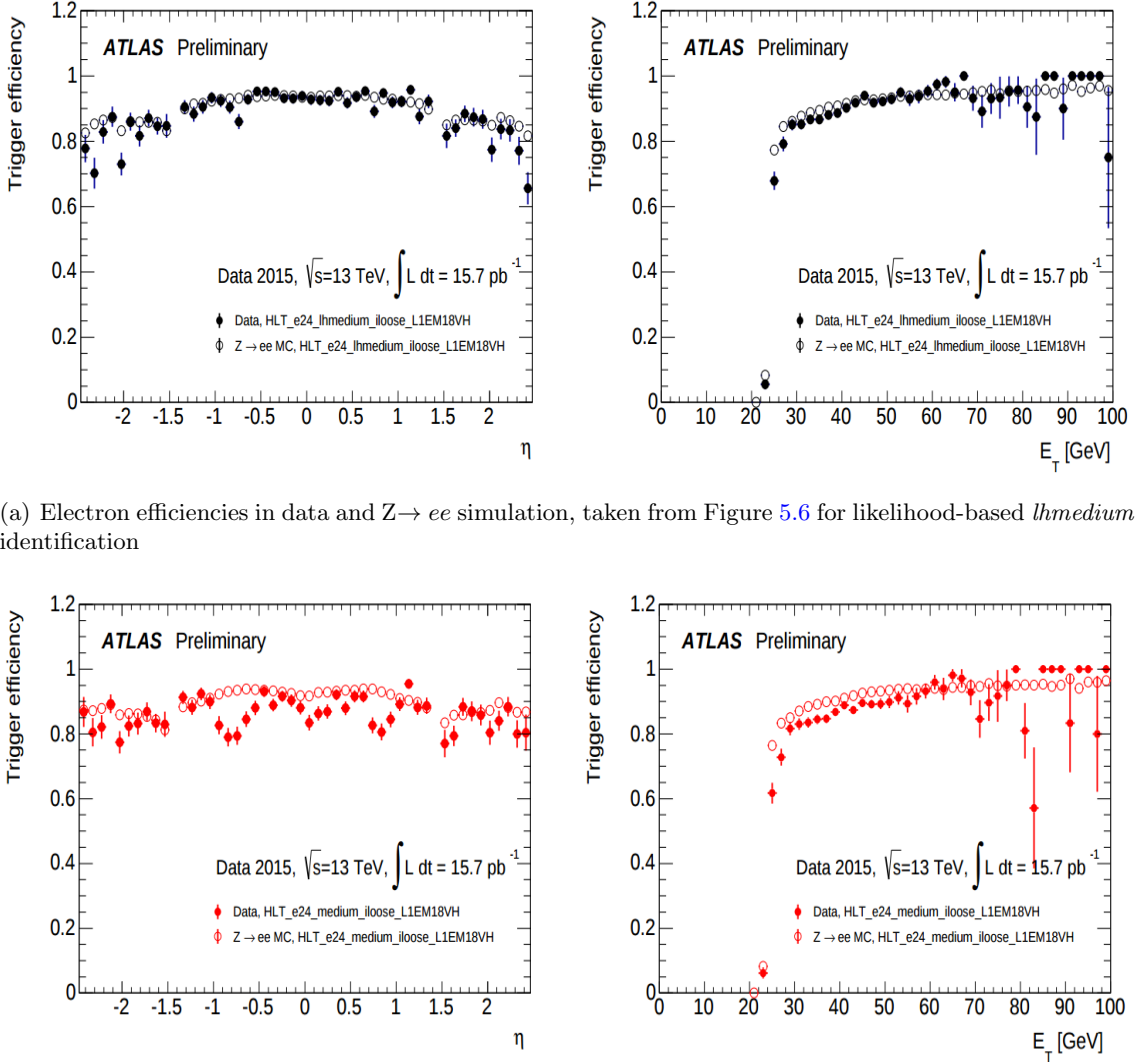


Figure 5.8: Single-electron trigger efficiencies for HLT\_e24\_(lh)medium\_iloose\_L1EM18VH triggers as a function of the offline electron candidate's  $E_T$  and  $\eta$ , measured with respect to the corresponding offline electron ID using data collected in June and July 2015. Data and simulation are compared with LH- (c) and cut-based-identifications (d).

## <sup>2117</sup> Chapter 6

# <sup>2118</sup> A Search for Electroweak SUSY in <sup>2119</sup> Three-Lepton Final States with <sup>2120</sup> Compressed Spectra in 8 TeV <sup>2121</sup> Data at ATLAS

### <sup>2122</sup> 6.1 Introduction

<sup>2123</sup> This chapter presents the search for electroweak supersymmetry, in particular direct  $\tilde{\chi}_1^\pm \tilde{\chi}_2^0$   
<sup>2124</sup> production and decay via SM gauge bosons or left-handed sleptons,  $\tilde{\ell}_L$ . The current limits  
<sup>2125</sup> on gluino and first- and second-generation squark masses are in the region of 1 TeV.  
<sup>2126</sup> If strongly interacting particles are heavy, then direct gaugino production may be the  
<sup>2127</sup> dominant SUSY cross-section at the LHC. Direct gaugino production can produce large  
<sup>2128</sup> lepton multiplicities through expected gaugino decays. The final state of three leptons  
<sup>2129</sup> and significant  $E_T^{miss}$  from the two escaping  $\tilde{\chi}_1^0$ s is a particularly distinctive signature; no  
<sup>2130</sup> hadronic activity comes from the hard process, making it hadronically quiet. A previous  
<sup>2131</sup> search was conducted with  $20.3 \text{ fb}^{-1}$  of 8 TeV proton-proton collision data delivered by  
<sup>2132</sup> the LHC and recorded with the ATLAS detector in 2012 [133]. No significant excess of  
<sup>2133</sup> events was found in data above SM expectations. Limits were placed on the gaugino  
<sup>2134</sup> masses; for simplified SUSY models with intermediate slepton decays, degenerate  $\tilde{\chi}_1^\pm \tilde{\chi}_2^0$   
<sup>2135</sup> masses up to 600 GeV were excluded for large mass differences with the  $\tilde{\chi}_1^0$ . For simplified  
<sup>2136</sup> SUSY models with gauge boson decays, degenerate  $\tilde{\chi}_1^\pm \tilde{\chi}_2^0$  masses up to 315 GeV were  
<sup>2137</sup> excluded for large mass differences with the  $\tilde{\chi}_1^0$ . However, this search was not sensitive

2138 to scenarios where the mass difference between the  $\tilde{\chi}_1^\pm \tilde{\chi}_2^0$  and  $\tilde{\chi}_1^0$  is less than 50 GeV.  
 2139 This near mass-degeneracy between the decaying gauginos and the final state gauginos is  
 2140 known as compressed scenarios and results in low  $p_T$  leptons and less significant  $E_T^{miss}$   
 2141 than would otherwise be seen with large mass differences. For more details on compressed  
 2142 spectra SUSY, refer to Section 2.7.

2143 This chapter describes a search for direct gaugino production with three leptons with  
 2144 compressed spectra in the final state. In order to explore  $\tilde{\chi}_2^0 - \tilde{\chi}_1^0$  mass splittings below 50  
 2145 GeV, this analysis utilises low- $p_T$  leptons and the emission of a hard jet coming from initial  
 2146 state radiation (ISR), which in turn boosts the  $E_T^{miss}$  in the event and provides interesting  
 2147 event topology. By requesting an ISR jet however, the level of hadronic activity in the final  
 2148 state increases, therefore hadronically quiet scenario of the previous search does not apply  
 2149 in this case. The intent of this search is to provide improved sensitivity to the compressed  
 2150 scenarios not covered by the previous  $3\ell$  searches.

2151 The author has contributed significantly to this analysis, including the development  
 2152 of the trigger strategy, signal region optimisation, track isolation studies, validation region  
 2153 optimisation and systematic uncertainty evaluation.

2154 This chapter will highlight the general analysis strategy in Section 6.2; the event  
 2155 selection is detailed in Section 6.3. The signal sensitivity is discussed in Section 6.4.4.  
 2156 The method of SM background estimation is described in Section 6.5, which includes both  
 2157 MC background estimation and data-driven estimation methods. The validation of the  
 2158 background modelling is explored in Section 6.6. Finally, the systematic and theoretical  
 2159 uncertainties are discussed in Section 6.7.

## 2160 6.2 Analysis Overview

2161 Events from SM background processes can produce three lepton final states that can mimic  
 2162 the final state of the SUSY scenarios considered. These events are suppressed using sets  
 2163 of discriminatory cuts on kinematic variables, which highlight the behaviour of the SUSY  
 2164 signal events. The combination of these cuts form dedicated “Signal Regions” (SRs), as  
 2165 described in Section 6.4. The cuts are optimised using MC simulation only to maximise  
 2166 the expected sensitivity to the signal model. The background contributions in these SRs  
 2167 are estimated using a combination of MC and data-driven methods. The performance of  
 2168 these estimation methods are then “validated” with data in separate dedicated validation  
 2169 regions (VRs), which are adjacent to but orthogonal to the SRs. They are designed such  
 2170 that the contamination from the signal model is low and such that they are dominated by

2171 the background process under consideration.

2172 Several sources of systematic uncertainty are considered for the SM background es-  
2173 timates and signal yield predictions. Regions are designed to be enhanced in a particular  
2174 SM process in order to assess the differences between data and MC. Both MC simulation  
2175 and data-driven techniques are used to estimate different components of the background  
2176 and are discussed in more detail in Section 6.5. The control regions (CRs) are defined  
2177 with kinematic properties similar to the SRs, yet are disjoint from the SRs to avoid signal  
2178 contamination. In this analysis, the CR are used to estimate the theoretical uncertainty  
2179 on the simulation of specific samples, which is discussed in further detail in Section 6.7.14.

2180 SRs are designed with MC estimation only. Data is not included as this could poten-  
2181 tially bias the signal region strategy. This method of optimisation is denoted as “blinded”.  
2182 Once the SRs are finalised, the uncertainties are effectively quantised and the agreement  
2183 between data and MC is sufficient in the VRs, the signal regions are then “unblinded”,  
2184 meaning the data is included in the signal regions to see if there is any excess above SM  
2185 expectations. In the absence of an observed excess of events in one or more signal regions,  
2186 the “model-dependent signal fit” is used to set exclusion limits in a particular model, where  
2187 the signal contribution from the particular model that is being tested is taken into account  
2188 in all CR and SR. Finally, in the “model-independent signal fit”, both CR and SR are  
2189 used in the same manner as for the model-dependent signal fit, but signal contamination  
2190 is not accounted for in the CR.

2191 The statistical interpretation of the results are described in detail in Chapter 7.

## 2192 6.3 Dataset and Event Selection

2193 The data used for the analysis presented in this chapter was collected during 2012, with a  
2194 centre-of-mass energy  $\sqrt{s} = 8$  TeV, giving a total integrated luminosity of  $\mathcal{L} = 20.3 \text{ fb}^{-1}$ ,  
2195 which satisfied the ”Good Runs List” (GRL) data quality criteria.

### 2196 6.3.1 Trigger Selection

2197 The event selection requires data to have passed a logical OR of all the leptonic triggers  
2198 summarised in Table 6.1. The offline lepton thresholds are taken into consideration, such  
2199 that if an event passes a certain trigger but not the corresponding  $p_T$  thresholds then it will  
2200 fail to be accepted by the respective trigger. However, the event may pass another trigger  
2201 and  $p_T$  threshold. The offline thresholds are required to ensure the signal leptons per event

are well into the plateau of the trigger efficiency. The signal leptons are also required to be within  $\Delta R < 0.15$  from the relevant trigger object. When a specific trigger lists “loose”, “medium” or “tight”, this applies to the type of offline lepton identification used in the trigger algorithm - see Section 4.4.5. The “vh” label is used to identify triggers where electrons are vetoed at the L1 stage if they have left energy significant deposits within the hadronic calorimeter. The “i” label identifies an additional isolation requirement for the trigger, where the sum of the track  $p_T$  with a cone of  $\Delta R < 0.2$  of a candidate lepton must be less than 10% (12%) of the lepton  $p_T$  if it is an electron (muon).

Table 6.1: Summary of leptonic triggers used in this analysis and the offline threshold used ensuring that the lepton(s) triggering the event are in the plateau region of the trigger efficiency.

Trigger Type	Trigger Name	Offline $p_T$ threshold [GeV]
Single Isolated $e$	EF_e24vhi_medium1	25
Single Isolated $\mu$	EF_mu24i_tight	25
Double $e$	EF_2e12Tvh_loose1	14,14
	EF_e24vh_medium1_e7_medium1	25,10
Double $\mu$	EF_2mu13	14,14
	EF_mu18_tight_mu8_EFFS	18,10
Combined $e\mu$	EF_e12Tvh_medium1_mu8	14( $e$ ),10( $\mu$ )
	EF_mu18_tight_e7_medium1	18( $\mu$ ),10( $e$ )
Triple $e$	EF_e18vh_medium1_2e7T_medium1	20,9,9
Triple $\mu$	3mu6	7,7,7
	mu18_tight_2mu4_EFFS	19,5,5
Combined $e\mu$	EF_2e7T_medium1_mu6	9( $e$ ),9( $e$ ),7( $\mu$ )
	EF_e7T_medium1_2mu6	9( $e$ ),7( $e$ ),7( $\mu$ )

To avoid overlap between data streams, it is required that only  $e$ ,  $ee$  or  $e\mu$  triggers are in the Egamma stream, while events in the Muon stream must fail these triggers and pass the  $\mu$ ,  $\mu\mu$  or  $\mu e$  triggers.

### 6.3.2 Event Cleaning

Event cleaning is a process whereby events are removed prior to data analysis if the quality of the reconstruction is lowered or partial due to the malfunction of part of the detector, or any other condition that would render the event invalid for physics analysis. These events are removed based on the ATLAS recommended procedures before the analysis specific cuts are made.

The procedure removes events where a timing, trigger and control processing (TTC) has restarted, which results in missing detector information. Events where bursts of noise

have been reported in the LAr calorimeters are rejected as well as events where data from the Tile calorimeter has become corrupted. Events with jets pointing to the Tile calorimeter “hot spot”, which is a problematic  $(\eta, \phi)$  region ( $-0.2 < \eta < 0.1$  and  $2.65 < \phi < 2.75$ ) are rejected. Events with jets potentially originating from detector effects are rejected. In order to suppress background from cosmic muons, events are rejected if they contain muons which have either an impact parameter  $d_0$  satisfying  $|d_0| > 0.2$  mm, or a projection of the impact parameter onto the  $z$  axis  $z_0 \sin\theta$  satisfying  $z_0 \sin\theta > 1$  mm. Furthermore events are rejected if muons have been poorly reconstructed due to mis-measurement, they are required to satisfy  $\frac{\sigma_{q/p}}{|q/p|} \geq 0.2$ , where  $q$  is the muon charge,  $p$  is muon momentum and  $\sigma_{q/p}$  is the uncertainty on the measurement of  $q/p$ .

Events with fake  $E_T^{miss}$  due to non operational cells in the TileCal and the HCAL are rejected. There are calorimeter modules which are either temporarily or permanently masked throughout all data taking periods. High- $p_T$  jets which fall within a masked module are usually undercorrected, while jets in modules adjacent to a masked module are undercorrected [134]. As the jet  $p_T$  is increased, this becomes a much more important contribution. Therefore it becomes important to reject events where such jets fall into masked regions, otherwise the jet will be poorly reconstructed. This is also important for  $E_T^{miss}$  reconstruction as these masked regions can create large amounts of fake  $E_T^{miss}$ .

## 6.4 Signal Region Optimisation

With the events that survive the event cleaning and quality requirements, the SRs are defined to discriminate for specific SUSY scenarios and against SM processes. These regions request a set of selections or cuts on various kinematic properties of interest, which are optimised using the statistical significance  $Z_N$ . This variable is a statistical measure of the relevance of an observation for a given region and is defined as:

$$Z_N = \sqrt{2}\operatorname{erf}^{-1}(1 - 2p(S + B, B, \delta B)), \quad (6.1)$$

where  $\operatorname{erf}$  is the error function,  $p$  indicates the probability to observe more data than the background-only hypothesis prediction (See Section 7.1.1),  $S$  is the number of expected signal events,  $B$  is the number of expected background events and  $\delta B$  is the uncertainty on the background MC estimation. A flat uncertainty on the background is assumed to be 30% in the case of the background estimation using MC-simulated events. In this case,

the background-only hypothesis is the Standard Model as modelled by MC samples. As the number of signal events increases beyond the number of SM events the significance increases. In signal optimisation, this property is maximised for each signal region as a function of the number of MC background and signal samples.

#### 6.4.1 Optimisation Strategy

Events are selected to satisfy a selection of cuts that highlight the most distinct features from direct gaugino production and decay via SM gauge bosons or  $\tilde{\ell}_L$ , this is defined as the “baseline” selection and will be explained in detail in the following sections. For the models considered, a total of exactly three leptons is always required. The baseline events are separated into channels depending on the request or veto of at least one ISR jet, defined as a jet in the event with transverse momentum above 50 GeV. The ISR signal regions request an ISR and the soft lepton signal regions veto them. This is to ensure the events do not overlap between the signal regions. This condition is known as *orthogonality*. In these two channels, the events are further split according the minimum possible invariant mass of the same flavour opposite sign pair of leptons in the event  $m_{SFOS}^{min}$ . For the ISR SRs, two channels are considered  $5 < m_{SFOS}^{min} < 15$  GeV and  $15 < m_{SFOS}^{min} < 25$  GeV. For the soft lepton SRs,  $4 < m_{SFOS}^{min} < 15$  GeV and  $15 < m_{SFOS}^{min} < 25$  GeV are considered. These channels are considered to target scenarios based on the mass difference between the  $\tilde{\chi}_1^\pm/\tilde{\chi}_2^0$  and  $\tilde{\chi}_1^0$ . The mass difference corresponds to the kinematic endpoint of the  $m_{SFOS}^{min}$  distribution. This leads to a total of four signal regions, with each channel requesting additional criteria in order to target scenarios individualised by a range of properties. A detailed description of the signal optimisation will be covered from Section 6.4.1.1 to Section 6.4.3.

##### 6.4.1.1 Baseline

In this analysis, baseline refers to a list of common cuts that are set before further optimisation is performed. The benchmark signal points shown in the baseline distributions correspond to simplified models via WZ with masses:  $m_{\tilde{\chi}_1^\pm\tilde{\chi}_2^0} = 100$  GeV,  $m_{\tilde{\chi}_1^0} = 87.5$  GeV and  $m_{\tilde{\chi}_1^\pm\tilde{\chi}_2^0} = 100$  GeV  $m_{\tilde{\chi}_1^0} = 75$  GeV. These cuts are as follows:

**Transverse momentum of the leading lepton ( $p_T^{1^{st}\ell}$ ):** The compressed scenarios explored in this analysis produce low  $p_T$  leptons in the final state. This is shown in Figure 6.1. The tails of the signal distributions in  $p_T$  tend to zero around 100 GeV,

whilst the SM background extends beyond 300 GeV. An upper cut of  $p_T^{1^{st}\ell} < 30$  GeV is applied to preserve the signal events and remove the tails from the SM background. The optimisation for an upper cut on this variable is done using the N-1 method, where all signal region cuts are applied except the cut to be explored. This was done to maximise background discrimination whilst retaining most of the signal. The distributions are shown in Figure 6.2.

**B-veto** To reduce top containing backgrounds and heavy flavour Z-boson decays all  $b$ -jet containing events are vetoed. Although the request of an ISR means the final state is not “hadronically quiet”, the expected jet to be produced in compressed spectra will not be heavy flavour. Figure 6.3 shows the  $b$ -jet multiplicity of events with three leptons and a SFOS request. The majority of the signal events have zero  $b$ -jet multiplicity, while Higgs and  $t\bar{t}$ -V have a larger spread, with some events containing as many as 5  $b$ -jets.

**$E_T^{\text{miss}}$**  In order to discriminate against the Low Mass Drell-Yan processes and the Z+jets processes, which dominate in the low  $E_T^{\text{miss}}$  region a cut of  $E_T^{\text{miss}} > 50$  GeV is applied. Figure 6.4 shows the  $E_T^{\text{miss}}$  distribution for events with three leptons a SFOS request and a  $b$ -jet veto. Z+jets,  $J/\Psi$  and  $\Upsilon$  populate the  $E_T^{\text{miss}}$  below 60 GeV. The optimisation for this cut was done using the N-1 method and is shown in Figures 6.6(a) - (d). The cut was selected to reduce the Drell-Yan, Z+jets and diboson backgrounds.

**$m_{\text{SFOS}}$**  The  $\Upsilon$  meson has an invariant mass of 9.46 GeV. It can decay to a SFOS pair of leptons whose invariant mass would be within 1 GeV of the meson mass. This analysis has a lower threshold on the  $m_{\text{SFOS}}$  variable than the previous  $3\ell$  analysis, at 4 GeV for the “soft lepton” signal regions and 5 GeV for the “ISR signal regions”, and therefore would accept this background in the signal selection. To cleanly reject this background process a veto window of 1 GeV is applied on the  $m_{\text{SFOS}}$  distribution between 8.4 and 10.4 GeV. Figure 6.5 shows the  $m_{\text{SFOS}}$  distribution for events with three leptons, a SFOS request and a  $b$ -jet veto. The peak from the  $\Upsilon$  decays appears in the second bin of the distribution.

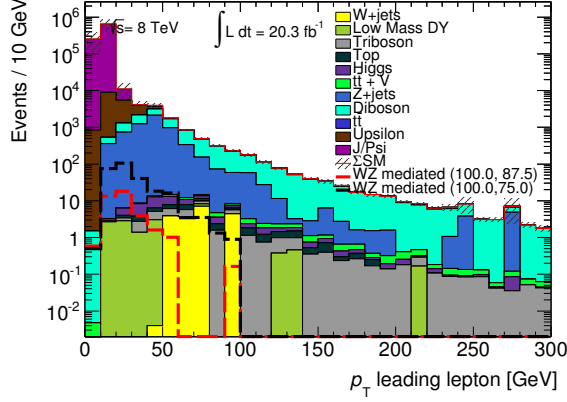


Figure 6.1: The leading lepton  $p_T$  distribution for  $3\ell$  events with a SFOS request and  $b$ -jet veto requirement applied.

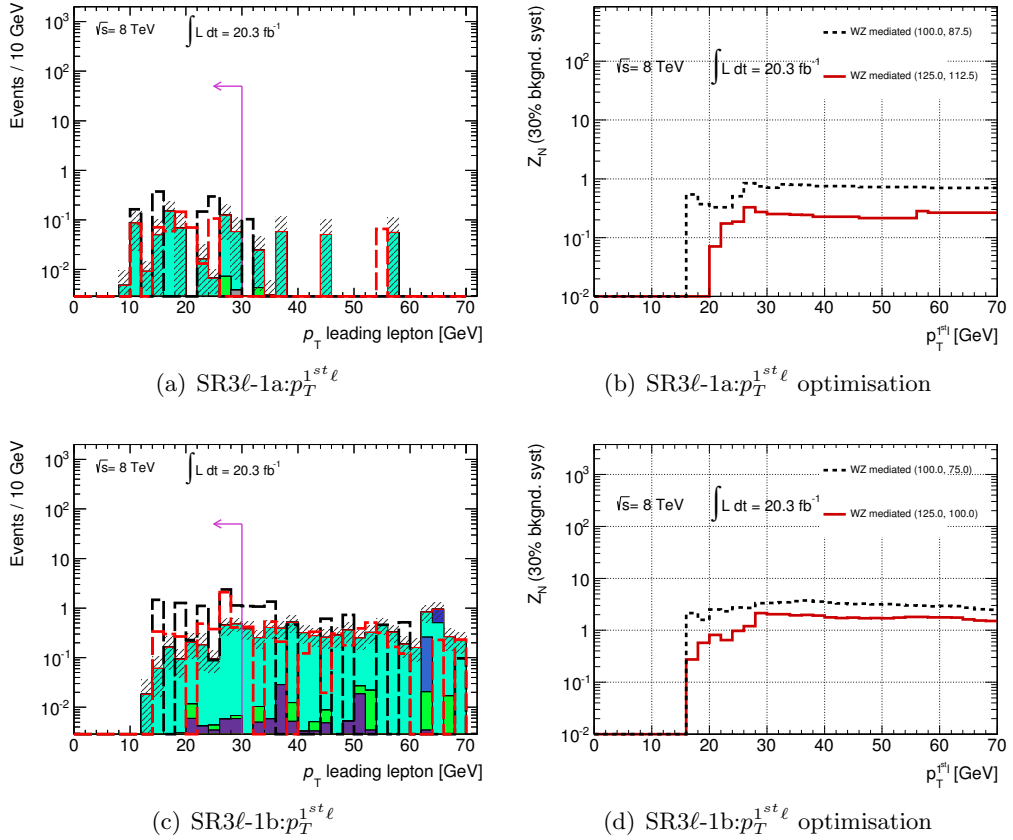


Figure 6.2: N-1 Distributions for  $p_T^{1st \ell}$ : All SR definition cuts applied except for the  $p_T^{1st \ell}$  cut. The colours assigned to the SM processes are the same as Figure 6.1.

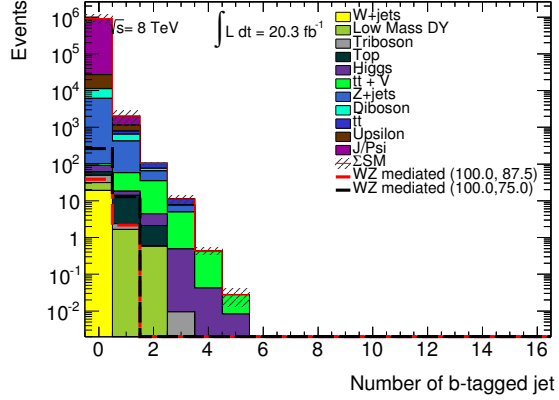


Figure 6.3: The  $b$ -jet multiplicity distribution for  $3\ell$  events with a SFOS request applied.

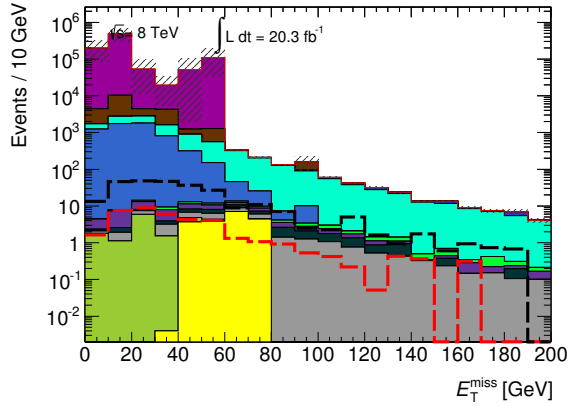


Figure 6.4: The  $E_T^{\text{miss}}$  distribution for  $3\ell$  events with a SFOS request and  $b$ -jet veto requirement applied. The colours assigned to the SM processes are the same as Figure 6.1.

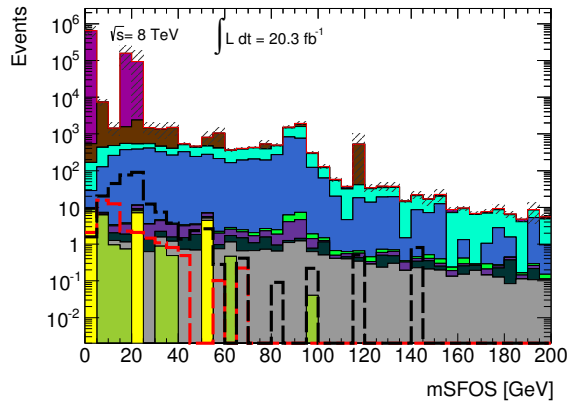


Figure 6.5: The  $m_{\text{SFOS}}$  distribution for  $3\ell$  events with a SFOS request and  $b$ -jet veto requirement applied. The colours assigned to the SM processes are the same as Figure 6.1.

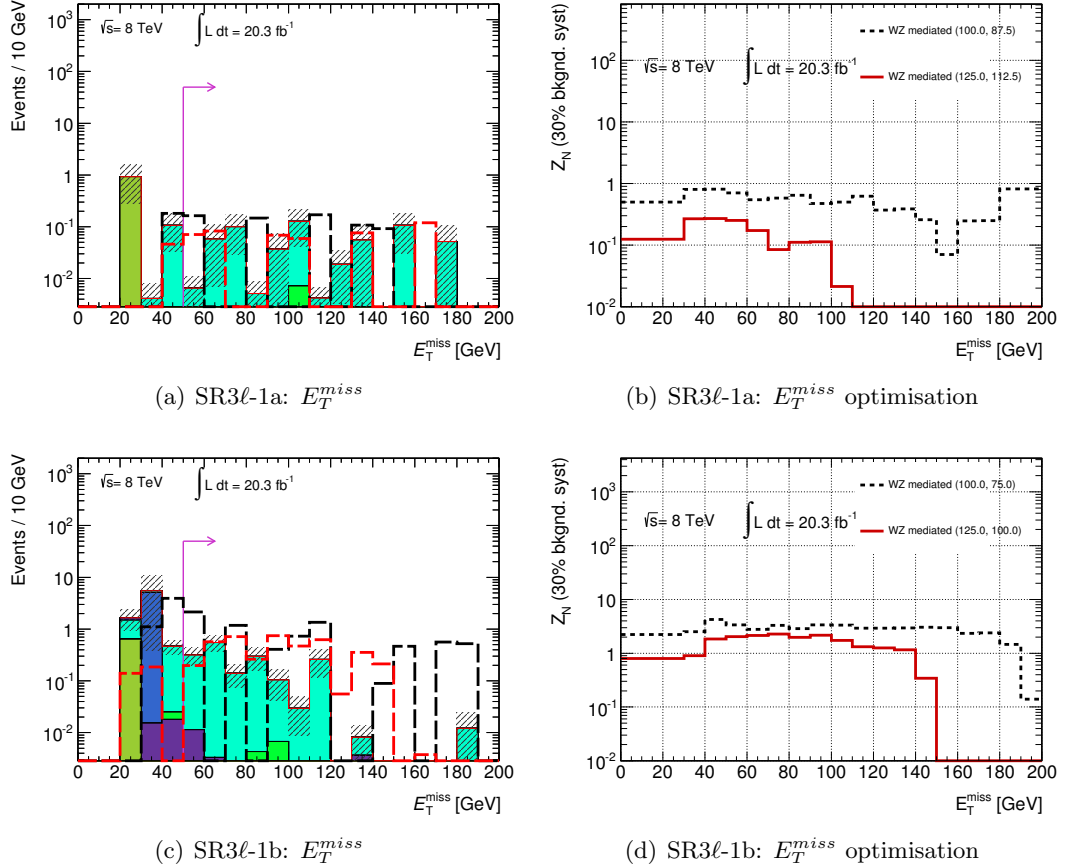


Figure 6.6: N-1 Distributions for  $E_T^{\text{miss}}$ : All SR definiton cuts applied except for the  $E_T^{\text{miss}}$  cut. The colours assigned to the SM processes are the same as Figure 6.1.

#### <sup>2309</sup> 6.4.1.2 Binning in $m_{\text{SFOS}}^{\text{min}}$

<sup>2310</sup> The leptons produced from compressed  $\tilde{\chi}_1^\pm \tilde{\chi}_2^0$  decays are soft, consequently the invariant  
<sup>2311</sup> mass of the SFOS pair will be typically softer than the equivalent for the SM background  
<sup>2312</sup> processes which produce harder leptons in the final state. The variable  $m_{\text{SFOS}}^{\text{min}}$  is defined  
<sup>2313</sup> as the lowest possible invariant mass calculated from the SFOS pair of leptons. The  
<sup>2314</sup> kinematic endpoint of the  $m_{\text{SFOS}}^{\text{min}}$  distribution corresponds to the mass difference between  
<sup>2315</sup>  $\tilde{\chi}_1^\pm$  and  $\tilde{\chi}_1^0$ . The signal regions are binned in this variable to target different mass  $\tilde{\chi}_1^\pm - \tilde{\chi}_1^0$   
<sup>2316</sup> mass splittings. SR3 $\ell$ -1a selects events with  $5 < m_{\text{SFOS}}^{\text{min}} < 15$  GeV to target the smallest  
<sup>2317</sup> mass splittings. SR3 $\ell$ -1b selects events with  $15 < m_{\text{SFOS}}^{\text{min}} < 25$  GeV to target the larger  
<sup>2318</sup> mass splittings. Binning also preserves orthogonality, allowing for the signal regions to  
<sup>2319</sup> be statistically combined for optimal sensitivity to new physics. Figure 6.7 shows the  
<sup>2320</sup>  $m_{\text{SFOS}}^{\text{min}}$  for events with three leptons, a SFOS request and a  $b$ -jet veto. The signal points  
<sup>2321</sup> shown correspond to simplified models via WZ with masses:  $m_{\tilde{\chi}_1^\pm \tilde{\chi}_2^0} = 100$  GeV,  $m_{\tilde{\chi}_1^0} =$   
<sup>2322</sup> 87.5 GeV and  $m_{\tilde{\chi}_1^\pm \tilde{\chi}_2^0} = 100$  GeV,  $m_{\tilde{\chi}_1^0} = 75$  GeV. The distinct kinematic endpoints are

at 12.5 GeV for the former point and 25 GeV for the latter point. By binning in this variable two approaches can be applied to signal optimisation. For the most compressed scenario, more stringent cuts can be used including the angular distributions of the ISR jet. For the less compressed scenario, there will still be sensitivity in the most compressed signal region. However, for the optimisation cuts can be loosened as the production cross-section is higher for these points, resulting in higher initial yields, with longer tails in the considered kinematic variables than the most compressed points. The optimisation of the  $m_{SFOS}^{min}$  variable was performed using the N-1 method. Figure 6.8 shows the optimal upper cuts, indicated by the event distribution and the one-dimensional  $Z_N$  curves. An optimal  $Z_N$  is achieved in SR3 $\ell$ -1a with an upper cut of 15 GeV, using benchmark signal points, which correspond to simplified models via WZ with masses:  $m_{\tilde{\chi}_1^\pm \tilde{\chi}_2^0} = 100$  GeV,  $m_{\tilde{\chi}_1^0} = 87.5$  GeV and  $m_{\tilde{\chi}_1^\pm \tilde{\chi}_2^0} = 125$  GeV,  $m_{\tilde{\chi}_1^0} = 112.5$  GeV. An optimal  $Z_N$  is achieved in SR3 $\ell$ -1b with an upper cut of 25 GeV, using benchmark signal points, which correspond to simplified models via WZ with masses:  $m_{\tilde{\chi}_1^\pm \tilde{\chi}_2^0} = 100$  GeV,  $m_{\tilde{\chi}_1^0} = 75$  GeV and  $m_{\tilde{\chi}_1^\pm \tilde{\chi}_2^0} = 125$  GeV,  $m_{\tilde{\chi}_1^0} = 100$  GeV. These signal points are used in the following optimisation stages.

#### 6.4.2 ISR Signal Region Procedure

**ISR Jet Request** Compressed signal production can be targeted by requesting at least one jet in the event with a sizeable transverse momentum minimum requirement. Figure 6.9 shows the leading jet  $p_T$  distribution with a SFOS request, a  $b$ -jet veto and at least one jet request in the  $5 < m_{SFOS}^{min} < 15$  GeV bin. The optimal value is 50 GeV for both regions as shown in Figure 6.10. This value is also chosen to be identical to the  $E_T^{miss}$  due to the ISR jet recoiling against the invisible decay products as discussed in Section 2.7. The ISR jet definition is common to both signal regions SR3 $\ell$ -1a and SR3 $\ell$ -1b, as such the next sections will address the individual cuts for each region.

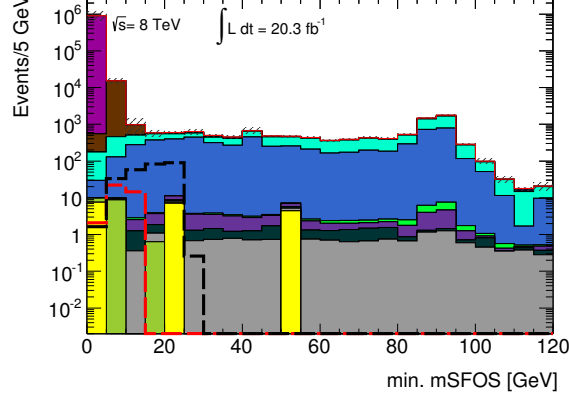


Figure 6.7: The  $m_{SFOS}^{min}$  distribution for  $3\ell$  events with a SFOS request and  $b$ -jet veto requirement applied. The colours assigned to the SM processes are the same as Figure 6.1.

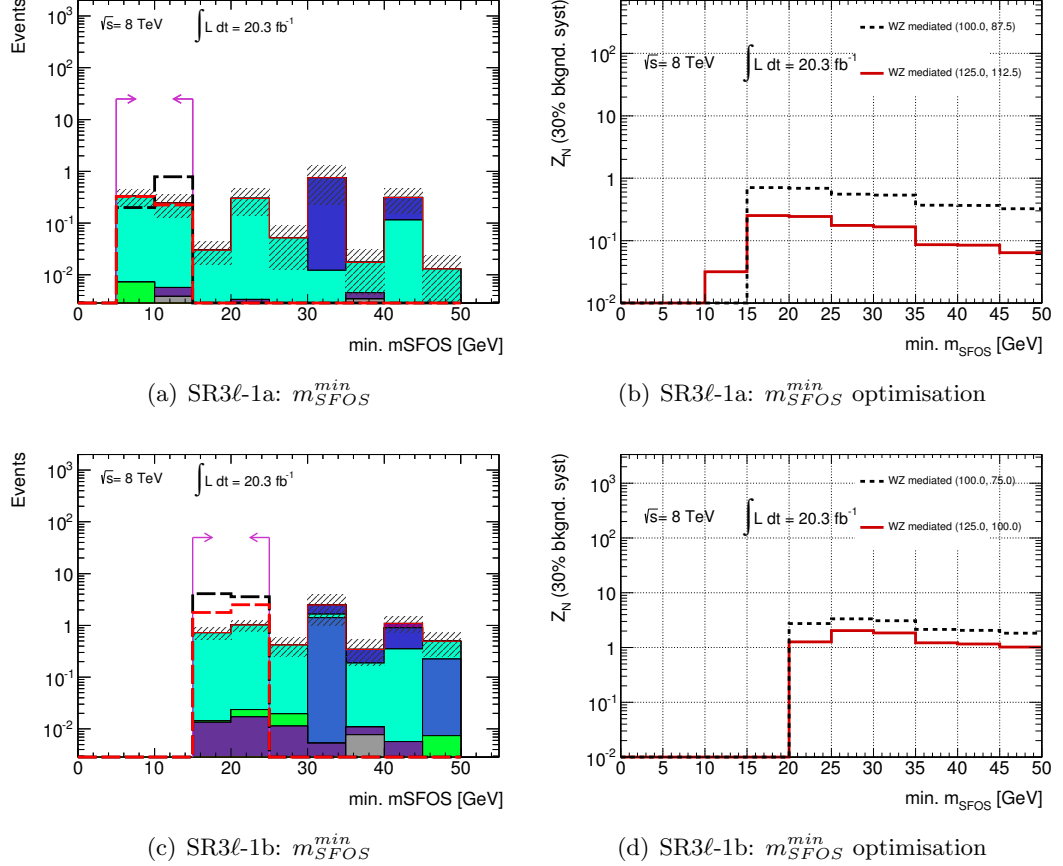


Figure 6.8: N-1 Distributions for  $m_{SFOS}^{min}$ : all SR definition cuts applied except for the upper cut on  $m_{SFOS}^{min}$ . The one-dimensional  $Z_N$  distributions show the effect of an upper cut on the  $m_{SFOS}^{min}$  variable. The colours assigned to the SM processes are the same as Figure 6.1.

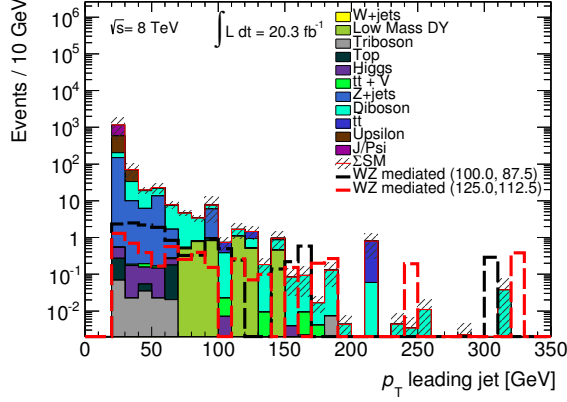


Figure 6.9: The leading jet  $p_T$  distribution for  $3\ell$  events with a SFOS request and  $b$ -jet veto applied in the SR $3\ell$ -1a  $m_{SFOS}^{min}$  bin. At least one jet is requested in the event selection.

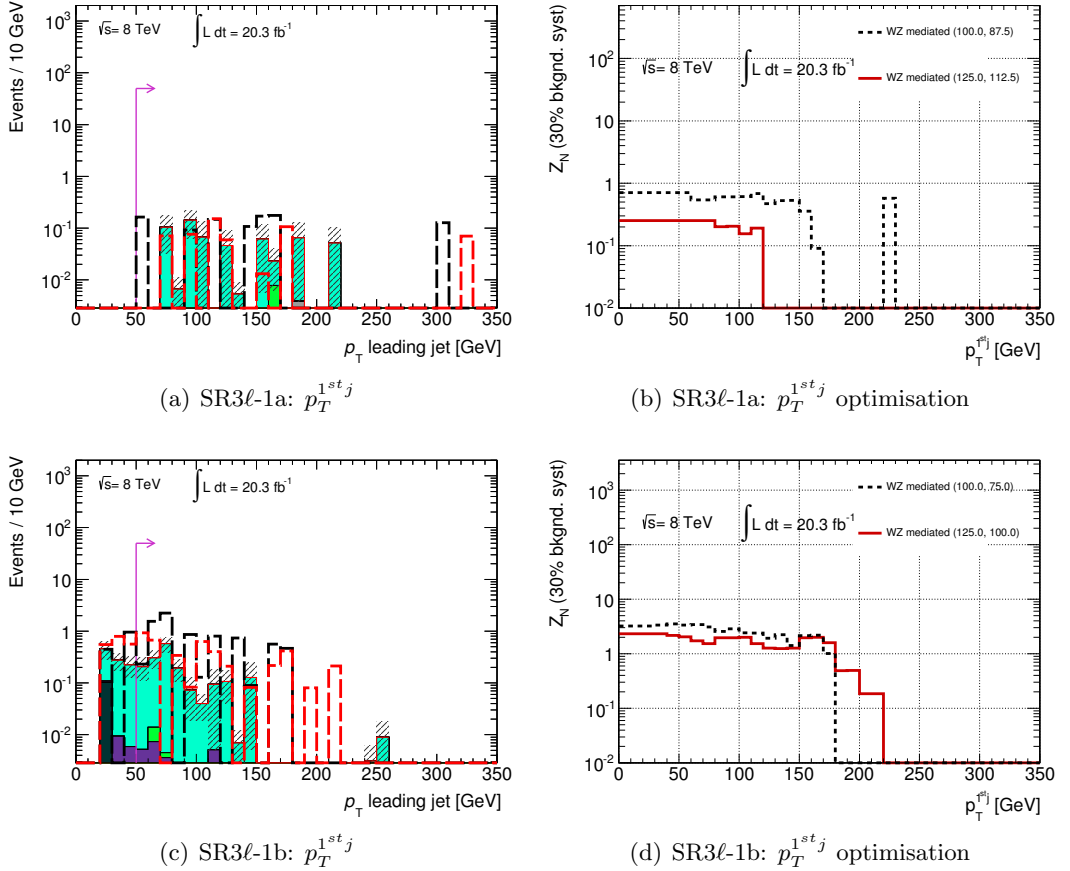


Figure 6.10: N-1 Distributions for  $p_T^{1st j}$ : all SR definition cuts applied except for the  $p_T^{1st j}$  cut. The colours assigned to the SM processes are the same as Figure 6.1.

#### 2348 6.4.2.1 SR $3\ell$ -1a Cuts

2349 **Polar angle between  $E_T^{\text{miss}}$  and ISR Jet ( $\Delta\phi(E_T^{\text{miss}}, \text{Jet1})$ ):** In the final state, the  
2350  $p_T$  of the leptons can be assumed negligible compared to the  $E_T^{\text{miss}}$  and the ISR jet. The

initial state momentum of a proton-proton collision is assumed to be zero. To conserve final state momentum, the ISR jet and the  $E_T^{miss}$ , both assumed to be carrying the majority of the final state momentum, will be produced back to back. This can be quantified by taking the angular distribution -  $\Delta\phi$  - between  $E_T^{miss}$  and the ISR jet in the event. The signal events should have  $\Delta\phi$  close to  $\pi$ , this is shown in Figure 6.11, where the signal events populate the bins close to  $\pi$ , whereas the SM background has a flat distribution from 0 to  $\pi$ . Using the N-1 optimisation method a cut above 2.7 rad was selected, which obtains optimal  $Z_N$  for the benchmark signal points shown in Figure 6.12.

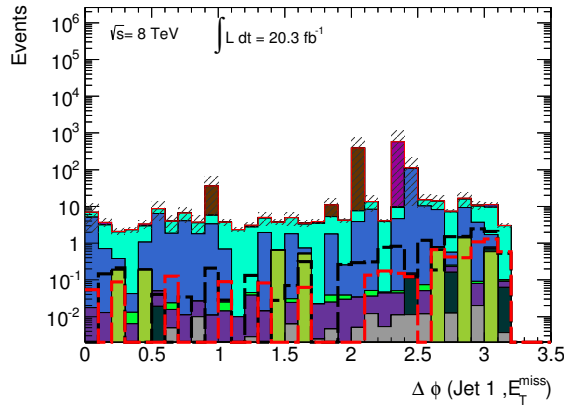


Figure 6.11: The  $\Delta\phi(E_T^{miss}, \text{Jet1})$  distribution for  $3\ell$  events with a SFOS request and  $b$ -jet veto applied in the SR $3\ell$ -1a  $m_{SFOS}^{min}$  bin. At least one jet is requested in the event selection. The colours assigned to the SM processes are the same as Figure 6.1.

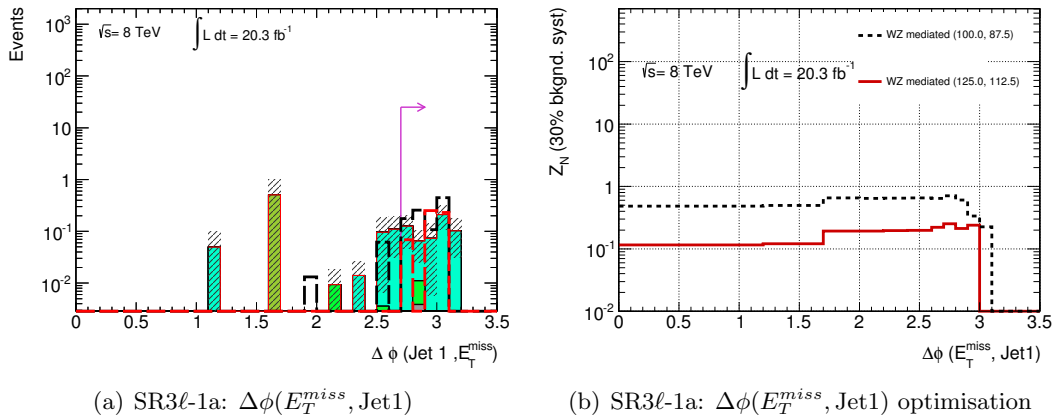


Figure 6.12: N-1 Distributions for  $\Delta\phi(E_T^{miss}, \text{Jet1})$ : all SR definition cuts applied except for the  $\Delta\phi(E_T^{miss}, \text{Jet1})$  cut. The colours assigned to the SM processes are the same as Figure 6.1.

Ratio of the  $p_T$  of the leading lepton to ISR jet ( $p_T^{1^{st}\ell}/p_T^{1^{st}j}$ ): The ISR jet together with  $E_T^{miss}$  carries the majority of the momentum in the final state. If the ratio of  $p_T$  between the leading lepton and the ISR jet is calculated, the ratio value should be less

than one for compressed scenario signal events and close to unity for SM background processes. This is shown in Figure 6.13, which shows the  $p_T^{1^{st}\ell}/p_T^{1^{st}j}$  distribution for  $3\ell$  events with a SFOS request and  $b$ -jet veto applied in the SR3 $\ell$ -1a  $m_{SFOS}^{\min}$  bin. The signal events populate values below 1 whereas the SM backgrounds exhibits a flat distribution between 0 and 1.5. Using the N-1 method, the optimal cut lies at below 0.1, which is shown in Figure 6.14(b). However to maximise signal yields a slightly more conservative upper cut of 0.2 is applied.

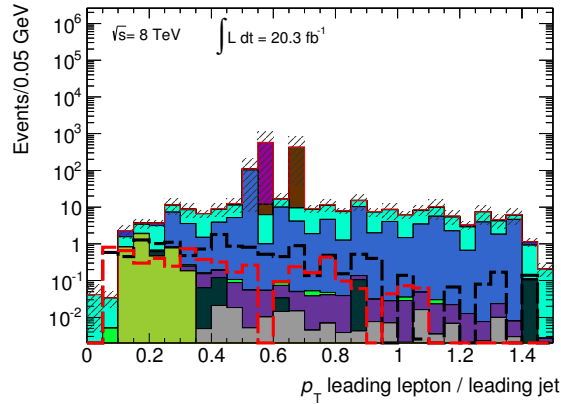


Figure 6.13: The  $p_T^{1^{st}\ell}/p_T^{1^{st}j}$  distribution for  $3\ell$  events with a SFOS request and  $b$ -jet veto applied in the SR3 $\ell$ -1a  $m_{SFOS}^{\min}$  bin. At least one jet is requested in the event selection. The colours assigned to the SM processes are the same as Figure 6.1.

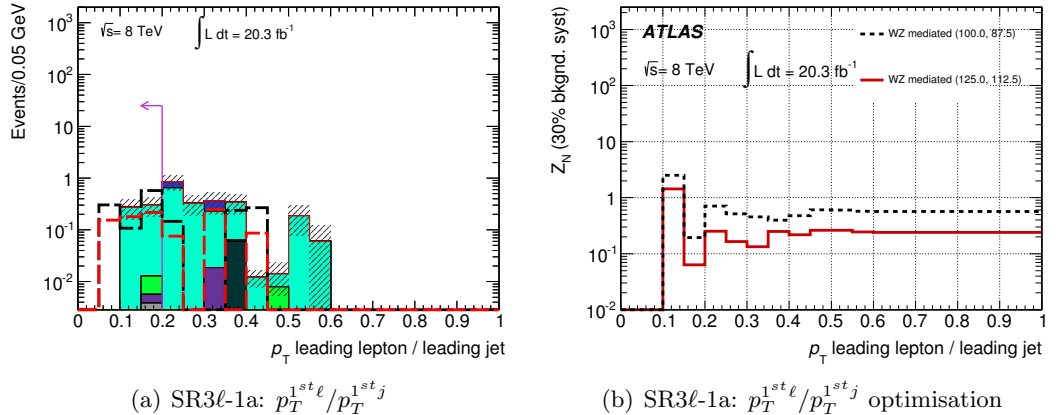


Figure 6.14: N-1 Distributions for  $p_T^{1^{st}\ell}/p_T^{1^{st}j}$ : all SR definition cuts applied except for the  $p_T^{1^{st}\ell}/p_T^{1^{st}j}$  cut. The colours assigned to the SM processes are the same as Figure 6.1.

#### 6.4.2.2 SR3 $\ell$ -1b Cuts

Polar angle between  $E_T^{\text{miss}}$  and the three leptons in the final state ( $\Delta\phi(E_T^{\text{miss}}, 3\ell)$ ): The topology between the  $E_T^{\text{miss}}$  and leading jet in the event has been exploited in Section 6.4.2.1. However, the leptons are not as strongly correlated with the direction of

the ISR jet or  $E_T^{miss}$ , and show a roughly flat distribution as shown in Figure 6.15. The  $\Delta\phi(E_T^{miss}, 3\ell)$  distribution is shown for  $3\ell$  events with a SFOS request and  $b$ -jet veto applied in the SR3 $\ell$ -1b  $m_{SFOS}^{min}$  bin. The two  $\Delta m_{\tilde{\chi}_1^\pm \tilde{\chi}_2^0 - \tilde{\chi}_1^0}$  benchmark signal points exhibit a flat distribution between 0 and  $\pi$ . Using the N-1 method for this variable, a cut of  $<2.2$  rad removes the remaining  $t\bar{t}$  process contribution as shown in Figure 6.16(b).

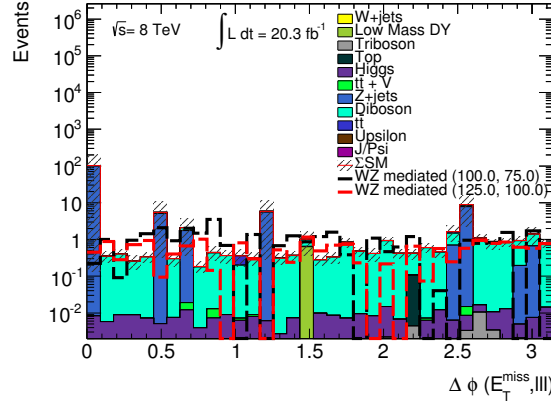


Figure 6.15: The  $\Delta\phi(E_T^{miss}, 3\ell)$  distribution for  $3\ell$  events with a SFOS request and  $b$ -jet veto applied in the SR3 $\ell$ -1b  $m_{SFOS}^{min}$  bin. At least one jet is requested in the event selection.

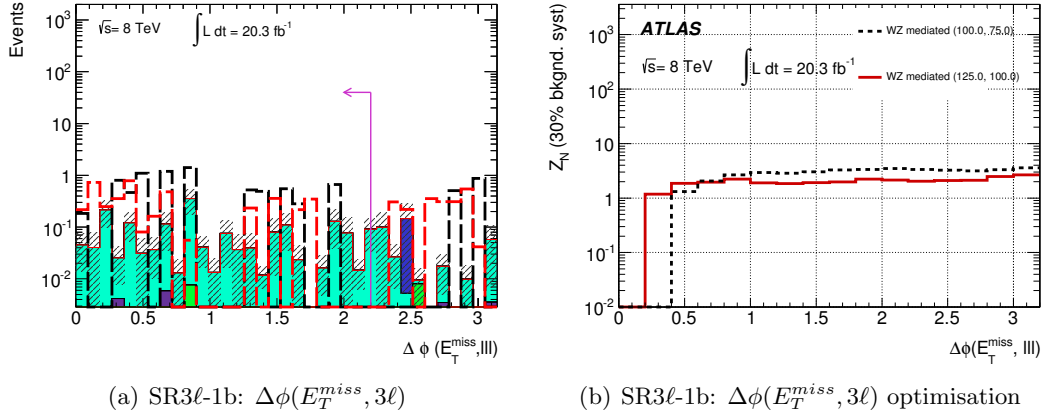


Figure 6.16: N-1 Distributions for  $\Delta\phi(E_T^{miss}, 3\ell)$ : all SR definition cuts applied except for the  $\Delta\phi(E_T^{miss}, 3\ell)$  cut. The colours assigned to the SM processes are the same as Figure 6.1.

The soft lepton signal region procedure is discussed in Section 6.4.3. The focus of this thesis is the ISR signal regions, so only the N-1 optimisation distributions are shown and discussed for the soft lepton signal regions.

### 2381 6.4.3 Soft Lepton Signal Region Procedure

2382 Compressed signal production can be targeted by exploring the kinematic variables and  
 2383 angular distributions of the three low  $p_T$  leptons in the final state. These signal regions  
 2384 veto all jets in order to ensure all soft lepton signal region events do not overlap with the  
 2385 ISR signal region events. The baseline selection defined in Section 6.4.1.1 is used. The  
 2386  $m_{SFOS}^{min}$  binning strategy is similar to the ISR signal regions with SR3 $\ell$ -0a targeting the  
 2387 smallest  $\tilde{\chi}_2^0 - \tilde{\chi}_1^0$  mass splittings by selecting events with  $m_{SFOS}^{min}$  between 4 and 15 GeV  
 2388 and SR3 $\ell$ -0b targeting the slightly larger mass splittings by selecting events with  $m_{SFOS}^{min}$   
 2389 between 15 and 25 GeV. Both SR3 $\ell$ -0a and SR3 $\ell$ -0b are defined with  $E_T^{miss} > 50$  GeV  
 2390 and the invariant mass of the three lepton system  $m_{\ell\ell\ell}$  is between 30 and 60 GeV to reject  
 2391 diboson processes. The  $m_{\ell\ell\ell}$  N-1 optimisation are shown in Figures 6.17(a) - (d), where  
 2392 the upper cut  $Z_N$  distribution is shown in Figures 6.17(b) and (d). SR3 $\ell$ -0a utilises the  
 2393 transverse mass variable,  $m_T$ , defined as  $m_T(\vec{p}_T^{\ell/\tau}, E_T^{miss}) = \sqrt{2p_T^{\ell/\tau} E_T^{miss} - 2\vec{p}_T^{\ell/\tau} \cdot E_T^{miss}}$   
 2394 Where the lepton used in the calculation is not used to form the SFOS lepton pair with  
 2395 mass closest to the Z boson mass. The transverse mass is required to be less than 20  
 2396 GeV to reduce the WZ SM background. The N-1 optimisation for this variable is shown  
 2397 in Figures 6.18(a) and (b). Four  $\tilde{\chi}_1^\pm \tilde{\chi}_2^0$  via WZ benchmark signal points are used for the  
 2398 optimisation. Two with  $\Delta m_{\tilde{\chi}_1^\pm \tilde{\chi}_2^0 - \tilde{\chi}_1^0} = 12.5$  GeV and two with 25 GeV. With points with  
 2399  $m(\tilde{\chi}_1^\pm \tilde{\chi}_2^0, \tilde{\chi}_1^0) = (125, 100), (100, 75), (125, 112.5), (100, 87.5)$  GeV.

### 2400 6.4.4 Signal Region Summary

2401 The final optimised cuts for each of the four signal regions are detailed in Table 6.2.  
 2402 The significance  $Z_N$  was calculated for the two  $m_{SFOS}^{min}$  bins in the soft lepton and ISR  
 2403 signal regions. They were combined to give an estimation of the performance of each  
 2404 signal region in both the  $\tilde{\chi}_1^\pm \tilde{\chi}_2^0$  via WZ and via  $\tilde{\ell}_L$  simplified models. The significance  
 2405 was calculated for each point in the simplified model grids and displayed on histograms  
 2406 with the significance as a function of the parameter space. The  $x$  and  $y$  axes display the  
 2407  $\tilde{\chi}_1^\pm, \tilde{\chi}_2^0$  and  $\tilde{\chi}_1^0$  masses respectively. Delaunay triangulation [135] is used to interpolate  
 2408 the significance values for bins in between the points where the signal samples exist in  
 2409 order to ensure the significance changes smoothly as a function of horizontal and vertical.  
 2410 A significance value of 1.64 or greater corresponds to an exclusion of the signal scenario  
 2411 considered with a 95% confidence level [136].

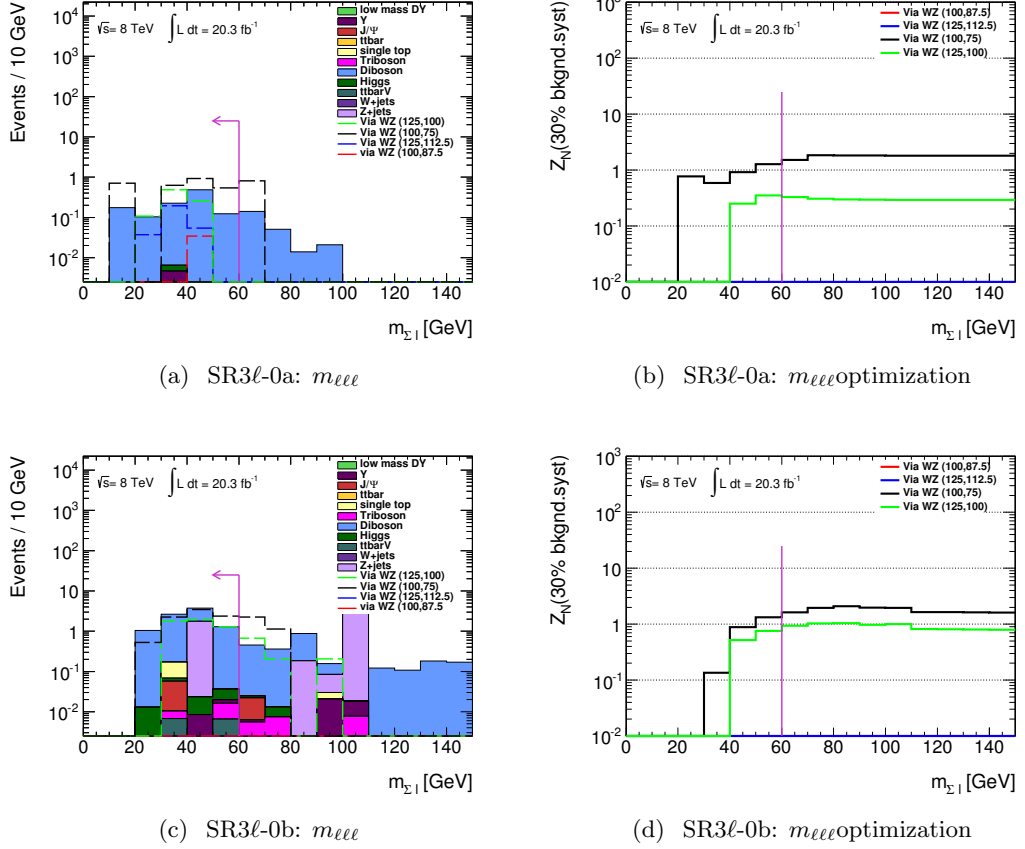


Figure 6.17: The N-1  $m_{\ell\ell\ell}$  distributions for each bin in SR3 $\ell$ -0: all SR definition cuts applied except for the  $m_{\ell\ell\ell}$  cut. The signal significance for WZ SUSY benchmark points is shown on the right plots as an upper cut on  $m_{\ell\ell\ell}$  is varied. (Produced by another analyser, taken from [137]).

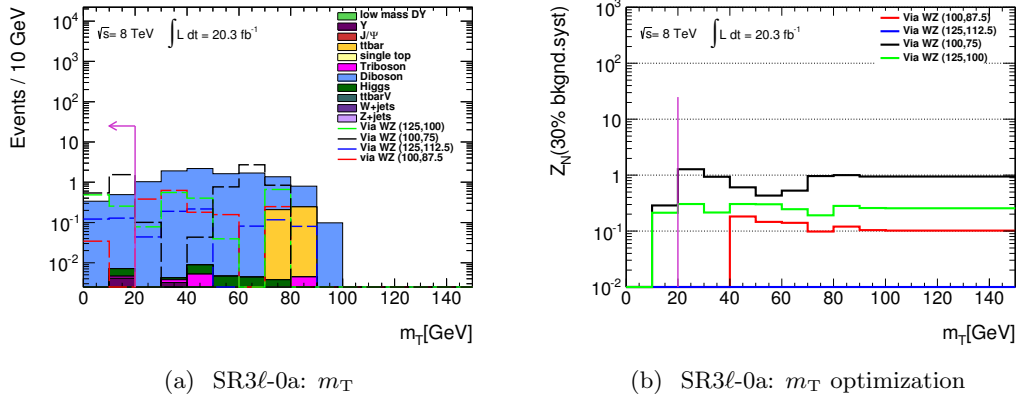


Figure 6.18: The N-1  $m_T$  distributions for SR3 $\ell$ -0a: all SR definition cuts applied accept  $m_T$ . The vertical black lines indicate bin edges. The signal significance for WZ SUSY benchmark points is shown on the right plots as an upper cut on  $m_T$  is varied (Produced by another analyser, taken from [137]).

Table 6.2: The selection requirements for the three-lepton signal regions, targeting  $\tilde{\chi}_1^\pm \tilde{\chi}_2^0$  production with small mass splittings between the  $\tilde{\chi}_1^\pm / \tilde{\chi}_2^0$  and  $\tilde{\chi}_1^0$ .

$m_{\text{SFOS}}$	Common			
	SR	SR3 $\ell$ -0a	SR3 $\ell$ -0b	veto 8.4–10.4 GeV
Central jets		no jets $p_T > 50$ GeV		$\geq 1$ jet $p_T > 50$ GeV
$m_{\text{SFOS}}^{\text{min}}$	4–15 GeV	15–25 GeV		5–15 GeV
Other	$30 < m_{\ell\ell\ell} < 60$ GeV	$30 < m_{\ell\ell\ell} < 60$ GeV	$\Delta\phi(E_T^{\text{miss}}, \text{jet } 1) > 2.7$ rad	$15\text{--}25$ GeV
	$m_T < 20$ GeV		$p_T^{\text{lep } 1}/p_T^{\text{jet } 1} < 0.2$	$\Delta\phi(E_T^{\text{miss}}, 3\ell) < 0.7\pi$ rad

#### **2412 6.4.5 Significance in Soft Lepton and ISR Signal Regions**

2413 To determine the significance of the searches for new physics, the MC expected background  
 2414 is used. The significance is calculated for all four signal regions separately. The ISR signal  
 2415 regions SR3 $\ell$ -1a and SR3 $\ell$ -1b are in orthogonal bins of  $m_{SFOS}^{min}$ , therefore the calculated  
 2416 significances can be combined. The same applies for the soft lepton signal regions SR3 $\ell$ -  
 2417 0a and SR3 $\ell$ -0b. The calculations of the  $Z_N$  values for each of the simplified models  
 2418 considered are done with two scenarios: MC-based estimates for all SM backgrounds and  
 2419 MC-based estimates for only the irreducible backgrounds and data driven matrix method  
 2420 estimates for the reducible backgrounds. The uncertainty on the MC-based estimates is  
 2421 taken as a flat 30% while the uncertainty on the reducible backgrounds estimated with  
 2422 the matrix method is taken directly from combined systematic uncertainties from the  
 2423 matrix method as described in Section 6.7.15. The MC-based scenario results are shown  
 2424 in Figures 6.19, 6.21, 6.23 and 6.25. The MC and data driven matrix method scenario  
 2425 results are shown in Figures 6.20, 6.22, 6.24 and 6.26. For reference, the compressed region  
 2426 in the parameter space is defined  $\Delta m_{\tilde{\chi}_1^\pm \tilde{\chi}_2^0 - \tilde{\chi}_1^0} \leq 50$  GeV. Due to the stringent requirements  
 2427 in all signal regions, the total and in particular reducible background statistics are very low.  
 2428 When the data driven matrix method fake estimate is included, the reducible statistics  
 2429 increase by 200-300%, which significantly affects the expected sensitivity.

##### **2430 6.4.5.1 $\tilde{\chi}_1^\pm \tilde{\chi}_2^0$ via $\tilde{\ell}$**

2431 The significance  $Z_N$  was calculated for the simplified model,  $\tilde{\chi}_1^\pm \tilde{\chi}_2^0$  decay via intermediate  
 2432 sleptons with the soft lepton and ISR signal regions. Starting with the ISR signal regions,  
 2433 for the MC-based only estimate  $\tilde{\chi}_1^\pm \tilde{\chi}_2^0$  masses can be excluded up to 350 GeV in the  
 2434 compressed region with a  $\tilde{\chi}_1^0$  mass of 300 GeV. For the MC and data driven matrix method  
 2435 estimate  $\tilde{\chi}_1^\pm \tilde{\chi}_2^0$  masses can be excluded up to 320 GeV in the compressed region with a  
 2436  $\tilde{\chi}_1^0$  mass 300 GeV. For the soft lepton regions, considering the MC-based only estimate  
 2437  $\tilde{\chi}_1^\pm \tilde{\chi}_2^0$  masses can be excluded up to 270 GeV with a  $\tilde{\chi}_1^0$  mass of 230 GeV. Considering  
 2438 the MC and data driven matrix method estimate  $\tilde{\chi}_1^\pm \tilde{\chi}_2^0$  masses can be excluded up to 200  
 2439 GeV with a  $\tilde{\chi}_1^0$  mass of 150 GeV. Improvements to the compressed region of the parameter  
 2440 space are seen for both signal regions compared to [133].

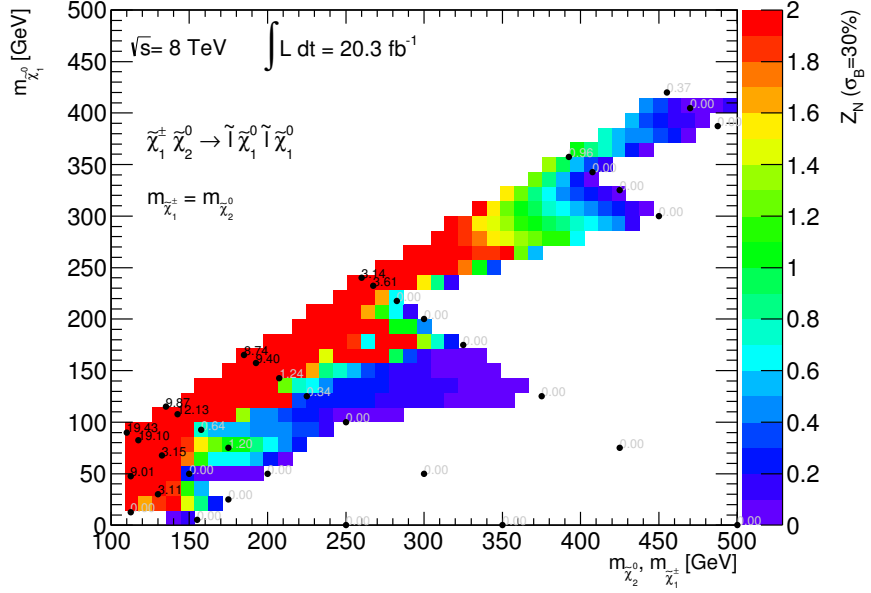


Figure 6.19: Combined expected significance for  $\tilde{\chi}_1^\pm \tilde{\chi}_2^0$  production via  $\tilde{\ell}$  in SR3 $\ell$ -1a and SR3 $\ell$ -1b. The overall values for the total systematic uncertainty are shown on the z-axis for each bin in SR3 $\ell$ -1.

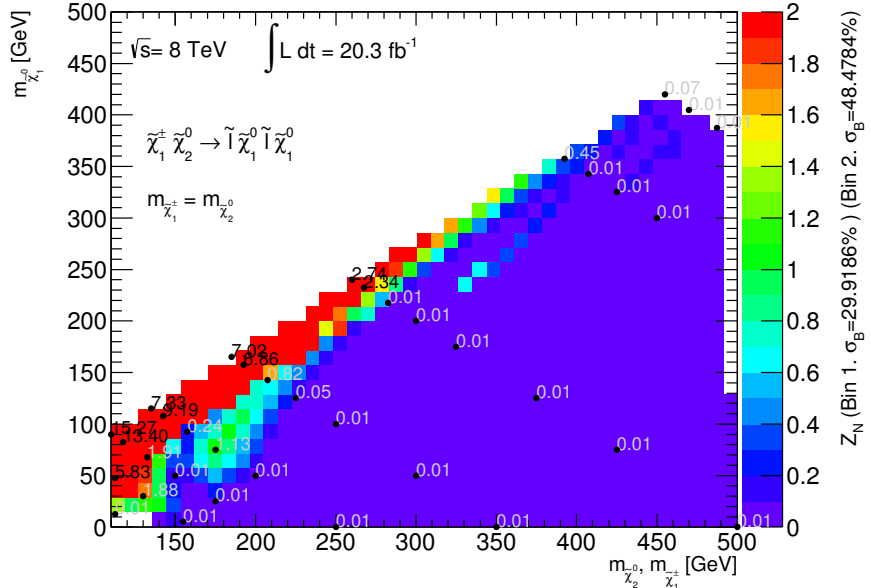
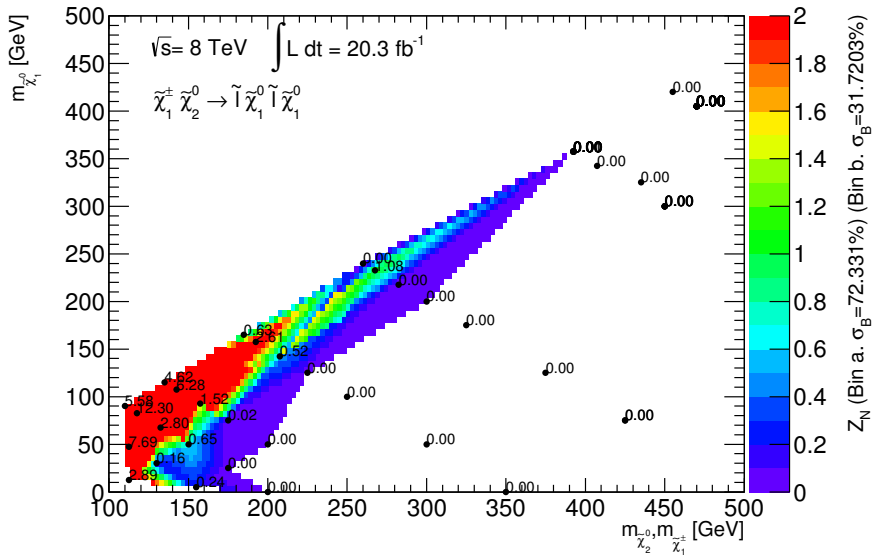
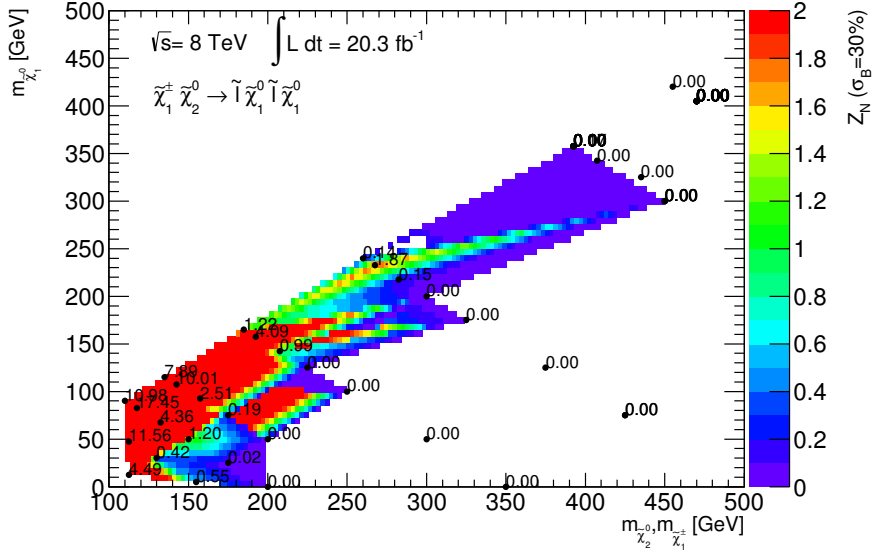


Figure 6.20: Combined expected significance for  $\tilde{\chi}_1^\pm \tilde{\chi}_2^0$  production via  $\tilde{\ell}$  in SR3 $\ell$ -1a and SR3 $\ell$ -1b. The overall values for the total systematic uncertainty are shown on the z-axis for each bin in SR3 $\ell$ -1.



<sup>2441</sup> **6.4.5.2  $\tilde{\chi}_1^\pm \tilde{\chi}_2^0$  via WZ**

<sup>2442</sup> The significance  $Z_N$  was calculated for the simplified model,  $\tilde{\chi}_1^\pm \tilde{\chi}_2^0$  decay via intermediate  
<sup>2443</sup> SM gauge bosons with the soft lepton and ISR signal regions. Starting with the ISR signal  
<sup>2444</sup> regions, for the MC-based only estimate  $\tilde{\chi}_1^\pm \tilde{\chi}_2^0$  masses can be excluded up to 150 GeV in  
<sup>2445</sup> the compressed region with  $m_{\tilde{\chi}_1^0}$  of 125 GeV. For the MC and data driven matrix method  
<sup>2446</sup> estimate only one point in the compressed region is excluded with  $\tilde{\chi}_1^\pm \tilde{\chi}_2^0$  masses up to 100  
<sup>2447</sup> GeV and a  $\tilde{\chi}_1^0$  mass of 75 GeV. For the soft lepton regions, considering the MC-based  
<sup>2448</sup> only estimate  $\tilde{\chi}_1^\pm \tilde{\chi}_2^0$  masses can be excluded up to 100 GeV with a  $\tilde{\chi}_1^0$  mass of 75 GeV.  
<sup>2449</sup> Considering the MC and data driven matrix method estimate no points in the compressed  
<sup>2450</sup> region are excluded. No significant improvement to the compressed region is observed for  
<sup>2451</sup> this simplified model, primarily due to the lower production cross sections compared to  
<sup>2452</sup> the via  $\tilde{\ell}_L$  model.

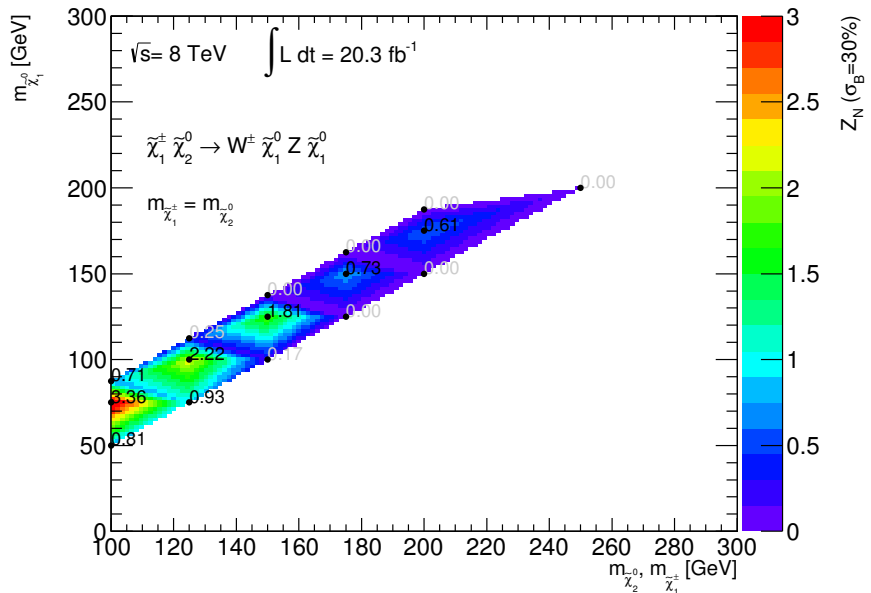


Figure 6.23: Combined expected significance for  $\tilde{\chi}_1^\pm \tilde{\chi}_2^0$  production via  $WZ$  in SR3 $\ell$ -1a and SR3 $\ell$ -1b. The overall values for the total systematic uncertainty are shown on the z-axis for each bin in SR3 $\ell$ -1.

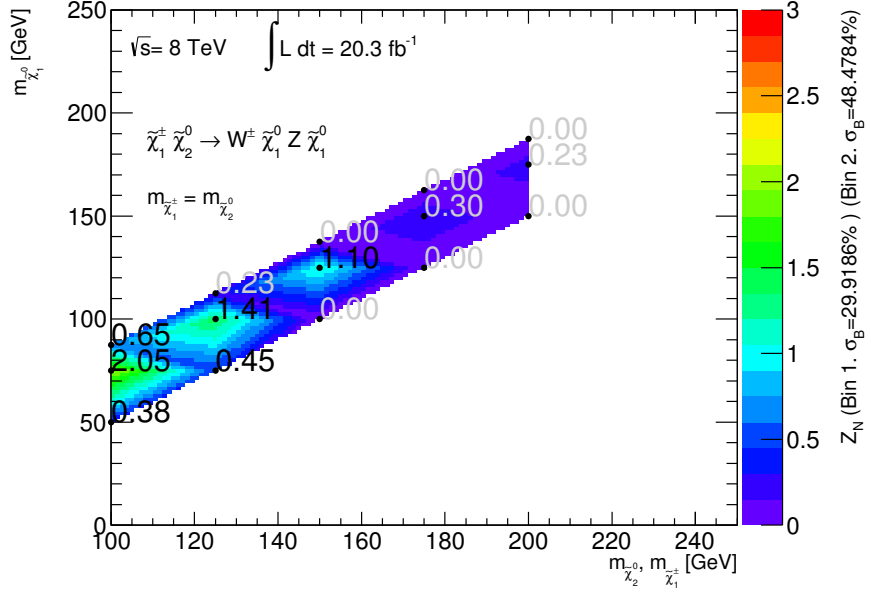


Figure 6.24: Combined expected significance for  $\tilde{\chi}_1^\pm \tilde{\chi}_2^0$  production via  $WZ$  in SR3 $\ell$ -1a and SR3 $\ell$ -1b. The overall values for the total systematic uncertainty are shown on the z-axis for each bin in SR3 $\ell$ -1.

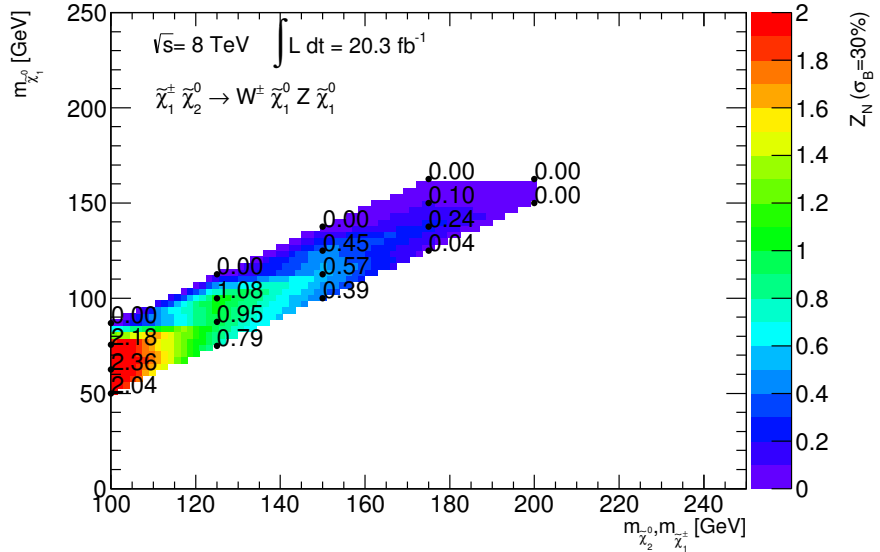


Figure 6.25: Combined expected significance for  $\tilde{\chi}_1^\pm \tilde{\chi}_2^0$  production via  $WZ$  in SR3 $\ell$ -0a and SR3 $\ell$ -0b. The overall values for the total systematic uncertainty are shown on the z-axis for each bin in SR3 $\ell$ -0 (Produced by another analyser, taken from [137]).

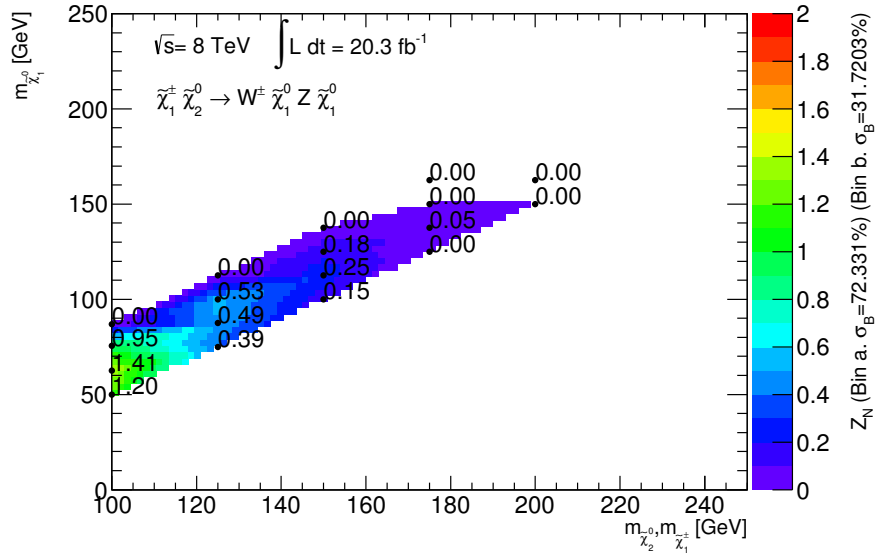


Figure 6.26: Combined expected significance for  $\tilde{\chi}_1^\pm \tilde{\chi}_2^0$  production via  $WZ$  in SR3 $\ell$ -0a and SR3 $\ell$ -0b. The overall values for the total systematic uncertainty are shown on the z-axis for each bin in SR3 $\ell$ -0 (Produced by another analyser, taken from [137]).

## 2453 6.5 Standard Model Background Estimation

### 2454 6.5.1 Standard Model Background Model Overview

2455 There are SM processes that can mimic the SUSY signature of three leptons and missing  
 2456 transverse momentum. These processes are classified into *irreducible backgrounds*, i.e.  
 2457 processes leading to events with three real leptons and *reducible backgrounds*, i.e. processes  
 2458 leading to events with at least one fake lepton. Here real lepton refers to a prompt -  
 2459 meaning originating from a primary vertex - genuinely isolated lepton and a fake lepton  
 2460 is a non-prompt or non-isolated lepton. The fake lepton object can arise from several  
 2461 sources:

- 2462     • Mis-identification of light flavour jets
- 2463     • Real but non-prompt leptons originating from semi-leptonic decays of heavy flavour  
     2464        decays ( $b$ - and  $c$ -quarks)
- 2465     • Real electrons produced from Bremsstrahlung photon conversions

2466 In addition to the identification of real, prompt leptons, there are processes that can  
 2467 mimic the  $E_T^{miss}$  signature due to mis-measurement of the momentum of a lepton or jet.

2468 This results in a large imbalance of momentum in the calculation for  $E_T^{miss}$  as shown in  
 2469 Equation 4.6.

The event selection outlined in Section 6.3.2 and Table 6.2 reduce the contributions from these background processes effectively, but not completely. Therefore the backgrounds need to be understood and estimated as accurately as possible in order to determine the compatibility of the observed data results with Standard Model predictions. In order to construct an accurate and precise background estimate, a dedicated approach is assigned to each category of background. The irreducible processes are modelled with MC simulation. The reducible backgrounds are difficult to model with MC simulation, and so a data-driven method, which extrapolates the background estimate from control regions in the data to the signal regions is utilised. The list below provides an overview of all source of backgrounds considered in this analysis:

• Irreducible background:

- 3 real leptons:  $WZ/\gamma^*$ ,  $ZZ/\gamma^*$ ,  $t\bar{t} + Z/W/WW$ , where the gauge boson can be off-shell;

• Reducible background:

- 2 real and 1 fake lepton:  $t\bar{t}$ , single top ( $Wt$ ),  $WW$ ,  $Z/\gamma^*$ , accompanied by a heavy flavour jet, or a light flavour jet or a conversion
- 1 real lepton and 2 fake leptons: single top ( $s$ -channel,  $t$ -channel),  $W$  accompanied by two fake leptons (from heavy flavour, light flavour, conversion)

There are some background processes estimated using MC predictions, which are then used for background composition studies and for comparing with results obtained with the data driven method. For example, the measurement of the weighted average efficiencies for the matrix method (Section 6.5.3) uses MC samples to model the fake lepton backgrounds.

### 6.5.2 MC Background Estimation

MC background estimation is vital for this analysis and is used in three distinct ways. Firstly to estimate the backgrounds from processes that give three prompt leptons in the final state. Secondly, they are used in the matrix method to extract the efficiencies of real and fake leptons. Lastly, they are used in the simulation-based optimisation of signal regions as discussed in Section 6.4. Therefore it is important that the samples used are well understood and describe ATLAS data as accurately as possible.

There are discrepancies that arise in the simulation of ATLAS data. Some are due to the lack of knowledge regarding the exact run conditions when the samples were simulated, for example the amount of pileup. Others discrepancies are corrected using data due to imperfect ATLAS detector simulation, for example reconstruction efficiencies. Corrections

2503 for these effects are derived from data-driven measurements and applied to the MC samples  
 2504 to improve their modelling of the data. The corrections applied to the MC is detailed  
 2505 below:

- 2506     • Pileup is simulated by overlaying soft QCD interactions over SM events. The distribution  
           2507 in the number of pile up interactions in the MC is not an exact match to that found in data. This distribution in the MC is fixed before all the data is collected, consequently, reweighting is applied to the MC events to ensure the distributions are  
           2509 the same.
- 2511     • Scale factors are applied to account for differences in the reconstruction and identification efficiencies between MC and data. The scale factors are measured by the  
           2512 ATLAS Egamma performance group in  $Z \rightarrow ee$  events with a tag-and-probe method  
           2513 and applied to events with electrons to correct the MC event weight as detailed in  
           2515 [87].
- 2516     • Scale factors are applied to account for the differences in muon reconstruction efficiency  
           2517 between MC and data. The scale factors are provided by the ATLAS Muon performance group, which are measured in  $Z \rightarrow \mu\mu$  and  $J/\psi \rightarrow \mu\mu$  events as detailed  
           2519 in [89]. The scale factors are then applied to events with muons to correct the MC  
           2520 event weight.
- 2521     • The muon  $p_T$  resolution is not in complete agreement between MC and data, therefore  
           2522 smearing is applied to the muon  $p_T$  in the MC events is done to give a closer  
           2523 agreement.
- 2524     • Tau scale factors are applied to the MC to correct for the tau BDT efficiency. These  
           2525 are provided by the ATLAS Tau performance group.
- 2526     • Scale factors for  $b$ -tagging algorithms described in Sections 4.4.7 are used to correct  
           2527 for the  $b$ -tagging efficiency differences between MC and data. These scale factors  
           2528 take into account both the efficiency to tag  $b$ -jets as well as the mis-tag efficiency  
           2529 for non- $b$ -jets.

### 2530 6.5.3 Data Driven Background Estimation: The Matrix Method

2531 The matrix method is a technique used for estimating the fake lepton background by  
 2532 exploiting the object characteristics between real and fake leptons on a statistical basis.  
 2533 Leptons are classified as “loose” (L) or “tight” (T) leptons according to the isolation and  
 2534 object reconstruction quality requirements. In this analysis, loose leptons are baseline  
 2535 leptons and tight leptons are signal leptons. The method assumes that the number of

events with varying loose and tight leptons in an event can be expressed as a linear combination of the numbers of events with real and fake leptons in terms of the probabilities for real and fake leptons to pass the tight selection. For example, in the dilepton final state, the number of events with two tight leptons  $N_{TT}$  can be expressed as:

$$N_{TT} = \epsilon_1 \epsilon_2 \times N_{RR} + \epsilon f_2 \times N_{RF} + f_1 \epsilon_2 \times N_{FR} + f_1 f_2 \times N_{FF} \quad (6.2)$$

where  $\epsilon$  is the probability that a real loose lepton is identified as a tight lepton,  $f$  is the probability that a loose fake lepton is mis-identified as a tight lepton,  $N_{RR}$  is the number of events with two real leptons,  $N_{RF} + N_{FR}$  is the number of events with one real and one fake lepton, and  $N_{FF}$  is the number of events with two fake leptons. If the values of  $\epsilon$  and  $f$  are known, the matrix can be inverted and the number of events with one or two fake leptons ( $N_{FR}, N_{RF}, N_{FF}$ ) can be determined. The inversion of the matrix results in factors proportional to  $(\epsilon - f)^{-1}$ , so a good separation between the values for the fake rate and real efficiencies is required or the numerical results will be unstable.

For the three lepton final state, the matrix would be an  $8 \times 8$  matrix to account for all possible combinations of real and fake leptons. For processes that produce fake leptons in a three lepton selection, the highest- $p_T$  lepton will be real for the majority of the time ( $> 95\%$  of events) [133]. This is due to the fact that light lepton fakes tend to have a softer  $p_T$  spectrum than their real lepton counterparts. The feature is accounted for by ignoring the leading light lepton in the three-lepton matrix method. This simplifies the method by reducing the dimensionality of the  $8 \times 8$  matrix to  $4 \times 4$ :

$$\begin{pmatrix} N_{TT} \\ N_{TL'} \\ N_{L'T} \\ N_{L'L'} \end{pmatrix} = \begin{pmatrix} \epsilon_1 \epsilon_2 & \epsilon f_2 & f_1 \epsilon_2 & f_1 f_2 \\ \epsilon_1 (1 - \epsilon_2) & \epsilon_1 (1 - f_2) & f_1 (1 - \epsilon_2) & f_1 (1 - f_2) \\ (1 - \epsilon_1) \epsilon_2 & (1 - \epsilon_1) f_2 & (1 - f_1) \epsilon_2 & (1 - f_1) f_2 \\ (1 - \epsilon_1) (1 - \epsilon_2) & (1 - \epsilon_1) (1 - f_2) & (1 - f_1) (1 - \epsilon_2) & (1 - f_1) (1 - f_2) \end{pmatrix} \cdot \begin{pmatrix} N_{RR} \\ N_{RF} \\ N_{FR} \\ N_{FF} \end{pmatrix}, \quad (6.3)$$

where on the left hand side,  $N_{TT}$ ,  $N_{TL'}$ ,  $N_{L'T}$  and  $N_{L'L'}$  denote the number of events with one tight lepton and two additional leptons; the two indices indicate if the second- and third-leading lepton in  $p_T$  is a tight lepton or a loose lepton that fails tight requirements ( $L'$ ).

Inverting Equation 6.3 gives the composition of real and fake leptons at the loose

2560 selection level. The total number of events with fake leptons is then given by

$$\begin{aligned}
 N_{RF} + N_{FR} + N_{FF} = & \frac{1}{(\epsilon_1 - f_1)(\epsilon_2 - f_2)} [(\epsilon_1\epsilon_2 - \epsilon_1f_2 - f_1\epsilon_2 + f_1 + f_2 - 1)N_{TT} \\
 & + (\epsilon_1\epsilon_2 - \epsilon_1f_2 - f_1\epsilon_2 + f_2)N_{TL} \quad (6.4) \\
 & + (\epsilon_1\epsilon_2 - \epsilon_1f_2 - f_1\epsilon_2 + f_1)N_{LT} + (\epsilon_1\epsilon_2 - \epsilon_1f_2 - f_1\epsilon_2)N_{LL}].
 \end{aligned}$$

2561 The analysis uses signal leptons, therefore the final step involves extrapolating the  
2562 fake lepton estimate to the tight-tight selection:

$$N_{fake \rightarrow TT} = \epsilon_1 f_2 \times N_{RF} + f_1 \epsilon_2 \times N_{FR} + f_1 f_2 \times N_{FF}. \quad (6.5)$$

2563 Note that in the expression for  $N_{fake \rightarrow TT}$  the real-real component,  $N_{RR}$  is neglected  
2564 because it does not contribute to the fake lepton estimate. From Equation 6.5, the matrix  
2565 method requires the input of the real efficiencies and fake rates for each selected lepton.  
2566 To complete the method, the variables which comprise Equation 6.3 need to be measured.  
2567 For each signal region, the number of events with one tight lepton and two additional  
2568 leptons (the left hand side of Equation 6.3) is obtained by applying all of the signal region  
2569 cuts but loose selected leptons are used instead of signal leptons. The leading lepton in  $p_T$   
2570 is required to be tight since it does not participate in the method. Each event consequently  
2571 belongs to one of the TT, TL, LT or LL categories. The matrix equation is then used for  
2572 every event to get a “fake weight”. The sum of the fake weights for each event gives the  
2573 fake lepton estimate for the corresponding signal region.

### 2574 6.5.3.1 Weighted Average Fake Rates

2575 Measuring the fake rates for the matrix method presents several challenges. The fake rate  
2576 for a given lepton  $\ell = \mu, e$  (labelled  $f$  in Equation 6.3) depends on the fake candidate  
2577 (heavy flavour, light flavour and conversion) and on the originating process. For example,  
2578 the fake rate of leptons from heavy flavour jets in top decays is smaller than the rate from  
2579 heavy flavour jets from WZ production due to the harder  $b$ -quark spectrum in top decays.  
2580 Consequently, the fake rates measured in a dedicated control region in data will not be  
2581 directly applicable to another region where the fake type composition and originating  
2582 processes are significantly different. In this analysis, the approach is to obtain the fake  
2583 rate of each type from all MC simulated samples - properly weighted for luminosity -  
2584 the rates are then corrected with type-dependent scale factors to account for the possible

2585 differences between data and simulation.

2586 A weighted average fake rate to be used in the region  $\text{XR} = \text{SR}$ ,  $\text{CR}$  (where  $\text{SR}$  and  
2587  $\text{CR}$  stand for generic signal/control region) is therefore defined as:

$$f_{\text{XR}}^{\ell} = \sum_{i,j} (sf^i \times R_{\text{XR}}^{ij} \times f^{ij}), \quad (6.6)$$

2588 where  $i$  indicates the fake type: light flavour (LF), heavy flavour (HF), or conversion  
2589 (CO);  $j$  indicates the process category the fake originates: Top (T) or Gauge Boson (V);  
2590 the dependence on  $p_T$  and  $|\eta|$  for electrons and on  $p_T$  for muons is implied for all terms  
2591 as described below:

2592 **Scale Factor**  $sf^i$  is the fake rate scale factor for the type  $i$ ; it is assumed to be inde-  
2593 pendent of the process category  $j$  and of the region  $\text{XR}$ . No significant dependences on  $p_T$   
2594 and  $\eta$  are observed.

2595 **Fake Fraction**  $R_{\text{XR}}^{ij}$  is the fraction of type  $i$  originating from process category  $j$  in  
2596 the region  $\text{XR}$ ; it is measured as the ratio of fake candidates of type  $i$  originating from  
2597 the process category  $j$  with respect to the total number of all fake candidates from all  
2598 processes. The fractions are obtained in each region  $\text{XR}$  summing over all relevant MC  
2599 simulated samples properly weighted for their luminosity.

2600 **Fake Rate**  $f^{ij}$  is the fake rate for the type  $i$  originating from the process category  $j$ ;  
2601 it is measured as the ratio of the number of signal leptons over the number of baseline  
2602 leptons for a given type and a given process. To be consistent with the MM, the rates  
2603 are measured on the next-to-leading and next-to-next-to-leading leptons in events where  
2604 the leading lepton is tight. Furthermore, the events must pass the quality cuts and the  
2605 trigger requirements. The fake rates are parameterised in  $p_T$  for muons and  $p_T$  and  $\eta$   
2606 for electrons. A systematic uncertainty is assigned to cover for potential dependence on  
2607  $E_T^{\text{miss}}$ .

### 2608 6.5.3.2 Fake Rates

2609 The fake rates and fake fractions are measured in the three lepton inclusive region with  
2610 the truth information of all expected background MC samples. The fake origin fraction is  
2611 measured in each region with the baseline leptons.

2612 **6.5.3.3 Scale Factors**

2613 The MC-based estimated fake rates require validation with data. To do this, control  
2614 regions are defined to validate the MC truth fake rates and extract a data-MC scale factor  
2615 for each fake type. Each control region is designed to enhance the purity of the respective  
2616 fake sources: real efficiency (RE), conversion (CO), heavy flavour (HF) and light flavour  
2617 (LF). Due to the difficulty in defining a region which has good enough purity for light  
2618 flavour fakes with three-lepton events, the light flavour fakes scale factor is assumed to be  
2619  $1.00 \pm 0.10$ . The scale factor measurements are outlined in the following paragraphs for  
2620 the remaining fake types.

2621 **Real Lepton Identification Efficiency** The measurement is carried out using the tag-  
2622 and-probe method with  $Z \rightarrow ee$  events (as outlined in Section 5.2.1). The tag-and-probe  
2623 selection is applied as follows:

- 2624 • exactly two SFOS leptons, passing the baseline selection
- 2625 • at least one lepton should pass the trigger strategy outlined in Table 6.1 and the  
2626 signal lepton object selection requirements
- 2627 •  $m_{\ell\ell}$  should be within 10 GeV of the on-shell Z-boson mass of 91.2 GeV

2628 These cuts are chosen to target events with electrons originating from on-shell Z-boson  
2629 decays, which are “standard candle” events used in the tag-and-probe selection.

2630 There was no significant dependence on  $p_T$ ,  $\eta$  and the number of vertices observed for  
2631 the real lepton efficiency scale factor, therefore the final result is obtained without binning:  
2632  $SF_e^{RE} = 1.00 \pm 0.01$ ,  $SF_\mu^{RE} = 0.99 \pm 0.01$ .

2633 **Fake Rate Scale Factor for Electrons from Conversions** The conversion fakes  
2634 consist of misidentified leptons from photon radiation, which are mostly real leptons. For  
2635 muons, this fake contribution is negligible. Therefore, electrons are the sole focus for this  
2636 measurement. The conversion control region is set to enhance the  $Z/\gamma^* \rightarrow \mu\mu$  process  
2637 with one radiated photon from one of the muons, as follows:

- 2638 • an inclusive OR of the single & dimuon triggers, with at least one signal muon  
2639 matching a trigger object and above the appropriate  $p_T$  threshold in data;
- 2640 • exactly two opposite sign signal muons with  $m_{\mu\mu} > 40$  GeV, to ensure the muons  
2641 have sizeable  $p_T$  for straight-forward identification;
- 2642 • exactly one baseline electron, which is selected as the probe;
- 2643 • The invariant mass of the three leptons in the event composed of  $\mu,\mu$  and  $e$  must lie

2644       within 10 GeV of the on-shell Z mass, 91.2 GeV, such that the  $\mu\mu e$  invariant mass  
 2645       is consistent with a Z boson.

- 2646     •  $b$ -jet veto (MV1 @ 70% rejecting  $t\bar{t}$ )
- 2647     •  $E_T^{miss} < 40$  GeV (rejecting WZ)

2648       There is no significant dependence on  $p_T$ ,  $|\eta|$  or number of good vertices observed,  
 2649       therefore the scale factor obtained without binning:  $SF_e^{CO} = 1.41 \pm 0.06$ .

2650       This SF is particularly larger than the other scale factors due to underestimation of  
 2651       the rate of electrons from conversions in MC at  $p_T$  values above 50 GeV.

2652       **Fake Rate Scale Factor for Leptons from Heavy Flavour** If a  $b$ -quark decays  
 2653       leptonically and the resulting lepton is identified as a signal lepton, then heavy flavour  
 2654       jets can pass into the final selection as a fake contribution. The corresponding fake rate  
 2655       is measured in control regions enhanced for the  $b\bar{b}$  or  $c\bar{c}$  processes using a tag-and-probe  
 2656       method with a  $b\bar{b}$  and  $c\bar{c}$  selection. A requirement of  $p_T > 20$  GeV is applied to all jets in  
 2657       all regions. The heavy flavour (HF) control region is defined as follows:

- 2658     • satisfy the standard event quality criteria;
- 2659     • contain exactly two baseline leptons;
- 2660     • the event contains exactly one  $b$ -jet
- 2661     • a tagged muon must have a  $p_T > 20$  GeV being the one that fired the EF\_mu18\_tight  
   2662       leg of the EF\_mu18\_tight\_mu8\_EFFS trigger;
- 2663     • the tagged muon is overlapped with a  $b$ -tagged jet within  $\Delta R < 0.4$
- 2664     • the probe lepton is separated from any jets by  $\Delta R > 0.4$
- 2665     •  $E_T^{miss} < 60$  GeV to suppress the background to non heavy flavour leptons.
- 2666     • The probe lepton  $m_T < 50$  GeV to suppress W events

2667       Despite the fact that tight selections are used, other backgrounds sources prove difficult  
 2668       to suppress due to the low  $p_T$  requirement of this analysis. Therefore, all non-HF (i.e.  
 2669       light flavour, conversion, real) sources are subtracted from the data and MC fake rate  
 2670       estimates using the MC-truth information in this control region. With no scale factor  
 2671       dependency on the parameters,  $p_T$ ,  $|\eta|$  and number of good vertices, the central value of  
 2672       the scale factor is calculated without binning from the  $p_T$  distributions. The scale factors  
 2673       for heavy flavour fake rates are found to be:  $SF_e^{HF} = 0.876 \pm 0.085$ ;  $SF_\mu^{HF} = 0.878 \pm 0.062$

## <sup>2674</sup> 6.6 Background Model Validation

### <sup>2675</sup> 6.6.1 Validation Regions

<sup>2676</sup> To validate the background modelling, the MC estimates for irreducible backgrounds and  
<sup>2677</sup> the data-driven estimates for the reducible backgrounds estimated in VRs are compared  
<sup>2678</sup> to the observed data. Low- $E_T^{miss}$  validation regions (“a” regions) are defined that are  $WZ$ ,  
<sup>2679</sup>  $Z$ ,  $J/\psi$ , and/or  $\Upsilon$  rich, and high- $E_T^{miss} + b$ -jet validation regions (“b” region) that are  $t\bar{t}$   
<sup>2680</sup> rich. Two sets of validation regions are defined to validate the background modelling with  
<sup>2681</sup> or without the presence of an ISR jet. VR3 $\ell$ -0 vetoes the ISR jet and VR3 $\ell$ -1 requests  
<sup>2682</sup> the ISR jet. The explicit definitions are given in Table 6.3. The observed data counts and  
<sup>2683</sup> SM expectations are in good agreement within statistical and systematic uncertainties as  
<sup>2684</sup> shown in Table 6.4 and Figures 6.27 and 6.28. This indicates that the reducible background  
<sup>2685</sup> is well described by the matrix method and the irreducible background is well described by  
<sup>2686</sup> the MC. The following sections show the most interesting kinematic distributions relevant  
<sup>2687</sup> to each validation region.

Table 6.3: The selection requirements for the three-lepton validation regions.

Common				
$\ell$ flavor/sign	$\ell^\pm \ell^\mp \ell, \ell^\pm \ell^\mp \ell'$			
$m_{SFOS}^{\min}$	> 4 GeV			
$m_{SFOS}$	veto 8.4–10.4 GeV			
SR	VR3 $\ell$ -0a	VR3 $\ell$ -0b	VR3 $\ell$ -1a	VR3 $\ell$ -1b
Central jets	no jets $p_T > 50$ GeV		$\geq 1$ jet $p_T > 50$ GeV	
$N_{b-jets}$	0	1	0	1
$E_T^{miss}$	< 30 GeV	> 30 GeV	< 50 GeV	> 50 GeV
$Z$ boson	veto	–	veto	veto
$p_T^{\text{lep} 1}$	< 30 GeV	–	–	–
Target Process				
Irreducible	$WZ$	$WZ$	$WZ$	$WZ$
Reducible	$Z+jets, \Upsilon$	$t\bar{t}$	$Z+jets$	$t\bar{t}$

Table 6.4: Estimated and observed yields in the three-lepton validation regions. The uncertainties shown include both statistical and systematic components. The “Others” background category includes  $t\bar{t}V$ ,  $VVV$  and SM Higgs boson production.

	VR3 $\ell$ -0a	VR3 $\ell$ -0b	VR3 $\ell$ -1a	VR3 $\ell$ -1b
$WZ$	$108 \pm 20$	$35 \pm 7$	$36 \pm 7$	$9.7^{+2.0}_{-2.2}$
$ZZ$	$63 \pm 11$	$5.9 \pm 1.3$	$5.2 \pm 1.1$	$0.33^{+0.08}_{-0.07}$
Reducible	$990^{+300}_{-270}$	$159^{+40}_{-35}$	$56 \pm 16$	$102^{+23}_{-19}$
Others	$1.0 \pm 0.8$	$4.8 \pm 1.7$	$1.5 \pm 0.6$	$9.9^{+3.4}_{-3.5}$
Total SM	$1160^{+300}_{-280}$	$200 \pm 40$	$99 \pm 17$	$122^{+24}_{-20}$
Data	1247	212	95	93

### 2688 6.6.1.1 VR3 $\ell$ -1 Regions

2689 Six kinematic distributions in validation region VR3 $\ell$ -1a with three light leptons and at  
2690 least one ISR jet are shown in Figure 6.27: lepton<sup>1,2,3</sup>  $p_T$ ,  $m_{\text{SFOS}}^{\min}$ , leading jet  $p_T$  and  
2691  $\Delta\phi(E_T^{\text{miss}}, 3\ell)$ . These variables are used to define the ISR signal regions therefore must  
2692 be correctly modelled. Two benchmark signal points are used with  $\Delta m_{\tilde{\chi}_1^\pm - \tilde{\chi}_1^0} = 12.5$  and  
2693 25 GeV. The shapes of the distributions are seen to agree well with data. Six kinematic  
2694 distributions in validation region VR3 $\ell$ -1b with three light leptons and at least one ISR  
2695 jet are shown in Figure 6.28: lepton<sup>1,2,3</sup>  $p_T$ ,  $E_T^{\text{miss}}$ ,  $m_T$ ,  $M_{\ell\ell\ell}$  and leading jet  $p_T$ . These  
2696 variables are used to define the ISR signal regions therefore must be correctly modelled.  
2697 Two benchmark signal points are used with  $\Delta m_{\tilde{\chi}_1^\pm - \tilde{\chi}_1^0} = 12.5$  and 25 GeV. The shapes of  
2698 the distributions are seen to agree well with data.

### 2699 6.6.1.2 VR3 $\ell$ -0 Regions

2700 Four kinematic distributions in validation region VR3 $\ell$ -0a with three light leptons and  
2701 an ISR jet veto are shown in Figures 6.29:  $m_{\text{SFOS}}^{\min}$ ,  $m_{\ell\ell\ell}$ ,  $m_T$  and jet multiplicity. These  
2702 variables are used to define the soft lepton signal regions therefore must be correctly  
2703 modelled. One benchmark signal points is used with  $\Delta m_{\tilde{\chi}_1^\pm - \tilde{\chi}_1^0} = 25$  GeV. The shapes  
2704 of the distributions are seen to agree well with data. Four kinematic distributions in  
2705 validation region VR3 $\ell$ -0a with three light leptons and an ISR jet veto are shown in  
2706 Figures 6.29: lepton<sup>1,2,3</sup>  $p_T$   $E_T^{\text{miss}}$ ,  $m_T$  and jet multiplicity. These variables are used to  
2707 define the soft lepton signal regions therefore must be correctly modelled. One benchmark  
2708 signal points is used with  $\Delta m_{\tilde{\chi}_1^\pm - \tilde{\chi}_1^0} = 25$  GeV. The shapes of the distributions are seen  
2709 to agree well with data.

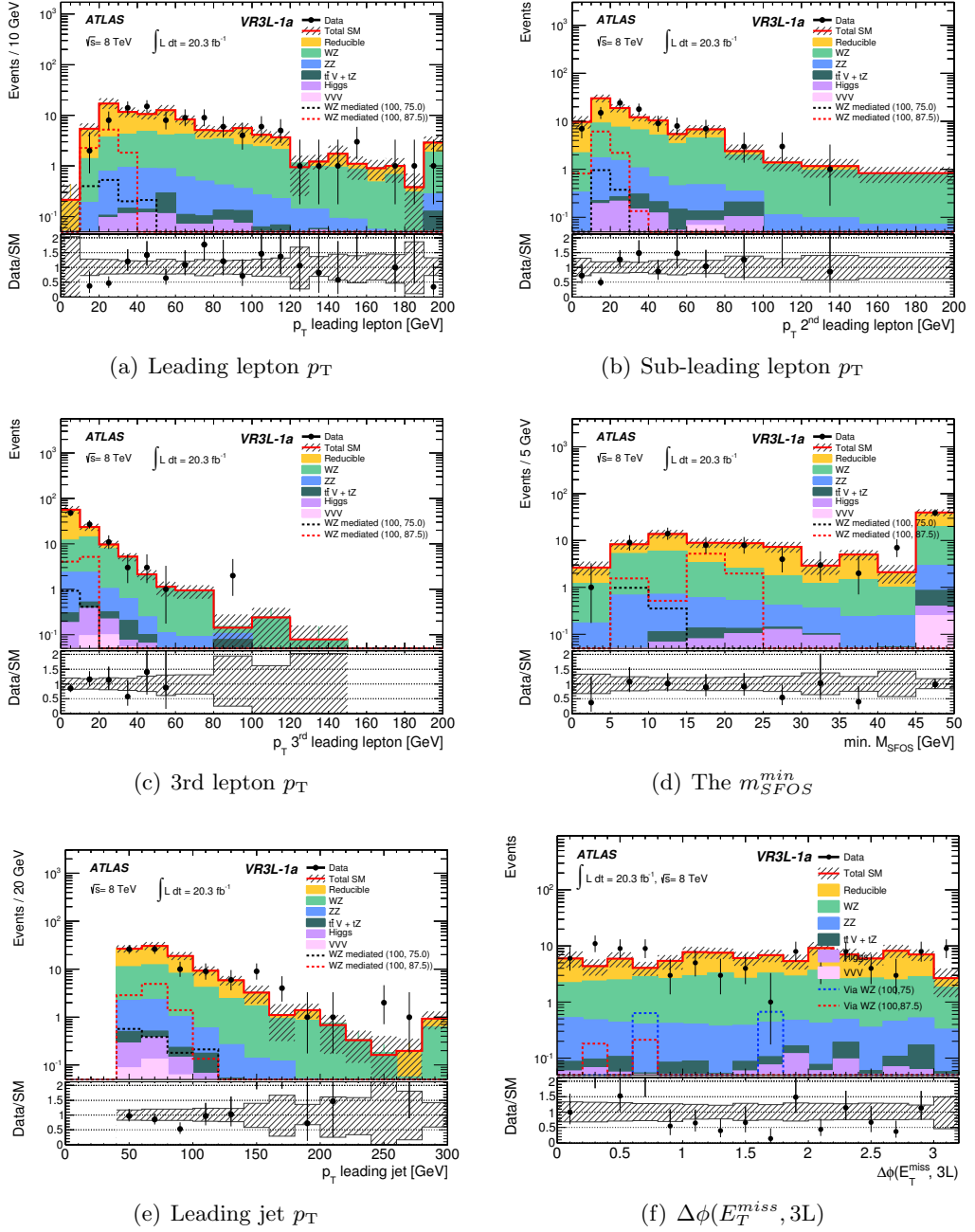


Figure 6.27: Kinematic distributions in VR3L-1a. The uncertainties are statistical and systematic.

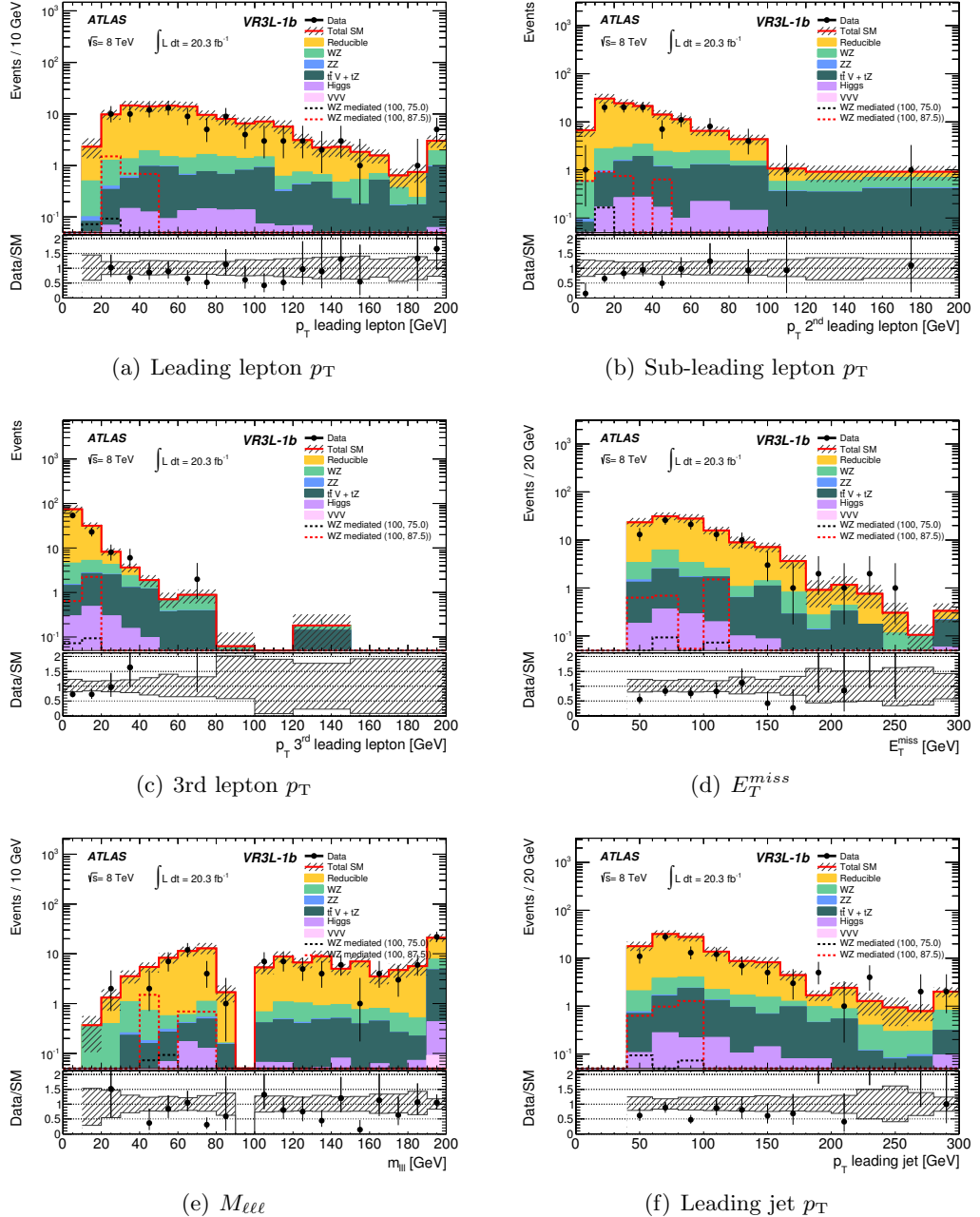


Figure 6.28: Kinematic distributions in VR3 $\ell$ -1b. The uncertainties are statistical and systematic.

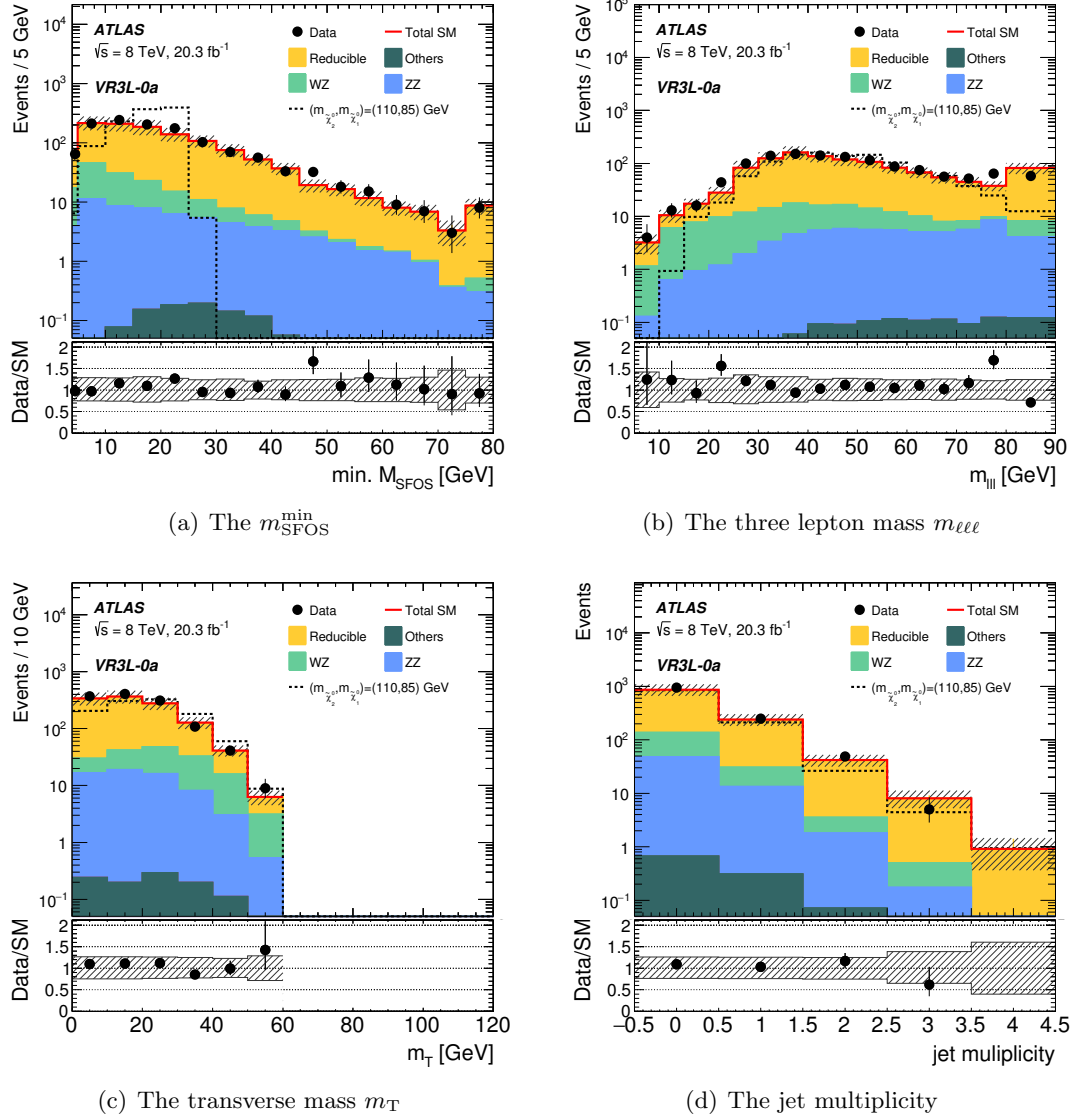


Figure 6.29: Kinematic distributions in VR3 $\ell$ -0a (Produced by another analyser, taken from [137]).

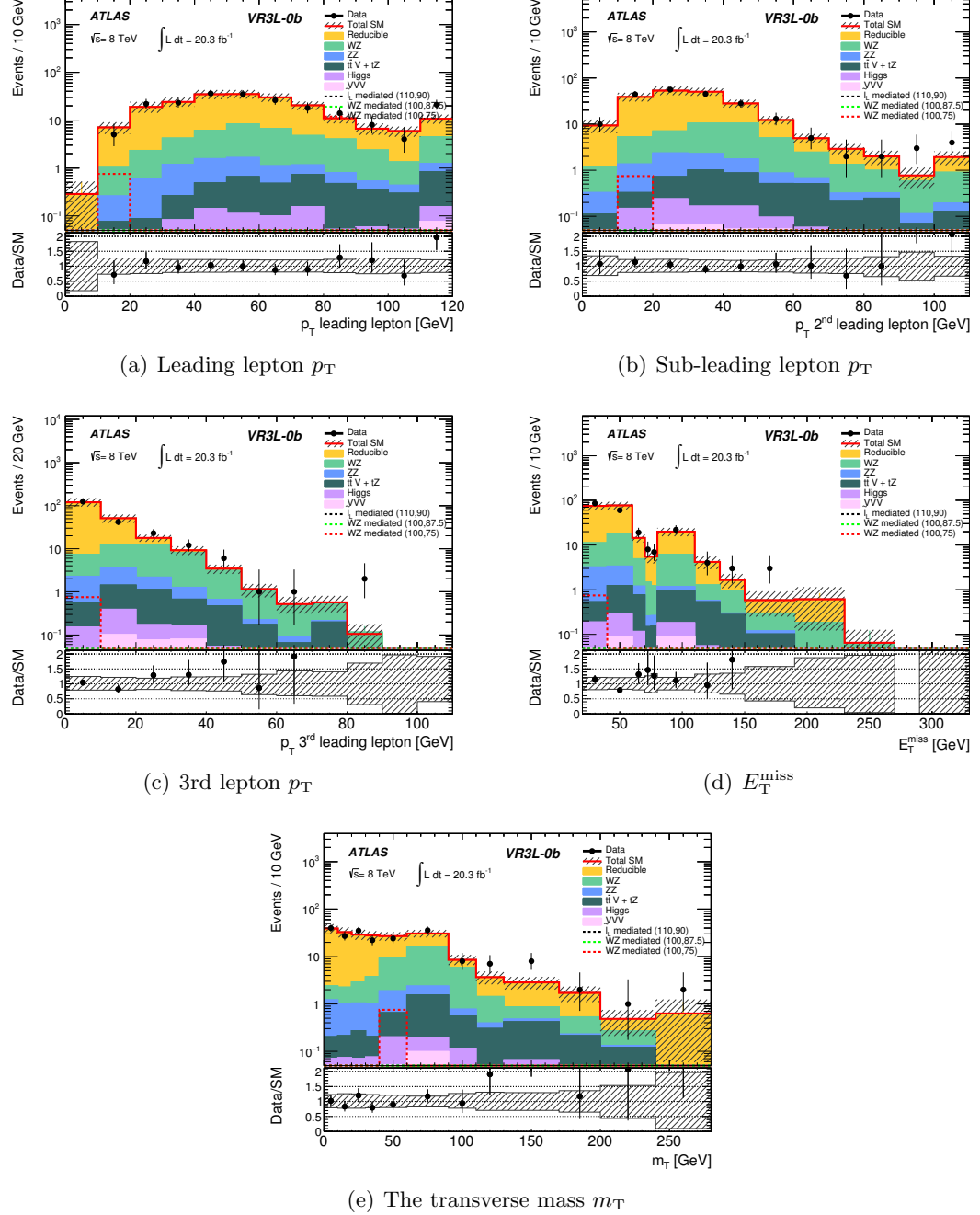


Figure 6.30: Kinematic distributions in VR3L-0b (Produced by another analyser, taken from [137]).

## 2710 6.7 Systematic Uncertainties

2711 Several sources of uncertainty arise in the analysis, due to the MC background estimate  
2712 and data driven fake estimate.

### 2713 6.7.1 MC Statistics

2714 Since MC statistics is limited, it is a source of systematic uncertainty. This uncertainty is  
2715 one of the dominating uncertainties for the signal regions as they have stringent cuts that  
2716 limit the MC events to the order of 5 events. It is treated as uncorrelated between regions  
2717 and MC samples.

### 2718 6.7.2 MC Cross Section

2719 Each cross section for a given background process has an uncertainty provided centrally  
2720 by ATLAS, together with the generated MC samples, these are estimated by varying the  
2721 renormalisation and factorisation scales. The cross-section uncertainties for the irreducible  
2722 backgrounds used are 30% for  $t\bar{t}+Z/W/WW$  [138] [114], 50% for  $tZ$ , 5% for  $ZZ$  [139],  
2723 7% for  $WZ$  [139]: these are recommended by ATLAS and found by comparing the results  
2724 of calculations with the MCFM and MC@NLO generators and MSTW and CTEQ PDF  
2725 sets. The uncertainty for triboson production is set to 100%. For the Higgs boson samples,  
2726 a 20% uncertainty is used for VH and vector boson fusion (VBF) production [122], while  
2727 a 100% uncertainty is assigned to  $t\bar{t}H$  and Higgs boson production via gluon fusion [122].

### 2728 6.7.3 PDF

The PDF uncertainties for the SHERPA WZ and ZZ samples were calculated using the PDF4LHC recommendations [140] [141] on the full eigenset of the PDF set CT10 [142]. The PDF set was provided by the CTEQ collaboration. The CTEQ PDF set is based on 26 free parameters and the resulting 90% confidence level upper and lower variations in these parameters form the “error set” for the PDF. The asymmetric positive and negative uncertainties of the PDFs ( $f_a$ ) are computed as

$$\sigma_+[f] = \frac{1}{C_{90}} \sqrt{\sum_{i=1}^{26} (\max[(f_i^+ - f_0), (f_i^- - f_0), 0])^2},$$

$$\sigma_-[f] = \frac{1}{C_{90}} \sqrt{\sum_{i=1}^{26} (\max[(f_0 - f_i^+), (f_0 - f_i^-), 0])^2}.$$

2729 Where  $C_{90} = 1.64485$  is a re-scaling factor to convert the 90% CL variations into  $1\sigma$   
 2730 variations and  $f_0$  is the nominal eigenvector value. The impact of the PDF uncertainties  
 2731 on the acceptance was found to be negligible ( $<3\%$ ).

#### 2732 6.7.4 MC Background Uncertainties

2733 Backgrounds which produce three prompt leptons are modeled by MC simulation and as  
 2734 such are subject to statistical and systematic uncertainties.

#### 2735 6.7.5 Electrons

2736 Two sources of uncertainty arise on the electron energy, the electron energy scale (EES)  
 2737 and the electron energy resolution (EER). EES is the uncertainty arising from any mis-  
 2738 calibration of the electron energy using MC. EER considers the resolution of the ECAL  
 2739 sub-detector. Both uncertainties are calculated using an  $E_T$  and  $\eta$  dependent function to  
 2740 select W and Z events from data.  $J/\Psi$  events are used to estimate these uncertainties  
 2741 for low- $p_T$  electrons [85]. The resulting uncertainties are applied to both the electrons  
 2742 and their associated component in the  $E_T^{miss}$  calculation. The electron scale factor (ESF)  
 2743 accounts for uncertainty in reconstruction and identification efficiency of electrons. This  
 2744 scale factor is also  $E_T$  and  $\eta$  dependent and is calculated by the ATLAS electron working  
 2745 group using W and Z events.

#### 2746 6.7.6 Muons

2747 The muon energy scale (MES) uncertainty is composed of energy scale uncertainties from  
 2748 the inner detector track, known as Muon Inner Detector (MID), and the muon spec-  
 2749 trometer track, known as the Muon Muon Spectrometer (MMS). These are calculated  
 2750 using data events for  $J/\Psi \rightarrow \mu\mu$ ,  $Z \rightarrow \mu\mu$  and  $\Upsilon \rightarrow \mu\mu$  compared to MC [89]. The  
 2751 resulting uncertainties are applied to both muons and their associated component in the  
 2752  $E_T^{miss}$  calculation. The muon scale factor (MSF) accounts for the uncertainty in muon  
 2753 reconstruction, is calculated as a function of muon  $p_T$  [89].

#### 2754 6.7.7 Jets

2755 The Jet Energy Scale (JES) uncertainty is estimated by using a combination of *in situ*  
 2756 techniques exploiting the transverse momentum balance between a jet and a reference  
 2757 object such as a photon or Z boson for  $20 \leq p_T^{\text{jet}} < 1000$  GeV. The uncertainty is applied  
 2758 to jets with  $p_T > 15$  GeV and  $|\eta| < 4.5$  and their corresponding  $E_T^{miss}$  components [143].

the jet energy resolution (JER) uncertainty is estimated by smearing the  $p_T$  of each jet to a Gaussian distribution with unit mean and width, using a resolution dependent on the  $p_T$  and  $\eta$  [144]. The Jet Vertex Fraction as defined in Section 4.4.7 has a uncertainty as a specific cut is applied on this discriminant.

### 6.7.8 Missing Transverse Energy

The pileup-suppressed soft term in the  $E_{x(y)}^{softjets}$  in Equation 4.6 has an associated uncertainty which can be estimated by adjusting the energy scale and the resolution, and using these adjustments to recalculate the total resulting  $E_T^{miss}$ . The uncertainty in the other contributions to the  $E_T^{miss}$  are accounted for by the uncertainties of the objects associated with them as detailed above.

### 6.7.9 B-tagging Efficiency

The  $b$ -tagging algorithm performance was evaluated by the ATLAS flavour-tagging performance group using light and heavy jet samples. The associated uncertainty on the real efficiency and mis-tag rates for the 2011 and 2012 algorithms (JetFitterCombNN and MV1) was then propagated as an overall scale factor.

### 6.7.10 Trigger

An uncertainty of 5% is applied to MC samples to cover differences in efficiency observed for the leptonic triggers between data and the MC trigger simulation.

### 6.7.11 Luminosity

An uncertainty of 2.8% is prescribed for the ATLAS 2012 dataset based on preliminary calibration of the luminosity scale using beam separation scans in 2012 [145].

### 6.7.12 Pile-up

The uncertainty due to the modelling of the pileup in the MC simulation samples is estimated by varying the distribution of the number of interaction per bunch crossing overlaid in the MC samples by  $\pm 10\%$ .

2784 **6.7.13 Signal**

2785 The systematic uncertainties on the SUSY signal processes include theoretical uncertain-  
2786 ties on the calculated NLO cross sections. This includes cross-section predictions using  
2787 different PDF sets and factorisation and renormalisation scales. These theoretical sys-  
2788 tematic uncertainties on all signal processes are evaluated by varying the factorisation  
2789 and re-normalisation scales in PROSPINO and are calculated using the method described  
2790 in [146]. For  $\tilde{\chi}_1^\pm \tilde{\chi}_2^0$  signal simulations that are sensitive to ISR, the impact of the choice of  
2791 renormalisation scales, factorisation scales, the scale for the first emission in the so-called  
2792 MLM matching scale [147] are evaluated by varying these individually between 0.5 and 2  
2793 times the nominal values in MADGRAPH.

2794 **6.7.14 Theoretical Systematic Uncertainties**

2795 Typically to assess the theoretical modelling of the SM processes by MC, two generators  
2796 would be compared in particular regions enriched in the processes being assessed. As  
2797 a consequence of the analysis exploring compressed scenarios, the  $p_T$  thresholds on the  
2798 leptons were lowered from 10 to 7 GeV for electrons and from 10 to 5 GeV for muons,  
2799 also the  $m_{SFOS}$  threshold was lowered from 12 to 4 GeV, meaning only one generator,  
2800 POWHEG, with the correct lepton  $p_T$  filters could be used for the simulation of the  $WZ$   
2801 and  $ZZ$  processes, which are the dominant irreducible backgrounds in all signal regions.  
2802 In order to place an uncertainty on the modelling, the MC distributions were compared  
2803 with the data, to assess the agreement. A conservative uncertainty of 20% was placed  
2804 on the theoretical uncertainty to account for the differences between data and MC. The  
2805 control regions are defined to be enriched in the  $WZ$  and  $ZZ$  processes. The definitions  
2806 are summarised in Sections 6.7.14.1 and 6.7.14.2.

2807 **6.7.14.1 WZ Control Region**

2808 The definition of the  $WZ$  control region requires exactly three light leptons.  $b$ -jets are  
2809 vetoed to reduce contributions from  $t\bar{t}$ . There is an ISR request in order to make the  
2810 control region signal like, as the dominant background in the signal regions is  $WZ$ , correct  
2811 modelling of signal like  $WZ$  events is crucial. The  $p_T$  on all the leptons is greater than  
2812 30 GeV in order for the control region to remain orthogonal to the signal regions. The  $E_T^{\text{miss}}$   
2813 is greater than 30 GeV and less than 50 GeV to target the peak of the  $E_T^{\text{miss}}$  distribution,  
2814 where better agreement is observed between data and MC. At least one possible pair of

leptons in the event must be SFOS as there should be a  $Z$  boson decay in the event. In addition, a dilepton and trilepton  $Z$  veto, where the invariant mass of the system is outside of the 10 GeV window of the on shell  $Z$  boson mass. This cut is designed to target off-shell  $Z$  mass decays. The full list of definitions are shown in Table 6.5. Kinematic distributions in Figure 6.31 show the agreement between data and MC: jet multiplicity,  $E_T^{\text{miss}}$ , leading jet  $p_T$ , leading lepton  $p_T$ ,  $m_T$  and the ratio between the leading lepton and leading jet  $p_T$ . The data and MC is shown to agree within 15%. The MC-based and MM estimates are shown in Table 6.6.

Variable	WZ Control Region Selection	ZZ Control Region Selection
$\ell$ flavour/sign	$\ell^\pm \ell^\mp \ell$	$\ell^\pm \ell^\mp \ell^\pm \ell^\mp$
$b$ -jet	veto	veto
jets	$\geq 1$	-
$m_{\text{SFOS}}/m_{\ell\ell\ell}$	veto [81.2-101.2]	$m_{\text{SFOS}}$ request [81.2-101.2]
$E_T^{\text{miss}}$	30 – 50	< 50 GeV
$p_T^{1^{\text{st}}l}$	> 30	> 10 GeV

Table 6.5:  $WZ$  and  $ZZ$  control region definition. Units are in GeV

### 6.7.14.2 ZZ Control Region

The definition of the  $ZZ$  control region requires exactly four leptons as both  $Z$ -bosons are expected to decay leptonically. The  $E_T^{\text{miss}}$  of all leptons is greater than 10 GeV to remove contributions from  $Z+jets$ . The  $E_T^{\text{miss}}$  is required to be less than 50 GeV as there is no expected  $E_T^{\text{miss}}$  from the  $Z$ -boson decays.. There is a request for two same flavour-opposite sign pairs, with both pairs having an invariant mass within 10 GeV of the on-shell  $Z$ -boson ( $m_z = 91.2$  GeV), this is to target two on-shell  $Z$ -boson decays. The full list of definitions are shown in Table 6.5. Kinematic distributions in Figure 6.32 show the agreement between data and MC. Specifically these distributions are: jet multiplicity,  $E_T^{\text{miss}}$ , leading jet  $p_T$ , leading lepton  $p_T$ ,  $m_{\ell\ell\ell}$  and the ratio of the leading lepton to the leading jet  $p_T$ . The MC-based and MM estimates are shown in Table 6.7. Due to the request for four leptons, the  $WZ$  process is treated as a reducible process. The typical reducible processes described in Section 6.5 are reduced to zero due to the request for four leptons as these processes produce three leptons or less in the final state. The data and MC are found to agree within 15%.

	$WZ$	$ZZ$	$t\bar{t} + V$	$VV V$	Higgs	Reducible	$\Sigma$ SM	Data
CRWZ	$8.2^{+1.1}_{-1.3}$	$0.73^{+0.08}_{-0.10}$	$0.27^{+0.18}_{-0.18}$	$0.11^{+0.11}_{-0.11}$	$0.06^{+0.04}_{-0.04}$	$0.33^{+0.39}_{-0.40}$	$9.7^{+1.2}_{-1.4}$	9

Table 6.6:  $WZ$  control region yields. The uncertainties quoted are combined statistical and systematic.

	$ZZ$	$t\bar{t} + V$	$VV V$	Higgs	Reducible (incl. WZ)	$\Sigma$ SM	Data
CRZZ	$140^{+11}_{-11}$	$0.18^{+0.08}_{-0.07}$	$0.14^{+0.15}_{-0.15}$	$0.35^{+0.09}_{-0.10}$	$0.0^{+0.0}_{-0.0}$	$141^{+11}_{-11}$	141

Table 6.7: MC-only estimated yields in the  $ZZ$  control region. The uncertainties quoted are combined statistical and systematic.

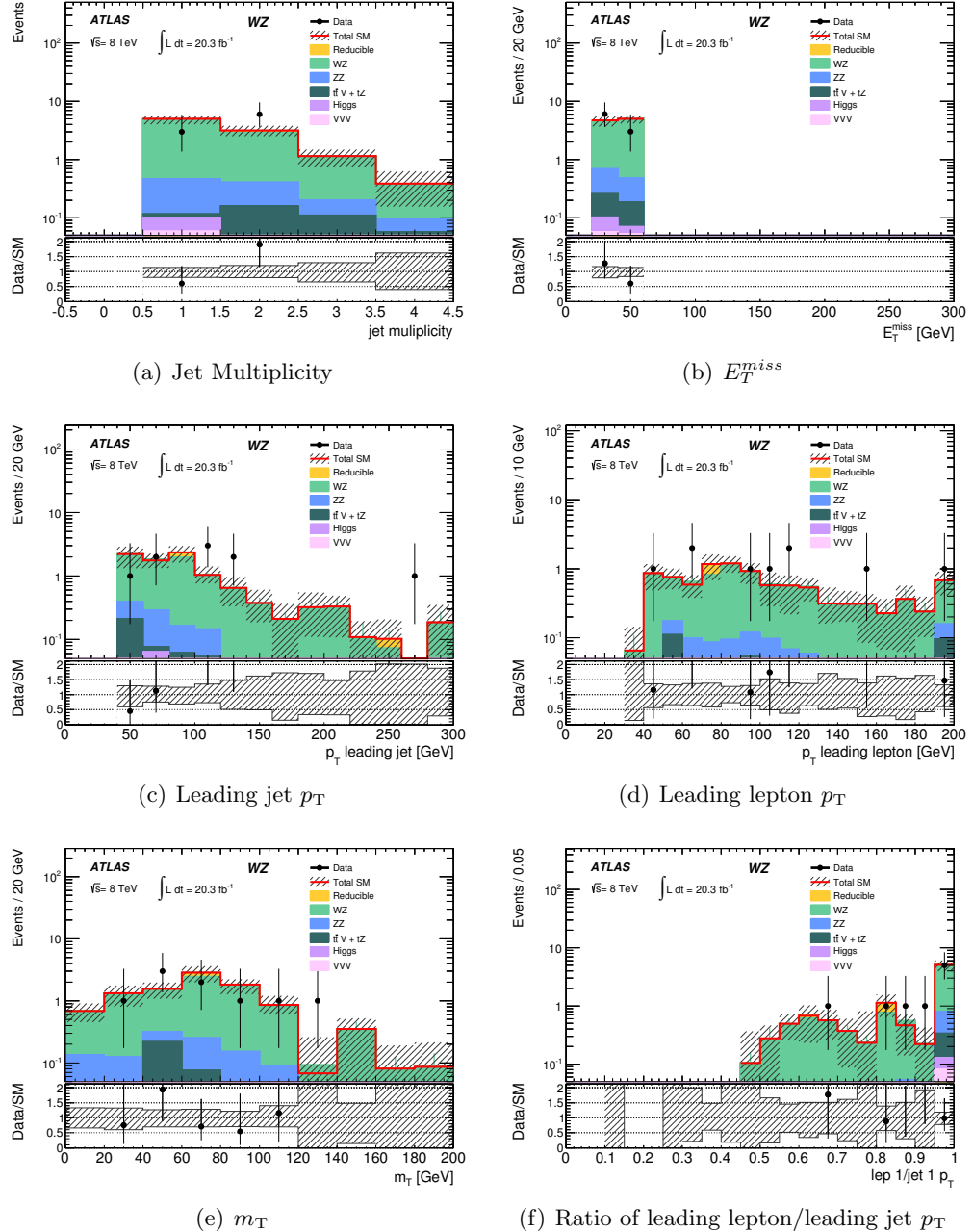
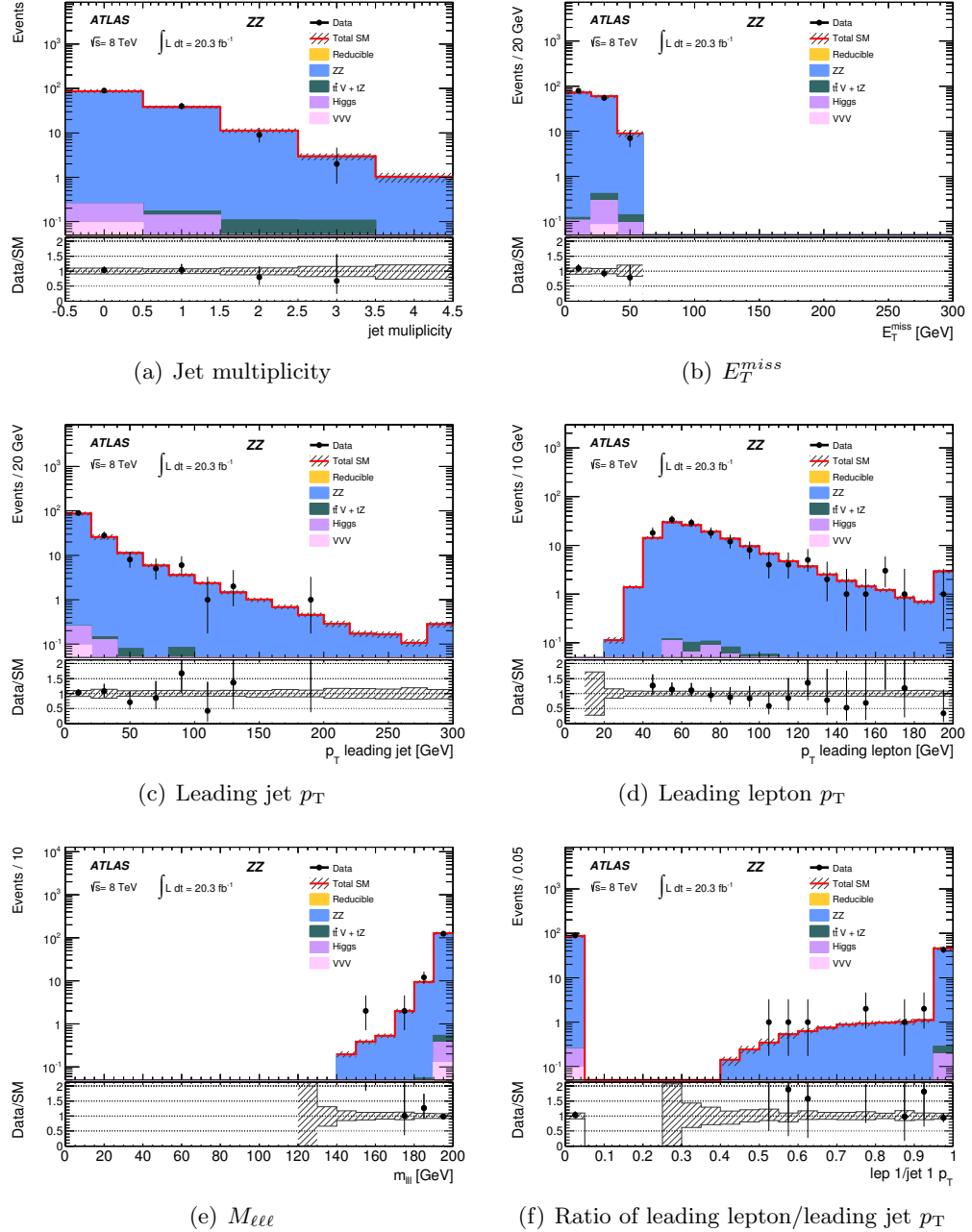


Figure 6.31: Kinematic distributions for the  $WZ$  control region.

Figure 6.32: Kinematic distributions for the  $ZZ$  control region.

### 2838 6.7.15 Systematic uncertainties on the reducible background

2839 Systematics uncertainties on the reducible background estimated with the matrix method  
 2840 are assessed. The uncertainties can be categorised into the systematics arising from the  
 2841 input components of the weighted average fake rates defined in Equation 6.6: the fake rate  
 2842 and real lepton efficiencies ( $f$  and  $\epsilon$  respectively), the scale factors ( $sf$ ) and the fake frac-  
 2843 tions ( $R$ ), defined in Section 6.5.3. The following will discuss these sources of systematic  
 2844 uncertainties affecting the final data driven estimate of the reducible background.

2845  **$f$  and  $\epsilon$  Efficiencies** The measured fake rate and real lepton efficiencies are taken from  
 2846 MC-simulated events which are corrected for any discrepancies with respect to data. These  
 2847 efficiencies showed a dependence on  $p_T$  and  $\eta$  and are therefore parameterised in these  
 2848 variables. The dependency of these efficiencies on variables used in the event selection of  
 2849 the signal regions were thoroughly investigated by the analysis team and found to be very  
 2850 similar to those taken into account for the previous  $3\ell$  analysis [133].

2851 **Fake Rate SF** The measurement of the fake rate scale factors for the different fake  
 2852 sources showed no strong dependence in  $p_T$ ,  $|\eta|$  and number of good vertices. Therefore,  
 2853 they are fitted to a constant function. The central values for the scale factors were cal-  
 2854 culated without parameterisation on any variable and the differences with respect to the  
 2855 results of the fit in these considered variables are assigned as a systematic uncertainty of  
 2856 the order of 5%.

2857 **Fake Fractions** The uncertainty on the fake fractions originates from a potential lack  
 2858 of knowledge of the relative contributions of certain types of SM physics processes in a  
 2859 given signal or validation region. To account for this uncertainty, the yields of the physics  
 2860 processes are varied by the following amounts: diboson processes by 50%, top processes  
 2861 by 50% and V+jets processes by 30%.

2862 Also included is the statistical uncertainty on the data events, which are used to apply the  
 2863 matrix equation and the statistical uncertainty from the fake rates measured in simulation.

### 2864 6.7.16 Systematic Uncertainties Summary

2865 The dominating systematic sources are summarised in Table 6.8. In SR $3\ell$ -0 and SR $3\ell$ -  
 2866 1 the dominant systematic uncertainties are the statistical uncertainty and the muon  
 2867 misidentification probability. The former arises due to the very low statistics in all signal

2868 regions. The latter arises due to the low muon  $p_T$  threshold, which introduces muons  
2869 which are harder to identify due to the likelihood of having increased jet activity around  
2870 the reconstructed muon object. The systematic uncertainties are presented graphically for  
2871 each signal region in Appendix B.

Table 6.8: Breakdown of the dominant systematic uncertainties on background estimates in the three-lepton signal regions. The percentages show the size of the uncertainty relative to the total expected background. Taken from [3].

Source of uncertainty	SR3 $\ell$ -0a	SR3 $\ell$ -0b	SR3 $\ell$ -1a	SR3 $\ell$ -1b
Reducible background				
- statistical uncertainty	34%	14%	11%	30%
- muon misidentification probability	30%	11%	< 1%	11%
- electron misidentification probability	21%	10%	2%	9%
- heavy-flavor relative contribution	22%	5%	< 1%	2%
- light-flavor relative contribution	23%	4%	n/a	< 1%
- conversion relative contribution	2%	6%	< 1%	10%
$E_T^{\text{miss}}$ soft-term scale	12%	7%	< 1%	1%
Statistical uncertainty on MC samples	4%	3%	25%	10%
Theoretical modeling of $WZ$	2%	5%	12%	8%
Cross-section	2%	2%	6%	4%
Total	59%	25%	33%	39%

## <sup>2872</sup> Chapter 7

# <sup>2873</sup> Results and Interpretations for <sup>2874</sup> Run-1 Compressed Spectra SUSY <sup>2875</sup> Analysis

<sup>2876</sup> In Chapter 6, the analysis strategy for the search for compressed SUSY events with three  
<sup>2877</sup> lepton final states with Run-1 data has been described. This chapter presents the inter-  
<sup>2878</sup> pretation of the results obtained in data, beginning with an introduction into the statistical  
<sup>2879</sup> approach to interpretation used, followed by an assessment of the compatibility between  
<sup>2880</sup> the expected SM background and the observed events in data in all signal regions, lastly  
<sup>2881</sup> the statistical interpretation of the results for each SUSY model considered is presented.

### <sup>2882</sup> 7.1 Statistical Procedure

#### <sup>2883</sup> 7.1.1 The $CL_s$ Method

<sup>2884</sup> A  $p$ -value is defined as the probability of an experiment to get a certain outcome or one  
<sup>2885</sup> that is more unlikely than the one that was observed, i.e. the  $p$ -value is calculated as  
<sup>2886</sup> the integral over the probability density function, integrated from the observed value to  
<sup>2887</sup> infinity,

$$\int_{q_{obs}}^{\infty} f(q) dq, \quad (7.1)$$

<sup>2888</sup> where  $q$  is the test statistic, which is a scalar quantity representative of the experiment. It  
<sup>2889</sup> is defined to represent the two hypotheses and determine which best describes the observed  
<sup>2890</sup> data. Therefore, to assess the statistical significance of the number of events in data with

respect to the expected background, the probability that the observation agrees with the background-only hypothesis ( $H_0$ ) or the signal plus background hypothesis ( $H_1$ ). The  $p$ -values for  $H_0$  and  $H_1$  are defined as:

$$p_0 = P(q \leq q_{obs}|H_0) = \int_{-\infty}^{q_{obs}} f(q|b)dq$$

$$p_1 = P(q \geq q_{obs}|H_1) = \int_{q_{obs}}^{\infty} f(q|s+b)dq,$$

where  $f(q|b)$  and  $f(q|s+b)$  are the probability density functions (pdfs) of the test statistic,  $q$  and  $q_{obs}$  is the observed result.

A given “signal” hypothesis, which would correspond to a particular SUSY model in this case, can be considered to be excluded if  $p_1 \leq 0.05$ , this means the probability of rejecting the hypothesis given the hypothesis is true is 5%. This is equivalent to saying the hypothesis is excluded at 95% Confidence Level (CL), which equivalent to a value of  $Z_N$  of  $1.64\sigma$ , refer to Equation 6.1 for the exact calculation. However, it is possible that this can lead to a signal being incorrectly excluded in the case that the analysis does not expect a large ratio of signal to background events in the observed region - i.e. the analysis has a low sensitivity to the considered signal. To protect against this, a variation of the CL method, the  $CL_s$  method [148] [149], takes the ratio of  $p$ -values and is defined as:

$$CL_s = \frac{CL_{s+b}}{CL_b}, \quad (7.2)$$

where  $s$  is the expected signal, and

$$CL_{s+b} = P(q \geq q_{obs}|s+b), \quad (7.3)$$

and

$$CL_b = P(q \geq q_{obs}|b). \quad (7.4)$$

Using this method, a signal hypothesis is said to be excluded at 95% CL if the condition:

$$CL_s \leq 0.05 \quad (7.5)$$

is satisfied.

This analysis uses a profile log-likelihood ratio [150] formalism to define the test statistic  $q$ , which is used to obtain the relevant  $p$ -values and the  $CL_s$ . The likelihood is given

<sup>2911</sup> by:

$$L(n_{obs}|\mu S, B, \eta) = \text{Pois}(n_{obs}|\mu S + B) \times \prod_{\eta} G_{syst}(\eta^0, \eta), \quad (7.6)$$

<sup>2912</sup> where  $S$  is the number of signal events,  $B$  is the number of expected background events,  
<sup>2913</sup>  $\mu$  is the SUSY signal strength to be tested, and  $\eta$  are the various systematics, described  
<sup>2914</sup> as nuisance parameters.  $\text{Pois}(n_{obs}|\mu S + B)$  is the Poisson distribution for the expected  
<sup>2915</sup> events in a signal region, given the expected signal and background, and  $G_{syst}(\eta^0, \eta)$  is a  
<sup>2916</sup> Gaussian, which is centered on the nominal value  $\eta^0$ , around which the nuisance parameters  
<sup>2917</sup> can be varied when maximising the likelihood. Each nuisance parameter is described as a  
<sup>2918</sup> separate Gaussian, with  $\sigma=1$ , and the product of these is then taken.

<sup>2919</sup> The likelihood can be concisely rewritten as  $L(\mu, \nu(\mu))$ , where  $\nu$  represents the full  
<sup>2920</sup> signal plus background model, which is a function of the signal strength  $\mu$ . Given this  
<sup>2921</sup> notation, the profile likelihood ratio  $\lambda_p(\mu)$  is given by:

$$\lambda_p(\mu) = \frac{L(\mu, \hat{\nu}(\mu))}{L(\hat{\mu}, \hat{\nu}(\hat{\mu}))}. \quad (7.7)$$

<sup>2922</sup> In this definition,  $\hat{\nu}$  represents using an “unconditional” likelihood fit to maximise the  
<sup>2923</sup> likelihood, which means that  $\mu$  and  $\nu$  are both varied simultaneously, whilst  $\hat{\nu}$  represents a  
<sup>2924</sup> “conditional” maximisation of the likelihood, which involves fixing  $\mu$  whilst  $\nu$  is varied. The  
<sup>2925</sup> dependence on the nuisance parameters is removed by maximising likelihood or “profiling”  
<sup>2926</sup> procedure. The profile likelihood ratio tends to unity if the observation is compatible with  
<sup>2927</sup> the hypothesised value of  $\mu$ .

<sup>2928</sup> The test statistic,  $q$ , is defined as a function of the log likelihood ration  $\lambda_p(\mu)$  given  
<sup>2929</sup> by:

$$q = \begin{cases} -2 \ln \lambda_p(\mu) & \hat{\mu} \leq \mu \\ 0 & \hat{\mu} > \mu, \end{cases} \quad (7.8)$$

<sup>2930</sup> where  $\hat{\mu}$  is an estimator of the signal strength  $\mu$ . The probability of observing the  
<sup>2931</sup> number of events predicted by the signal hypothesis or more given the signal strength is  
<sup>2932</sup> used to define the discovery  $p$ -value. This can be expressed as the integral of the pdf of  
<sup>2933</sup> the test statistic for a given  $\mu$  value,  $f(q|\mu)$ . The integral is calculated between the limits  
<sup>2934</sup> of the test statistic using the observed values  $q_{obs}$  and infinity in order to evaluate the  
<sup>2935</sup> total probability of obtaining a higher number of events than those observed. This gives

<sup>2936</sup> the definition of the discovery  $p$ -value in terms of the log-likelihood ratio  $\lambda_p(\mu)$ :

$$p_\mu = \int_{q_{obs}}^{\infty} f(q|\mu) dq \quad (7.9)$$

<sup>2937</sup> The  $p$ -value is said to be “one-sided” [136], as an excess of events constitutes a signal  
<sup>2938</sup> observation, but an underfluctuation does not. The modelling of the likelihood, calculation  
<sup>2939</sup> of the  $CL_s$  and  $p$ -values, were performed using the ATLAS HistFitter package [149] [151],  
<sup>2940</sup> a tool able to perform likelihood fits and their statistical interpretation.

### <sup>2941</sup> 7.1.2 Combination of Signal Regions

<sup>2942</sup> All signal regions considered in this analysis (see Section 6.4) are orthogonal and in turn  
<sup>2943</sup> can be statistically combined for overall improvement in signal sensitivity. The method  
<sup>2944</sup> involves a combined likelihood, defined as:

$$L(\mu, \nu) = \prod_i^N L_i(\mu, \nu_i), \quad (7.10)$$

<sup>2945</sup> for  $N$  signal regions. If a signal region has no sensitivity to a given signal, the corres-  
<sup>2946</sup> ponding likelihood will not be a function of  $\mu$ , and therefore it will not contribute to the  
<sup>2947</sup> combined likelihood for that signal scenario.

## <sup>2948</sup> 7.2 Observations in 8 TeV Data

<sup>2949</sup> After the signal regions are finalised, they are unblinded, which involves running the data  
<sup>2950</sup> through the signal regions to see if there is any excess over the Standard Model predictions.  
<sup>2951</sup> The results and background yields in the signal regions are shown in Table 7.1 for SR3 $\ell$ -0  
<sup>2952</sup> and SR3 $\ell$ -1. No excess in the number of events is observed when comparing to the expect  
<sup>2953</sup> SM background. There is good agreement between the data and the SM background  
<sup>2954</sup> within systematic uncertainties. The quantitative analysis of the differences between the  
<sup>2955</sup> number of expected and observed events is discussed in Section 7.3. The main kinematic  
<sup>2956</sup> variables used to define the ISR signal regions SR3 $\ell$ -1 are shown in this section not only  
<sup>2957</sup> highlighting the agreement with data and MC but also the shape and kinematic features  
<sup>2958</sup> of the ISR signal.

Table 7.1: Expected and observed yields in the three-lepton signal regions. The uncertainties shown include both statistical and systematic components. The “Others” background category includes  $t\bar{t}V$ ,  $VVV$  and SM Higgs boson production [3].

	SR3 $\ell$ -0a	SR3 $\ell$ -0b	SR3 $\ell$ -1a	SR3 $\ell$ -1b
$WZ$	$0.59^{+0.47}_{-0.32}$	$5.0^{+1.5}_{-1.2}$	$0.54^{+0.20}_{-0.19}$	$1.6 \pm 0.4$
$ZZ$	$0.23^{+0.09}_{-0.07}$	$0.66 \pm 0.16$	$0.024 \pm 0.013$	$0.10^{+0.05}_{-0.04}$
Reducible	$2.8^{+1.5}_{-2.2}$	$9.7^{+3.1}_{-3.6}$	$0.09 \pm 0.08$	$1.4^{+1.0}_{-1.1}$
Others	$0.0033^{+0.0036}_{-0.0033}$	$0.07 \pm 0.05$	$0.013 \pm 0.010$	$0.038 \pm 0.021$
Total SM	$3.7^{+1.6}_{-2.2}$	$15.4^{+3.5}_{-3.9}$	$0.67^{+0.22}_{-0.21}$	$3.1^{+1.1}_{-1.2}$
Data	4	15	1	3

### 2959 7.2.1 Kinematic Distributions

2960 Figures 7.1 and 7.2 shows the SM expectations and the observations in data in the SR3 $\ell$ -1a  
 2961 and SR3 $\ell$ -1b signal regions respectively. For illustration purposes, the distributions are  
 2962 also shown for two  $\tilde{\chi}_1^\pm \tilde{\chi}_2^0$  via WZ and one  $\tilde{\chi}_1^\pm \tilde{\chi}_2^0$  via  $\tilde{\ell}_L$  benchmark points with  $m(\tilde{\chi}_1^\pm \tilde{\chi}_2^0, \tilde{\chi}_1)$   
 2963 = (100, 87.5), (100, 75) and (110, 90) GeV. These are points are chosen to show the  
 2964 sensitivity for varying mass differences in the signal regions for WZ-mediated and  $\tilde{\ell}_L$ -  
 2965 mediated simplified models. Figures 7.3 and 7.4 shows the SM expectations and the  
 2966 observations in data in the SR3 $\ell$ -0 signal regions.

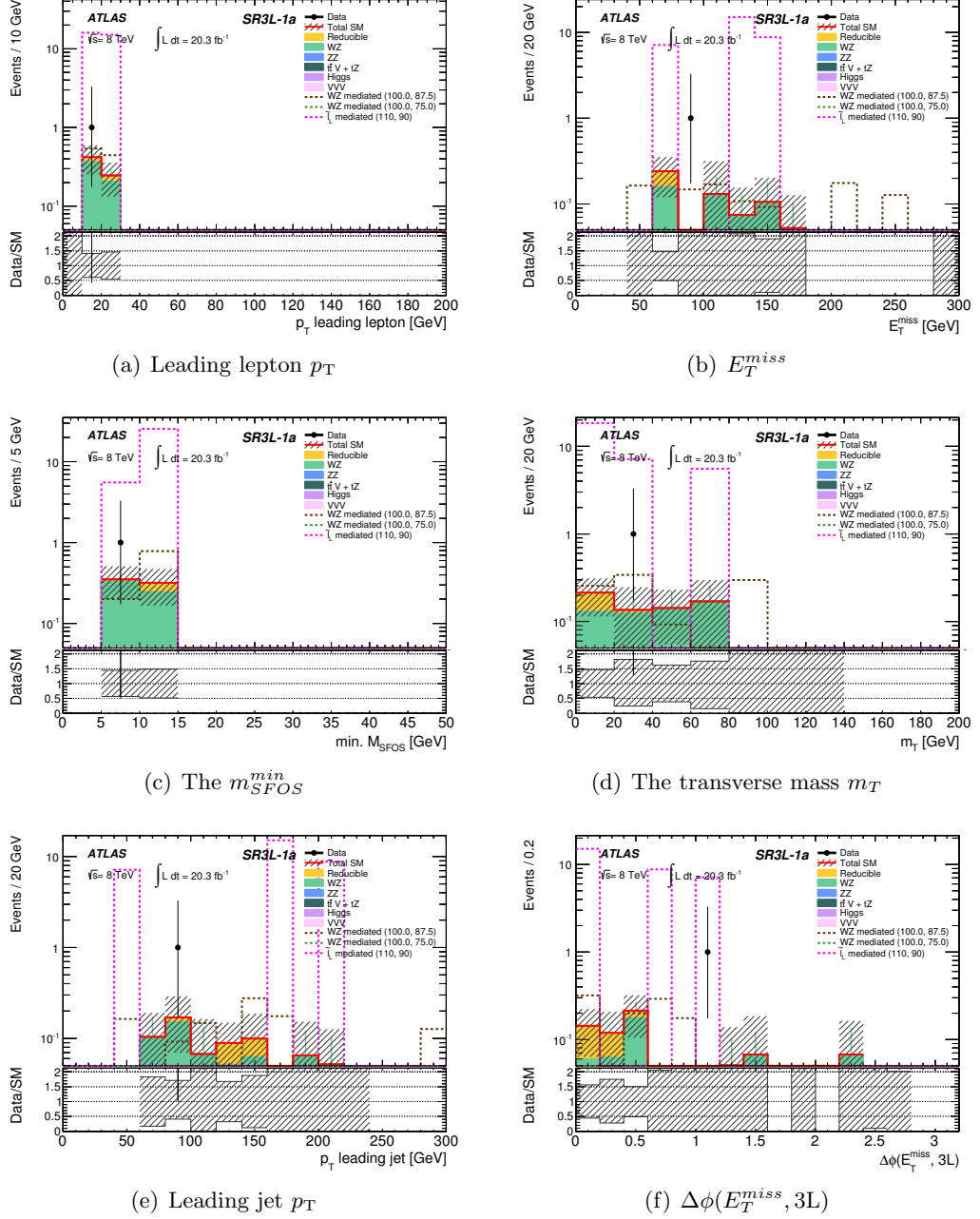


Figure 7.1: Kinematic distributions in SR3 $\ell$ -1a. (a)  $p_T^{1st\ell}$ , (b)  $E_T^{\text{miss}}$ , (c)  $m_{SFOS}^{min}$ , (d)  $m_T$ , (e)  $p_T^{1stj}$ , (f)  $\Delta\phi(E_T^{\text{miss}}, 3\ell)$ . The uncertainty band covers systematic and statistical uncertainties. The plots also show the distribution for signal hypotheses, where the parentheses following the simplified model denote the mass parameters in GeV as  $(m(\tilde{\chi}_1^\pm \tilde{\chi}_2^0), m(\tilde{\chi}_1^0))$ .

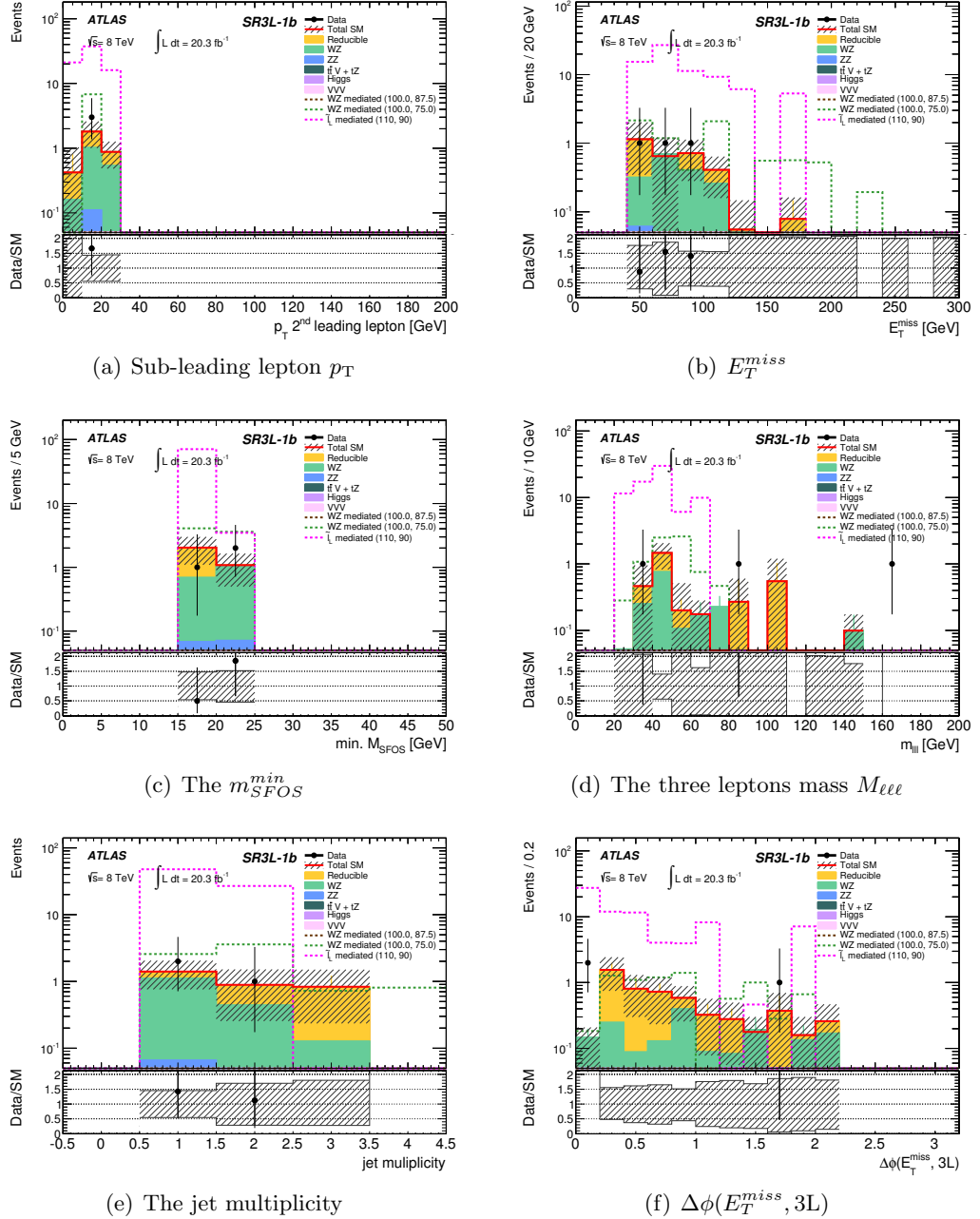


Figure 7.2: Kinematic distributions in SR3 $\ell$ -1b. (a)  $p_T^{2\text{nd}\ell}$ , (b)  $E_T^{\text{miss}}$ , (c)  $m_{\text{SFOS}}^{\min}$ , (d)  $M_{\ell\ell\ell}$ , (e) Jet multiplicity, (f)  $\Delta\phi(E_T^{\text{miss}}, 3\text{L})$ . The uncertainty band covers systematic and statistical uncertainties. The plots also show the distribution for signal hypotheses, where the parentheses following the simplified model denote the mass parameters in GeV as  $(m(\tilde{\chi}_1^\pm \tilde{\chi}_2^0), m(\tilde{\chi}_1^0))$ .

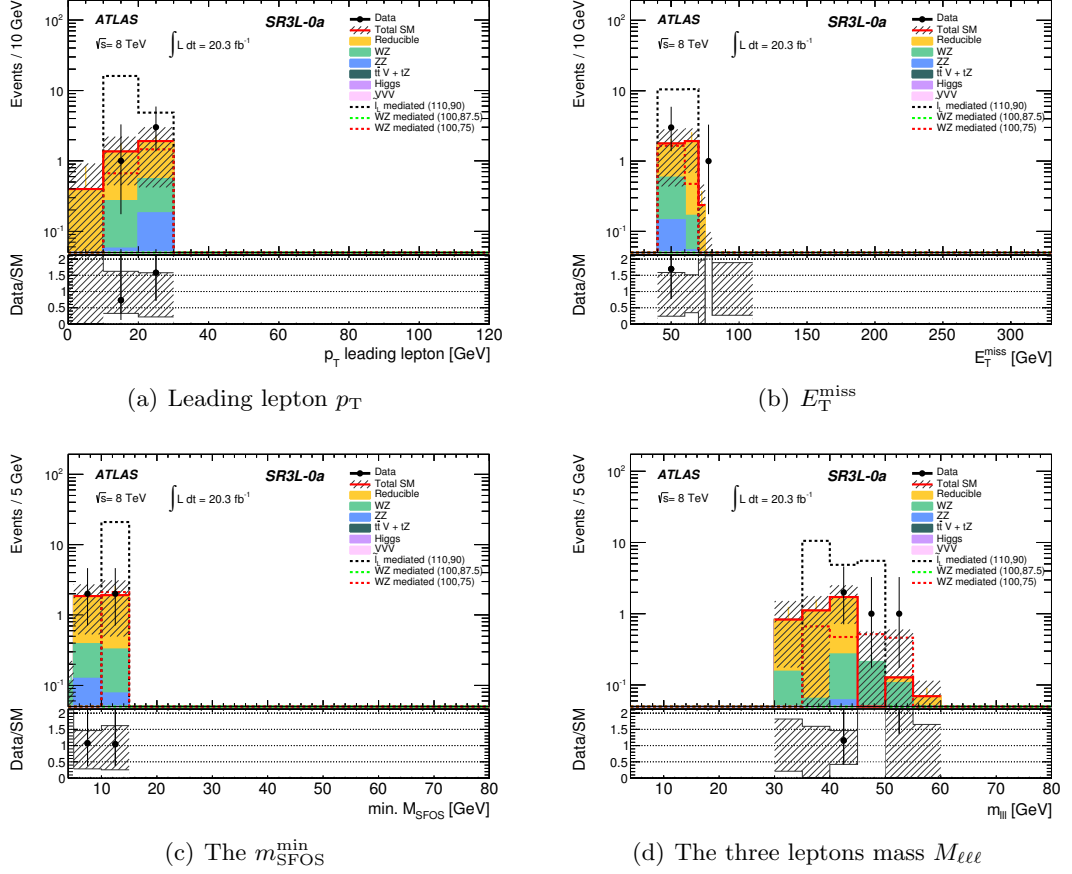


Figure 7.3: Kinematic distributions in SR3L-0a. (a)  $p_T^{1^{\text{st}}\ell}$ , (b)  $E_T^{\text{miss}}$ , (c)  $m_{\text{SFOS}}^{\text{min}}$ , (d)  $M_{\ell\ell\ell}$ . The uncertainty band covers systematic and statistical uncertainties. The plots also show the distribution for signal hypotheses, where the parentheses following the simplified model denote the mass parameters in GeV as  $(m(\tilde{\chi}_1^\pm \tilde{\chi}_2^0), m(\tilde{\chi}_1^0))$  (Produced by another analyser, taken from [137]).

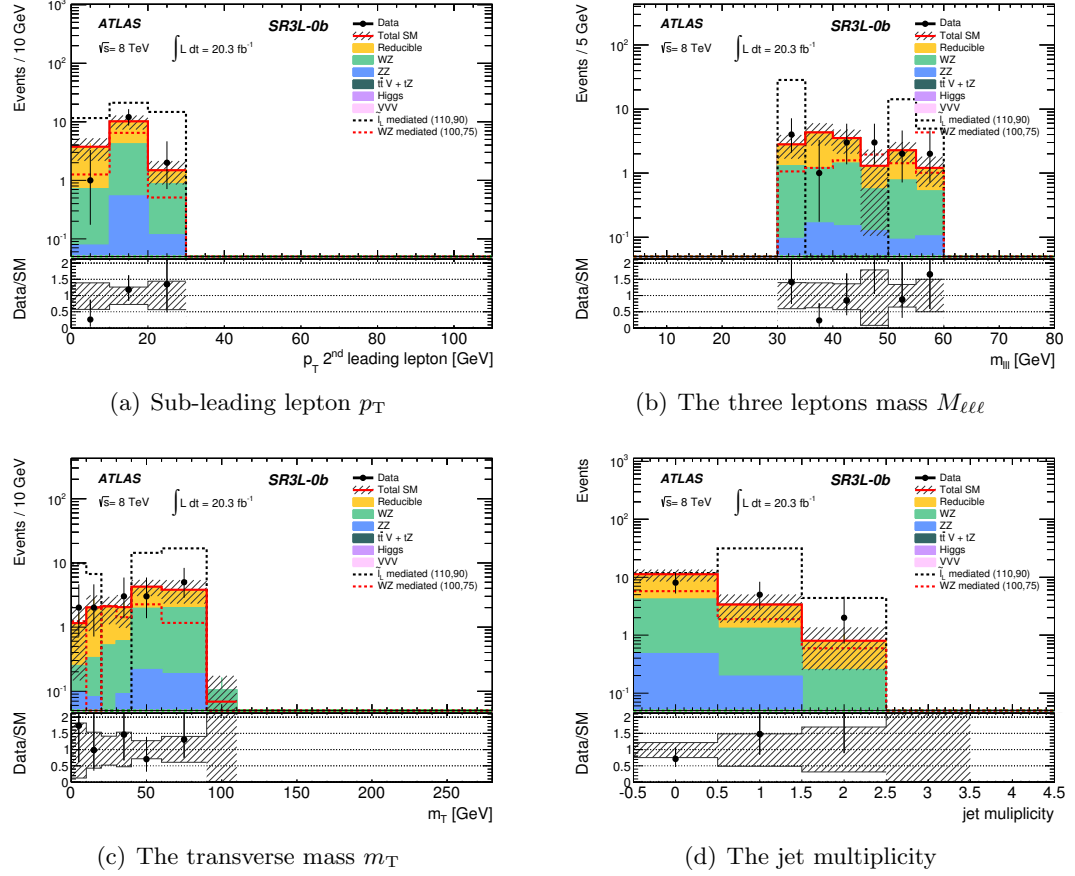


Figure 7.4: Kinematic distributions in SR3L-0b. (a)  $p_T^{2nd\ell}$ , (b)  $M_{\ell\ell\ell}$ , (c)  $m_T$ , (d) Jet multiplicity. The uncertainty band covers systematic and statistical uncertainties. The plots also show the distribution for signal hypotheses, where the parentheses following the simplified model denote the mass parameters in GeV as  $(m(\tilde{\chi}_1^\pm \tilde{\chi}_2^0), m(\tilde{\chi}_1^0))$  (Produced by another analyser, taken from [137]).

## 2967 7.3 Statistical Interpretation of Results

### 2968 7.3.1 Model Independent Limits

2969 In addition to considering the interpretation for the specific SUSY scenarios this analysis  
 2970 was optimised for, the compatibility of the observed data with the background-only hypo-  
 2971 thesis  $b$  can be assessed. This corresponds to signal strength  $\mu = 0$ . In order to quantify  
 2972 the probability of the background-only hypothesis to fluctuate to the number of observed  
 2973 events or higher, the one-sided  $p_0$ -value is calculated and truncated to 0.5 for  $p_0 > 0.5$ .  
 2974 The upper limits at 95% CL on the expected and observed number of beyond the SM  
 2975 event ( $S_{exp}^{95}, S_{obs}^{95}$ ) for each signal region are calculated using the  $CL_s$  method. For both of  
 2976 these calculations the profile likelihood ratio is used as a test-statistic. The  $p_0$  and  $CL_s$   
 2977 values are calculated using pseudo-experiments. This is useful for an estimate on sensit-

ivity to any new physics scenarios. The upper limit on the visible cross-section is set for any new physics scenarios. The visible cross section is defined as the cross section times the branching ratio times acceptance times efficiency ( $\sigma \times BR \times A \times \epsilon$ ) of new physics processes satisfying the signal region requirements. Upper limits are derived by evaluation  $p_\mu$  at a large (and hence easily excluded) starting value of  $\mu$  until  $p_\mu$  exceeds 0.5. This visible cross can be used to test scenarios not considered in this work using the observed data in the SRs. The model-independent limits are shown in Table 7.2.

	SR3ℓ-0a	SR3ℓ-0b	SR3ℓ-1a	SR3ℓ-1b
Total SM	$3.7^{+1.6}_{-2.2}$	$15.4^{+3.5}_{-3.9}$	$0.67^{+0.22}_{-0.21}$	$3.1^{+1.1}_{-1.2}$
Data	4	15	1	3
$p_0$	0.47	0.50	0.36	0.50
$S_{\text{obs}}^{95}$	8.3	12.6	4.0	6.1
$S_{\text{exp}}^{95}$	$8.2^{+1.7}_{-2.2}$	$12.6^{+5.2}_{-3.0}$	$3.8^{+0.6}_{-0.3}$	$6.0^{+2.1}_{-1.3}$
$\langle \epsilon \sigma \rangle_{\text{obs}}^{95} [\text{fb}]$	0.41	0.62	0.20	0.30
$\text{CL}_b$	0.59	0.50	0.69	0.54

Table 7.2: The model-independent limits are shown, calculated from the three-lepton signal region observations: the one-sided  $p_0$ -values; the expected and observed upper limits at 95% CL on the number of beyond-the-SM events ( $S_{\text{exp}}^{95}$  and  $S_{\text{obs}}^{95}$ ) for each signal region, calculated using pseudo-experiments and the  $\text{CL}_s$  prescription; the observed 95% CL upper limit on the signal cross-section times efficiency ( $\langle \epsilon \sigma \rangle_{\text{obs}}^{95}$ ); and the  $\text{CL}_b$  value for the background-only hypothesis [3].

### 7.3.2 Model Dependent Limits: Simplified Models

Both the WZ- and  $\tilde{\ell}_L$ -mediated simplified models are considered for limit setting. The observed and expected 95% CL limit contours are calculated using MC pseudo-experiments for each SUSY model point, taking into account the theoretical and experimental uncertainties on the SM background and the experimental uncertainties on the signal,  $\sigma_{\text{exp}}$  in addition to the Poissonian fluctuations on the number of observed events. The yellow bands in the figures for the exclusion contours show the impact of  $\pm 1\sigma$  variations of  $\sigma_{\text{exp}}$  on the expected limit. The impact of the theoretical uncertainty on the signal cross section  $\sigma_{\text{theory}}^{\text{SUSY}}$  are shown as  $\pm 1\sigma$  variation bands (red dashed lines) on the observed limit. The combination of SR3ℓ-0 and SR3ℓ-1 showed no significant improvements in sensitivity to the WZ-mediated model compared to the limits produced in [133]. Only one compressed mass splitting point could be excluded. The 1D upper limit on the production cross-section for  $\Delta m(\tilde{\chi}_1^\pm - \tilde{\chi}_1^0) = 25$  GeV is shown in Figures 7.5. The excluded point corresponds to  $m(\tilde{\chi}_1^\pm) = 100$  GeV and  $m(\tilde{\chi}_1^0) = 75$  GeV. The difficulty in improving sensitivity in this

2999 simplified model is largely due to the smaller production cross-sections compared to the  
3000 via  $\tilde{\ell}_L$  model.

3001 Limits are set on the  $\tilde{\chi}_1^\pm \tilde{\chi}_2^0$  scenarios with  $\tilde{\ell}_L$ -mediated decays, with slepton masses  
3002 set halfway and 95% between the  $\tilde{\chi}_1^\pm$  and the  $\tilde{\chi}_1^0$  masses, where both the  $\tilde{\chi}_1^\pm$  and the  $\tilde{\chi}_1^0$   
3003 masses are varied. Figure 7.6 shows the combination of the compressed scenario analyses  
3004 and the previous published results, with  $\tilde{\ell}_L$  halfway between  $\tilde{\chi}_1^\pm \tilde{\chi}_2^0$  and  $\tilde{\chi}_1^0$  masses, with  
3005 an improved sensitivity to compressed scenarios up to  $\tilde{\chi}_1^\pm$  masses of 250 GeV. The results  
3006 for the scenario where the  $\tilde{\ell}_L$  mass is 95% between the  $\tilde{\chi}_1^\pm$  and the  $\tilde{\chi}_1^0$  masses is combined  
3007 with the previous three lepton results and the same-sign, two lepton analysis [3] and is  
3008 shown in Figure 7.7. In scenarios with large mass splittings,  $\tilde{\chi}_1^\pm$  masses are excluded  
3009 up to 700 GeV. In the compressed areas of the parameter space, where the  $\tilde{\ell}_L$  mass is  
3010 halfway between the  $\tilde{\chi}_1^\pm$  and  $\tilde{\chi}_1^0$  masses, the identification of three leptons in the final  
3011 state is possible and so the three-lepton analysis has the strongest sensitivity. However,  
3012 where the  $\tilde{\ell}_L$  mass is 95% between the  $\tilde{\chi}_1^\pm$  and  $\tilde{\chi}_1^0$  masses, one of the leptons may have  
3013 momentum too low to be reconstructed, as such the two same-sign lepton analysis, which  
3014 was designed to compliment the three-lepton search shows the strongest sensitivity. These  
3015 results highlight that utilizing low  $p_T$  leptons and ISR jets to probe the compressed  $\tilde{\chi}_1^\pm \tilde{\chi}_2^0$   
3016 production provides improvements in sensitivity to this scenario.

### 3017 7.3.3 Summary of Electroweak SUSY Searches at 8 TeV

3018 The ATLAS results for electroweakino searches at 8 TeV in the simplified models frame-  
3019 work are summarised in Figure 7.8 in the  $m(\tilde{\chi}_1^\pm, \tilde{\chi}_2^0)$  -  $m(\tilde{\chi}_1^0)$  plane. Each of the  $\tilde{\chi}_1^\pm / \tilde{\chi}_2^0 / \tilde{\chi}_3^0$   
3020 decays considered in the plot is assumed to have 100% branching fraction and the produc-  
3021 tion cross-section is for pure wino  $\tilde{\chi}_1^+ \tilde{\chi}_1^-$  and  $\tilde{\chi}_1^\pm \tilde{\chi}_2^0$ , and pure higgsino  $\tilde{\chi}_2^0 \tilde{\chi}_3^0$ . The limits for  
3022  $\tilde{\chi}_1^+ \tilde{\chi}_1^-$  and  $\tilde{\chi}_1^\pm \tilde{\chi}_2^0$  and  $\tilde{\chi}_2^0 \tilde{\chi}_3^0$  production with  $\tilde{l}_L$ -mediated decays combine the compressed  
3023 spectra, same-sign, two-lepton analyses with the previously published analyses. It is ob-  
3024 served that for  $\tilde{\chi}_1^\pm \tilde{\chi}_2^0 \tilde{\chi}_3^0$  masses up to 740 GeV are excluded at the 95% CL for massless  $\tilde{\chi}_1^0$ .  
3025 Improvements in sensitivity are also seen in the near  $\tilde{\chi}_1^\pm, \tilde{\chi}_1^0$  mass degenerate region,  
3026 which is due to the inclusion of the combined compressed  $3\ell$  analyses and the same-sign,  
3027 two-lepton analysis. In the high mass region, with large mass differences between the  $\tilde{\chi}_1^\pm$   
3028 and the  $\tilde{\chi}_1^0$  the exclusion limit has increased by 20 GeV. In the compressed region, near  
3029 the boundary where  $m_{\tilde{\chi}_1^\pm} = m_{\tilde{\chi}_1^0}$ , the exclusion limit has been extended closer to the mass  
3030 degenerate boundary up to 200 GeV more with the inclusion of the compressed spectra  
3031 analyses.

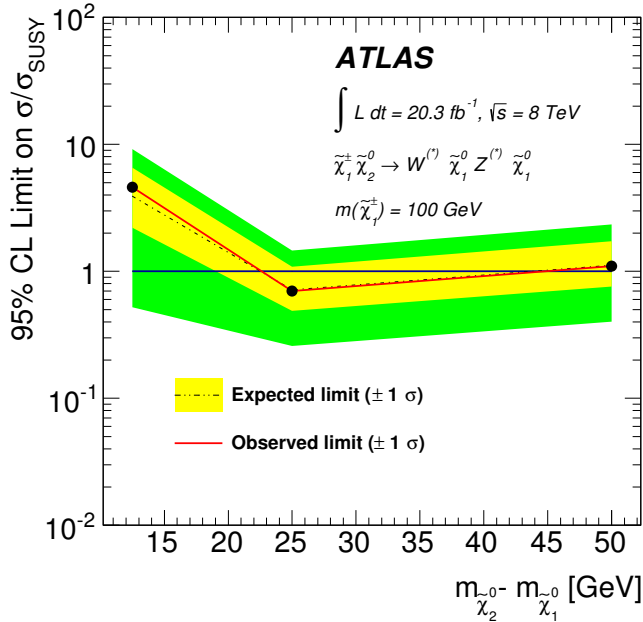


Figure 7.5: 95% CL upper limit on the cross section normalised to the SUSY production cross section for chargino and neutralino production in the WZ-mediated simplified models with  $m(\tilde{\chi}_1^\pm) = 100$  GeV. The limits have been set with respect to the mass difference between  $\tilde{\chi}_1^\pm - \tilde{\chi}_1^0$ . Produced by other analyser, taken from [137].

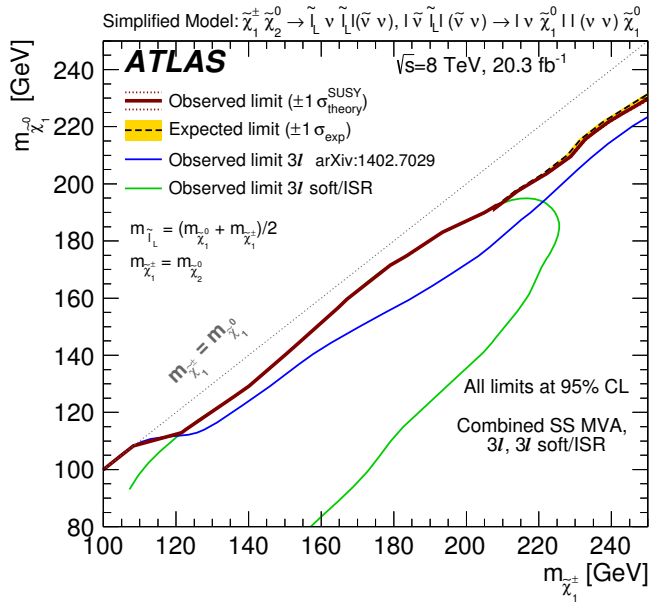


Figure 7.6: The 95% CL exclusion limits on  $\tilde{\chi}_1^\pm \tilde{\chi}_2^0$  production with  $\tilde{L}_L$ -mediated decays, as a function of the  $\tilde{\chi}_1^\pm$  and  $\tilde{\chi}_2^0$  masses, where the intermediate slepton mass is set to the  $\tilde{\chi}_1^0$  mass plus 50% of the difference between the  $\tilde{\chi}_1^\pm$  and the  $\tilde{\chi}_1^0$  masses. The red contour corresponds to the limits set using a combination of the  $3\ell$  analysis from [133], the compressed scenario  $3\ell$  analysis and the same-sign, two lepton analysis [3]. The green contour corresponds to the combined SR $3\ell$ -0 and SR $3\ell$ -1 limits.

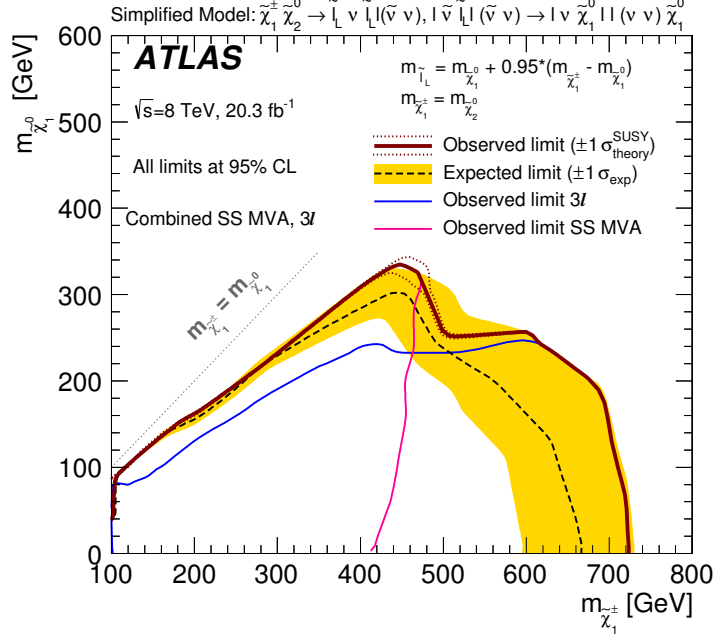
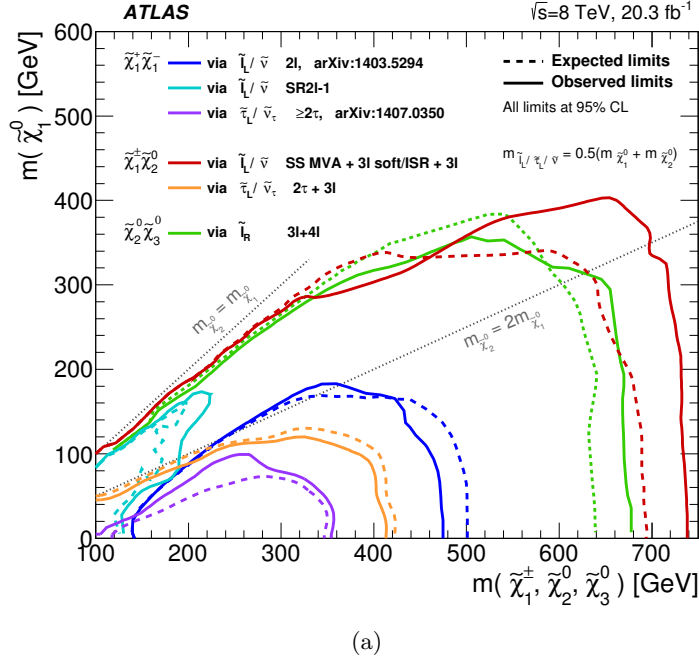


Figure 7.7: The 95% CL exclusion limits on  $\tilde{\chi}_1^\pm \tilde{\chi}_2^0$  production with  $\tilde{l}_L$ -mediated decays, as a function of the  $\tilde{\chi}_1^\pm$  and  $\tilde{\chi}_2^0$  masses, where the intermediate slepton mass is set to the  $\tilde{\chi}_1^0$  mass plus 95% of the difference between the  $\tilde{\chi}_1^\pm$  and the  $\tilde{\chi}_1^0$  masses. The red contour corresponds to the combined limits for the  $3\ell$  analysis from [133], the compressed scenario  $3\ell$  analysis and the same-sign, two lepton analysis [3]. The blue contour corresponds to the combined limits of the  $3\ell$  analyses and the pink contour corresponds to the limits from the same-sign, two lepton analysis.



(a)

Figure 7.8: The 95% CL exclusion limits on  $\tilde{\chi}_1^+ \tilde{\chi}_1^-$ ,  $\tilde{\chi}_1^\pm \tilde{\chi}_2^0$  and  $\tilde{\chi}_2^0 \tilde{\chi}_3^0$  production with  $\tilde{l}_L$ -mediated decays, as a function of the  $\tilde{\chi}_1^\pm$ ,  $\tilde{\chi}_2^0$  and  $\tilde{\chi}_3^0$  masses. The production cross-section is for pure wino  $\tilde{\chi}_1^+ \tilde{\chi}_1^-$  and  $\tilde{\chi}_1^\pm \tilde{\chi}_2^0$ , and pure higgsino  $\tilde{\chi}_2^0 \tilde{\chi}_3^0$  [3].

## <sup>3033</sup> Chapter 8

# <sup>3034</sup> Looking Into the Future: A First <sup>3035</sup> Optimisation for an Electroweak <sup>3036</sup> SUSY Search with Three-Lepton <sup>3037</sup> Final States at 13 TeV

## <sup>3038</sup> 8.1 Introduction

<sup>3039</sup> This chapter presents a search for electroweak supersymmetry, in particular direct  $\tilde{\chi}_1^\pm \tilde{\chi}_2^0$   
<sup>3040</sup> production with decay via intermediate left-handed sleptons,  $\tilde{\ell}_L$ . The search is simulation  
<sup>3041</sup> based, with Run-2 conditions i.e.  $\sqrt{s} = 13$  TeV with a projected integrated luminosity  
<sup>3042</sup> of  $10\text{fb}^{-1}$  of  $pp$ -collision simulated data. With higher beam energies and expected higher  
<sup>3043</sup> luminosities during Run-2, improved sensitivity to SUSY production is expected. This is  
<sup>3044</sup> shown in Figure 8.1, where the cross-section for gaugino pair-production is  $\sim$  four times  
<sup>3045</sup> greater at 14 TeV than

<sup>3046</sup> 8 TeV for  $m(\tilde{\chi}) = 500$  GeV. Electroweak SUSY production will not immediately benefit  
<sup>3047</sup> from the increase in beam energies due to the relatively small production cross-sections  
<sup>3048</sup> compared to strong production. However, electroweak SUSY production will benefit from  
<sup>3049</sup> the increase in luminosity. This analysis is designed to give a preliminary projection of the  
<sup>3050</sup> sensitivity to electroweak SUSY production with the expected Run-2 data to be collected  
<sup>3051</sup> from 2015-2016. The selections presented for the signal regions are not final and are likely  
<sup>3052</sup> to be subject to change by other analysers until publication.

<sup>3053</sup> This analysis targets two scenarios: where the  $m_{\tilde{\chi}_1^\pm, \tilde{\chi}_2^0} = 600$  GeV - 1 TeV (heavy),

3054 or 100 - 600 GeV (intermediate). The difference in mass between  $\tilde{\chi}_1^\pm \tilde{\chi}_2^0$  and  $\tilde{\chi}_1^0$  is of  
 3055 the same order for the respective scenarios. This region of the  $m(\tilde{\chi}_1^\pm \tilde{\chi}_2^0 - \tilde{\chi}_1^0)$  parameter  
 3056 space is different from the compressed scenarios discussed in Chapters 6 and 7, where  
 3057 the final state objects had relatively low  $p_T$ . Therefore the optimisation strategy utilises  
 3058 different variables, which highlight the larger  $E_T^{miss}$ ,  $m_T$  and lepton  $p_T^{1,2,3}$ . The general  
 3059 analysis strategy is discussed in Section 8.2. The Run-2 trigger selection is shown in  
 3060 Section 8.4. The definitions of the physics objects used for this analysis are described  
 3061 in Section 8.5, where only differences to the Run-1 analysis are highlighted. The signal  
 3062 region optimisation strategy is described in Section 8.6. The expected signal sensitivity is  
 discussed in Section 8.7.

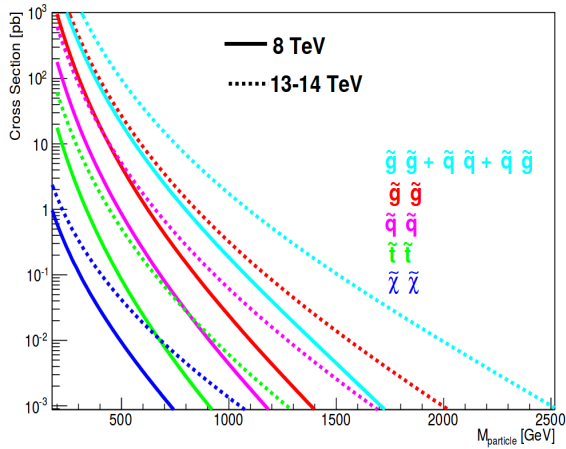


Figure 8.1: Cross-sections for SUSY particle production at  $\sqrt{s} = 8$  TeV and 13-14 TeV. The coloured particle cross sections are from NLL-FAST [152] and evaluated at  $\sqrt{s} = 8$  TeV and 13 TeV; the electroweak pure higgsino cross sections are from PROSPINO [153] and evaluated at  $\sqrt{s} = 8$  TeV and 14 TeV. Taken from [154].

3063

## 3064 8.2 Analysis Overview

## 3065 8.3 SUSY Simplified Models Considered

3066 In this analysis, one  $\tilde{\chi}_1^\pm \tilde{\chi}_2^0$  production mode is explored in the content of simplified models:  
 3067 direct  $\tilde{\chi}_1^\pm \tilde{\chi}_2^0$  with intermediate sleptons( $\tilde{\ell}$ ) leading to a final state of three leptons and  $E_T^{miss}$   
 3068 as illustrated in Figure 2.3.

3069 The  $\tilde{\chi}_1^\pm$  and  $\tilde{\chi}_2^0$  are considered purely wino and mass degenerate, the  $\tilde{\ell}$  are assumed to  
 3070 be left-handed ( $\tilde{\ell}_L$ ) and their masses are halfway between the  $\tilde{\chi}_1^\pm, \tilde{\chi}_2^0$  and  $\tilde{\chi}_1^0$ . The  $\tilde{\chi}_1^\pm$  and  
 3071  $\tilde{\chi}_2^0$  are allowed to decay only through  $\tilde{\ell}_L$  with all the slepton flavours allowed with equal  
 3072 branching ratios.

This analysis is simulation based and was designed with an integrated luminosity of  $10 \text{ fb}^{-1}$  of data with  $\sqrt{s} = 13 \text{ TeV}$ . The MC simulated samples are the same as those described in Section 4.6.4.

## 8.4 Trigger Selection

This analysis selects events with at least two leptons with  $p_T > 25 \text{ GeV}$  in order to increase signal efficiency. Dileptonic triggers were chosen in the analysis instead of single lepton triggers, to provide uniformity with the Run-2 two-lepton analysis, which exclusively uses dileptonic triggers. The impact of sensitivity in the simulation based signal regions was explored and found to be negligible.

Trigger Type	Trigger Name	Offline $p_T$ threshold [GeV]
Double $e$	HLT_2e12_lhloose_L12EM10VH	14,14
Double $\mu$	HLT_mu18_mu8noL1	14,14
Combined $e\mu$	HLT_e17_lhloose_mu14	14( $e$ ),10( $\mu$ )

Table 8.1: Summary of leptonic triggers used in this analysis and the offline threshold used ensuring that the lepton(s) triggering the event are in the plateau region of the trigger efficiency.

## 8.5 Object Selection

### 8.5.1 Electrons

Baseline electrons must have  $p_T > 10 \text{ GeV}$  and satisfy the loose likelihood ID criteria (refer to likelihood based lepton identification in Section 5.3). Signal electrons must have  $p_T > 25 \text{ GeV}$ , satisfy the medium likelihood ID criteria and be isolated with respect to other high- $p_T$  charged particles, satisfying a loose isolation criteria [155]. Signal electron candidates must also satisfy the IP conditions  $d_0/\sigma_{d_0} < 5$  and  $z_0 \sin\theta < 0.5 \text{ mm}$ . The electron selection is summarised in Table 8.2.

### 8.5.2 Muons

Baseline muons must have  $p_T > 10 \text{ GeV}$ . Signal muons must have  $p_T > 25 \text{ GeV}$ , satisfy the medium likelihood ID criteria and be isolated with respect to other high- $p_T$  charged particles, satisfying the loose criteria as assigned to signal electrons. Signal muon candidates must also satisfy the IP conditions  $d_0/\sigma_{d_0} < 3$  and  $z_0 \sin\theta < 0.5 \text{ mm}$ . The muon selection is summarised in Table 8.3.

Requirement	Value/description
<b>Baseline Electron</b>	
Acceptance	$p_T > 10 \text{ GeV},  \eta^{\text{clust}}  < 2.47$
PID Quality	Loose likelihood
<b>Signal Electron</b>	
Acceptance	$p_T > 25 \text{ GeV},  \eta^{\text{cluster}}  < 2.47$
PID Quality	Medium likelihood
Isolation	Loose
Impact parameter	$ z_0 \sin \theta  < 0.5 \text{ mm}$ $ d_0/\sigma_{d_0}  < 5$

Table 8.2: Summary of the electron selection criteria. The signal selection requirements are applied on top of the baseline selection and after overlap removal.

Requirement	Value/description
<b>Baseline Muon</b>	
Acceptance	$p_T > 10 \text{ GeV},  \eta  < 2.4$
<b>Signal Muon</b>	
Acceptance	$p_T > 25 \text{ GeV},  \eta  < 2.4$
PIDQuality	Medium likelihood
Isolation	Loose
Impact parameter	$ z_0 \sin \theta  < 0.5 \text{ mm}$ $ d_0/\sigma_{d_0}  < 3$

Table 8.3: Summary of the muon selection criteria. The signal selection requirements are applied on top of the baseline selection after overlap removal.

### 3096 8.5.3 Jets

3097 Baseline jets are required to have  $p_T > 20 \text{ GeV}$  and are required to satisfy  $|\eta| < 2.8$ . Signal  
 3098 jets are required to pass a *JVT* cut of  $> 0.59$  if the jet  $p_T$  is less than 60 GeV and it  
 3099 resides with  $|\eta| < 2.4$ . *B*-tagged jets are identified with the *b*-tagger algorithm (MV2c20)  
 3100 with an efficiency of 77% [156]. The jet selection is summarised in Table 8.4.

### 3101 8.5.4 Missing Transverse Momentum

3102 The missing transverse momentum ( $E_T^{\text{miss}}$ ) definition uses selected analysis objects and  
 3103 tracks using an algorithm [157], which assigns topological clusters to reconstructed objects  
 3104 and calibrates according to the object. Calibrated baseline electrons, muons and jets,  
 3105 where the full  $\eta$  range is used for jets, are considered in the  $E_T^{\text{miss}}$  calculation.

Requirement	Value/description
<b>Baseline jet</b>	
Acceptance	$p_T > 20 \text{ GeV},  \eta  < 2.8$
<b>Signal jet</b>	
JVT	$ JVT  > 0.59$ for jets with $p_T < 60 \text{ GeV}$ and $ \eta  < 2.4$
<b>Signal <math>b</math>-jet</b>	
$b$ -tagger Algorithm	MV2c20
Efficiency	77 %

Table 8.4: Summary of the jet and  $b$ -jet selection criteria. The signal selection requirements are applied on top of the baseline requirements after Overlap Removal has been performed.

## 3106 8.6 Signal Region Optimisation

3107 This section motivates the signal optimisation strategy that offers sensitivity to the  $\tilde{\chi}_1^\pm \tilde{\chi}_2^0$   
 3108 via intermediate  $\tilde{\ell}_L$  scenario. The signal regions are optimised using the variable  $Z_N$  as  
 3109 described in Equation 6.1. Two signal regions are defined to target different regions of  
 3110 the  $m(\tilde{\chi}_1^\pm \tilde{\chi}_2^0) - m(\tilde{\chi}_1^0)$  parameter space: SR3 $\ell$ -H targets the high mass spectra, where  
 3111 the  $\tilde{\chi}_1^\pm \tilde{\chi}_2^0$  masses are above 600 GeV and the mass difference with the  $\tilde{\chi}_1^0$  is greater than  
 3112 100 GeV; SR3 $\ell$ -I targets intermediate mass spectra, where the  $\tilde{\chi}_1^\pm \tilde{\chi}_2^0$  masses are greater  
 3113 than 100 GeV and up to 600 GeV and the mass difference with the  $\tilde{\chi}_1^0$  is up to 400 GeV.  
 3114 These signal regions require three leptons, one SFOS pair and veto all events with  $b$ -tagged  
 3115 jets. In the following, this selection is referred to as the baseline selection as motivated in  
 3116 Section 6.4.1.1.

3117 Each cut used in this signal region will be defined and motivated using the event  
 3118 distributions for each variable in tandem with one-dimensional  $Z_N$  distributions. The  
 3119 distributions will be shown at the baseline and at the signal region definition with the cut  
 3120 for the corresponding variable removed, i.e. N-1 stage. For SR3 $\ell$ -H, four high mass signal  
 3121 points are chosen for optimisation, with the following masses for  $m(\tilde{\chi}_1^\pm \tilde{\chi}_2^0, \tilde{\chi}_1^0)$ : (900,300),  
 3122 (800,0), (900,0), (800,200) GeV. For SR3 $\ell$ -I, four intermediate mass signal points are  
 3123 chosen for optimisation, with the following masses for  $m(\tilde{\chi}_1^\pm \tilde{\chi}_2^0, \tilde{\chi}_1^0)$ : (300,200), (600,400),  
 3124 (400,200), (500,400) GeV. The high mass points were chosen because they were outside of  
 3125 the exclusion contour for the combined two and three-lepton analyses shown in Figure 7.8.  
 3126 The intermediate mass points were chosen because they were close to the mass-degenerate  
 3127 region of the parameter space or outside of the aforementioned exclusion contour.

### <sup>3128</sup> 8.6.1 High Mass Signal Region - SR3 $\ell$ -H

#### <sup>3129</sup> 8.6.1.1 Transverse momentum of third-leading lepton

<sup>3130</sup> The event distribution for this variable at baseline is shown in Figure 8.2(a). The SM  
<sup>3131</sup> background dominates in values below 100 GeV with a short tail that drops off at approx-  
<sup>3132</sup> imately 250 GeV. The benchmark signal points display a flat distribution with less skew  
<sup>3133</sup> to lower values of  $p_T$ . Judging from the shapes of these distributions and the requirement  
<sup>3134</sup> for hard- $p_T$  leptons in the high mass region of the parameter space, a cut above 50 GeV  
<sup>3135</sup> would be a good cut to discriminate against the SM background. Figure 8.2(b) shows  
<sup>3136</sup> the N-1 distribution, the magenta line highlights the optimal cut for this variable, which  
<sup>3137</sup> is above 90 GeV. With this cut, the majority of the diboson contribution, which is the  
<sup>3138</sup> dominant irreducible background is removed.

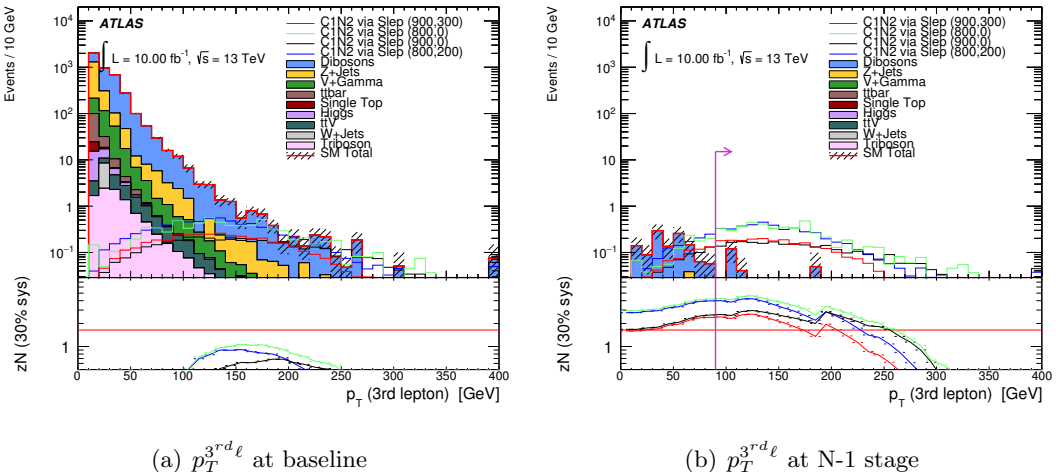


Figure 8.2: Baseline and N-1 distributions for the transverse momentum of the  $3^{rd}$  lepton. The  $Z_N$  curves are produced assuming a flat 30% relative uncertainty to account for systematic uncertainties.

#### <sup>3139</sup> 8.6.1.2 Missing transverse momentum

<sup>3140</sup> The Z+jets SM process dominates the low  $E_T^{\text{miss}}$  values at below 100 GeV at baseline, as  
<sup>3141</sup> shown in Figure 8.3(a), whereas the signal distributions have large tails extending beyond  
<sup>3142</sup> 350 GeV, which is due to the expected heavy  $\tilde{\chi}_1^0$  in the final state. This shows that  
<sup>3143</sup> the  $E_T^{\text{miss}}$  distribution is a good discriminator against the main reducible background.  
<sup>3144</sup> Figure 8.3(b) shows a possible cut is at 80 GeV, with most of the signal yields preserved  
<sup>3145</sup> in the tails of the distribution.

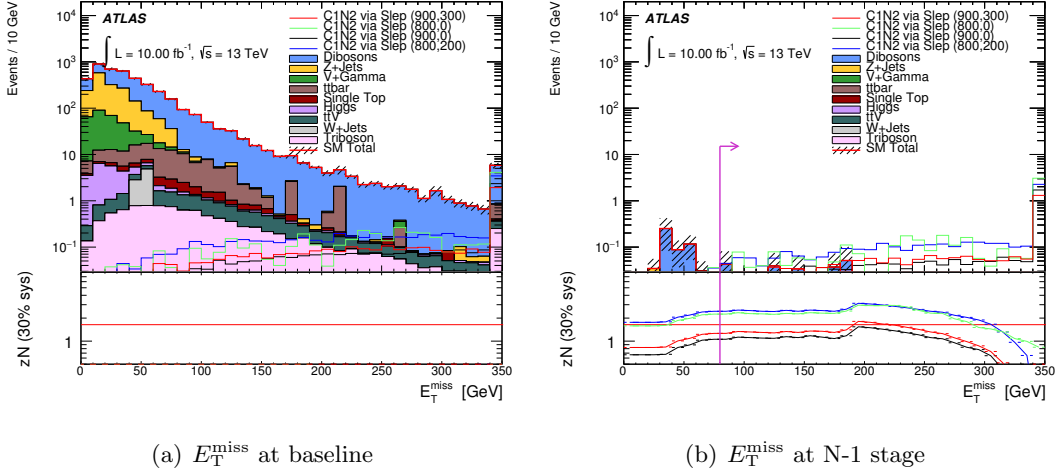


Figure 8.3: Baseline and N-1 distributions for the missing transverse momentum. The  $Z_N$  curves are produced assuming a flat 30% relative uncertainty to account for systematic uncertainties.

### 3146 8.6.1.3 Transverse Mass

3147 The transverse mass variable (refer to Section 6.4.3 for definition) is useful for targeting  
 3148 heavy decaying particles with invisible decay products in the final state. A large value of  
 3149  $m_T$  discriminates against backgrounds containing W-bosons, such as  $WW$  or  $WZ$ , where  
 3150 the kinematic endpoint for these processes should be around the mass of the W-boson,  
 3151 80.3 GeV. For the signal points where the  $\tilde{\chi}_1^\pm \tilde{\chi}_2^0$  are expected to have masses to the order  
 3152 of several hundred GeV, their  $m_T$  distributions are flatter with a larger tail and a much  
 3153 higher kinematic endpoint, which is shown in Figure 8.4(a). Figure 8.4(b) shows the  
 3154 optimal cut at above 100 GeV indicated by the magenta line.

### 3155 8.6.1.4 Invariant Mass of the SFOS leptons

3156 The invariant mass of the SFOS pair of leptons is useful for discriminating for or against  
 3157 processes that contain an on-shell Z-boson which decays to a pair of SFOS leptons with an  
 3158 invariant mass close to the mass of the Z-boson. Both signal and background processes that  
 3159 contain an on-shell Z-boson have a peak in their  $m_{SFOS}$  distribution around 91.2 GeV. The  
 3160 leptons originating from decays via intermediate sleptons do not exhibit this behaviour  
 3161 and show no distinct peak in the distribution. For high mass signal points, the leptons  
 3162 in the final state are hard- $p_T$  and as such will have a large invariant mass, resulting in  
 3163 large tails as shown in Figure 8.5(a). Figure 8.5(b) shows that a cut above 101.2 GeV is  
 3164 effective at removing the Z-containing backgrounds, whilst having minimal effect on the  
 3165 signal yields.

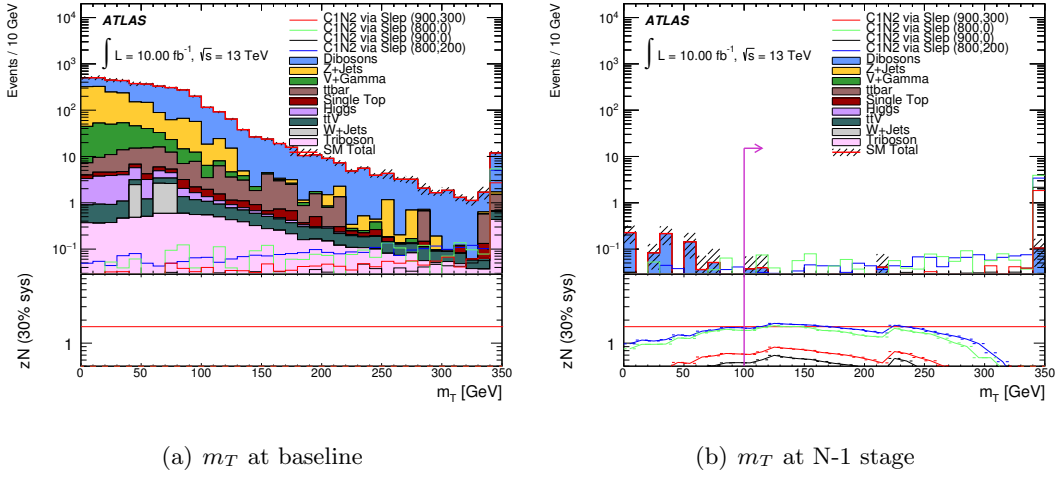


Figure 8.4: Baseline and N-1 distributions for the transverse mass. The  $Z_N$  curves are produced assuming a flat 30% relative uncertainty to account for systematic uncertainties.

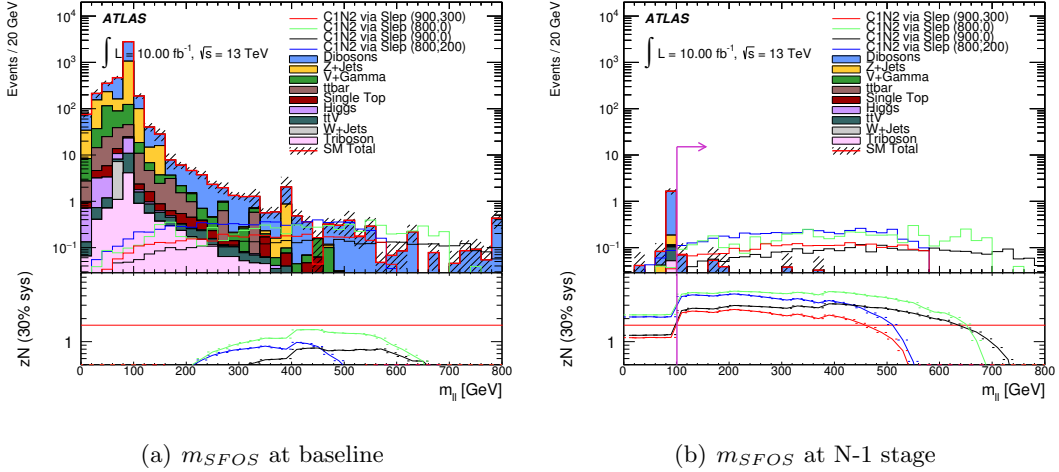


Figure 8.5: Baseline and N-1 distributions for the invariant mass of the SFOS lepton pair. The  $Z_N$  curves are produced assuming a flat 30% relative uncertainty to account for systematic uncertainties.

### <sup>3166</sup> 8.6.1.5 Sum of the transverse momentum of the three leptons

<sup>3167</sup> This variable is used to discriminate for the high- $p_T$  leptons produced from high mass  
<sup>3168</sup>  $\tilde{\chi}_1^\pm \tilde{\chi}_2^0$  decays. The benchmark signal point distributions start at  $\approx 300$  GeV, whereas  
<sup>3169</sup> the SM background starts at 20 GeV as shown in Figure 8.6(a). The N-1 distribution in  
<sup>3170</sup> Figure 8.6(b) shows that a cut of above 400 GeV is effective at maximising the significance  
<sup>3171</sup> for the high mass points and reducing the remaining diboson background contribution.

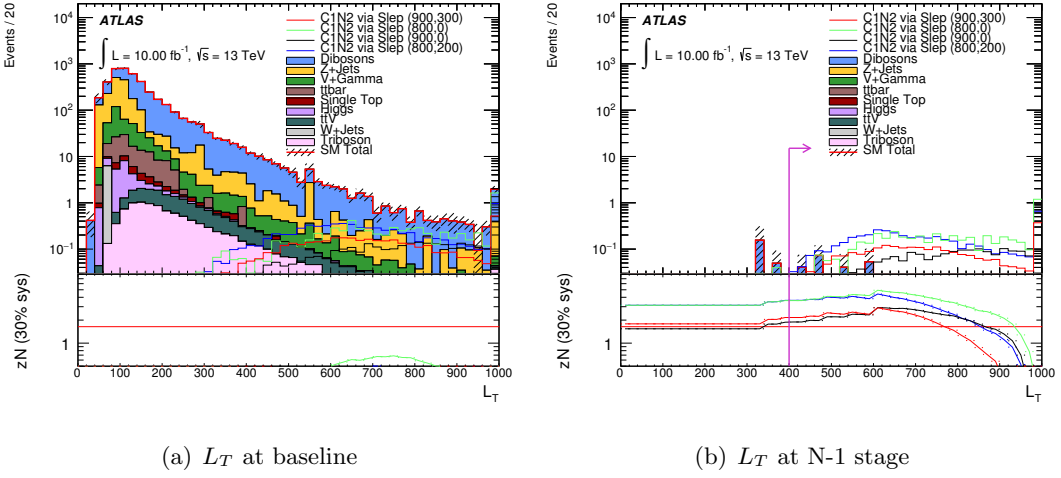


Figure 8.6: Baseline and N-1 distributions for the sum of the transverse momentum of the three leptons. The  $Z_N$  curves are produced assuming a flat 30% relative uncertainty to account for systematic uncertainties.

### 3172 8.6.1.6 Polar angle between SFOS pair of leptons and the missing transverse 3173 momentum

<sup>3174</sup> The topology of the  $E_T^{\text{miss}}$  and the SFOS pair of leptons can be exploited as these final state objects are produced back-to-back in signal events due to the high  $p_T$  of the leptons and large  $E_T^{\text{miss}}$  from the invisible  $\tilde{\chi}_1^0$  carrying the majority of the transverse momentum in the final state. This is shown in Figure 8.7(a), where the signal distributions dominate bins close to  $\pi$ , whereas the SM background distributions are comparatively flat. The

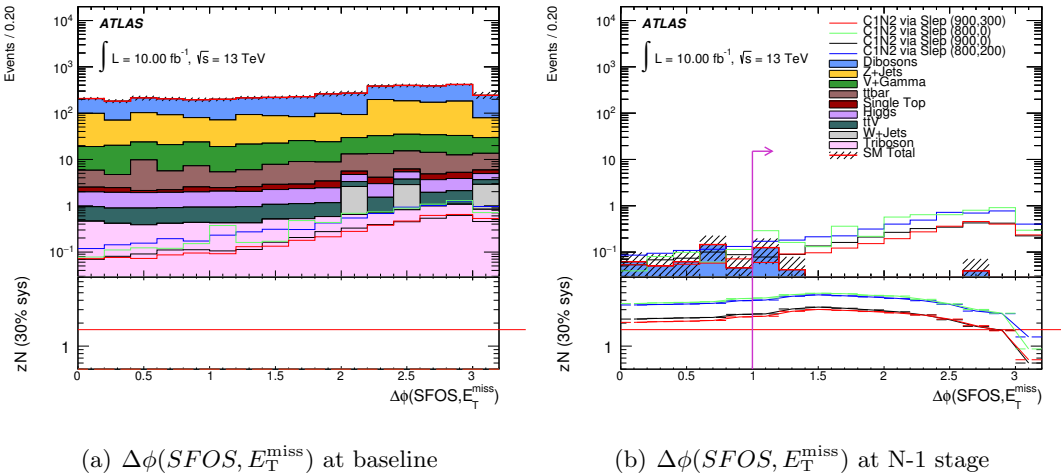


Figure 8.7: Baseline and N-1 distributions  $\Delta\phi$  between the SFOS pair of leptons and missing transverse momentum. The  $Z_N$  curves are produced assuming a flat 30% relative uncertainty to account for systematic uncertainties.

3178

<sup>3179</sup> N-1 distribution shown in Figure 8.7(b) shows an optimal cut placed at 1 is effective at

removing the remaining diboson background contribution.

### 8.6.2 Intermediate Mass Signal Region - SR3 $\ell$ -I

#### 8.6.2.1 Transverse momentum of third-leading lepton

Unlike the high mass signal points, the distribution of the intermediate mass points in  $p_T$  is softer and more like the SM background, with similar peaks around 20-30 GeV as shown in Figure 8.8(a). Consequently, a softer cut on this variable is optimal, to preserve the signal yields. The N-1 distribution shown in Figure 8.8(b) shows the most optimal cut for the points considered is at 30 GeV.

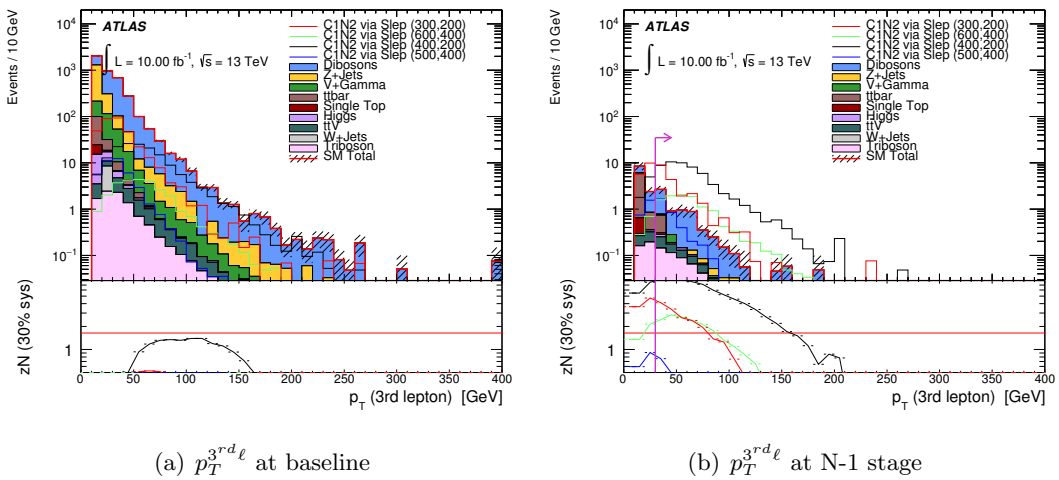


Figure 8.8: Baseline and N-1 distributions for the transverse momentum of the 3<sup>rd</sup> lepton. The  $Z_N$  curves are produced assuming a flat 30% relative uncertainty to account for systematic uncertainties.

3187

#### 8.6.2.2 Missing transverse momentum

Similar to the high mass signal points, the  $E_T^{miss}$  distribution of the intermediate mass points are flatter than the SM background with large tails, due to the heavy neutralinos produced in the final state. As the requirement on the  $p_T$  of the third lepton is softer, the  $E_T^{miss}$  cut can be tighter to remove the Z+jets and diboson contributions, as shown in Figure 8.9(b), a cut of above 120 GeV is optimal.

#### 8.6.2.3 Transverse Mass

The transverse mass is strongly correlated to the  $E_T^{miss}$  in an event, as the mass of the decaying particles increases, the amount of energy available to the final state particles increases. Consequently, the distribution of  $m_T$  shows similar behaviour to  $E_T^{miss}$  for the

<sup>3198</sup> intermediate mass points. A similar cut of above 110 GeV is used to discriminate against the diboson SM background process, as shown in Figure 8.10(b).

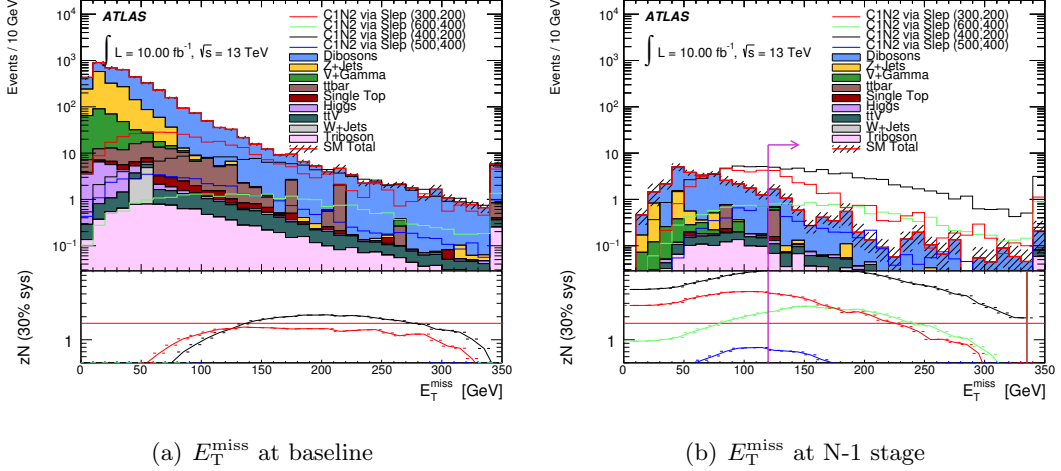


Figure 8.9: Baseline and N-1 distributions for the missing transverse momentum. The  $Z_N$  curves are produced assuming a flat 30% relative uncertainty to account for systematic uncertainties.

<sup>3199</sup>

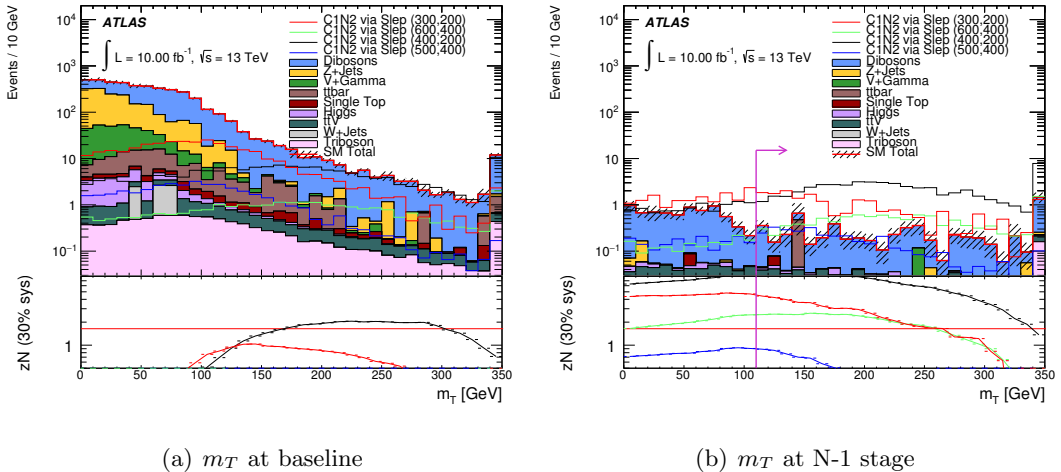


Figure 8.10: Baseline and N-1 distributions for the transverse mass. The  $Z_N$  curves are produced assuming a flat 30% relative uncertainty to account for systematic uncertainties.

### <sup>3200</sup> 8.6.2.4 Invariant Mass of the SFOS leptons

<sup>3201</sup> The leptons produced in the final state are significantly softer for the intermediate mass  
<sup>3202</sup> points than the high mass points. The  $m_{\text{SFOS}}$  spectrum is softer and the signal yields are  
<sup>3203</sup> concentrated in a much smaller range of up to 200 GeV as shown in Figure 8.11(a). In  
<sup>3204</sup> order to discriminate against the Z-containing backgrounds, events with a SFOS pair of  
<sup>3205</sup> leptons with an invariant mass within 10 GeV of on-shell Z-boson mass are vetoed.

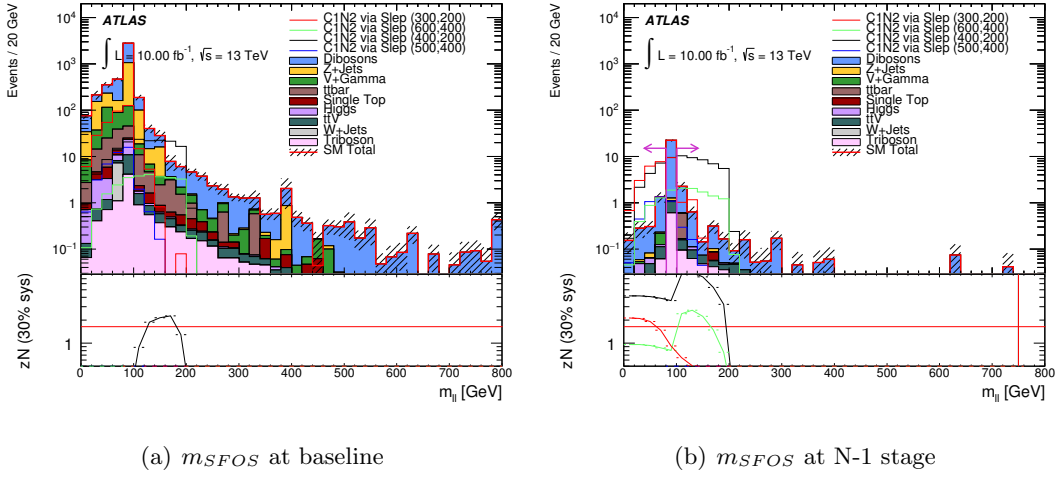


Figure 8.11: Baseline and N-1 distributions for the invariant mass of the SFOS lepton pair. The  $Z_N$  curves are produced assuming a flat 30% relative uncertainty to account for systematic uncertainties.

### 3206 8.6.3 Signal Region Summary

3207 The preliminary signal regions developed for an early 13 TeV analysis are defined in  
 3208 Table 8.5. The cut-by-cut yields for SR $3\ell$ -H and SR $3\ell$ -I are given in Tables 8.6 and 8.7  
 3209 respectively. Table 8.6 shows the discriminating power of each cut in the high mass SR,  
 3210 which culminates in reducing the total SM background from  $\approx 4000$  events to  $< 1$  event.  
 3211 The dominating background in the SR is the diboson processes, which consist of ZZ, WZ  
 3212 and WW. Considering the benchmark signal point yields, the SR $3\ell$ -H signal acceptance  
 3213 is  $\approx 60\%$  with respect to baseline yields. This shows that this signal region is effective at  
 3214 preserving the high mass signal points, by targeting the tails of the distributions of the  
 3215 cut variables, where these signal points dominate.

3216 Table 8.7 shows the discriminating power of each cut in the intermediate mass SR,  
 3217 which culminates in reducing the total SM background from  $\approx 4000$  events to 6.5 events.  
 3218 The dominating background in this SR are the diboson and triboson processes. Consider-  
 3219 ing the benchmark signal point yields, the SR $3\ell$ -I signal acceptance varies from 10-35%.  
 3220 Although the signal acceptance for this region is lower than for SR $3\ell$ -H, the production  
 3221 cross-section for the light mass points are higher, leading to overall higher yields than the  
 3222 high mass points.

Table 8.5: Three lepton Signal Regions. Units are in GeV.

Variable	SR3 $\ell$ -I	SR2 $\ell$ -H
lepton $p_T >$	30	90
$E_T^{\text{miss}} >$	120	80
$m_T >$	110	100
$m_{SFOS} >$	81.2 ( $< 101.2$ )	101.2
$L_T >$	–	400
$\Delta\phi(SFOS, E_T^{\text{miss}}) >$	–	1

## 3223 8.7 Significance in Signal Regions

3224 An estimation of the performance of each signal region for the chosen SUSY scenarios  
 3225 made by calculating the significance  $Z_N$  for each mass point and filling a three dimensional  
 3226 histogram with the significance as a function of the parameter space. The  $x$  axis displays  
 3227 the  $\tilde{\chi}_1^\pm \tilde{\chi}_2^0$  masses, the  $y$  axis displays the  $\tilde{\chi}_1^0$  mass and the  $z$  axis displays the significance.  
 3228 A significance value of 1.64 or greater corresponds to an exclusion of the SUSY scenario  
 3229 considered with 95% confidence level [148] [149].

### 3230 8.7.1 Significance in Intermediate Mass Signal Region

3231 Figure 8.12 displays the two-dimensional histogram for the SR3 $\ell$ -I scenario where a flat  
 3232 30% relative uncertainty is considered in the  $Z_N$  calculation. This signal region provides  
 3233 sensitivity to the intermediate mass signal points.  $\tilde{\chi}_1^\pm \tilde{\chi}_2^0$  masses up to 700 GeV with  $\tilde{\chi}_1^0$   
 3234 masses  $\leq 400$  GeV are excluded. There is sensitivity to the near mass-degenerate region  
 3235 with  $\tilde{\chi}_1^\pm \tilde{\chi}_2^0$  masses up to 400 GeV excluded with a mass splitting of 50 GeV. The gain in  
 3236 sensitivity to the low mass points is achieved by having less stringent cuts on the  $p_T$  of the  
 3237 leptons and vetoing events with two leptons close to the Z-mass, as the leptons from this  
 3238 scenario originate from sleptons. As the Z-mass window is small - 20 GeV - the majority  
 3239 of the signal event yields are retained.

Sample	Baseline	$p_T^{3rd\ell} > 90$	$m_T > 100$	$E_T^{\text{miss}} > 80$	$m_{SFOS} > 101.2$	$L_T > 400$	$\Delta\phi(SFOS, E_T^{\text{miss}}) > 1$
$t\bar{t}$	93.69 ± 6.77	0.0 ± 0.0	0.0 ± 0.0	0.0 ± 0.0	0.0 ± 0.0	0.0 ± 0.0	0.0 ± 0.0
Single top	11.48 ± 0.63	0.0 ± 0.0	0.0 ± 0.0	0.0 ± 0.0	0.0 ± 0.0	0.0 ± 0.0	0.0 ± 0.0
$Z + \text{jets}$	1370.83 ± 104.82	3.83 ± 1.53	0.97 ± 0.68	0.22 ± 0.08	0.02 ± 0.01	0.02 ± 0.01	0.0 ± 0.0
$W + \text{jets}$	6.01 ± 3.51	0.0 ± 0.0	0.0 ± 0.0	0.0 ± 0.0	0.0 ± 0.0	0.0 ± 0.0	0.0 ± 0.0
Diboson	2427.96 ± 18.5	25.17 ± 1.65	8.08 ± 0.81	3.87 ± 0.49	0.76 ± 0.22	0.49 ± 0.14	0.19 ± 0.09
$t\bar{t} + V$	10.41 ± 0.09	0.4 ± 0.02	0.19 ± 0.01	0.13 ± 0.01	0.04 ± 0.01	0.03 ± 0.01	0.02 ± 0.0
$V/\gamma$	261.65 ± 4.65	1.14 ± 0.09	0.34 ± 0.05	0.03 ± 0.02	0.0 ± 0.0	0.0 ± 0.0	0.0 ± 0.0
Higgs	20.4 ± 0.1	0.03 ± 0.01	0.01 ± 0.01	0.01 ± 0.01	0.0 ± 0.0	0.0 ± 0.0	0.0 ± 0.0
Triboson	9.64 ± 0.09	0.33 ± 0.02	0.22 ± 0.01	0.17 ± 0.01	0.09 ± 0.01	0.07 ± 0.01	0.04 ± 0.01
Total background	4212.06 ± 106.82	30.9 ± 2.25	9.82 ± 1.05	4.42 ± 0.49	0.92 ± 0.22	0.61 ± 0.14	0.25 ± 0.09
<hr/>							
via Slep (800,200)	7.72 ± 0.12	5.93 ± 0.11	5.57 ± 0.1	5.39 ± 0.1	5.17 ± 0.1	5.11 ± 0.1	4.58 ± 0.09
via Slep (900,0)	4.1 ± 0.06	3.36 ± 0.06	3.19 ± 0.06	3.12 ± 0.06	3.06 ± 0.06	3.05 ± 0.06	2.67 ± 0.05
via Slep (800 ,0)	7.59 ± 0.38	6.02 ± 0.34	5.73 ± 0.33	5.61 ± 0.33	5.48 ± 0.33	5.39 ± 0.32	5.0 ± 0.31
via Slep (900 , 300)	4.06 ± 0.06	3.15 ± 0.06	2.94 ± 0.05	2.85 ± 0.05	2.74 ± 0.05	2.72 ± 0.05	2.43 ± 0.05

Table 8.6: MC estimated yields per cut in high mass signal region SR3 $\ell$ -H. The uncertainties are statistical only.

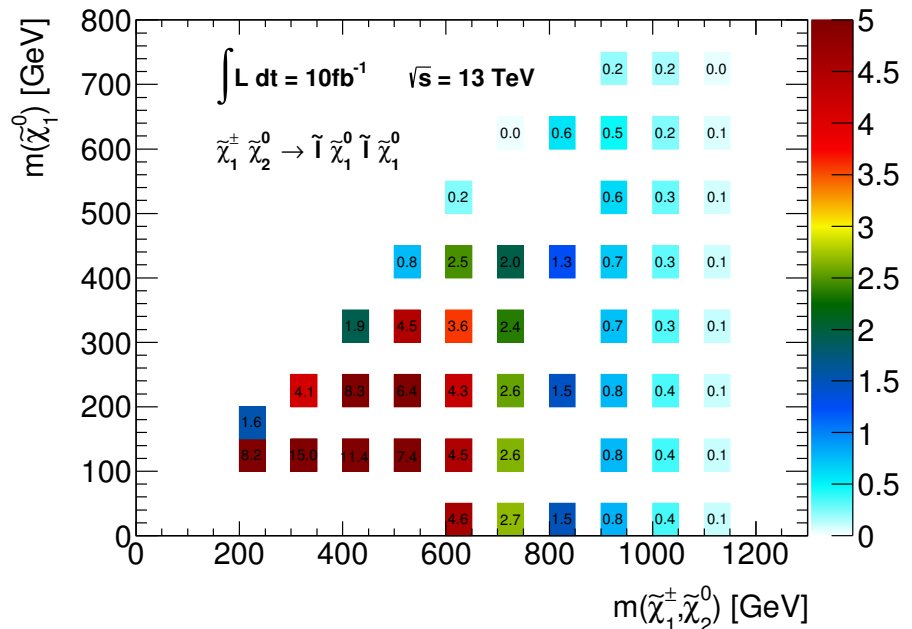
### 3240 8.7.2 Significance in High Mass Signal Region

3241 Figure 8.13(a) displays the two-dimensional histogram for the SR3 $\ell$ -H scenario where a flat  
 3242 30% relative uncertainty is considered in the  $Z_N$  calculation. This signal region provides  
 3243 sensitivity to the high mass signal points, where  $\tilde{\chi}_1^\pm \tilde{\chi}_2^0$  masses up to 1 TeV are excluded.  
 3244 The smallest mass splitting of 50 GeV, suffers in this region, with no sensitivity seen for  
 3245 the points closest to the mass-degenerate region. This is due to low  $p_T$  spectra of the  
 3246 final state products in this region, which are removed with the stringent cuts in the high  
 3247 mass SR. The decrease in significance with increasing  $\tilde{\chi}_1^\pm \tilde{\chi}_2^0$  mass is caused by decreasing  
 3248 cross-section for the considered process. Figure 8.13(b) shows the sensitivity with 100%  
 3249 relative uncertainty considered in the  $Z_N$  calculation, this adjustment was considered due  
 3250 to the low statistics in this signal region, which would lead to large systematic uncertainties  
 3251 on the data driven fake estimation. Using 100% relative uncertainty gives a “worst case  
 3252 scenario” in terms of sensitivity.  $\tilde{\chi}_1^\pm \tilde{\chi}_2^0$  masses can be excluded up to 900 GeV with this  
 3253 scenario, which corresponds to a 100 GeV worsening of exclusion reach compared to the  
 3254 conservative 30% relative uncertainty scenario.

### 3255 8.7.3 Combined Significance in Signal Regions

3256 The two signal regions offer sensitivity to different regions of the parameter space, the  
 3257 signal regions are not orthogonal and are can not be combined. To present the best case  
 3258 with the two signal regions, the best significance is shown per point, considering SR3 $\ell$ -H  
 3259 and SR3 $\ell$ -I in Figure 8.14(a). The best signal region per point is shown in Figure 8.14(b).  
 3260 This shows that SR3 $\ell$ -H dominates in providing sensitivity to  $\tilde{\chi}_1^\pm \tilde{\chi}_2^0$  masses above 500 GeV  
 3261 and SR3 $\ell$ -I dominates in providing sensitivity to the  $\tilde{\chi}_1^\pm \tilde{\chi}_2^0$  masses below 500 GeV and the  
 3262 near mass degenerate region.

3263 Sensitivity to electroweak SUSY production profits from increasing luminosity, given  
 3264 the relatively low production cross-section compared to strong SUSY production. With  
 3265 the combination of increasing luminosity and variables such as  $E_T^{\text{miss}}$  and  $m_T$ , which offer  
 3266 more discriminatory power at higher beam energies, electroweak production of SUSY will  
 3267 continue to be well motivated and could provide an insight into BSM physics in future  
 3268 LHC data.

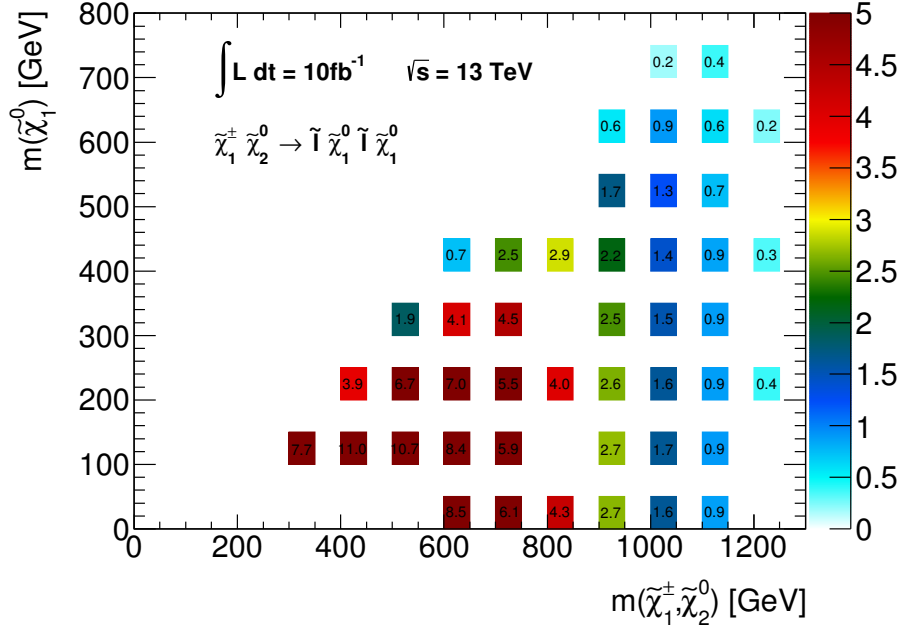


(a) Significance with MC-only estimates - 30% relative uncertainty.

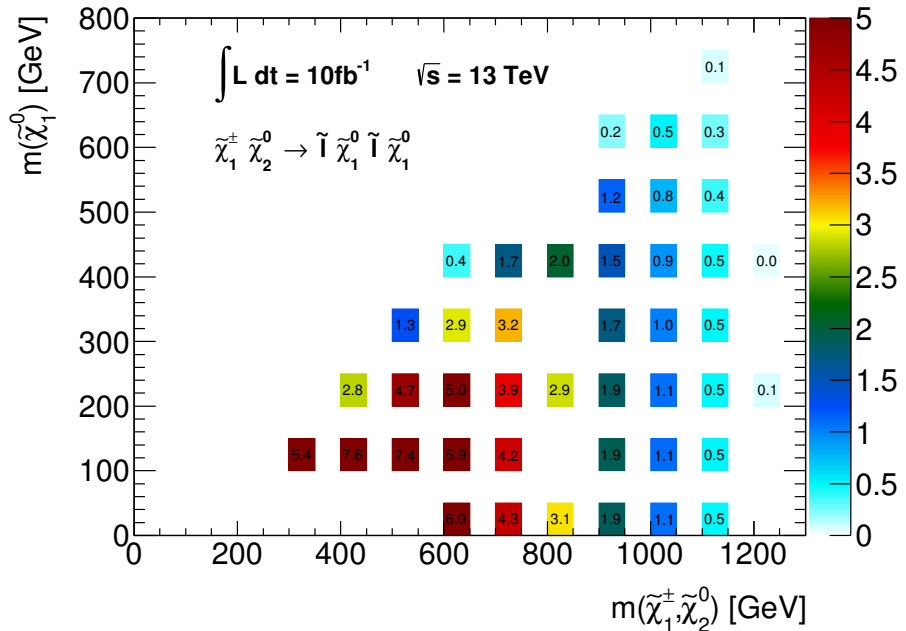
Figure 8.12: Significance in SR3 $\ell$ -I. The calculation of the significance values are based on MC-only for all SM backgrounds. The uncertainty in the MC background estimate is 30% flat uncertainty to cover systematic uncertainty.

Sample	Baseline	$p_T^{3^{rd}\ell} > 30$	$E_T^{\text{miss}} > 120$	$m_T > 110$	$ m_{SFOS} - m_Z  > 10$
$t\bar{t}$	93.69 ± 6.77	5.2 ± 1.57	0.93 ± 0.66	0.42 ± 0.42	0.42 ± 0.42
Single top	11.48 ± 0.63	0.57 ± 0.14	0.07 ± 0.05	0.03 ± 0.03	0.03 ± 0.03
Z+jets	1370.83 ± 104.82	99.1 ± 15.46	-0.18 ± 0.89	0.23 ± 0.09	0.1 ± 0.07
W+jets	6.01 ± 3.51	0.0 ± 0.0	0.0 ± 0.0	0.0 ± 0.0	0.0 ± 0.0
Diboson	2427.96 ± 18.5	1009.66 ± 12.97	68.61 ± 1.78	25.88 ± 1.17	4.9 ± 0.55
$t\bar{t} + V$	10.41 ± 0.09	6.19 ± 0.07	1.54 ± 0.03	0.75 ± 0.02	0.3 ± 0.02
V/ $\gamma$	261.65 ± 4.65	65.55 ± 2.22	0.13 ± 0.09	0.12 ± 0.09	0.1 ± 0.09
Higgs	20.4 ± 0.1	2.51 ± 0.05	0.18 ± 0.02	0.1 ± 0.02	0.08 ± 0.02
Triboson	9.64 ± 0.09	5.53 ± 0.07	1.63 ± 0.03	1.14 ± 0.03	0.54 ± 0.02
Total background	4212.06 ± 106.82	1194.31 ± 20.37	72.91 ± 2.1	28.69 ± 1.25	6.48 ± 0.7
via Slep (500,400)	41.22 ± 0.6	24.17 ± 0.47	7.14 ± 0.26	4.48 ± 0.21	3.43 ± 0.18
via Slep (400,200)	155.47 ± 1.93	137.16 ± 1.82	75.5 ± 1.36	64.3 ± 1.25	54.76 ± 1.15
via Slep (600 ,400)	26.72 ± 0.33	23.81 ± 0.31	14.75 ± 0.25	12.98 ± 0.23	11.06 ± 0.21
via Slep (300, 200)	331.23 ± 4.96	192.17 ± 3.81	51.21 ± 2.01	29.31 ± 1.52	20.61 ± 1.27

Table 8.7: MC estimated yields per cut in intermediate mass signal region SR3 $\ell$ -I. The uncertainties are statistical only. Negative events for Z+jets due to negative weights at NLO assigned by SHERPA.



(a) Significance with MC-only estimates - 30% relative uncertainty.



(b) Significance with MC-only estimates - 100% relative uncertainty.

Figure 8.13: Significance in SR3 $\ell$ -H. The calculation of the significance values are based on MC-only for all SM backgrounds. The uncertainty in the MC background estimate is (a) 30% or (b) 100% flat uncertainty to cover systematic uncertainty.

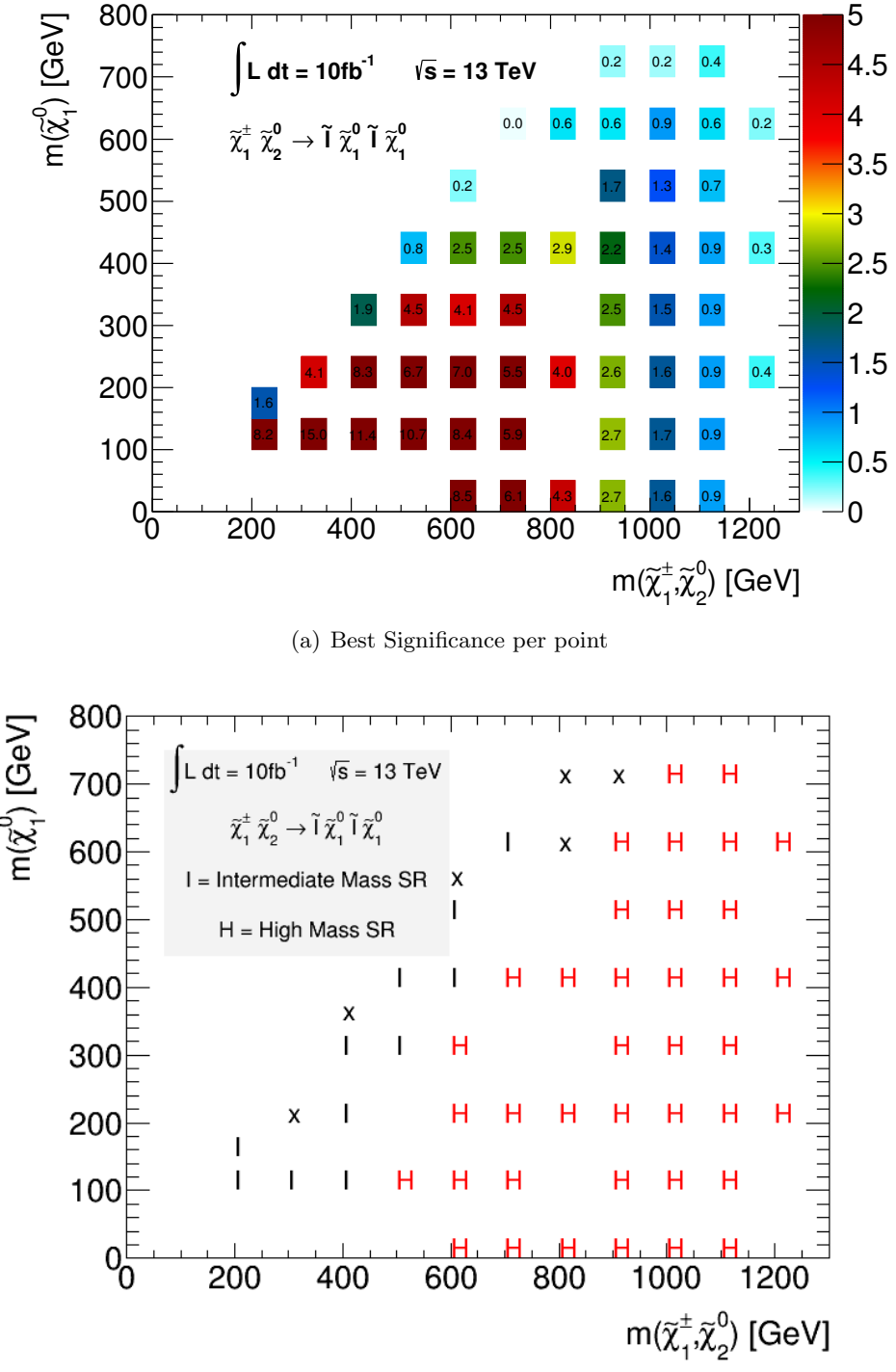


Figure 8.14: (a) Best expected significance and (b) best signal region per  $\tilde{\chi}_1^\pm \tilde{\chi}_2^0$  production via  $\tilde{l}$  point in SR3 $\ell$ . The calculation of the significance values are based on MC-only for all SM backgrounds. The uncertainty in the MC background estimate is a 30% flat uncertainty to cover systematic uncertainty. In (b) H refers to the SR3 $\ell$ -H signal region, I refers to the SR3 $\ell$ -I signal region and X indicates a zero  $Z_N$  value for both regions.

## <sup>3269</sup> Chapter 9

## <sup>3270</sup> Conclusions

<sup>3271</sup> This thesis presents results produced by ATLAS on the search for the electroweak pro-  
<sup>3272</sup> duction of supersymmetric particles in events with three leptons and missing transverse  
<sup>3273</sup> energy, with particular focus on compressed scenarios, using the full  $\mathcal{L} = 20.3 \text{ fb}^{-1}$  dataset  
<sup>3274</sup> at  $\sqrt{s} = 8 \text{ TeV}$ .

<sup>3275</sup> R-parity conserving supersymmetric scenarios were targeted with optimised selection  
<sup>3276</sup> criteria applied to events containing three electrons or muons. For scenarios where the mass  
<sup>3277</sup> of the  $\tilde{\chi}_1^\pm, \tilde{\chi}_2^0$  is near degenerate with the  $\tilde{\chi}_1^0$ , low- $p_T$  leptons and an initial-state-radiation  
<sup>3278</sup> jet were required in the event selection. No significant deviation was seen between observed  
<sup>3279</sup> data and Standard Model expectations, within the statistical and systematic uncertainties.  
<sup>3280</sup> A statistical interpretation of the results was conducted in order to set 95% CL exclusion  
<sup>3281</sup> limits on the mass parameters of the models considered, as well as model-independent  
<sup>3282</sup> limits on the visible cross-section for relevant beyond-the-Standard Model scenarios.

<sup>3283</sup> Simplified models were considered where pure-wino  $\tilde{\chi}_1^\pm \tilde{\chi}_2^0$ ,  $\tilde{\chi}_1^\pm \tilde{\chi}_1^\mp$  and pure higgsino  
<sup>3284</sup>  $\tilde{\chi}_2^0 \tilde{\chi}_3^0$  pairs are produced, which then decay with 100% branching fraction to three-lepton  
<sup>3285</sup> final states. Limits at 95% CL were extracted for chargino and neutralino decays via  
<sup>3286</sup> intermediate sleptons, by combining results from this (compressed spectra) analysis, the  
<sup>3287</sup> recent same-sign two-lepton analysis [3] and previously published analyses [133]. Chargino  
<sup>3288</sup> and heavy neutralino masses up to 740 GeV were excluded at 95% CL for massless  $\tilde{\chi}_1^0$ . This  
<sup>3289</sup> improves on existing mass limits by approximately 20 GeV. More significant improvements  
<sup>3290</sup> were seen in the region of the parameter space where the  $\tilde{\chi}_1^\pm, \tilde{\chi}_2^0$  are nearly degenerate  
<sup>3291</sup> with the  $\tilde{\chi}_1^0$ . In this compressed region, the main improvements come from the analysis  
<sup>3292</sup> performed by the author and presented in this thesis.

<sup>3293</sup> Looking forward to Run-2, a first optimisation of an event selection for electroweak  
<sup>3294</sup> production of supersymmetric particles at 13 TeV was conducted. To that purpose, Monte

3295 Carlo simulated events were used, based on a projected integrated luminosity of  $10 \text{ fb}^{-1}$  in  
3296 13 TeV data. The preliminary 13 TeV analysis targets two distinct scenarios, with different  
3297 regimes for mass splittings between the  $\tilde{\chi}_1^\pm \tilde{\chi}_2^0$  and  $\tilde{\chi}_1^0$ . At the time of writing, the signal  
3298 region optimisation for  $\tilde{\chi}_1^\pm \tilde{\chi}_2^0$  production with decays via intermediate sleptons was still  
3299 ongoing, with improvements expected on the selection presented in the last chapter of this  
3300 thesis. With sensitivity to electroweak supersymmetry production expected to improve  
3301 with luminosity, the ATLAS detector will continue to probe supersymmetry beyond the  
3302 limits set in Run-1.

<sup>3303</sup> **Appendix A**

<sup>3304</sup> **Multilepton Trigger Results**

<sup>3305</sup> **A.1 Introduction**

<sup>3306</sup> This section provides one-dimensional efficiencies and scale factors for the leptonic triggers  
<sup>3307</sup> used in the analysis described in Chapter 6. The efficiencies are for a given leptonic leg of  
<sup>3308</sup> the trigger chain are derived using the Tag and Probe method as described in Section 5.2.  
<sup>3309</sup> These are shown as a function of  $p_T$ ,  $\eta$  and number of primary vertices. The scale factors  
<sup>3310</sup> are defined as:

$$sf_{trig} = \frac{\epsilon_{trig}^{Data}}{\epsilon_{trig}^{MC}}, \quad (\text{A.1})$$

<sup>3311</sup> and are shown for each trigger as a function of the aforementioned variables. The trigger  
<sup>3312</sup> efficiency scale factors are found to be 1 within a 29% uncertainty for the leptonic triggers,  
<sup>3313</sup> which are treated as a systematic in the analysis. These results are given for reference  
<sup>3314</sup> only.

<sup>3315</sup> A.2 Three-Lepton Trigger Efficiencies

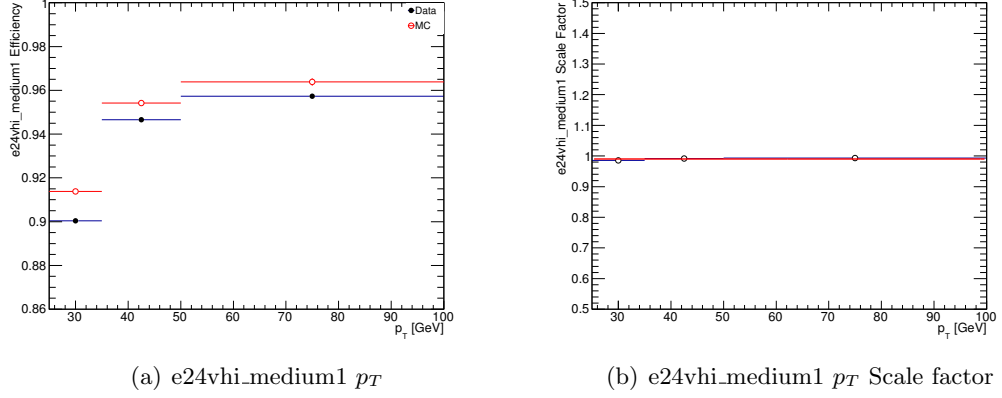


Figure A.1: Trigger efficiency for EFe24vhi\_medium1 as a function of electron  $p_T$  in MC and data and efficiency scale factor. Uncertainties are statistical.

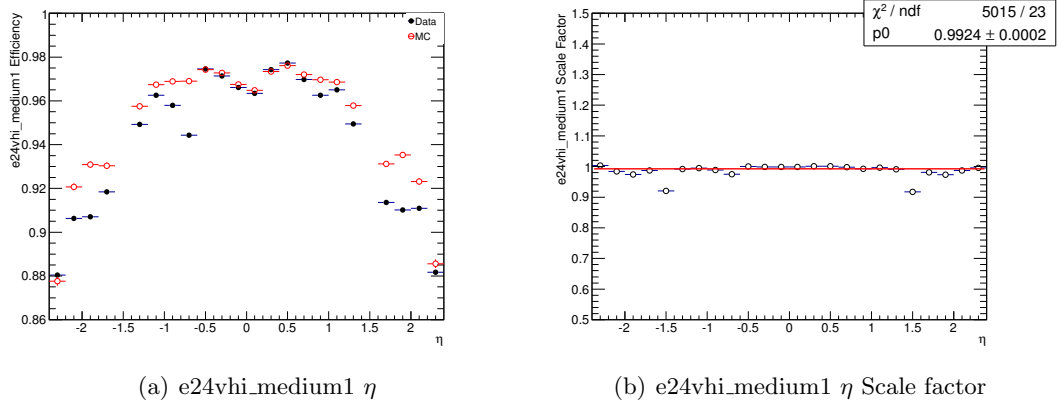


Figure A.2: Trigger efficiency for EFe24vhi\_medium1 as a function of electron  $\eta$  in MC and data and efficiency scale factor. Uncertainties are statistical.

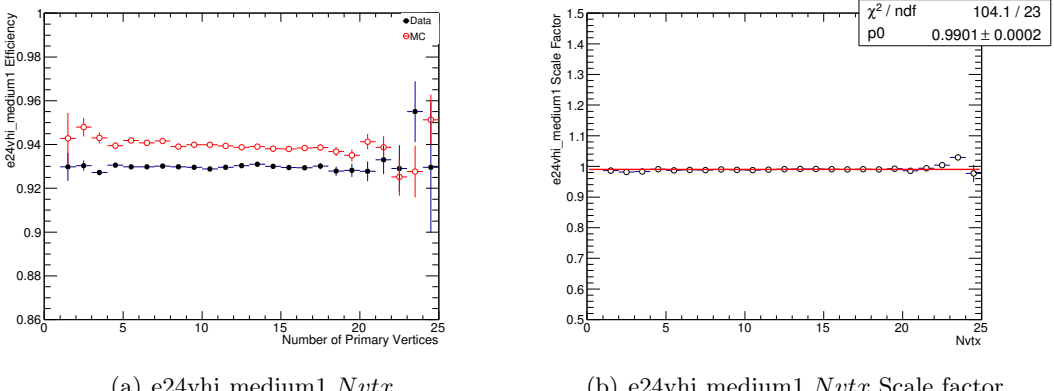


Figure A.3: Trigger efficiency for EFe24vhi\_medium1 as a function of electron  $Nvtx$  in MC and data and efficiency scale factor. Uncertainties are statistical.

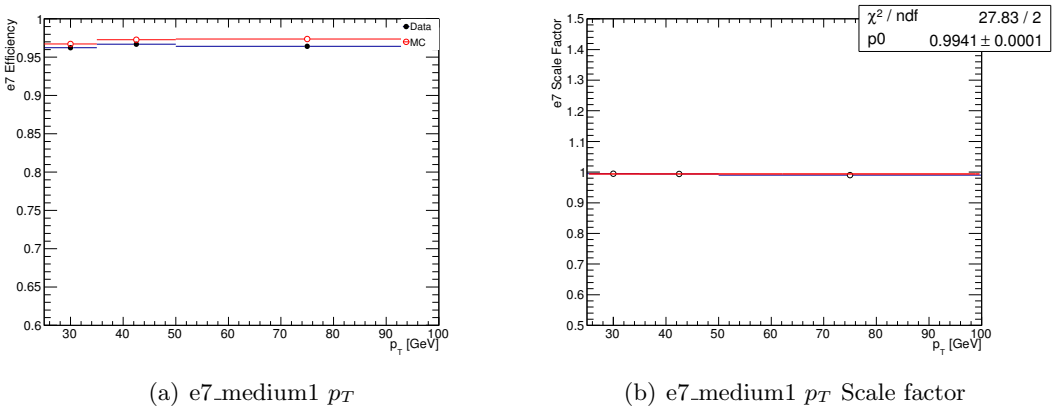


Figure A.4: Trigger efficiency for EFe7\_medium1 as a function of electron  $p_T$  in MC and data and efficiency scale factor. Uncertainties are statistical.

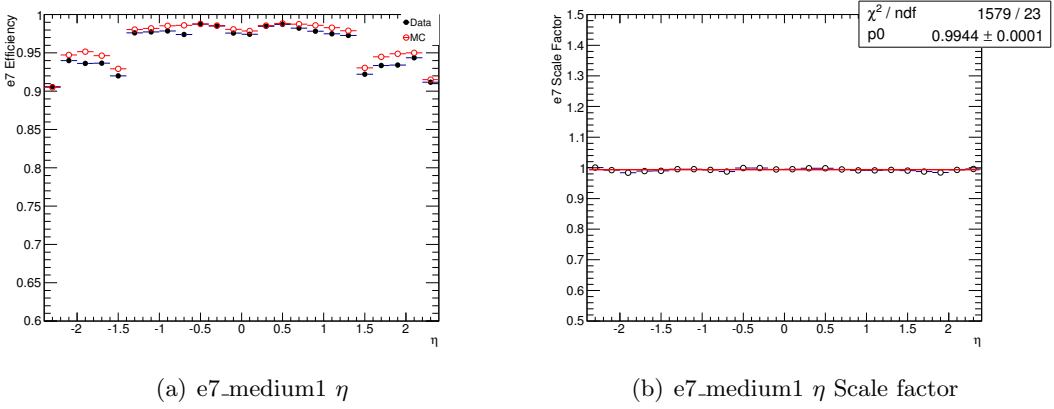


Figure A.5: Trigger efficiency for EFe7\_medium1 as a function of electron  $\eta$  in MC and data and efficiency scale factor. Uncertainties are statistical.

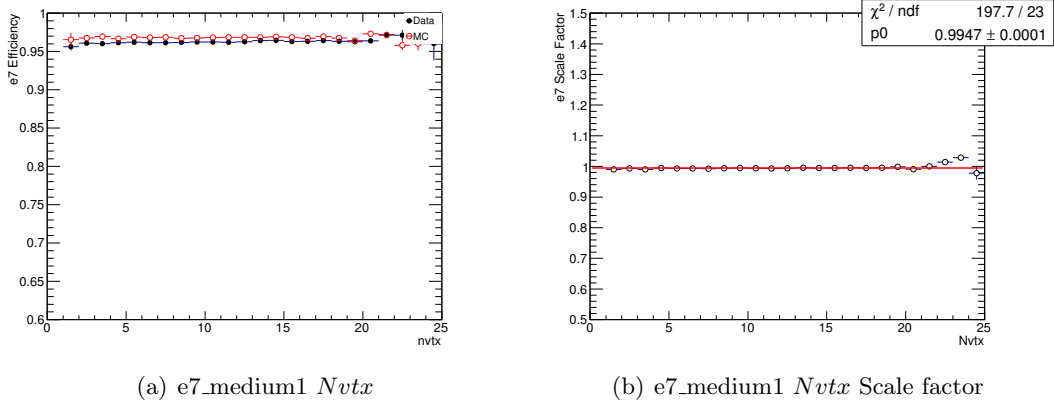


Figure A.6: Trigger efficiency for EFe7\_medium1 as a function of electron  $N_{vtx}$  in MC and data and efficiency scale factor. Uncertainties are statistical.

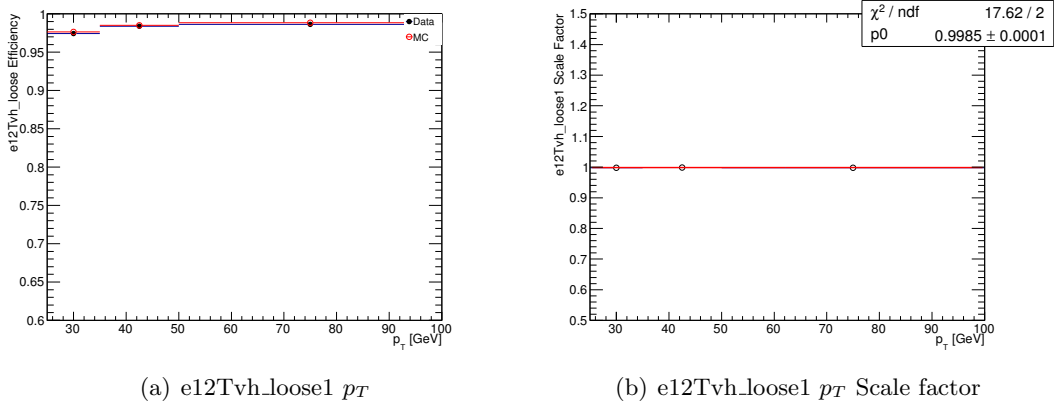


Figure A.7: Trigger efficiency for EFe12Tvh\_loose1 as a function of electron  $p_T$  in MC and data and efficiency scale factor. Uncertainties are statistical.

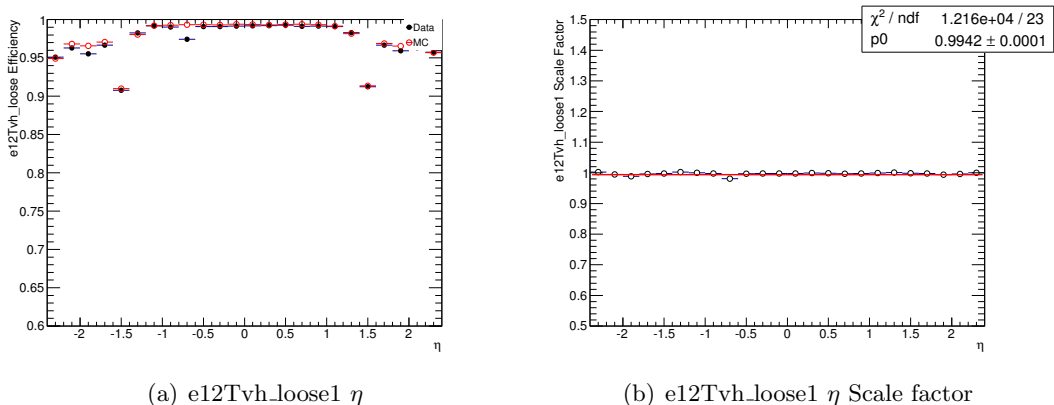


Figure A.8: Trigger efficiency for EFe12Tvh\_loose1 as a function of electron  $\eta$  in MC and data and efficiency scale factor. Uncertainties are statistical.

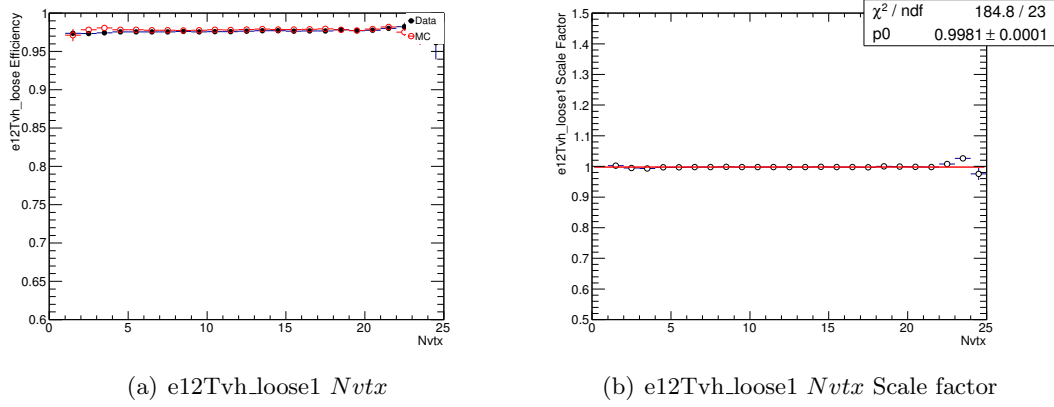


Figure A.9: Trigger efficiency for EFe12Tvh\_loose1 as a function of electron  $Nvtx$  in MC and data and efficiency scale factor. Uncertainties are statistical.

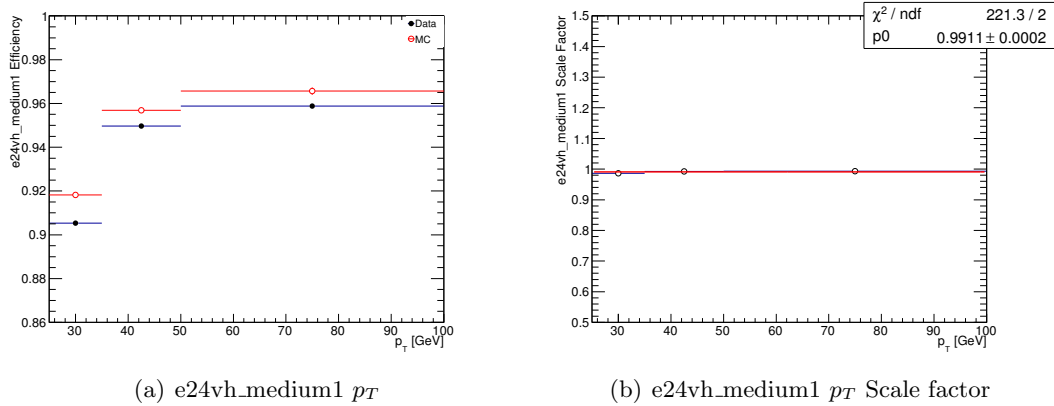


Figure A.10: Trigger efficiency for EFe24vh\_medium1 as a function of electron  $p_T$  in MC and data and efficiency scale factor. Uncertainties are statistical.

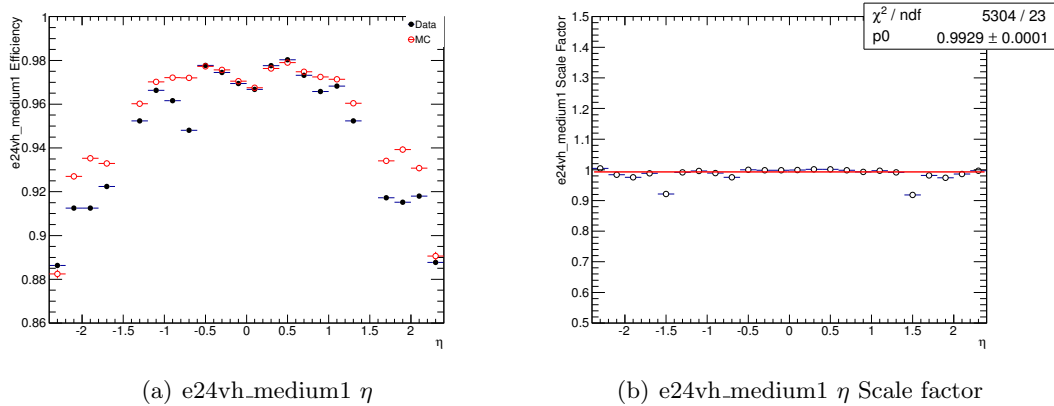


Figure A.11: Trigger efficiency for EFe24vh\_medium1 as a function of electron  $\eta$  in MC and data and efficiency scale factor. Uncertainties are statistical.

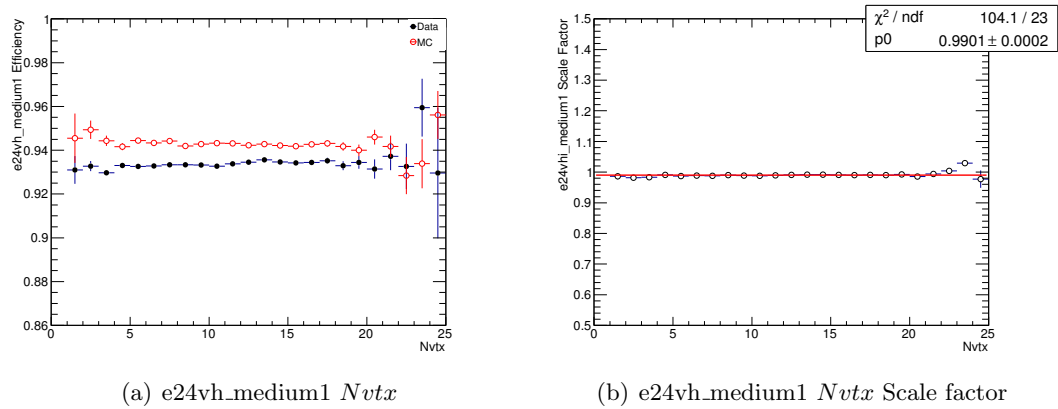


Figure A.12: Trigger efficiency for EFe24vh\_medium1 as a function of electron  $N_{vtx}$  in MC and data and efficiency scale factor. Uncertainties are statistical.

<sup>3316</sup> A.2.0.1 Muon Trigger Efficiencies

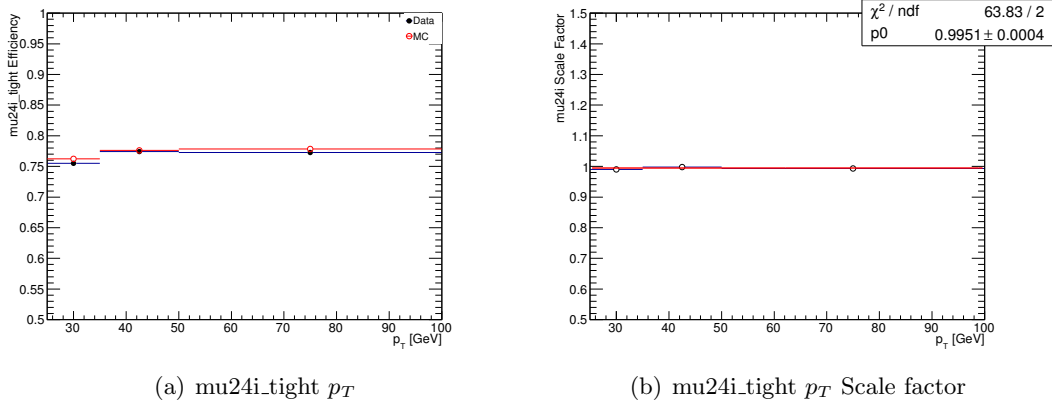


Figure A.13: Trigger efficiency for EFmu24i\_tight as a function of muon  $p_T$  in MC and data and efficiency scale factor. Uncertainties are statistical.

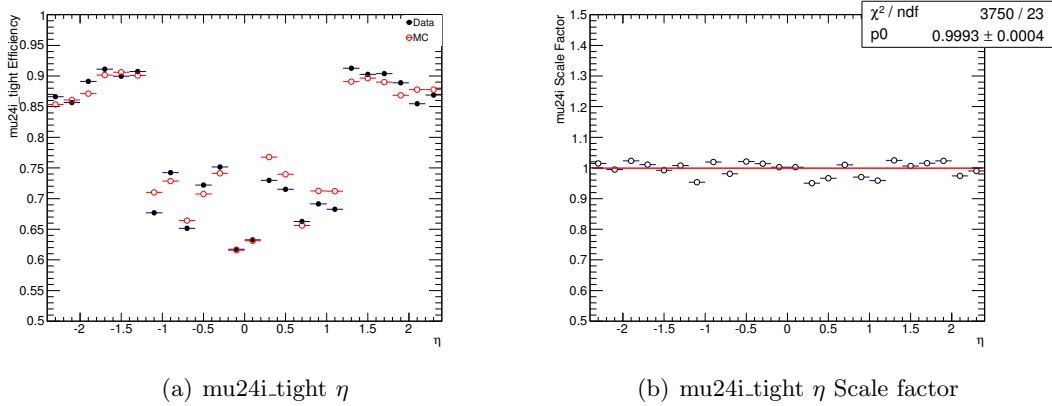


Figure A.14: Trigger efficiency for EFmu24i\_tight as a function of muon  $\eta$  in MC and data and efficiency scale factor. Uncertainties are statistical.

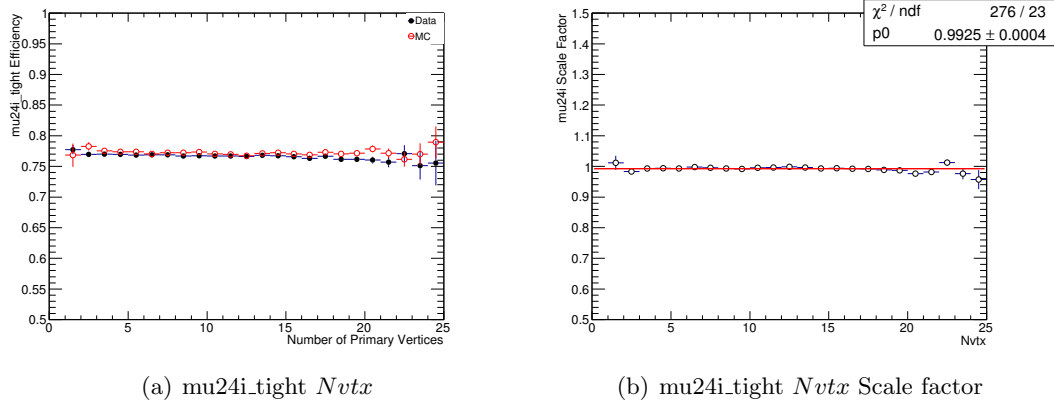


Figure A.15: Trigger efficiency for EFmu24i\_tight as a function of muon  $N_{vtx}$  in MC and data and efficiency scale factor. Uncertainties are statistical.

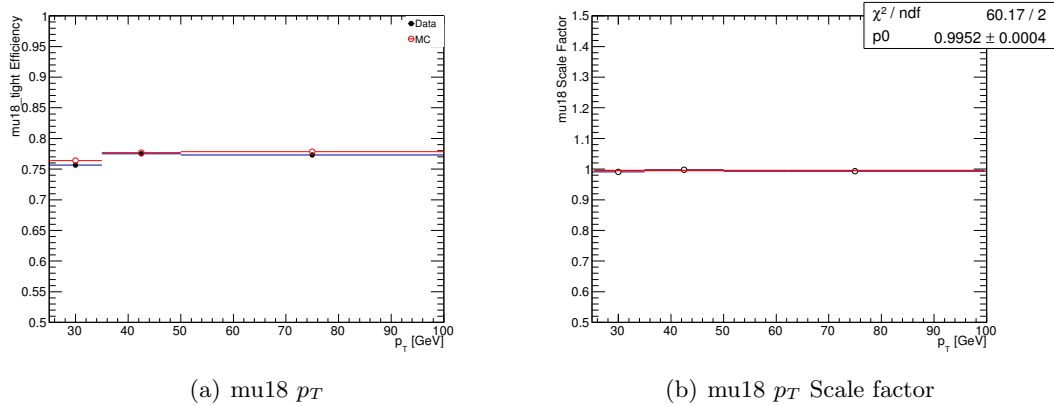


Figure A.16: Trigger efficiency for EFmu18 as a function of muon  $p_T$  in MC and data and efficiency scale factor. Uncertainties are statistical.

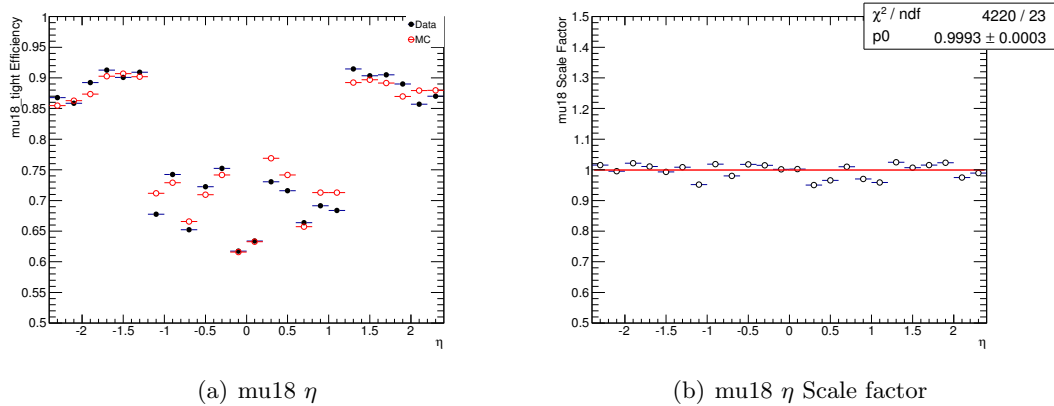


Figure A.17: Trigger efficiency for EFmu18 as a function of muon  $\eta$  in MC and data and efficiency scale factor. Uncertainties are statistical.

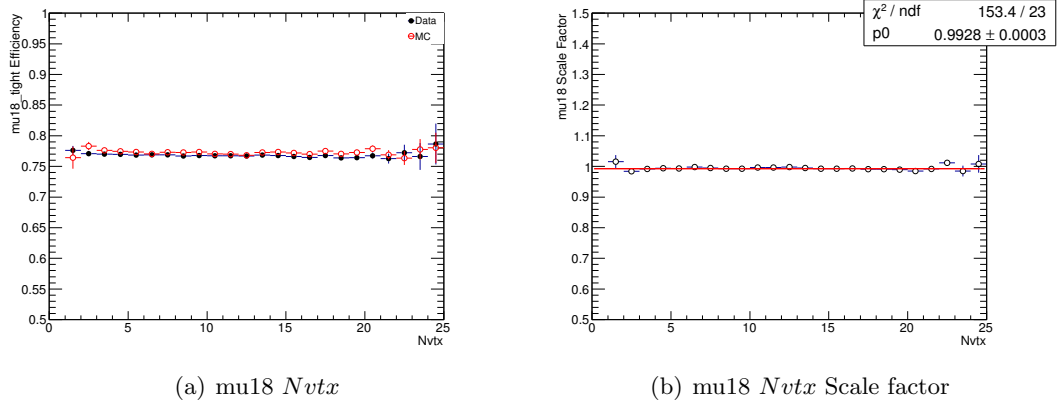


Figure A.18: Trigger efficiency for EFmu18 as a function of muon  $N_{vtx}$  in MC and data and efficiency scale factor. Uncertainties are statistical.

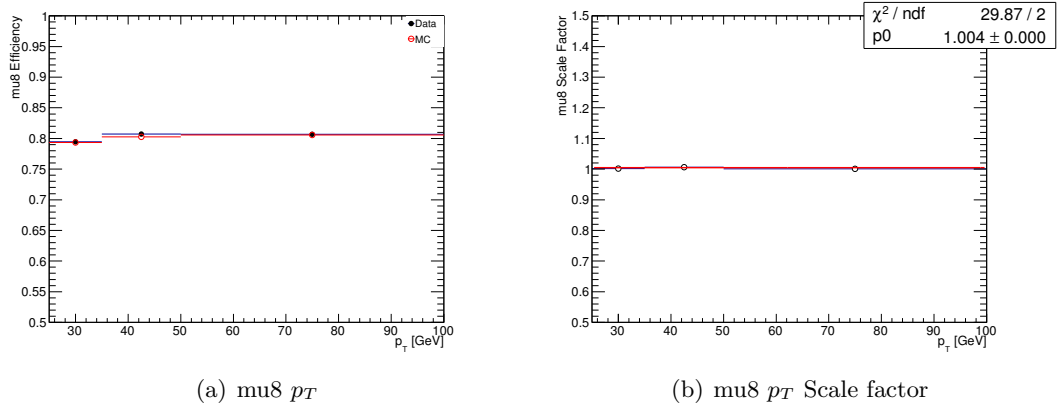


Figure A.19: Trigger efficiency for EFmu8 as a function of muon  $p_T$  in MC and data and efficiency scale factor. Uncertainties are statistical.

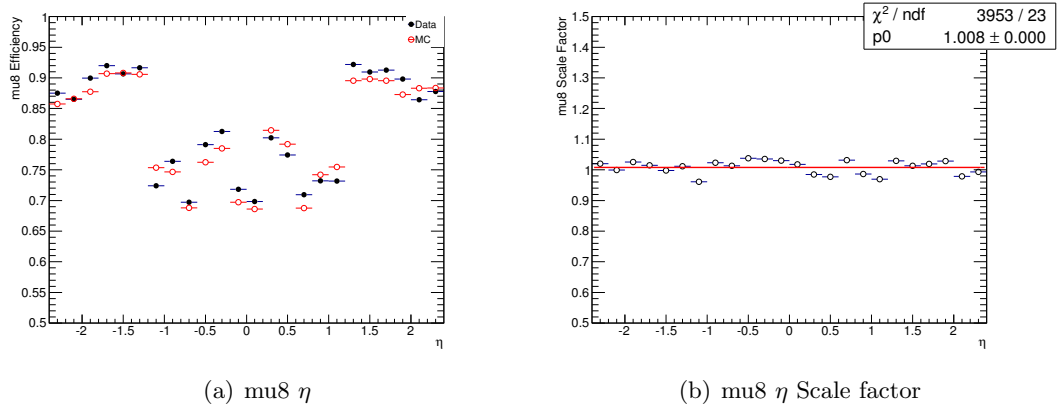


Figure A.20: Trigger efficiency for EFmu8 as a function of muon  $\eta$  in MC and data and efficiency scale factor. Uncertainties are statistical.

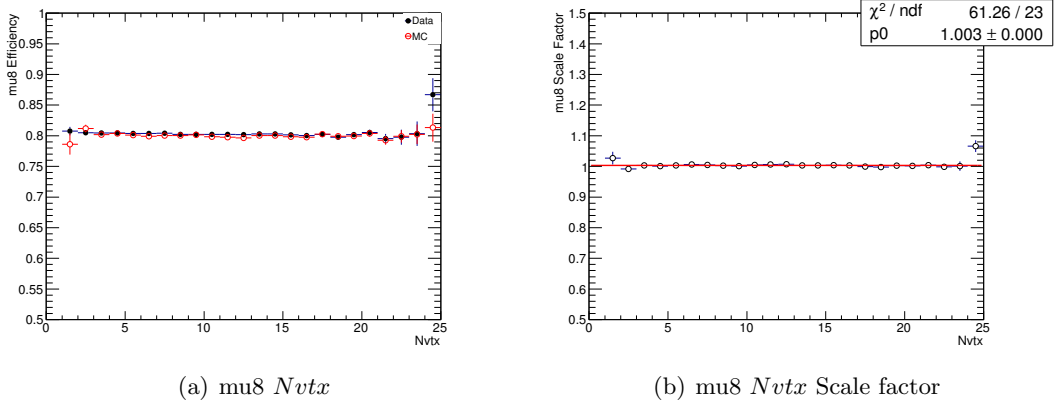


Figure A.21: Trigger efficiency for EFmu8 as a function of muon  $N_{vtx}$  in MC and data and efficiency scale factor. Uncertainties are statistical.

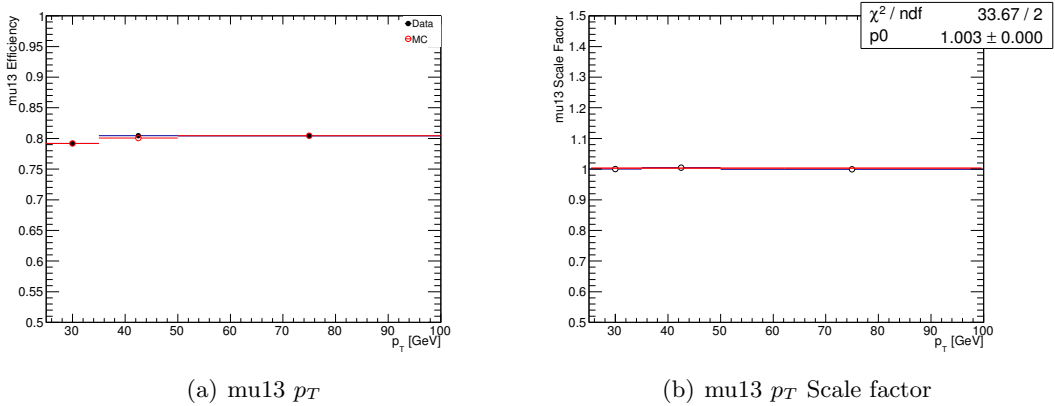


Figure A.22: Trigger efficiency for EFmu13 as a function of muon  $p_T$  in MC and data and efficiency scale factor. Uncertainties are statistical.

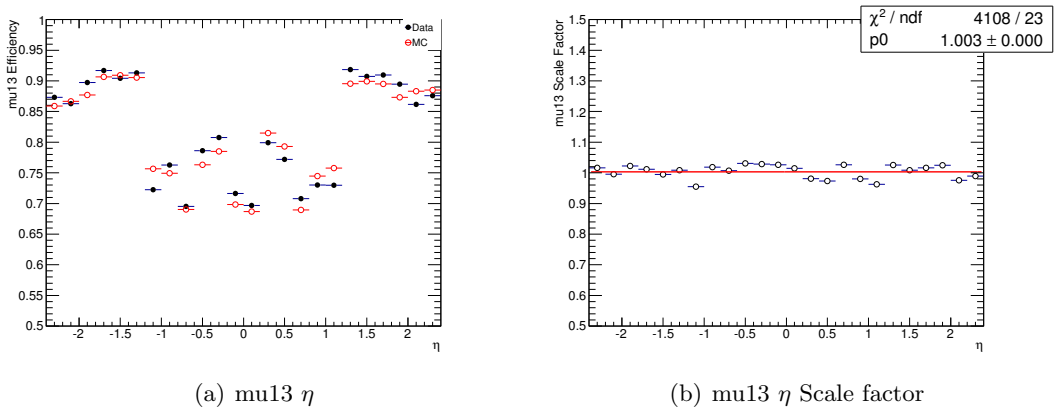


Figure A.23: Trigger efficiency for EFmu13 as a function of muon  $\eta$  in MC and data and efficiency scale factor. Uncertainties are statistical

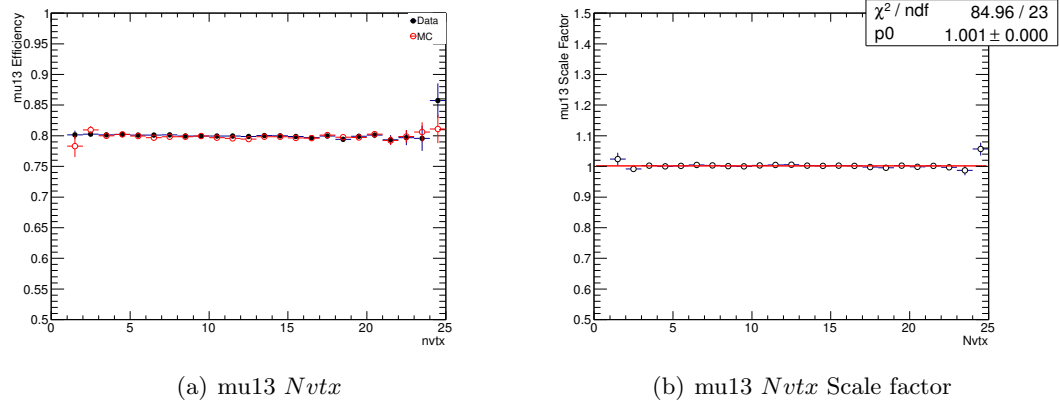


Figure A.24: Trigger efficiency for EFmu13 as a function of muon  $N_{vtx}$  in MC and data and efficiency scale factor. Uncertainties are statistical

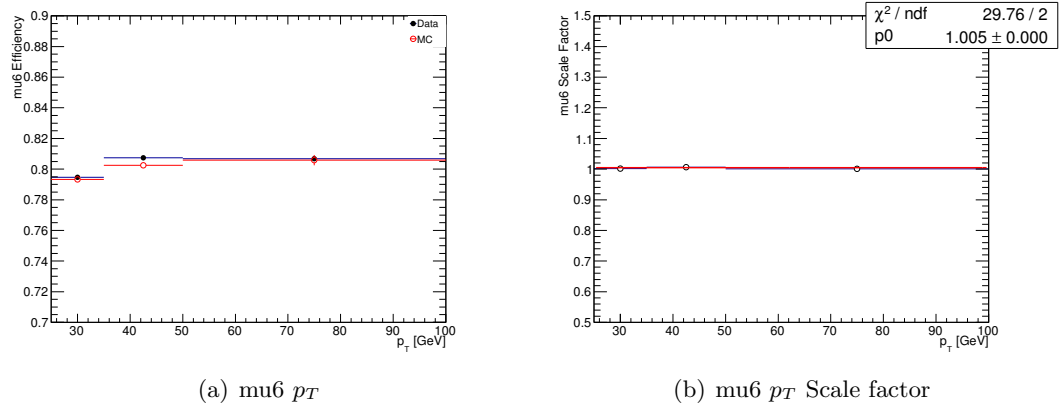


Figure A.25: Trigger efficiency for EFmu6 as a function of muon  $p_T$  in MC and data and efficiency scale factor. Uncertainties are statistical.

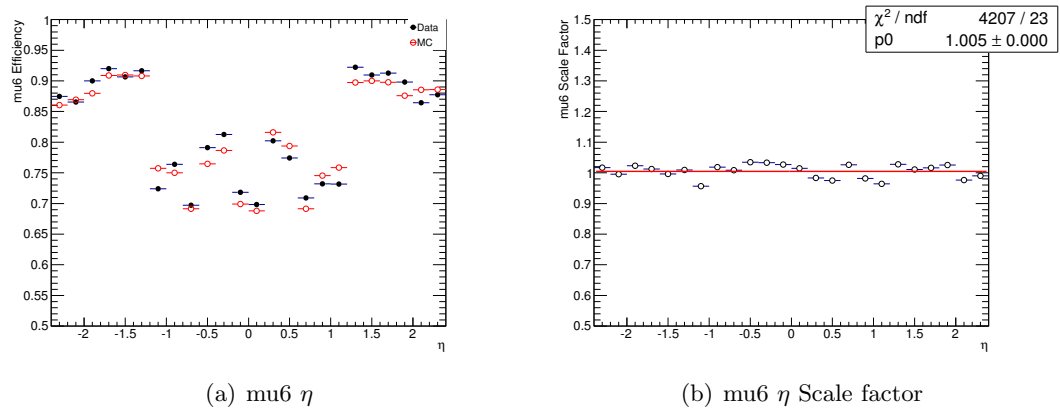


Figure A.26: Trigger efficiency for EFmu6 as a function of muon  $\eta$  in MC and data and efficiency scale factor. Uncertainties are statistical.

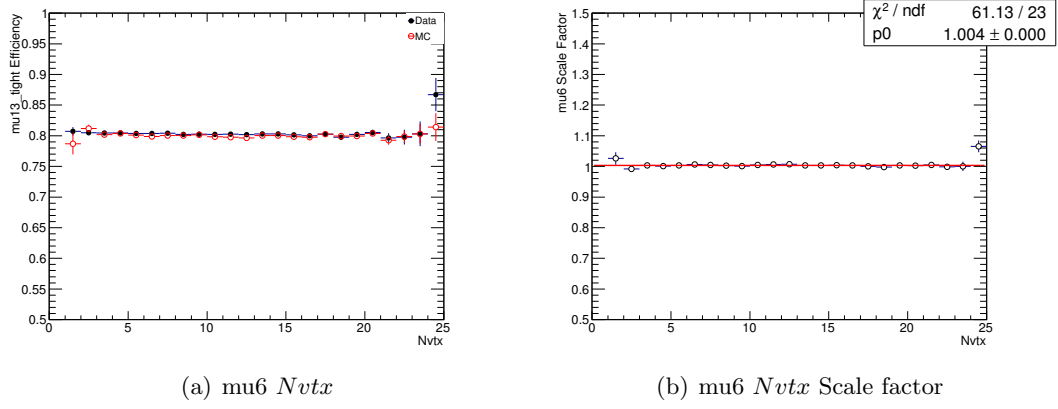


Figure A.27: Trigger efficiency for EFmu6 as a function of muon  $N_{\text{vtx}}$  in MC and data and efficiency scale factor. Uncertainties are statistical.

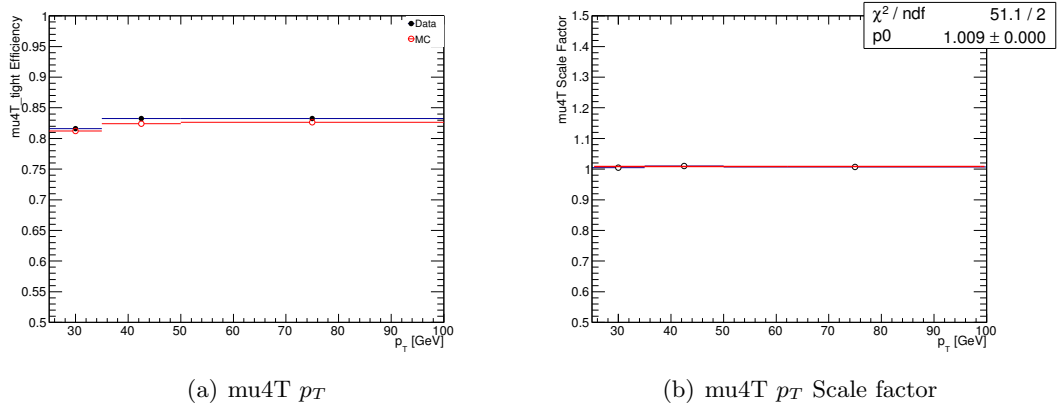


Figure A.28: Trigger efficiency for EFmu4T as a function of muon  $p_T$  in MC and data and efficiency scale factor. Uncertainties are statistical.

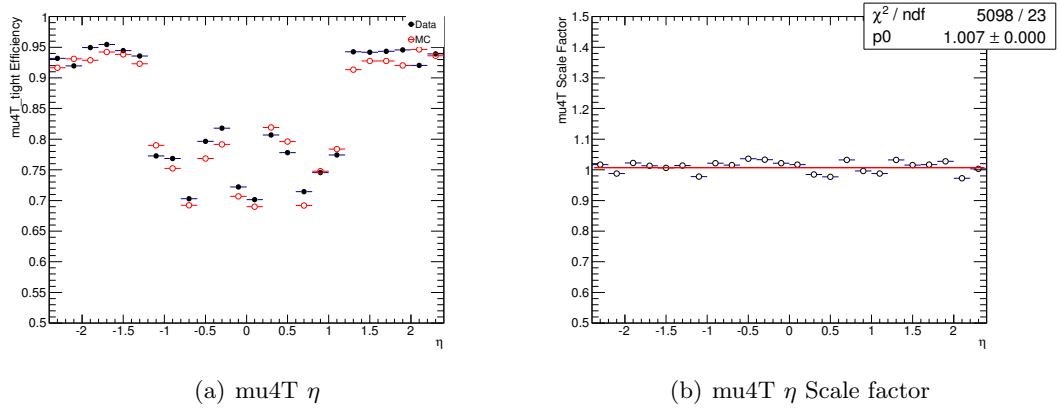


Figure A.29: Trigger efficiency for EFmu4T as a function of muon  $\eta$  in MC and data and efficiency scale factor. Uncertainties are statistical

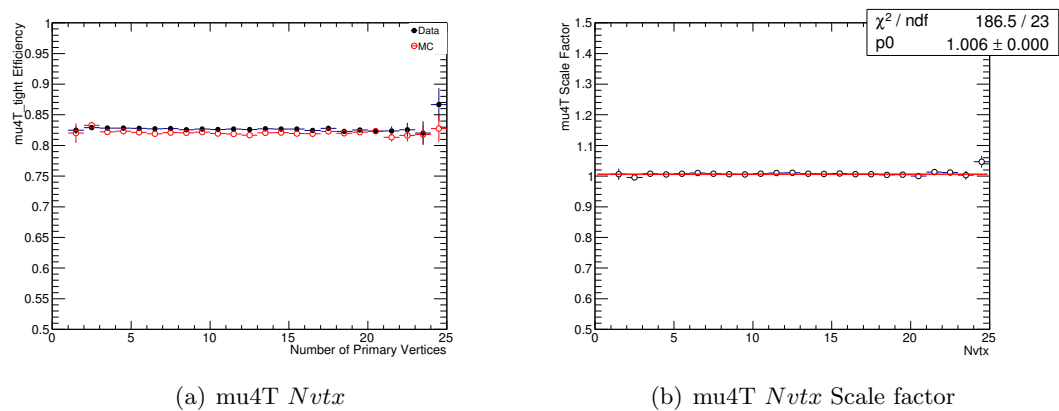


Figure A.30: Trigger efficiency for EFmu4T as a function of muon  $N_{vtx}$  in MC and data and efficiency scale factor. Uncertainties are statistical

## <sup>3317</sup> Appendix B

# <sup>3318</sup> Appendix B Systematic <sup>3319</sup> Uncertainties

### <sup>3320</sup> B.1 Introduction

<sup>3321</sup> An overview of the systematic uncertainties is given in Section 6.7. In this appendix, the  
<sup>3322</sup> systematic uncertainties in each bin are graphically represented in Figures B.1- B.2. The  
<sup>3323</sup> abbreviations in these figures are:

### <sup>3324</sup> B.2 Glossary

<sup>3325</sup> **Total** the total uncertainty in each bin (red) and per sample. The different sources of  
<sup>3326</sup> uncertainties are added in quadrature for uncorrelated systematic uncertainties and added  
<sup>3327</sup> linearly for correlated systematics. The cross-section, the PDF and the generator uncer-  
<sup>3328</sup> tainties are treated as correlated between regions but uncorrelated between background  
<sup>3329</sup> processes. All other uncertainties are treated as correlated between regions and between  
<sup>3330</sup> samples, except the uncertainty from limited MC statistics which is not correlated. Due to  
<sup>3331</sup> technical limitations, a systematic uncertainty is always treated as either fully correlated  
<sup>3332</sup> or fully uncorrelated.

<sup>3333</sup> **MC Stat** Monte Carlo statistics

<sup>3334</sup> **MM Stat** Matrix Method statistics

<sup>3335</sup> **JES** Jet energy scale

<sup>3336</sup> **JER** Jet energy resolution

<sup>3337</sup> **JVF** Jet vertex fraction

<sup>3338</sup> **ESF** Electron identification efficiency (electron scale factor)

<sup>3339</sup> **MEFF** Muon identification efficiency

<sup>3340</sup> **BJET** *b*-tagging

<sup>3341</sup> **CJET** *c*-tagging

<sup>3342</sup> **BMISTAGJET** *l*-tagging (*b*-mistagging)

<sup>3343</sup> **TauID SF** Tau identification efficiency

<sup>3344</sup> **EES low** Electron energy scale for low- $p_{\mathrm{T}}$  electrons

<sup>3345</sup> **EES mat** Electron energy scale due to additional material

<sup>3346</sup> **EES ps** Electron energy scale in presampler

<sup>3347</sup> **EES Z** electron energy scale in  $Z \rightarrow ee$  measurement

<sup>3348</sup> **EER** Electron energy resolution

<sup>3349</sup> **MID** Muon track resolution in inner detector

<sup>3350</sup> **MMS** Muon track resolution in muon spectrometer

<sup>3351</sup> **TES** Tau energy scale

<sup>3352</sup> **Scale ST**  $E_{\mathrm{T}}^{\mathrm{miss}}$  energy scale

<sup>3353</sup> **Reso ST**  $E_{\mathrm{T}}^{\mathrm{miss}}$  energy resolution

<sup>3354</sup> **Lumi** Luminosity

<sup>3355</sup> **MM elec eff** Matrix Method electron real efficiency

<sup>3356</sup> **MM muon eff** Matrix Method muon real efficiency

<sup>3357</sup> **MM elec fr** Matrix method electron fake rate

<sup>3358</sup> **MM muon fr** Matrix method muon fake rate

<sup>3359</sup> **TIDSF** Tau identification scale factor

<sup>3360</sup> **TES** Tau scale factor

### <sup>3361</sup> B.3 Systematic Uncertainty Figures

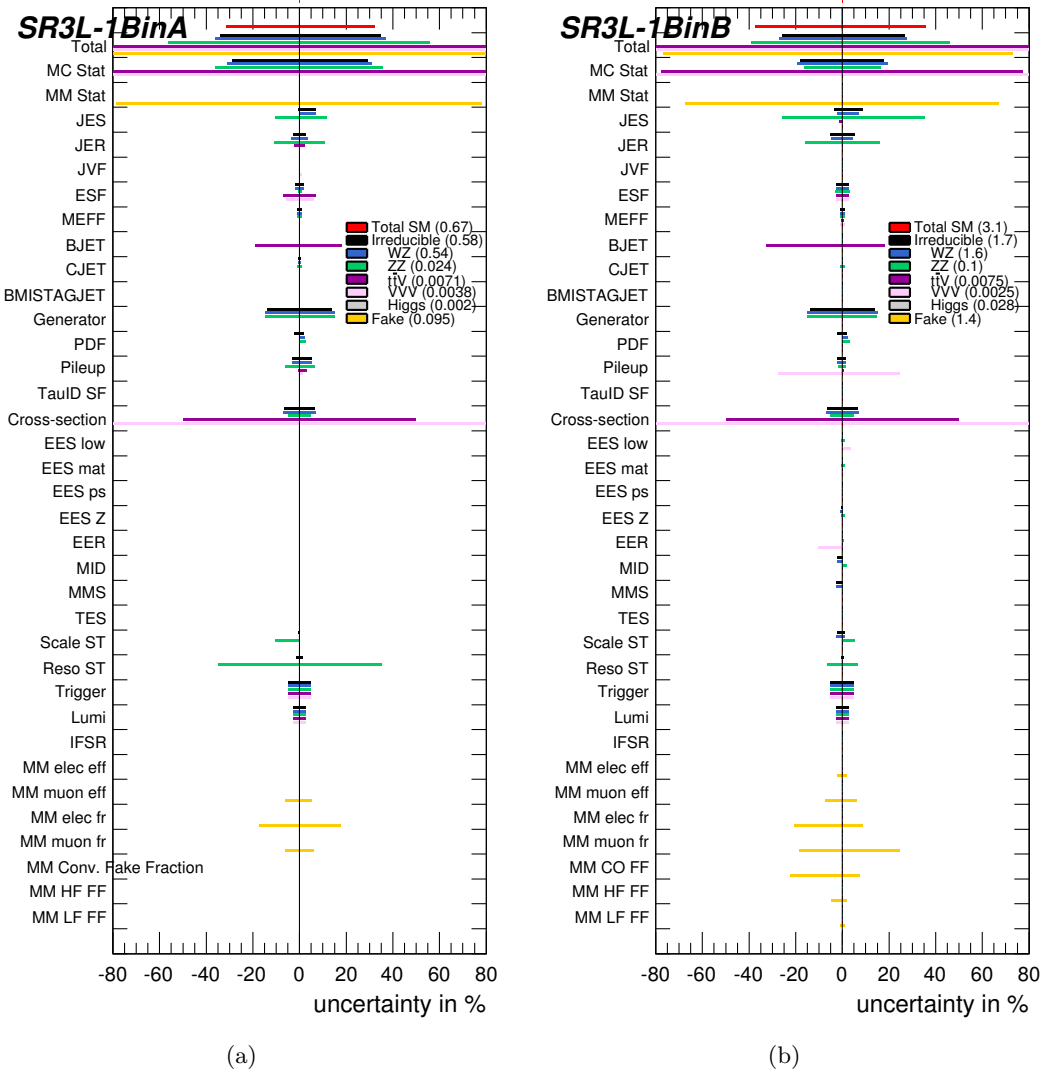


Figure B.1: Systematic uncertainties in Bin A and Bin B of SR3 $\ell$ -1

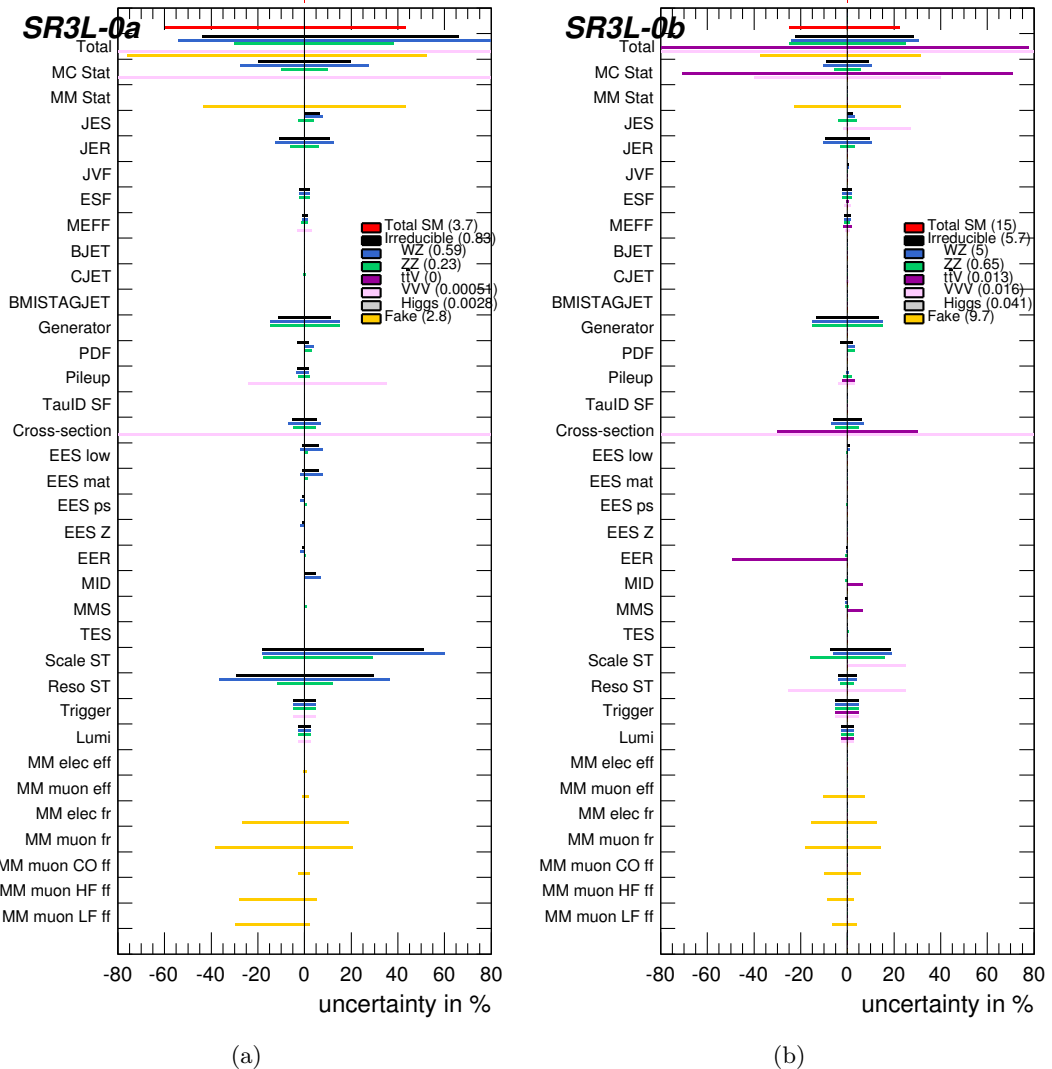


Figure B.2: Systematic uncertainties in Bin A and Bin B of SR3 $\ell$ -0

# <sup>3362</sup> Bibliography

- <sup>3363</sup> [1] ATLAS Collaboration, *The ATLAS experiment at the CERN Large Hadron*  
<sup>3364</sup> *Collider*, Journal of Instrumentation **3** no. 08, (2008) S08003.  
<sup>3365</sup> <http://stacks.iop.org/1748-0221/3/i=08/a=S08003>. [1](#), [27](#), [30](#), [33](#), [34](#), [35](#), [37](#),  
<sup>3366</sup> [38](#)
- <sup>3367</sup> [2] O. S. Brüuning, P. Collier, P. Lebrun, S. Myers, R. Ostojic, J. Poole and P.  
<sup>3368</sup> Proudlock, *LHC Design Report*, <https://cds.cern.ch/record/782076>. [1](#)
- <sup>3369</sup> [3] ATLAS Collaboration, *Search for the electroweak production of supersymmetric*  
<sup>3370</sup> *particles in  $\sqrt{s} = 8$  TeV pp collisions with the ATLAS detector*,  
<sup>3371</sup> [arXiv:1509.07152 \[hep-ex\]](https://arxiv.org/abs/1509.07152). [1](#), [134](#), [139](#), [144](#), [145](#), [146](#), [147](#), [167](#)
- <sup>3372</sup> [4] W. N. Cottingham and D. A. Greenwood, *An introduction to the standard model*.  
<sup>3373</sup> Cambridge, 1998. [2](#)
- <sup>3374</sup> [5] M. Herrero, *The Standard Model*, <https://arxiv.org/abs/hep-ph/9812242>. [3](#), [6](#)
- <sup>3375</sup> [6] ATLAS Collaboration, *Observation of a New Particle in the Search for the*  
<sup>3376</sup> *Standard Model Higgs Boson with the ATLAS Detector at the LHC*, *Phys.Lett.*  
<sup>3377</sup> **B716** (2012), [arXiv:1207.7214 \[hep-ex\]](https://arxiv.org/abs/1207.7214). [3](#)
- <sup>3378</sup> [7] CMS Collaboration, *Observation of a new boson at a mass of 125 GeV with the*  
<sup>3379</sup> *CMS experiment at the LHC*, *Phys.Lett.* **B716** (2012), [arXiv:1207.7235](https://arxiv.org/abs/1207.7235)  
<sup>3380</sup> [hep-ex]. [3](#)
- <sup>3381</sup> [8] ATLAS, CMS Collaborations, *Combined Measurement of the Higgs Boson Mass in*  
<sup>3382</sup> *pp Collisions at  $\sqrt{s} = 7$  and 8 TeV with the ATLAS and CMS Experiments*, *Phys.*  
<sup>3383</sup> *Rev. Lett.* **114** (2015), [arXiv:1503.07589 \[hep-ex\]](https://arxiv.org/abs/1503.07589). [3](#)
- <sup>3384</sup> [9] J. H. Schwarz, *The Early History of String Theory and Supersymmetry*,  
<sup>3385</sup> [arXiv:1201.0981 \[physics.hist-ph\]](https://arxiv.org/abs/1201.0981). [3](#)
- <sup>3386</sup> [10] A. Pich, *The Standard Model of Electroweak Interactions*, [arXiv:1201.0537](https://arxiv.org/abs/1201.0537)  
<sup>3387</sup> [hep-ph]. [4](#)
- <sup>3388</sup> [11] K. A. Olive et al. (Particle Data Group), *Review of Particle Physics*, *Chin.Phys. C*

- 3389 **38(9) (2014). 5, 6, 19**

3390 [12] M. E. Peskin, D. V. Schroeder, *An Introduction to Quantum Field Theory*.  
Westview Press, 1995. 6

3391 [13] F. Englert and R. Brout, *Broken Symmetry and the Mass of Gauge Vector Bosons*,  
*Phys. Rev. Lett.* **13** (1964) 321–323. 7

3392 [14] P. W. Higgs, *Broken Symmetries and the Masses of Gauge Bosons*, *Phys. Rev. Lett.* **13** (1964) 508–509. 7

3393 [15] T. W. B. Kibble, *Symmetry Breaking in Non-Abelian Gauge Theories*, *Phys. Rev.* **155** (1967) 1554–1561. <http://link.aps.org/doi/10.1103/PhysRev.155.1554>. 7

3394 [16] J. Goldstone, A. Salam and S. Weinberg, *Broken Symmetries*, *Phys. Rev.* **127** (1962) 965–970. 8

3395 [17] ATLAS Collaboration, *Observation of  $J/\psi$  resonances consistence with pentaquark states in  $\Lambda_b^0 \rightarrow J/\psi K^- p$  decays*, *Phys. Rev. Lett.* **115** (2015), [arXiv:1507.03414 \[hep-ex\]](https://arxiv.org/abs/1507.03414). 9

3396 [18] S. Weinberg, *Implications of Dynamical Symmetry Breaking*, *Phys. Rev.* **D19** (1976) 1277–1280. 10

3397 [19] M. C. Gonzalez-Garcia and M. Maltoni, *Phenomenology with massive neutrinos*, *Physics Reports* **460** no. 1-3, (2008) 1 – 129. 10

3398 [20] E. Kh. Akhmedov, et. al, *Seesaw mechanism and structure of neutrino mass matrix*, *Phys. Lett.* **B478** (1999). 10

3399 [21] V. C. Rubin and W. K. Ford, Jr., *Rotation of the Andromeda Nebula from a Spectroscopic Survey of Emission Regions*, *Astrophysical Journal* **159** (1970) 379. 10

3400 [22] R. Massey, T. Kitching, and J. Richard, *The dark matter of gravitational lensing*, *Reports on Progress in Physics* **73** no. 8, (2010) 086901.  
<http://arxiv.org/abs/1001.1739>. 11

3401 [23] A. Challinor, *CMB anisotropy science: a review*, [arXiv:1210.6008 \[astro-ph.CO\]](https://arxiv.org/abs/1210.6008). 11

3402 [24] B. Novosyadlyj, V. Pelykh, Yu. Shtanov, A. Zhuk, *Dark Energy: Observational Evidence and Theoretical Models*, [arXiv:1502.04177 \[astro-ph.CO\]](https://arxiv.org/abs/1502.04177). 11

3403 [25] S. P. Martin, *A Supersymmetry Primer*, [arXiv:hep-ph/9709356](https://arxiv.org/abs/hep-ph/9709356). 11, 16, 20

3404 [26] M. Dine, W. Fischler, and M. Srednicki, *Supersymmetric Technicolor*, *Nucl. Phys.* **B187** (1981). 16

3405 [27] M. Dine, W. Fischler, and M. Srednicki, *Supersymmetric Technicolor*, *Nucl. Phys.* **B187** (1981). 16

3406 [28] M. Dine, W. Fischler, and M. Srednicki, *Supersymmetric Technicolor*, *Nucl. Phys.* **B187** (1981). 16

3407 [29] M. Dine, W. Fischler, and M. Srednicki, *Supersymmetric Technicolor*, *Nucl. Phys.* **B187** (1981). 16

3408 [30] M. Dine, W. Fischler, and M. Srednicki, *Supersymmetric Technicolor*, *Nucl. Phys.* **B187** (1981). 16

3409 [31] M. Dine, W. Fischler, and M. Srednicki, *Supersymmetric Technicolor*, *Nucl. Phys.* **B187** (1981). 16

3410 [32] M. Dine, W. Fischler, and M. Srednicki, *Supersymmetric Technicolor*, *Nucl. Phys.* **B187** (1981). 16

3411 [33] M. Dine, W. Fischler, and M. Srednicki, *Supersymmetric Technicolor*, *Nucl. Phys.* **B187** (1981). 16

3412 [34] M. Dine, W. Fischler, and M. Srednicki, *Supersymmetric Technicolor*, *Nucl. Phys.* **B187** (1981). 16

3413 [35] M. Dine, W. Fischler, and M. Srednicki, *Supersymmetric Technicolor*, *Nucl. Phys.* **B187** (1981). 16

3414 [36] M. Dine, W. Fischler, and M. Srednicki, *Supersymmetric Technicolor*, *Nucl. Phys.* **B187** (1981). 16

3415 [37] M. Dine, W. Fischler, and M. Srednicki, *Supersymmetric Technicolor*, *Nucl. Phys.* **B187** (1981). 16

3416 [38] M. Dine, W. Fischler, and M. Srednicki, *Supersymmetric Technicolor*, *Nucl. Phys.* **B187** (1981). 16

3417 [39] M. Dine, W. Fischler, and M. Srednicki, *Supersymmetric Technicolor*, *Nucl. Phys.* **B187** (1981). 16

3418 [40] M. Dine, W. Fischler, and M. Srednicki, *Supersymmetric Technicolor*, *Nucl. Phys.* **B187** (1981). 16

3419 [41] M. Dine, W. Fischler, and M. Srednicki, *Supersymmetric Technicolor*, *Nucl. Phys.* **B187** (1981). 16

3420 [42] M. Dine, W. Fischler, and M. Srednicki, *Supersymmetric Technicolor*, *Nucl. Phys.* **B187** (1981). 16

3421 [43] M. Dine, W. Fischler, and M. Srednicki, *Supersymmetric Technicolor*, *Nucl. Phys.* **B187** (1981). 16

3422 [44] M. Dine, W. Fischler, and M. Srednicki, *Supersymmetric Technicolor*, *Nucl. Phys.* **B187** (1981). 16

- 3423 [27] L. J. Hall, J. D. Lykken and S. Weinberg, *Supergravity as the Messenger of*  
 3424 *Supersymmetry Breaking*, Phys. Rev. **D27** (1983) 2359–2378. 16
- 3425 [28] L. Randall and R. Sundrum, *A Large mass hierarchy from a small extra*  
 3426 *dimension*, Phys. Rev. Lett. **83** (1999) 3370–3373, arXiv:9905221 [hep-ph]. 16
- 3427 [29] L. Randall and R. Sundrum, *Out of this world supersymmetry breaking*, Nucl.  
 3428 Phys. **B557** (1999), arXiv:hep-th/9810155 [hep-th]. 16
- 3429 [30] L. J. Hall, D. Pinner, and J. T. Ruderman, *A natural SUSY Higgs near 125 GeV*,  
 3430 Journal of High Energy Physics **2012** no. 4, (2012) 1–25.  
 3431 [http://dx.doi.org/10.1007/JHEP04\(2012\)131](http://dx.doi.org/10.1007/JHEP04(2012)131). 17
- 3432 [31] J. A. Casas, et. al, *What is a Natural SUSY Scenario*, arXiv:1407.6966  
 3433 [hep-ph]. 18
- 3434 [32] M. Papucci, et. al, *Natural SUSY Endures*, arXiv:1110.6926 [hep-ph]. 19
- 3435 [33] ATLAS Collaboration, *Search for squarks and gluinos with the ATLAS detector in*  
 3436 *final states with jets and missing transverse momentum and  $20.3 \text{ fb}^{-1}$  of  $\sqrt{s} = 8$*   
 3437 *TeV proton-proton collisions.*, <https://cds.cern.ch/record/1547563>. 20
- 3438 [34] Johan Alwall, Philip C. Schuster and Natalia Toro, *Simplified models for a first*  
 3439 *characterization of new physics at the LHC*, Phys. Rev. D **D79** (2009). 21
- 3440 [35] [https://atlas.web.cern.ch/Atlas/GROUPS/PHYSICS/SUSY/FeynmanGraphs/  
 3441 C1N2-lllvN1N1-sls1.png](https://atlas.web.cern.ch/Atlas/GROUPS/PHYSICS/SUSY/FeynmanGraphs/C1N2-lllvN1N1-sls1.png). 22
- 3442 [36] [https://atlas.web.cern.ch/Atlas/GROUPS/PHYSICS/SUSY/FeynmanGraphs/  
 3443 C1N2-lllvN1N1-WZ.png](https://atlas.web.cern.ch/Atlas/GROUPS/PHYSICS/SUSY/FeynmanGraphs/C1N2-lllvN1N1-WZ.png). 23
- 3444 [37] [https://atlas.web.cern.ch/Atlas/GROUPS/PHYSICS/SUSY/FeynmanGraphs/  
 3445 C1N2-lllvN1N1g-WZ.png](https://atlas.web.cern.ch/Atlas/GROUPS/PHYSICS/SUSY/FeynmanGraphs/C1N2-lllvN1N1g-WZ.png). 23
- 3446 [38] D. Barducci, et. al, *Uncovering Natural Supersymmetry via the interplay between*  
 3447 *the LHC and Direct Dark Matter Detection*, arXiv:1504.02472v2 [hep-ph]. 23,  
 3448 24
- 3449 [39] G. Hinshaw, et. al, *Nine-Year Wilkinson Microwave Anisotropy Probe (WMAP)*  
 3450 *Observations: Cosmological Parameter Results*, arXiv:1212.5226 [astro-ph.CO].  
 3451 23
- 3452 [40] Planck Collaboration, *Planck 2013 results. XVI. Cosmological parameters*, A&A  
 3453 **571 A16** (2014), arXiv:1303.5076. 24
- 3454 [41] P. Schwaller, J. Zurita, *Compressed electroweakino spectra at the LHC*,  
 3455 arXiv:1312.7350 [hep-ph]. 24
- 3456 [42] S. Gori, S. Jung, L. Wang, *Cornering electroweakinos at the LHC*,

- 3457        [arXiv:1307.5952 \[hep-ph\]](https://arxiv.org/abs/1307.5952). 24
- 3458     [43] A. Barr, J. Scoville, *A boost for the EW SUSY hunt: monojet-like search for*  
 3459     *compressed sleptons at LHC14 with 100fb<sup>-1</sup>*, [arXiv:1501.02511 \[hep-ph\]](https://arxiv.org/abs/1501.02511). 24
- 3460     [44] CERN. Geneva, *LEP Design Report*,. <https://cds.cern.ch/record/102083>. 25
- 3461     [45] Berndt Muller, Jurgen Schukraft, Bolek Wyslouch, *First Results from Pb+Pb*  
 3462     *collisions at the LHC*, [arXiv:1202.3233 \[hep-ex\]](https://arxiv.org/abs/1202.3233). 26
- 3463     [46] C. Lefèvre, *The CERN accelerator complex*,.  
 3464        [http://cds.cern.ch/record/1260465](https://cds.cern.ch/record/1260465). 26
- 3465     [47] CMS Collaboration, *The CMS experiment at the CERN LHC*, Journal of  
 3466     Instrumentation **3** no. 08, (2008) S08004.  
 3467        [http://stacks.iop.org/1748-0221/3/i=08/a=S08004](https://stacks.iop.org/1748-0221/3/i=08/a=S08004). 27
- 3468     [48] LHCb Collaboration, et. al, *The LHCb Detector at the LHC*, **JINST** (2008). 27, 46
- 3469     [49] ALICE Collaboration, *The ALICE experiment at the CERN LHC*, Journal of  
 3470     Instrumentation **3** no. 08, (2008) S08002.  
 3471        [http://stacks.iop.org/1748-0221/3/i=08/a=S08002](https://stacks.iop.org/1748-0221/3/i=08/a=S08002). 27
- 3472     [50] ATLAS Collaboration, *The ATLAS Inner Detector commissioning and calibration*,  
 3473        *Eur. Phys. JC***70** , [arXiv:1004.5293](https://arxiv.org/abs/1004.5293). 30
- 3474     [51] ATLAS Collaboration, *Alignment of the ATLAS Inner Detector Upgraded for the*  
 3475     *LHC Run II*, Journal of Physics: Conference Series **664** no. 7, (2015) 072025.  
 3476        [http://stacks.iop.org/1742-6596/664/i=7/a=072025](https://stacks.iop.org/1742-6596/664/i=7/a=072025). 30
- 3477     [52] A. Bingl, *The ATLAS TRT and its Performance at LHC*, Journal of Physics:  
 3478        Conference Series **347** no. 1, (2012) 012025. [http://iopscience.iop.org/article/10.1088/1742-6596/347/1/012025/meta](https://iopscience.iop.org/article/10.1088/1742-6596/347/1/012025/meta). 32
- 3479     [53] ATLAS Collaboration, *ATLAS liquid-argon calorimeter: Technical Design Report*,.  
 3480        <https://cds.cern.ch/record/331061>. 34
- 3481     [54] ATLAS Collaboration, *ATLAS muon spectrometer: Technical design report*,.  
 3482        <https://cds.cern.ch/record/331068>. 36
- 3483     [55] ATLAS Collaboration, *Performance of the ATLAS Trigger System in 2010*, *Eur.*  
 3484        *Phys. J* **C72** (2012), [arXiv:1110.1530 \[hep-ex\]](https://arxiv.org/abs/1110.1530). 39, 42
- 3485     [56] Monika Grothe (on behalf of the ATLAS High Level Trigger Group), *Architecture*  
 3486        *of the ATLAS High Level Trigger Event Selection Software*,  
 3487        [arXiv:physics/0306097 \[physics.comp-ph\]](https://arxiv.org/abs/physics/0306097). 41
- 3488     [57] R. Frühwirth, *Application of Kalman filtering to track and vertex filtering*,  
 3489        *Nucl.Instrum.Meth.* **A262** (1987). 41, 53

- 3491 [58] ATLAS Collaboration, *ATLAS Insertable B-Layer Technical Design Report*,  
 3492 <https://cds.cern.ch/record/1291633>. 43
- 3493 [59] S. T. A. Salzburger and M. Wolter, *The ATLAS Tracking Geometry Description*,,  
 3494 <https://cds.cern.ch/record/1038098>. 43
- 3495 [60] E. Simoni, *The Topological Processor for the future ATLAS Level-1 Trigger: from*  
 3496 *design to commissioning*, [arXiv:1406.4316](https://arxiv.org/abs/1406.4316). 44
- 3497 [61] ATLAS Collaboration, *Fast TracKer (FTK) Technical Design Report*,.  
 3498 <https://cds.cern.ch/record/1552953>. 44
- 3499 [62] ATLAS Collaboration, *ATLAS Computing : technical design report*,.  
 3500 <https://cds.cern.ch/record/837738>. 46
- 3501 [63] G. Barrand, et. al, *GAUDI - A software architecture and framework for building*  
 3502 *HEP data processing applications*,.  
 3503 [http://dx.doi.org/10.1016/S0010-4655\(01\)00254-5](http://dx.doi.org/10.1016/S0010-4655(01)00254-5). 46
- 3504 [64] A. Buckley, J. Butterworth, S. Gieseke, D. Grellscheid, S. Hoche, et al.,  
 3505 *General-purpose event generators for LHC physics*, Phys.Rept. **504** (2011).  
 3506 <http://arXiv.org/abs/1101.2599>. 46
- 3507 [65] J. M. Butterworth, et. al, *Hard Processes in Proton-Proton Collisions at the Large*  
 3508 *Hadron Collider*, Annual Review of Nuclear and Particle Science **62** (2012). 48
- 3509 [66] J. M. Campbell, J. Houston and W. Stirling, *Hard Interactions of Quarks and*  
 3510 *Gluons: A Primer of LHC Physics*, Rept. Prog. Phys. **70** no. 1, (2007). 48
- 3511 [67] I. W. Stewart, F. J. Tackmann and W. J. Waalewijn, *Factorization at the LHC:*  
 3512 *From PDFs to Initial State Jets*, Phys.Rev. **D81** (2010).  
 3513 <http://arXiv.org/abs/0910.0467>. 48
- 3514 [68] A. D. Martin, *Proton structure, Partons, QCD, DGLAP and beyond*, Acta Phys.  
 3515 Polon. **B39** (2008). <http://arXiv.org/abs/0802.0161>. 48
- 3516 [69] G. Corcella, et al., *HERWIG 6: an event generator of hadron emission reactions*  
 3517 *with interfering gluons (including supersymmetric processes)*, J. High Energy Phys.  
 3518 **JHEP(2001)** (2001).  
 3519 <http://iopscience.iop.org/article/10.1088/1126-6708/2001/01/010/meta>.  
 3520 49, 70, 73
- 3521 [70] T.S., et al., *PYTHIA 6.4 physics and manual*, J. High Energy Phys. **JHEP(2006)**  
 3522 (2006).  
 3523 <http://iopscience.iop.org/article/10.1088/1126-6708/2006/05/026/meta>.  
 3524 49, 70

- 3525 [71] T. Gleisberg, et al., *Event generation with SHERPA 1.1*, J. High Energy Phys.  
 3526 **JHEP(2009)** (2009).  
 3527 <http://iopscience.iop.org/article/10.1088/1126-6708/2009/02/007/meta>.  
 3528 49
- 3529 [72] Bernd A. Berg, *Introduction to Markov Chain Monte Carlo Simulations and their*  
 3530 *Statistical Analysis*, [arXiv:cond-mat/0410490](https://arxiv.org/abs/cond-mat/0410490) [cond-mat]. 49
- 3531 [73] S. Catani, F. Krauss, R. Kuhn and B. Webber, *QCD Matrix Elements + Parton*  
 3532 *Showers*, **JHEP 0111** (2001), [arXiv:hep-ph/0109231](https://arxiv.org/abs/hep-ph/0109231) [hep-ph]. 49
- 3533 [74] M. L. Mangano, M. Moretti and R. Pittau, *Multijet Matrix Elements and Shower*  
 3534 *Evolution in Hadronic Collisions:  $Wb\bar{b} + n$  Jets as a Case Study*, **Nucl.Phys B632**  
 3535 (2001), [arXiv:0108069](https://arxiv.org/abs/0108069) [hep-ph]. 49
- 3536 [75] B. Andersson, S. Mohanty and F. Soderberg, *Recent Developments in the Lund*  
 3537 *Model*, [arXiv:hep-ph/0212122](https://arxiv.org/abs/hep-ph/0212122) [hep-ph]. 49
- 3538 [76] A. Kupco , *Cluster Hadronization in HERWIG 5.9*, [arXiv:hep-ph/9906412](https://arxiv.org/abs/hep-ph/9906412)  
 3539 [hep-ph]. 49
- 3540 [77] R. D. Field, *The Underlying Event in Hard Scattering Processes*,  
 3541 [arXiv:hep-ph/0201192](https://arxiv.org/abs/hep-ph/0201192) [hep-ph]. 50
- 3542 [78] J. M. Butterworth, J. R. Forshaw, M. H. Seymour Z. Phys. C **72** (1996).  
 3543 <http://arxiv.org/abs/hep-ph/9601371>. 50, 70
- 3544 [79] GEANT4 Collaboration, *Geant4 a simulation toolkit*, **Nucl. Instrum. Meth. A 506**  
 3545 (2003). 50
- 3546 [80] W. Lukas, *Fast Simulation for ATLAS: Atlfast-II and ISF*, **J. Phys.: Conf. Ser 396**  
 3547 no. 022031, (2012). 50
- 3548 [81] ATLAS Collaboration, *The simulation principle and performance of the ATLAS*  
 3549 *fast calorimeter simulation FastCaloSim.*,  
 3550 <https://cds.cern.ch/record/1300517>. 50
- 3551 [82] L. Evans and P. Bryant, *LHC Machine*, **JINST 3** (2008). 52
- 3552 [83] ATLAS Collaboration, *Luminosity Determination in pp Collisions at  $\sqrt{s} = 7$  TeV*  
 3553 *Using the ATLAS Detector at the LHC*, **Eur. Phys. J C71** (2011),  
 3554 [arXiv:1101.2185](https://arxiv.org/abs/1101.2185) [hep-ex]. 52
- 3555 [84] W. Lampl, et al., *Calorimeter Clustering Algorithms: Description and*  
 3556 *Performance*, <https://cds.cern.ch/record/1099735>. 54, 60
- 3557 [85] ATLAS Collaboration, *Electron performance measurements with the ATLAS*  
 3558 *detector using the 2010 LHC proton-proton collision data*, **Eur. Phys. J. C72**

- 3559 (2012). <http://arxiv.org/abs/1110.3174>. 55, 126
- 3560 [86] ATLAS Collaboration, *Electron reconstruction and identification efficiency*  
 3561 *measurements with the ATLAS detector using the 2011 LHC proton-proton*  
 3562 *collision data*, Eur. Phys. J. **74** no. 7, (2014), arXiv:1404.2240 [hep-ex]. 56, 57
- 3563 [87] ATLAS Collaboration, *Electron Efficiency measurements with the ATLAS detector*  
 3564 *using the 2012 LHC proton-proton collision data*,,  
 3565 <http://cds.cern.ch/record/1706245>. 58, 82, 113
- 3566 [88] R. Nicolaïdou, L. Chevalier, S. Hassani, J. F. Laporte, E. L. Menedeu, and A.  
 3567 Ouraou, *Muon identification procedure for the ATLAS detector at the LHC using*  
 3568 *Muonboy reconstruction package and tests of its performance using cosmic rays and*  
 3569 *single beam data*, Journal of Physics: Conference Series **219** no. 3, (2010) 032052.  
 3570 <http://stacks.iop.org/1742-6596/219/i=3/a=032052>. 59
- 3571 [89] ATLAS Collaboration, *Measurement of the muon reconstruction performance of*  
 3572 *the ATLAS detector using 2011 and 2012 LHC proton-proton collision data*, Eur.  
 3573 Phys. J. C **74** (2014). 60, 113, 126
- 3574 [90] ATLAS Collaboration, *Properties of Jets and Inputs to Jet Reconstruction and*  
 3575 *Calibration with the ATLAS Detector Using Proton-Proton Collisions at  $\sqrt{s} = 7$*   
 3576 *TeV*,. <http://cds.cern.ch/record/1281310/files/ATLAS-CONF-2010-053.pdf>.  
 3577 60
- 3578 [91] G. S. M. Cacciari, G. P. Salam, *The Anti- $k(t)$  jet clustering algorithm*, JHEP **0804**  
 3579 (2008), arXiv:0802.1189 [hep-ph]. 61
- 3580 [92] ATLAS Collaboration, *Jet energy scale and its systematic uncertainty in*  
 3581 *proton-proton collisions at  $\sqrt{s} = 7$  TeV with ATLAS 2011 data*,,  
 3582 <https://cds.cern.ch/record/1509552>. 61
- 3583 [93] ATLAS Collaboration, *Pile-up corrections for jets from proton-proton collisions at*  
 3584  *$\sqrt{s} = 7$  TeV in ATLAS in 2011*,. <https://cds.cern.ch/record/1459529>. 61
- 3585 [94] ATLAS Collaboration, *Commissioning of the ATLAS high-performance b-tagging*  
 3586 *algorithms in the 7 TeV collision data*,. <https://cds.cern.ch/record/1369219>.  
 3587 62
- 3588 [95] ATLAS Collaboration, *Identification and energy calibration of hadronically*  
 3589 *decaying tau leptons with the ATLAS experiment in pp collisions at  $\sqrt{s} = 8$  TeV*,  
 3590 *Eur. Phys. J. C **75**:303 (2015)*. 62, 64
- 3591 [96] ATLAS Collaboration, *Performance of the Reconstruction and Identification of*  
 3592 *Hadronic Tau Decays with ATLAS*,. <https://cds.cern.ch/record/1398195>. 63

- 3593 [97] ATLAS Collaboration, *Performance of missing transverse momentum*  
 3594 *reconstruction in proton-proton collisions at  $\sqrt{s} = 7 \text{ TeV}$  with ATLAS*, *Eur. Phys.*  
 3595 *J. C* **75** no. 1844, (2012). 64, 65
- 3596 [98] ATLAS Collaboration, *Performance of Missing Transverse Momentum*  
 3597 *Reconstruction in ATLAS studied in Proton-Proton Collisions recorded in 2012 at*  
 3598  *$\sqrt{s} = 8 \text{ TeV}$* , <https://cds.cern.ch/record/1570993>. 65
- 3599 [99] M. Bahr, S. Gieseke, M. Gigg, D. Grellscheid, K. Hamilton, et al., *Herwig++*  
 3600 *Physics and Manual*, *Eur.Phys.J C* **58** (2008). 70
- 3601 [100] T. Gleisberg et al., *Event generation with SHERPA 1.1*, *JHEP* **02** (2009) 007. 70
- 3602 [101] M. L. Mangano et al., *ALPGEN, a generator for hard multiparton processes in*  
 3603 *hadronic collisions*, *JHEP* **07** (2003) 001. 70
- 3604 [102] J. Alwall, et al, *MadGraph/MadEvent v4: The New Web Generation*, *JHEP* **09**  
 3605 (2007). 70, 73
- 3606 [103] B. P. Kersevan and E. Richter-Was, *The Monte Carlo event generator AcerMC*  
 3607 *versions 2.0 to 3.8 with interfaces to PYTHIA 6.4, HERWIG 6.5 and ARIADNE*  
 3608 *4.1*, *Comput. Phys. Commun.* **184** (2013) 919 – 985. 70
- 3609 [104] S. Frixione, and P. Nason, and C. Oleari, *Matching NLO QCD computations with*  
 3610 *Parton Shower simulations: the POWHEG method*, *JHEP* **11** (2007) 070. 70
- 3611 [105] P. Nason, *A New method for combining NLO QCD with shower Monte Carlo*  
 3612 *algorithms*, *JHEP* **11** (2004) 040. 70
- 3613 [106] ATLAS Collaboration, *ATLAS tunes of PYTHIA 6 and Pythia 8 for MC11.*,  
 3614 <https://cds.cern.ch/record/1363300>. 72
- 3615 [107] H. L. Lai, et al., *New parton distributions for collider physics*, *Phys. Rev. D* **82**  
 3616 (2010). 72
- 3617 [108] M. S. W. Beenakker, R. Hopker and P. Zerwas, *Squark and gluino production at*  
 3618 *hadron colliders*, *Nucl.Phys* **B492** (1997). 73
- 3619 [109] S. P. Leif Lonnblad, *Merging Multi-leg NLO Matrix Elements with Parton Showers*,  
 3620 [arXiv:1211.7278](https://arxiv.org/abs/1211.7278). 73
- 3621 [110] W. Beenakker, et al., *The Production of Charginos/Neutralinos and Sleptons at*  
 3622 *Hadron Colliders*, *Phys.Rev.Lett* **83** (1999). 73
- 3623 [111] C. Borschensky, et al., *Squark and gluino production cross sections in pp collisions*  
 3624 *at  $\sqrt{s} = 13, 14, 33$  and  $100 \text{ TeV}$* , *European Physical Journal C* **74** no. 12, . 73
- 3625 [112] R. E. J. Campbell and C. Williams, *Vector boson pair production at the LHC*,  
 3626 *JHEP* **07** (2011). 74

- 3627 [113] J. Campbell and R. Ellis, *An Update on vector boson pair production at hadron*  
 3628 *colliders*, Phys.Rev. **D60** (1999). 74
- 3629 [114] A. Kardos, and Z. Trocsanyi, and C.G. Papadopoulos, *Top quark pair production*  
 3630 *in association with a Z-boson at next-to-leading order accuracy*, Phys. Rev. D **85**  
 3631 (2012). 74, 125
- 3632 [115] J. M. Campbell and R. K. Ellis, *tt*W<sup>+-</sup> production and decay at NLO, JHEP **07**  
 3633 (2012) 052. 74
- 3634 [116] J. Campbell, R. K. Ellis, and R. Rontsch, *Single top production in association with*  
 3635 *a Z boson at the LHC*, Phys. Rev. **D87** (2013) 114006. 74
- 3636 [117] M. Aliev, et al., *HATHOR - HAdronic Top and Heavy quarks crOss section*  
 3637 *calculatorR*, Computer Physics Communications **182** (2011). 74
- 3638 [118] N. Kidonakis, *Next-to-next-to-leading-order collinear and soft gluon corrections for*  
 3639 *t-channel single top quark production*, Phys. Rev. D **83** (2011) 091503. 74
- 3640 [119] N. Kidonakis, *NNLL resummation for s-channel single top quark production*, Phys.  
 3641 Rev. D **81** (2010) 054028. 74
- 3642 [120] N. Kidonakis, *Two-loop soft anomalous dimensions for single top quark associated*  
 3643 *production with a W- or H-*, Phys. Rev. D **82** (2010) 054018. 74
- 3644 [121] S. Catani et al., *Vector boson production at hadron colliders: A Fully exclusive*  
 3645 *QCD calculation at NNLO*, Phys. Rev. Lett. **103** (2009) 082001. 74
- 3646 [122] S. Dittmaier, et al., *Handbook of LHC Higgs Cross Sections: 2. Differential*  
 3647 *Distributions*, CERN-2012-002 (2012). 74, 125
- 3648 [123] ATLAS Collaboration, *Measurement of the low-mass Drell-Yan differential cross*  
 3649 *section at  $\sqrt{s} = 7 \text{ TeV}$  using the ATLAS detector*, JHEP **06** (2014). 74
- 3650 [124] J. P. Lansberg, *Total J/Psi and Upsilon production cross section at the LHC:*  
 3651 *theory vs. experiment*, arXiv:1012.2815 [hep-ph]. 74
- 3652 [125] ATLAS Collaboration, *Multi-Boson Simulation for 13 TeV ATLAS Analyses*,  
 3653 <https://cds.cern.ch/record/2119986>. 75
- 3654 [126] ATLAS Collaboration, *Modelling of the tt>H and tt>V ( $V = W, Z$ ) processes for  $\sqrt{s} = 13 \text{ TeV}$  ATLAS analyses*, <https://cds.cern.ch/record/2120826>. 75
- 3656 [127] ATLAS Collaboration, *Simulation of top quark production for the ATLAS*  
 3657 *experiment at  $\sqrt{s} = 13 \text{ TeV}$* , <https://cds.cern.ch/record/2120417>. 75
- 3658 [128] ATLAS Collaboration, *Monte Carlo Generators for the Production of a W or Z/ $\gamma^*$  Boson in Association with Jets at ATLAS in Run 2*,  
 3659 <https://cds.cern.ch/record/2120133>. 75

- 3661 [129] ATLAS Collaboration, *Studies of Monte Carlo generators in Higgs boson*  
 3662 *production for ATLAS Run 2*, <https://cds.cern.ch/record/1978192>. 75
- 3663 [130] ATLAS Collaboration, *Expected Performance of the ATLAS Experiment -*  
 3664 *Detector, Trigger and Physics*, [arXiv:0901.0512 \[hep-ex\]](https://arxiv.org/abs/0901.0512). 78
- 3665 [131] ATLAS Collaboration, *Performance of the ATLAS muon trigger in pp collisions at*  
 3666  $\sqrt{s} = 8 \text{ TeV}$ , *Eur. Phys. J. C* **75** no. 3, (2015). 80
- 3667 [132] J. Reichert, on behalf of the ATLAS Collaboration, *The Upgrade and Performance*  
 3668 *of the ATLAS Electron and Photon Triggers Towards Run 2*,  
 3669 <https://cds.cern.ch/record/2058100>. 83
- 3670 [133] ATLAS Collaboration, *Search for the electroweak production of supersymmetric*  
 3671 *particles in  $\sqrt{s} = 8 \text{ TeV}$  pp collisions with the ATLAS detector*, [arXiv:1402.7029](https://arxiv.org/abs/1402.7029)  
 3672 [hep-ex]. 87, 106, 114, 133, 144, 146, 147, 167
- 3673 [134] <https://twiki.cern.ch/twiki/bin/view/Sandbox/StevenScrammBCHSandbox>.  
 3674 91
- 3675 [135] M. Shamos, F. Preparata, *Computational Geometry: Algorithms and Applications*.  
 3676 Springer-Verlag, 2008. 103
- 3677 [136] G. Cowan, *Statistical Data Analysis*. Clarendon Press, 1998. 103, 138
- 3678 [137] ATLAS Collaboration, *Search for supersymmetry in compressed scenarios with two*  
 3679 *and three leptons and missing transverse momentum in the final state in  $20.3 \text{ fb}^{-1}$*   
 3680 *pp collisions at  $\sqrt{s} = 8 \text{ TeV}$  with the ATLAS detector*,  
 3681 <https://cds.cern.ch/record/2004862>. 104, 108, 110, 111, 123, 124, 142, 143,  
 3682 146
- 3683 [138] J. Campbell and R. Ellis,  $t\bar{t}W +$  production and decay at NLO, *JHEP* **1207**  
 3684 (2012). 125
- 3685 [139] J. Butterworth, et al., *Single Boson and Diboson Production Cross Sections in pp*  
 3686 *collisions at  $\sqrt{s} = 7 \text{ TeV}$* , Tech. Rep. ATL-COM-PHYS-2010-695 (2010). 125
- 3687 [140] [http://www.hep.ucl.ac.uk/pdf4lhc/PDF4LHC\\_practical\\_guide.pdf](http://www.hep.ucl.ac.uk/pdf4lhc/PDF4LHC_practical_guide.pdf). 125
- 3688 [141] S. Alekhin, et al., *The PDF4LHC Working Group Interim Report*,  
 3689 [arXiv:1101.0536](https://arxiv.org/abs/1101.0536). 125
- 3690 [142] P. M. Nadolsky, et al., *Implications of CTEQ global analysis for collider*  
 3691 *observables*, *Phys. Rev. D* **78** no. 013004, (2008). 125
- 3692 [143] ATLAS Collaboration, *Jet energy scale and its systematic uncertainty in*  
 3693 *proton-proton collisions at  $\sqrt{s} = 7 \text{ TeV}$  with ATLAS 2011 data*,  
 3694 <https://cds.cern.ch/record/1509552>. 126

- 3695 [144] ATLAS Collaboration, *Jet energy resolution and selection efficiency relative to*  
 3696 *track jets from in-situ techniques with the ATLAS detector using proton-proton*  
 3697 *collisions at a centre of mass energy  $\sqrt{s} = 7 \text{ TeV}$ .*  
 3698 <https://inspirehep.net/record/1204034>. 127
- 3699 [145] ATLAS Collaboration, *Improved luminosity determination in  $pp$  collisions in  $\sqrt{s} =$*   
 3700  *$7 \text{ TeV}$  using the ATLAS detector at the LHC*, *Eur. Phys. J.* **C73** no. 8, (2013)  
 3701 **2518**, [arXiv:1302.4393 \[hep-ex\]](https://arxiv.org/abs/1302.4393). 127
- 3702 [146] Krämer, et. al, *Supersymmetry production cross sections in  $pp$  collisions at  $\sqrt{s} = 7$*   
 3703  *$\text{TeV}$* , [arXiv:1206.2892v1 \[hep-ph\]](https://arxiv.org/abs/1206.2892v1). 128
- 3704 [147] J. Alwall, et. al, *Comparative study of various algorithms for the merging of parton*  
 3705 *showers and matrix elements in hadronic collisions*, *Eur. Phys. J.* **C53** (2007). 128
- 3706 [148] A. L. Read, *Presentation of search results: the  $CL_s$  technique*, *Journal of Physics*  
 3707 *G: Nuclear and Particle Physics* **28** no. 10, (2002) 2693.  
 3708 <http://stacks.iop.org/0954-3899/28/i=10/a=313>. 136, 160
- 3709 [149] A. L. Read, *Modified frequentist analysis of search results (the  $CL_s$  method)*,  
 3710 <https://cds.cern.ch/record/451614>. 136, 138, 160
- 3711 [150] E. Gross, *LHC Statistics for Pedestrians*,  
 3712 <https://cds.cern.ch/record/1099994>. 136
- 3713 [151] G. Cowan, et al., *Asymptotic formulae for likelihood-based tests of new physics*,  
 3714 *Eur. Phys. J.* **C71** (2011), [arXiv:1007.1727 \[physics.data-an\]](https://arxiv.org/abs/1007.1727). 138
- 3715 [152] W. Beenakker, et al., *Squark and Gluino Hadroproduction*, *Int. J. Mod. Phys.* **A26**  
 3716 (2011). 149
- 3717 [153] W.Beenakker, R.Hoepker, M.Spira, *PROSPINO: A Program for the Production of*  
 3718 *Supersymmetric Particles in Next-to-leading Order QCD*, [arXiv:hep-ph/9611232](https://arxiv.org/abs/hep-ph/9611232)  
 3719 [\[hep-ph\]](#). 149
- 3720 [154] Eva Halkiadakis, George Redlinger and David Shih, *Status and Implications of*  
 3721 *Beyond-the-Standard-Model Searches at the LHC*, *Annual Review of Nuclear and*  
 3722 *Particle Science* **64** (2014) 319–342, [arXiv:1411.1427 \[hep-ex\]](https://arxiv.org/abs/1411.1427). 149
- 3723 [155] ATLAS Collaboration, *Muon reconstruction performance in early  $\sqrt{s} = 13 \text{ TeV}$*   
 3724 *data*, <https://cds.cern.ch/record/2047831>. 150
- 3725 [156] ATLAS Collaboration, *Expected performance of the ATLAS b-jet trigger in Run-2*,  
 3726 <https://cds.cern.ch/record/2032280/>. 151
- 3727 [157] ATLAS Collaboration, *Performance of the Missing Transverse Energy*  
 3728 *Reconstruction and Calibration in Proton-Proton Collisions at a Centre-of-Mass*

3729      *Energy of 7 TeV with the ATLAS Detector,.*  
3730      <https://cds.cern.ch/record/1281330.151>